UNIVERSITE PARIS.DIDEROT (Paris 7)
ECOLE DOCTORALE : Particules, Noyaux et Cosmos - ED517

THESE DE DOCTORAT DE L'UNIVERSITE PARIS VII

Spécialité: Physique des Particules

présentée par

Rachel QUEVAL

pour obtenir le grade de

DOCTEUR DE L'UNIVERSITE PARIS VII

Characterization, Modelization and Optimization of the Double Chooz acrylic vessels: Physics Impact

Thèse dirigée par Thierry LASSERRE

soutenue le 16 septembre 2010

JURY

M. Thomas PATZAK, Président
M. Thierry LASSERRE, directeur de thèse
M. Clarence VIRTUE, Rapporteur
M. Fabrice PIQUEMAL, Rapporteur
Mme. Florence ARDELLIER-DESAGES, examinateur

Remerciements

C'est un plaisir de finir cette thèse par les remerciements, pour exprimer tout ce qu'on pense et qu'on ne dit jamais. Je m'excuse par avance envers ceux que je vais oublier, je pense à eux tout de même.

Je tiens tout d'abord à remercier Ursula Bassler, de m'avoir accueillie au Service de Physique des Particules du CEA Saclay, en tant que chef de service.

Je remercie également Fabrice Piquemal et Clarence Virtue d'avoir accepté d'être les rapporteurs de ma thèse, avec le travail supplémentaire que cela leur a demandé, ainsi que de participer au jury. Je remercie également Thomas Patzak, qui m'a fait l'honneur d'être mon président de jury, ainsi que Florence Ardellier-Desages, qui en plus de participer à mon jury de soutenance, a été pendant la première partie de ma thèse notre coordinatrice technique sur Double Chooz et qui m'a toujours prodigué de bons conseils.

Plus particulièrement, j'exprime ma reconnaissance envers Thierry Lasserre, mon directeur de thèse. Il a su m'orienter, me motiver et me stimuler dans mon travail, tout en me laissant la latitude nécessaire pour mener à bien mes projets de recherche. Ce qu'il faut comprendre dans cette phrase, c'est que le cadre qu'il a donné à ma thèse dès le début m'a permis ensuite d'évoluer librement dans mes choix; ses conseils et remarques au cours de ces trois ans m'ont fait progresser et me structurer dans mon travail. Et même quand j'étais un peu trop têtue (et oui, je le reconnais, cela peut m'arriver), ou que nous n'étions pas d'accord, il a su insister quand il fallait et me laisser libre quand j'en avais besoin. Sans ses relectures, ce manuscrit serait certainement beaucoup moins clair... Thierry, merci pour ces trois ans.

Guillaume, Maximilien, vous aussi vous êtes investis dans mon travail et mon apprentissage. Mes problèmes de code, de statistiques et autres, vous les résolviez comme par magie! Guillaume, tu as apporté à ce manuscrit et dans mon esprit une grande clarté notamment sur la théorie des neutrinos, et Maximilien, tu es aussi beaucoup pour la qualité de l'anglais. Egalement, vous avez supporté mes coups de fatigue, d'énervement, d'euphorie aussi, et dans cette ambiance de travail, vous avez su m'apporter des moments de détente et de franche rigolade, osons le dire! Je pense notamment à notre ami Germanium...
Michel, je t'envoie toute mon amitié, tu as donné à ma thèse des moments inoubliables. Merci pour tous tes conseils, il sont précieux.
Vincent, notre nouveau petit thésard, j'espère que j'ai pu te montrer tout ce que je savais avant de partir! Merci d'avoir été là quand il fallait.

Thomas et Tarek, c'est avec une certaine nostalgie que je veux parler de nos trois thèses que nous avons commencées et que nous avons partagées ensemble. C'était vraiment un bonheur

4

de vous avoir eu comme compagnons de route; nous avons découvert ensemble un monde qu'on ne connaissait pas vraiment, nous avons appris ensemble à y évoluer et je suis fière d'y avoir trouvé des amis. Thomas, nous avons été plus proches, d'abord de par notre situation géographique commune. S'est ensuite développée une belle amitié, autour de chiffons ISO4, de nettoyages d'échaffaudages immondes, de remplissages de gros tanks laborieux, d'escapades en shift d'intégration à Chooz... Merci à toi. Le groupe des thésards français va me manquer.

Je voudrais aussi remercier tout le groupe des ingénieurs et techniciens de Double Chooz de Saclay. Loris et Jeff, c'est un plaisir de vous rendre visite au 123 où les bons mots fusent à une rapidité impressionnante, François et ses fameux nains, Patrick, sans qui les voyages à Chooz ne seraient pas ce qu'ils sont, Pierre et Serge, toujours prêts à nous sauver de situations compliquées, comme fabriquer une tente propre à l'ALS en moins d'une après-midi, Claude, qui arrive toujours à trouver le matériel dont on a besoin même quand on pense que c'est impossible.

Merci aussi à l'agora: Philippe B, Dominique, Michel, Philippe G, Jean-Marc, vous avez toujours réussi à passer toutes mes commandes même avec les délais impossibles que je demandais! Et évidemment, merci pour Agorette, que j'emporterai avec moi...

Merci aussi à tous mes copains de discussion/café/cigarette, Emilie, Pierre mon parrain, Nathalie ma marraine de coeur, Andrea, Jessica, Michela que je ne vois pas assez souvent, Gilles, Niccolo, Claire, Eric, Jonathan et tous les autres.

Je tiens à remercier toute la collaboration Double Chooz en général, cela a été un plaisir de travailler avec vous. J'ai une pensée spéciale pour David et Alain au SPhN, je tiens à vous exprimer toute ma sympathie.

Enfin, je voudrais remercier mes parents, qui m'ont permis de réaliser tout ce que je voulais entreprendre, qui m'ont apporté soutien et réconfort. Je ne vois rien de plus significatif à dire que: je vous aime. Philippe, tu partages ma vie depuis quatre ans maintenant, et tu as supporté la fin de thèse avec brio, malgré tous les moments difficiles. Merci du plus profond de mon coeur, et j'ai hâte de commencer une nouvelle phase de notre vie à deux.

Je termine par une pensée pour Dario...

Contents

Introduction

Neutrino existence was postulated in 1930 to restore the conservation of energy in beta decay. Indeed, in 1914, J. CHADWICK showed that electrons emitted in beta decay did not have a discrete energy; instead, they had a continuous spectrum of energies. This is how in 1930, in a letter to the group of the Radioactives, W. PAULI first postulated the existence of a new subatomic particle to "save conservation energy law in beta decay". To produce the wanted energy spectrum, this new particle must be neutral and extremely light. The name neutrino (« little neutral one ») was found by the team of E. FERMI, who developed the first theory describing neutrino interactions. In 1933, they published a complete theory of the weak interaction, one of the three forces acting on elementary particles, including neutrinos. This article was refused by Nature for being « too far away from physical realities ». The problem was it seemed practically impossible to detect neutrinos after they had been emitted by radioactive atoms; actually, neutrinos could penetrate several light years depth of ordinary matter before they would be stopped. Thus, F. REYNES and his colleague C. L. COWAN decided to study the only one process which neutrinos could certainly cause: the inverse beta decay, consisting in the interaction of a neutrino with a proton with the emission of a positron and a neutron. This detection method is still used.

Nowadays, particle physics is described by the Standard Model, validated by a great many experimental results. In this model, neutrinos are massless particles. However, at the end of the XXth century, experiments have proved neutrinos to be massive through flavor oscillations they observed. The mass of neutrinos is the first evidence of physics beyond the Standard Model.

In the present report, after a brief theoretical introduction on the neutrino in the Standard Model and beyond, a phenomenological landscape is drawn stating the latest results on leptonic mixing parameters (chapter 1). I then focus on our subject of interest, measuring the last unknown mixing angle θ_{13} (chapter 2). Different experiments around the world are starting, with this measurement as a goal. Three reactor experiments (Double Chooz, Daya Bay and RENO) characteristics are compared, while their complementarity with accelerator ones (T2K and NOνA) is studied.

The rest of this thesis is dedicated to the Double Chooz experiment. It measures electronic antineutrino oscillations near the Chooz power plant (French Ardennes). It is conducted by an international collaboration at the CHOOZ experiment site, which actually gave the best constraint on θ_{13}. In order to improve this result, one has to increase the statistics, this by having a larger neutrino Target and a longer run. Also, systematic errors have to be reduced

by better understanding the backgrounds coming from natural radioactivity and cosmic rays, but also the uncertainties on the reactor antineutrino flux and the detector. Most of these almost cancel thanks to the use of a near detector, located close enough to the reactor cores so that detected antineutrinos have not oscillated yet. The detector design is based on the Russian nested dolls system. Its core is composed of two acrylic vessels filled with different liquid scintillators, the inner one to perform the actual neutrino detection and the outer one to catch the energy that might escape the first one. The construction of the acrylic vessels was a technical innovation; Néotec, the manufacturer, was awarded the Midest (world's leading industrial sub-contracting show) trophy 2009 in the category extraordinary realizations. The detector and these vessels in particular are described in chapters 3 and 4.

Since acrylic vessels are in the core of the detector, specific studies about them were performed (chapters 5 to 9). First of all, the material used had to be characterized optically, since they are located between the active medium and the detection system. This lead to the creation of a new acrylic material, developed by Degussa, the n°1 acrylic provider in Europe, and CEA Saclay. Furthermore, being surrounded by liquid scintillators, the vessels' radioactivity had to be checked to make sure the induced background is reduced to minimum. With this in mind, the whole production, construction and integration of the vessels was performed in a clean environment, since external dust might be slightly radioactive and also induce background. Moreover, external dust in the vessels might, once they are filled, cloud the liquids. I also performed physics studies for design optimization, such as the thickness of the vessels. These studies allowed to merge physics needs for a better antineutrino detection and mechanical constraints. Finally, to further reduce systematic errors, the vessels had to be as identical as possible. The different metrology devices as well as a statistical study to compare them are described in chapter 9.

The last chapter relates the fabrication and integration of the vessels, the integrated related systems, the issues overcome during these phases and the tests performed on the integrity of the vessels.

Chapter 1

The Neutrino

Neutrinos, they are very small.

They have no charge and have no mass

And do not interact at all.

The Earth is just a silly ball

To them, through which they simply pass,

Like dustmaids down a drafty hall

Or photons through a sheet of glass

J. Updike[1]

Neutrinos are elementary particles: they are constituents of matter which, up to now, do not appear to be composed of smaller elements. They do not carry electrical charge and are able to go through ordinary matter practically without interacting, which makes their detection a real challenge. Indeed, 26 years were needed to go from a theoretical prediction in 1930 to their experimental discovery!

1.1   Neutrinos and the Standard Model

The Standard Model of particle physics (SM) is a theory describing the strong, weak and electromagnetic interactions as well as all of the elementary particles constituting matter. This is a quantum field theory naturally based on quantum mechanics principles and relativity. There are 36 elementary particles described by the SM (cf. figure 1.1):

- 24 spin ½ fermions, the matter particles, separated in two categories: 6 quarks (and their antiquarks) which form hadrons and mesons, and 6 leptons (and their antileptons).

---

[1]From 'Cosmic Gall' in *Telephone Poles and Other Poems*, André Deutsch, London (1964)

These quarks and leptons are separated into families, which have the same intrinsic couplings (a measure of the strength of a type of interaction between particles) for the three interactions. Neutrinos fall into this category.

- 12 spin 1 bosons, the interaction particles: 8 gluons which mediate the strong interaction, the weak interaction bosons W^+, W^- and Z^0, and the photon which mediates the electromagnetic force. These mediation theories are called gauge theories because they have a characteristic symmetry called gauge invariance.

Finally, the Higgs boson, resulting from the spontaneous symmetry breaking of the electroweak field, is still to be discovered, possibly at the Large Hadron Collider at CERN [1]. There
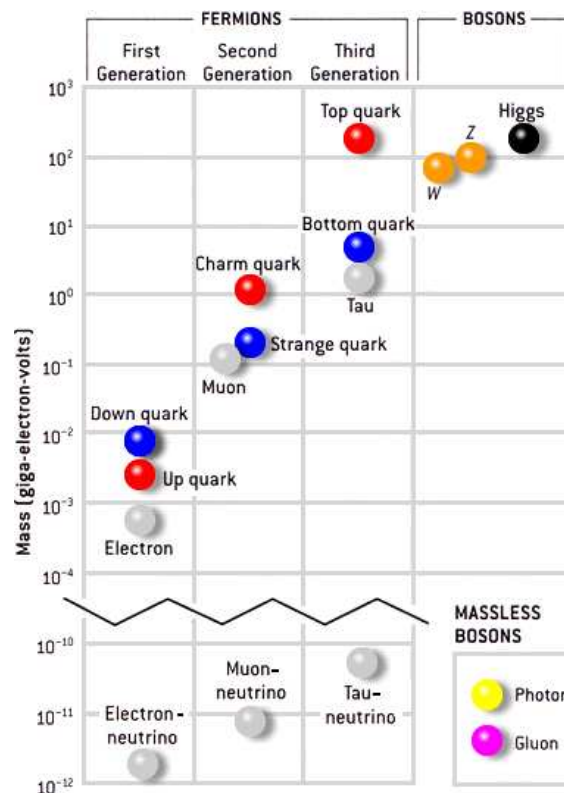
Figure 1.1: Standard model elementary particles and their mass hierarchy. In this figure, one can see that the neutrino masses order of magnitude is very different from the other particles. It is to note that the neutrino mass hierarchy is unknown at the moment.

are 4 fundamental interactions in the Universe. First, the gravitational force, acting on every particle, is described at a macroscopic scale by general relativity. Then, the electromagnetic force acts on electrically charged elementary particles. The weak force, acting on fermions, is mostly known as the origin of β radioactivity. Finally, the strong force acts on quarks and gluons and holds the atomic nucleus together. The SM does not take into account gravity, since there is no satisfactory microscopic description of it [2].

The three fundamental interactions of the SM are mediated by gauge bosons and they each have a coupling constant, which contributes to characterize the strength of an interaction and

depends on the energy (the low energy values are given here). The strong interaction bosons are massless and the coupling constant is 1. The weak interaction bosons are heavy and the coupling constant is 1/32. Finally, the electromagnetic force is mediated by massless photons and their coupling constant is 1/137. Then, why is the weak interaction the weakest of all? Two reasons can be found. First of all, the weak interaction can only occur at small ranges, once again because of the $W^\pm$, Z^0 bosons' large masses (80 - 90 GeV). The range of an interaction for a boson B is defined as [2]:

$$R = \frac{\hbar}{M_B c} \tag{1.1}$$

$\hbar$ being the Planck constant, c the speed of light. Therefore, the electromagnetic interaction has an infinite range, the exchanged particle being a massless photon. On the contrary, the weak interaction is associated with heavy bosons, leading to an interaction range of roughly 2×10^{-3} fm. This is small compared to the typical size of a nucleon (~ 1 fm). The weak interaction can then be approximated by a point interaction, corresponding to the limit $M_B \to \infty$ in equation (1.1). Second of all, the cross section of an interaction does not depend only on its coupling constant. According to the Born approximation [3], the probability amplitude for a particle to be scattered from an initial momentum $\mathbf{p_i}$ to a final momentum $\mathbf{p_f}$ by a potential $V(\mathbf{x})$, $\mathbf{x}$ being the particle displacement, is proportional to:

$$\mathcal{M}(\mathbf{p}) = \int d^3\mathbf{x}\, V(\mathbf{x}) e^{-i\mathbf{p}\cdot\mathbf{x}/\hbar} \tag{1.2}$$

with $\mathbf{p}$ being the momentum transfer ($\mathbf{p}$=$\mathbf{p}_f$-$\mathbf{p}_i$). Equation (1.2) gives :

$$\mathcal{M}(\mathbf{p}) = \frac{-g^2\hbar^2}{|\mathbf{p}|^2 + M_B^2 c^2} \tag{1.3}$$

M_B being the boson mass ($W^\pm$, Z^0). In the point-like approximation, $|\mathbf{p}|^2 \ll M_B^2 c^2$, thus equation (1.3) leads to

$$\mathcal{M}(\mathbf{p}) = -\left(\frac{g}{M_B c^2}\hbar c\right)^2 = -G \tag{1.4}$$

where G is a constant. In this approximation, the resulting point interaction is characterized by a single dimensional coupling constant G, the Fermi coupling constant, and not g and the boson mass separately. Then, even though the electromagnetic coupling is smaller than the weak interaction one, the bosons' huge mass implies that the so-called weak interaction is indeed the weaker one.

1.1.1 A little bit of history

The neutrino was first proposed in the physics community by W. PAULI in 1930 [4] to solve a problem that was quite dramatic at the time: the apparent violation of the energy conservation law in β decays. Indeed, β decays were thought to follow the reaction:

$$^A_Z X \to^A_{Z+1} Y + e^- \tag{1.5}$$

According to the energy conservation law, the electron energy was to be equal to the mass difference of the two nuclei involved in equation 1.5. The electron energy was thus supposed

to be peaked at a given energy, and instead a continuous energy spectrum was observed! This could be explained by the existence of a particle possessing the energy and momentum necessary to compensate the difference between the initial and final particles. This particle had to be neutral, of spin $1/2$, extremely light compared to the electron and would escape at a speed near the speed of light once created. In 1933, E. FERMI elaborated the first theory of the weak interaction in order to describe beta decay [5], including W. PAULI's hypothetical neutrino.

The neutrino was discovered experimentally only 26 years later by F. REINES and C. L. COWAN [6]. Their idea was to use the inverse beta decay reaction:

$$\overline{\nu_e} + p \rightarrow n + e^+ \tag{1.6}$$

The detector was made of multiple layers of scintillation counters (liquid scintillator, recently discovered) and target tanks filled with Cadmium Chloride ($CdCl_2$) and water. Free protons in the water (H atoms from H_2O molecules) tanks were used as targets for the incident neutrinos. The Cadmium Chloride was used for neutron detection; once produced, the neutron thermalized (loses its kinetic energy by collisions in the medium) in the liquid and then got captured by a Cadmium nucleus (cross section of 8×10^4 b for an incident neutron of $1/40$ eV), generating multiple gamma rays. The purpose of the liquid scintillator was to detect this gamma shower as well as the two 511 keV gammas coming from the annihilation of the positron with a medium electron. Three layers of the detector are shown in figure 1.2. The key point was that the
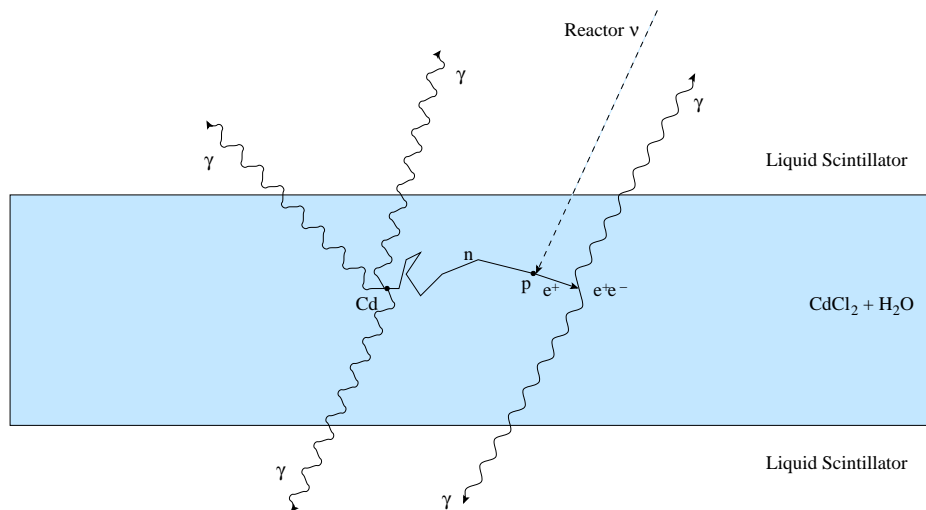
Figure 1.2:   Schematic picture of the neutrino detector imagined by F. REINES and C. L. COWAN [6]. The target was made of Cadmium Chloride and water and the detection medium was liquid scintillator. The antineutrino coming from the reactor interacted with a free proton in the water target, generating a positron, annihilating with an electron, and a neutron, being captured by a Cd nucleus, both events happening within a few microseconds.

two resulting particles from equation (1.6) were detected in time coincidence (within 20 microseconds). This means that the antineutrino signal was defined as two events of known energy detected within a definite time window. Such a coincidence was a strong signature of a neutrino event, leading to an easier determination of the signal versus background (internal radioactivity,

for example). The detector imagined by F. REINES and C. L. COWAN was a revolution in terms of size: they estimated that one ton of liquid would be necessary to compensate for the small interaction cross section, which is used to express the possibility of interaction between particles (10^{-45} cm^2 for neutrinos of the order of 1 MeV). Until that day, the largest detector ever made with liquid scintillator was one liter... In 1956, the two colleagues conducted their experiment near the nuclear plant of Savannah River, South Carolina, to use the large flux of neutrinos (10^{13} cm^{-2}s^{-1} for a 1,000 MW reactor) coming from the reactor. With a count rate of roughly 3 events per hour, they proved the existence of what was determined later to be the electron antineutrino [6].

Since the first discovered neutrino (or antineutrino) was clearly bound to the electron through inverse β decay, physicists were led to postulate the existence of a second neutrino species, or flavor, associated to the muon, which interacts in the same way as the electron but has a different mass. This new particle was discovered a few years later in the Brookhaven experiment, in 1962, by M. SCHWARTZ, L. M. LEDERMAN, J. STEINBERGER and J.-M. GAILLARD [7]. Finally, after the discovery in the 70's of the second cousin of the electron, the tau, it seemed logical to expect a third kind of neutrino, the tauic neutrino. However, it was discovered no sooner than 2000 by the DONuT experiment [8], partly because of the high mass of its associated lepton and thus the need for a highly energetic neutrino beam to initiate the detection reaction.

1.1.2 The electroweak interaction and particles masses

The Standard Model of particle physics is based on the relativistic quantum gauge field theory. In the 1920's, physicists tried to combine the quantum mechanics of W. HEISENBERG and E. SCHRÖDINGER with the special relativity of A. EINSTEIN. This is when relativistic quantum field theory emerged. For instance, in the classical electromagnetism case, Maxwell's equations possess a special local symmetry called gauge invariance whereby the photon field (or vector potential), transforms as:

$$A_\mu(x) \rightarrow A_\mu(x) - \partial_\mu \alpha(x) \qquad (1.7)$$

while leaving all physical observables unchanged. In this example, these transformations form a gauge group known as the unitary group U(1)^2. All three fundamental forces of the SM can be described in terms of unitary groups of different dimensions; this combination of gauge groups is written as SU(3)×SU(2)$_L$×U(1). The SU(3) group is the gauge group of the strong interaction theory. The SU(2)$_L$×U(1) group concerns electroweak unification. This group has massless gauge bosons to mediate the weak nuclear force (gauge invariance can be shown to imply that spin-1 gauge bosons have zero masses [2]). However, we know these bosons, $W^\pm$ and Z^0, are massive [9]. This anomaly is understood by assuming that particles interact with a new type of scalar field, the Higgs field, giving them masses in the process.

Let us have a closer look at the electroweak theory; the fermionic Lagrangian can be written

---

^{2}The unitary group U(N) is the group of N×N unitary matrices. SU(N) is a special unitary group; it is U(N) with det(U)=1.

as [10]:

$$\mathcal{L}_\text{F} = \sum_i \overline{\psi_i} \left(i\partial_\mu \partial^\mu - m_i - \frac{gm_i H}{2M_W} \right) \psi_i$$
$$- \frac{g}{2\sqrt{2}} \sum_i \overline{\psi_i}\gamma^\mu \left(1 - \gamma^5\right) \left(T^+ W_\mu^+ + T^- W_\mu^-\right) \psi_i$$
$$- e\sum_i q_i \overline{\psi_i}\gamma^\mu A_\mu \psi_i$$
$$- \frac{g}{2\cos\theta_W} \sum_i \overline{\psi_i}\gamma^\mu \left(g_V^i - g_A^i \gamma^5\right) Z_\mu \psi_i \qquad (1.8)$$

The first term of the fermionic Lagrangian (equation (1.8)) corresponds to the Dirac equation and the Higgs interaction. The second term represents the charged-current weak interaction, the third term the electromagnetic interaction and the last term the neutral-current weak interaction. Here, we are interested in the way fermions gain mass through the Higgs field, meaning we will not review all of the terms of the Lagrangian. Let's first consider the coupling to the $W^\pm$ bosons [11]:

$$\mathcal{L}_\text{W} = \frac{\text{g}}{\sqrt{2}} \left(W_\mu^+ J^\mu + W_\mu^- J^{\mu\dagger} \right) \qquad (1.9)$$

g being the weak interaction coupling constant, J^μ being the weak current that creates electrically charged particles, $J^{\mu\dagger}$ the one that annihilates them, defined in equation (1.10) [11]:

$$J^\mu = \sum_i u_{0i}^\dagger \sigma^\mu d_{0i} + \nu_{0i}^\dagger \sigma^\mu e_{0i} \qquad (1.10)$$

σ^μ is a 4-vector based on Pauli matrices, the 0 indices are linked to the flavor eigenstates. As
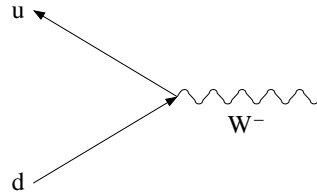
Figure 1.3: Feynman Diagram of a W^- coupling. A d quark is annihilated to create a u quark, raising this way the electrical charge. It is conserved through the production of a W^-.

an example, J^μ annihilates a left d quark (cf. figure 1.3) to create a left u quark, raising the electrical charge by one unit. It is however conserved through the absorption of a W^+ (or production of a W^-) in the $W^+ J^\mu$ coupling of the Lagrangian (equation (1.9)). One has to notice that in equation (1.9) the field conjugates are not to be found. This implies that they only act on left-handed fermions, or right-handed antifermions. The weak interaction does not act on right-handed fermions; they are singlets under this transformation. Therefore the weak force violates parity conservation, violation which was proved by C. S. Wu and coworkers in 1957 [12]. They placed a sample of ^{60}Co inside a solenoid and cooled it to a temperature of 0.01 K. At such temperatures, the interaction of the magnetic moments of the nuclei with the magnetic field overcomes the tendency to thermal disorder, and the nuclear spins align parallel to the field direction. The polarized ^{60}Co nuclei decay to an excited state of ^{60}Ni by the process:

$$^{60}Co \rightarrow {}^{60}Ni^* + e^- + \overline{\nu_e}$$

Parity transformation reverses all particle momenta **p** while leaving their orbital angular momenta **r** × **p**, and by analogy their spin angular momenta, unchanged. Hence, in the rest frame of the decaying nuclei its effect is to reverse the electron velocity while leaving the nuclear spins unchanged, as shown in figure 1.4. Parity invariance would then require that the rates for
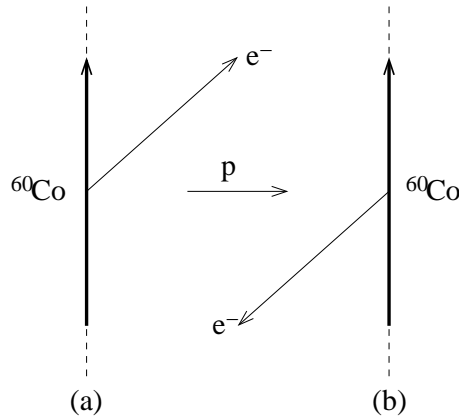
Figure 1.4: Effect of a parity transformation on ^{60}Co decay. The short thick arrows indicate the direction of the spin of the ^{60}Co nucleus, while the long arrows show the direction of the electron's momentum. Parity invariance would ensure that the rates for the two processes are equal.

the two processes shown in figure 1.4 were equal, so that equal numbers of electrons would be emitted in the forward and backward hemispheres, with respect to the nuclear spins. However, what was observed was a "forward-backward decay asymmetry", i.e. the fact that fewer electrons are emitted in the forward hemisphere than in the backward one with respect to the spins of the decaying nuclei. This asymmetry implies that the interaction as a whole violates parity conservation. In 1958, M. GOLDHABER et al. [13] performed an experiment to determine the neutrino helicity, concluding that neutrinos were left-handedly spin polarized. The helicity assignments for the leptons in the Standard Model emitted in nuclear β-decay are therefore as follows [14]:

$$\begin{array}{lcccc} \text{Particle} & e^+ & e^- & \nu & \bar{\nu} \\ \text{Helicity} & +v/c & -v/c & -1 & +1 \end{array} \tag{1.11}$$

The discovery of parity violation led to the V-A interaction theory. The letter V denotes a proper vector (one whose direction is reversed by parity transformation). Because parity is not conserved in weak interactions, the weak current has in addition to the proper vector another component whose direction is unchanged by a parity transformation. Such a quantity is called an axial vector (A). V- and A-interactions result in lepton and antilepton of opposite helicities [14], in agreement with M. GOLDHABER's experiment.

Therefore, the weak force only interacts with left-handed particles and parity is violated. Neutrinos only exist through the weak field, thus we can assume in the SM that right-handed neutrinos do not exist. This is not true for the other particles, since they interact with the electromagnetic current, which does not violate parity conservation, hence both right- and left-handed particles exist. This has a huge importance when we start thinking about masses. As

said earlier, particles gain masses through their interactions with the Higgs field: the isospin Higgs doublet (h^+, h^0) interacts with fermion doublets through Yukawa couplings [11].

$$
\begin{aligned}
\mathcal{L}_{\text{Yukawa}} \quad &= \sum_{i,j} \quad u_{0i}^c \, (Y_u)_{ij} \left[u_{0j} h^0 - d_{0j} h^+ \right] + d_{0i}^c \, (Y_d)_{ij} \left[u_{0j} h^{+\dagger} + d_{0j} h^{0\dagger} \right] \\
&+ \quad \nu_{0i}^c \, (Y_\nu)_{ij} \left[\nu_{0j} h^0 - e_{0j} h^+ \right] + e_{0i}^c \, (Y_e)_{ij} \left[\nu_{0j} h^{+\dagger} + e_{0j} h^{0\dagger} \right]
\end{aligned}
\tag{1.12}
$$

Yukawa couplings Y_u, Y_d, Y_ν and Y_e are complex 3×3 matrices giving the amplitude of the coupling between fermions and the Higgs bosons. Only the h^0 component may have a non-zero expectation value in vacuum, leading to spontaneous symmetry breaking: $\langle h^0 \rangle = v/\sqrt{2}$ (v being the vacuum energy value: 246 GeV).This implies a permanent interaction with fermions and then the mass term of each fermion is [11]:

$$
\begin{aligned}
\mathcal{L}_{\text{Mass}} \quad &= \sum_{i} \quad u_{0i}^c \, (Y_u)_{ij} \, u_{0j} \left\langle h^0 \right\rangle + d_{0i}^c \, (Y_d)_{ij} \, d_{0j} \left\langle h^0 \right\rangle^{\dagger} \\
&+ \quad \nu_{0i}^c \, (Y_\nu)_{ij} \, \nu_{0j} \left\langle h^0 \right\rangle + e_{0i}^c \, (Y_e)_{ij} \, e_{0j} \left\langle h^0 \right\rangle^{\dagger}
\end{aligned}
\tag{1.13}
$$

Here, one has to stop and realize that each term of the mass Lagrangian (equation (1.13)) contains the product of a fermionic field and its conjugate. By definition, this product annihilates a left-handed fermion to produce a right-handed fermion. This implies that for a neutrino to have mass, it has to exist in both left and right chiralities. However, in the SM of particle physics, only left-handed neutrinos have been included, for simplicity and because there is no evidence of right-handed neutrinos (they do not interact through weak interaction). Thus, it was assumed that neutrinos were massless particles.

1.2   Neutrinos beyond the Standard Model

In the 1960's physicists started to set up experiments to confirm the "nuclear star theory", focusing on our star, the Sun. In its core, interactions producing electronic neutrinos take place (see section 1.3.2). The most abundant neutrinos coming from the Sun are the pp neutrinos, of low energy (ν_e (pp), E < 0.42 MeV), the mono-energetic Beryllium neutrinos (ν_e (Be), E = 0.8 MeV) and the more energetic Boron neutrinos (ν_e (B), E < 14 MeV). The first experiment to detect electronic solar neutrinos was the Homestake experiment, lead by R. DAVIS JR, in a South Dakota mine, under 3,000 m of rock and earth. Its huge detector made of 600 tons of industrial solvent based on chlorine was supposed to test theoretical models explaining the internal behavior of the Sun, not to upgrade our knowledge on neutrinos. However in 1968, the results of R. DAVIS JR were a real surprise [15]. Indeed, they showed a huge lack of neutrinos compared to what was expected from the theoretical predictions: three times less neutrinos were observed! Other experiments, like SAGE (Russia) and GALLEX (Italy), were set up to explain this puzzle, the "solar neutrino problem". They all confirmed the lack of neutrinos: roughly 60 % of them were missing (this fraction depends on the neutrino energy). However, the detection of the other 40 % confirmed the nuclear star theory.

In 1999, the SNO experiment (Canada) started taking data [16]. A special feature of that experiment is that it can distinguish between the electronic neutrinos, to check their disappearance, and the total number of neutrinos from the Sun. Without any surprises, the lack of

electronic solar neutrinos was confirmed. But SNO discovered the appearance of the other two flavors of neutrinos in the solar neutrino flux [17, 18]. The meaning of this result is straightforward: during their journey towards the Earth, a portion of ν_e is transformed into ν_μ and ν_τ. The mechanism to explain this phenomenon is the neutrino oscillation, for which an early description was proposed by B. PONTECORVO in 1957 [19] through a neutrino, antineutrino oscillation.

1.2.1 Neutrino oscillation consequences

Neutrino oscillations have been unveiled by several experiments, leading to an evolution of the SM in the leptonic sector. This implies that the neutrinos have masses and that leptons mix.

In the theory of neutrino oscillations, a neutrino with flavor α and momentum $\mathbf{p}$ created in a charged-current weak interaction process from a charged lepton l_α^- or together with a charged antilepton l_α^+ is described by the flavor state

$$|\nu_\alpha\rangle = \sum_k U_{\alpha k}^* |\nu_k\rangle \tag{1.14}$$

$U_{\alpha k}^*$ being the "weight" of $|\nu_k\rangle$ in the flavor state $|\nu_\alpha\rangle$. We can describe with the Schrödinger equation the evolution of the neutrino as a plane wave when propagating in vacuum [20]:

$$|\nu_k(t)\rangle = e^{-iE_k t} |\nu_k(0)\rangle \tag{1.15}$$

Let us consider a flavor state $|\nu_\alpha(t)\rangle$ which describes a neutrino created with a definite flavor α at time t=0. From equations (1.14) and (1.15), the time evolution of this state is given by

$$|\nu_\alpha(t)\rangle = \sum_k U_{\alpha k}^* e^{-iE_k t} |\nu_k(0)\rangle \tag{1.16}$$

The amplitude of a transition from ν_α to ν_β as a function of time is given by

$$A_{\nu_\alpha \to \nu_\beta}(t) \equiv \langle \nu_\beta | \nu_\alpha(t) \rangle = \sum_k U_{\alpha k}^* U_{\beta k} e^{-iE_k t} \tag{1.17}$$

The transition probability is directly given by

$$P_{\nu_\alpha \to \nu_\beta}(t) = \left| A_{\nu_\alpha \to \nu_\beta}(t) \right|^2 = \sum_{k,j} U_{\alpha k}^* U_{\beta k} U_{\alpha j} U_{\beta j}^* e^{-i(E_k - E_j)t} \tag{1.18}$$

For ultrarelativistic neutrinos, the dispersion relation can be approximated by:

$$E_k = \sqrt{\mathbf{p}^2 + m_k^2} \simeq E + \frac{m_k^2}{2E}, \qquad \text{with } E = |\mathbf{p}| \tag{1.19}$$

Which means

$$E_k - E_j \simeq \frac{\Delta m_{kj}^2}{2E}, \qquad with \ \Delta m_{kj}^2 = m_k^2 - m_j^2 \tag{1.20}$$

Finally, one has to take into account the fact that in neutrino oscillation experiments the propagation time t is not measured. However, the distance L between the source and the detector is known, and since ultrarelativistic neutrinos propagate almost at the speed of light, it is possible to approximate $t = L$. So, substituting equation (1.20) into equation (1.18), one gets:

$$P_{\nu_\alpha \to \nu_\beta}(t) = \left| A_{\nu_\alpha \to \nu_\beta}(t) \right|^2 = \sum_{k,j} U^*_{\alpha k} U_{\beta k} U_{\alpha j} U^*_{\beta j} \, \exp\left(-i \frac{\Delta m^2_{kj} L}{2E} \right) \qquad (1.21)$$

Therefore, the probability of neutrino oscillation is directly related to the neutrino masses. This means that the obvious proofs collected by different experiments on neutrino oscillations also prove that neutrinos have mass, in contradiction with the SM.

1.2.2   Neutrino masses

The fermionic field can be decomposed according to chirality as: $\nu = \nu_L + \nu_R$, ν_L and ν_R being chiral fields[3]. If the fermion does not have any mass, the equations of motion of the fermionic chiral fields can be decoupled. Starting with the Dirac equation:

$$\left(i\gamma^\mu \partial_\mu - m_\psi \right) \psi = 0 \qquad (1.22)$$

γ^μ being the four (4 x 4) Dirac matrices and ψ the wavefunction representing the fermion of mass m_ψ in quantum field theory, one can write down:

$$\begin{cases} i\gamma^\mu \partial_\mu \nu_L &= 0 \\ i\gamma^\mu \partial_\mu \nu_R &= 0 \end{cases} \qquad (1.23)$$

Fermions of zero mass can then be described by only one chiral field (right- or left-handed) with two components, and the ν_L and ν_R spinors are called Weyl spinors. In the SM, neutrinos are described by left-handed Weyl spinors.

If the fermion is massive, the equations of motion of the chiral fields are coupled to the fermion mass m_ν:

$$\begin{cases} i\gamma^\mu \partial_\mu \nu_L &= m_\nu \nu_R \\ i\gamma^\mu \partial_\mu \nu_R &= m_\nu \nu_L \end{cases} \qquad (1.24)$$

Two descriptions are possible to introduce massive neutrinos, Dirac's and Majorana's.

1.2.2.1   Dirac mass

A Dirac neutrino mass can be generated with the same Higgs mechanism that gives masses to quarks and charged leptons in the SM (see section 1.1) and a similar Lagrangian. The only extension of the SM needed is the introduction of right-handed components $\nu_{\alpha R}$ of the neutrino

---

[3]Chiral projection: $\nu = (P_L + P_R)\nu = \left(\frac{1}{2}\left(1 - \gamma_5\right) + \frac{1}{2}\left(1 + \gamma_5\right) \right)\nu = \nu_L + \nu_R$; if we use the representation of Dirac matrices, γ_5 is the product: $\gamma_5 = i\gamma_0 \gamma_1 \gamma_2 \gamma_3$.

fields (α = e, μ, τ). Such a model is sometimes called the *minimally extended Standard Model*, in which the asymmetry in the SM between the lepton and quark sectors due to the absence of right-handed neutrino fields is eliminated.

The mass of a particle is its rest energy in vacuum. This energy can be represented by the particle Hamiltonian (kinetic and potential energies) which is linked to the Lagrangian through the kinetic energy:

$$\mathcal{L} = 2E_k - \mathcal{H} \tag{1.25}$$

$\mathcal{L}$ being the Lagrangian, E_k the particle kinetic energy, $\mathcal{H}$ the Hamiltonian. At rest, there is of course no kinetic energy and therefore equation (1.25) becomes $\mathcal{L} = -\mathcal{H}$. The Lagrangian formalism is usually preferred because space and time coordinates are viewed in the same way. The Dirac mass of neutrinos is written m_ν^D and the corresponding Lagrangian is:

$$\mathcal{L}_{mass}^D = -m_\nu^D \left(\overline{\nu_R} \nu_L + \overline{\nu_L} \nu_R \right) \tag{1.26}$$

Note that right-handed neutrino fields are singlets of SU(3) x SU(2)$_L$ and therefore invariant under the symmetries of the SM. They are called *sterile* because they do not have any interactions in the SM.

This solution is quite straightforward to make neutrinos massive but there still are unexplained features of this model. For example, the fact that the Yukawa coupling Y_ν introduced in the mass Lagrangian [20] would have to be 6 to 12 orders of magnitude smaller than the others in order to explain the smallness of neutrino masses is unexplained.

1.2.2.2   Majorana mass

Considering equation (1.24) leads us to speak about Majorana spinors. E. MAJORANA proposed that ν_L and ν_R are not independent, as they are in Dirac's description. Those two equations would then be two different expressions of the same equation under the condition that:

$$\nu_R = \xi \mathcal{C} \overline{\nu_L}^T = \eta_\mathcal{C} \nu_L^c \tag{1.27}$$

ξ being a phase factor that can be absorbed by rephasing ν_L and $\mathcal{C}$ being the charge conjugation matrix. Then, only the ν_L field appears in the equation and $\nu_L^{\mathcal{C}}$ is a right-handed field. The choice of the $\eta_\mathcal{C}$ phase is not important since charge conjugation is violated by the weak interaction and since neutrinos are only sensitive to this interaction [20]. We can then set this phase to 1. Finally, from equation (1.27):

$$\nu_L^c = \mathcal{C} \overline{\nu_L}^T \tag{1.28}$$

Equation (1.28) leads to the expression of the Majorana field:

$$\nu = \nu_L + \nu_L^c \qquad \text{implying} \qquad \nu = \nu^c \tag{1.29}$$

Therefore, in Majorana's description, the particle is equivalent to its antiparticle. A Majorana fermion has then to be neutral electrically speaking, as the neutrinos are.

As far as the fermion mass is concerned, one can write down a mass term $-m_\nu^M \overline{\nu}\nu$ with m_ν^M being the Majorana mass. The mass can be described by the following Lagrangian:

$$\mathcal{L}_{mass}^M = -\frac{1}{2}m_\nu^M \left(\overline{\nu_L^c}\nu_L + \overline{\nu_L}\nu_L^c \right) \tag{1.30}$$

The $^1\!/_2$ factor is added for arbitrary display reasons.

If one only considers the interactions, Dirac's and Majorana's descriptions are equivalent since the right-handed field does not contribute. Oscillation experiments, though sensitive to neutrino masses, cannot distinguish between these two possible descriptions.

The Majorana mass term (equation (1.30)) is not invariant under Gauge transformation U(1): $\nu_L \longrightarrow e^{i\phi}\nu_L$ since $\overline{\nu_L^c} = -\nu_L^T \mathcal{C}^\dagger$ [20] and the global leptonic number is not conserved. However, since neutrino masses are really small, this global leptonic number L is only weakly violated.

1.2.2.3   See-Saw mechanism

We just described two ways of restoring neutrino masses in the SM: Dirac and Majorana. The first description needs right-handed neutrinos to exist whereas the second one needs neutrinos to be Majorana particles (equation (1.29)); both are equally possible. It is however possible to regroup those two descriptions in what is called the See-Saw mechanism. One can then describe a Dirac-Majorana mass term with a mass matrix M:

$$\mathcal{L}_{mass}^{D+M} = \frac{1}{2} \begin{pmatrix} \overline{\nu_L} & \overline{\nu_L^c} \end{pmatrix} \begin{pmatrix} m_L & m_D \\ m_D & m_R \end{pmatrix} \begin{pmatrix} \nu_R^c \\ \nu_R \end{pmatrix} + h.c. \tag{1.31}$$

where m_D is the Dirac neutrino mass defined by the mass term in equation (1.26), m_L is is the Majorana left-handed neutrino mass defined in equation (1.30) and m_R is the equivalent for right-handed neutrinos. The two fields, ν_L and ν_R, are Majorana spinors. The Majorana mass term m_L for the ν_L field is not invariant under SM symmetries and then has to be generated beyond SM.

By diagonalizing the mass matrix M, one is able to determine the corresponding mass eigenstates:

$$m_\pm = \frac{1}{2}\rho_\pm \left(m_L + m_R \pm \sqrt{(m_L - m_R)^2 + 4m_D^2} \right) \tag{1.32}$$

The factor $\rho_\pm = \pm 1$ ensures that masses are positive and proportional to the CP phase of the considered neutrino field [20]. The flavor eigenstates $\nu_\pm$ are then described as a mixing of the ν_L and ν_R fields with the mixing parameter θ such as:

$$\tan(2\theta) = \frac{2m_D}{m_R - m_L} \tag{1.33}$$

Different situations can then be considered:

- The Dirac limit where $m_L = m_R = 0$ and $\theta = 45$. The two flavor eigenstates are then degenerate since $m_\pm = m_D$ and CP parities are opposed. This situation gets back to the pure Dirac description of the neutrino, which is then the combination of two degenerate Majorana fields $\nu_\pm$.

- The pseudo-Dirac limit where $m_D \gg m_L, m_R$ and $\theta \approx 45$. This situation is equivalent to the previous situation.

- The Majorana limit where $m_D = 0$. This is the pure Majorana description of the neutrino.

- The See-Saw mechanism where $m_R \gg m_D$ and $m_L = 0$. The hypothesis of a Majorana mass m_L equal to zero can be explained by the fact that the Majorana mass for the left-handed field is forbidden by the SM. This is not the case for the right-handed neutrino which is a singlet of the SM. We then have two mass eigenstates:

$$m_+ \approx m_R \qquad \text{and} \qquad m_- \approx \frac{m_D^2}{m_R} \tag{1.34}$$

So, m_+ corresponds to a ν_+ neutrino as heavy as m_R whereas m_- corresponds to a light ν_- neutrino, hence the name "See-Saw mechanism". The mixing angle θ is really small since

$$\tan(2\theta) = 2\frac{m_D}{m_R} \ll 1 \tag{1.35}$$

We can then describe ν_+ as a sterile neutrino ν_R and ν_- as an active neutrino ν_L.

An important feature of the See-saw mechanism is that it explains the smallness of the neutrino mass, while generating the Dirac mass m_D according to the Higgs mechanism as for all the SM fermions. The Dirac mass is of the same order of magnitude as for the other fermions and is inferior to the electroweak scale ($\sim 10^2$ GeV) because of the SM symmetries. The enigma of the fermions' mass in the SM, already mentioned, can then be resolved without considering an extraordinarily small Yukawa coupling for neutrinos. On the other hand, this mechanism explains that right-handed neutrinos cannot be observed because of their huge mass. The symmetries of the SM do not apply to the right-handed neutrinos and their Majorana mass, which can be generated in the frame of new physics beyond SM, could be of the order of magnitude of grand unification (10^{14-16} GeV).

1.2.3   Neutrino oscillations formalism

As described in section 1.2.1, neutrino flavor changing evidenced by several experiments can only be explained if neutrinos are massive, contradicting what is described in the SM. The flavor eigenstates (ν_e, ν_μ and ν_τ) are different than the mass eigenstates (ν_1, ν_2 and ν_3). There is a mixing matrix relating these states [21], a unitary matrix called U_{PMNS} (B. PONTECORVO, Z. MAKI, M. NAKAGAWA, S. SAKATA), of dimension 3. This way, a flavor eigenstate α is the superposition of mass eigenstates i:

$$|\nu_\alpha\rangle = \sum_i U_{\alpha i}^* |\nu_i\rangle \qquad \text{or} \qquad \begin{pmatrix} |\nu_e\rangle \\ |\nu_\mu\rangle \\ |\nu_\tau\rangle \end{pmatrix} = U_{PMNS} \begin{pmatrix} |\nu_1\rangle \\ |\nu_2\rangle \\ |\nu_3\rangle \end{pmatrix} \tag{1.36}$$

This matrix describes transitions between neutrino flavors and is parametrized thanks to three mixing angles:

$$U_{PMNS} = \begin{pmatrix} c_{12}c_{13} & s_{12}c_{13} & s_{13}e^{i\delta} \\ -s_{12}c_{23} - c_{12}s_{23}s_{13}e^{i\delta} & c_{12}c_{23} - s_{12}s_{23}s_{13}e^{i\delta} & s_{23}c_{13} \\ s_{12}s_{23} - c_{12}c_{23}s_{13}e^{i\delta} & -c_{12}s_{23} - s_{12}c_{23}s_{13}e^{i\delta} & c_{23}c_{13} \end{pmatrix} \begin{pmatrix} 1 & & \\ & e^{i\alpha} & \\ & & e^{i\beta} \end{pmatrix} \tag{1.37}$$

where $c_{ij} = \cos\theta_{ij}$ and $s_{ij} = \sin\theta_{ij}$. The usual parametrization is to represent the U_{PMNS} matrix by the product of a certain number of independent matrices Ω_{ij}, each one of these containing only one mixing angle, as in equation (1.38).

$$
U_{MNSP} = \begin{pmatrix} 1 & & \\ & c_{23} & s_{23} \\ & -s_{23} & c_{23} \end{pmatrix} \begin{pmatrix} c_{13} & & s_{13}e^{-i\delta} \\ & 1 & \\ -s_{13}e^{i\delta} & & c_{13} \end{pmatrix} \begin{pmatrix} c_{12} & s_{12} & \\ -s_{12} & c_{12} & \\ & & 1 \end{pmatrix} \begin{pmatrix} 1 & & \\ & e^{i\alpha} & \\ & & e^{i\beta} \end{pmatrix}
$$
(1.38)

The δ_{ij} phases associated with CP violation only appear in the matrices describing mixing between non adjoining families. Then, in our case, there is only one CP violation phase δ. α and β are two extra CP violation phases that would appear if neutrinos possess Majorana phases, which requires a lepton number violation. In this form, the mixing matrix is decomposed into terms that can be associated with different regimes of mixing that have been explored by different classes of experiment. The (23) sector is identified as the atmospheric sector, θ_{23} (or θ_{atm}), measured thanks to atmospheric neutrinos. θ_{12} (or θ_{sol}) was measured thanks to solar neutrinos experiment. Finally, θ_{13} has not been measured yet but its best limit comes from reactor neutrino experiments.

The flavor transitions of neutrinos have been observed in two different ways: by oscillations in vacuum or in matter thanks to the MSW (S. MIKHEYEV, A. SMIRNOV, L. WOLFENSTEIN) effect. These two phenomena helped characterize several different parameters of the PMNS matrix.

1.2.4   Neutrino oscillations and flavor conversions in matter

1.2.4.1   Oscillations in vacuum

The probability for a ν_α to oscillate into a ν_β is given by equation (1.21). In order for this probability to be of interest the phase has to be of order 1; this means that the ratio distance source to detector - neutrino energy E/L has to have the same order of magnitude of the mass difference Δm^2_{ij}. If $E/L \gg \Delta m^2_{ij}$, the oscillation does not have time to happen; $\exp\left(-i\frac{\Delta m^2_{kj}L}{2E}\right) \simeq 1$ and therefore $P_{\nu_\alpha \to \nu_\beta} \simeq 1$. Considering that L and E are characteristics of an experiment, and that usually the neutrino source cannot be changed to adjust the energy to our need, this basically means the detector is too close to the neutrino source. On the contrary, if the detector is too far away from the source, then $E/L \ll \Delta m^2_{ij}$ and oscillations are averaged when they reach the detector.

If the various mass differences are not too close to one another, then an experiment will be sensitive only to a two-flavor mixing because of its definite parameters L and E ($\Delta m^2 \sim E/L$). In that case, the mixing matrix becomes a simple 2 x 2 rotation matrix:

$$
\begin{pmatrix} \nu_\alpha \\ \nu_\beta \end{pmatrix} = \begin{pmatrix} \cos\theta & \sin\theta \\ -\sin\theta & \cos\theta \end{pmatrix} \begin{pmatrix} \nu_i \\ \nu_j \end{pmatrix}
$$
(1.39)

Then there is only one mixing angle θ and the probability of flavor transition depends on one Δm^2. From equation (1.21), one can determine the probability for a two flavor oscillation:

$$P_{\nu_\alpha \to \nu_\beta}(L, E) = \sin^2(2\theta)\sin^2\left(\frac{\Delta m^2 L}{4E}\right) \tag{1.40}$$

This probability is more often used with different units, more adapted to oscillation experiment [22]:

$$P_{\nu_\alpha \to \nu_\beta}(L, E) = \sin^2(2\theta)\sin^2\left(1.27\frac{\Delta m^2 \left[eV^2\right] \cdot L\left[km\right]}{E\left[GeV\right]}\right) \tag{1.41}$$

Experimentally, it is possible to look for the appearance of ν_β in a ν_α flux, or to look for the disappearance of ν_α. For a disappearance experiment, what is measured is the reduction of the neutrino flux coming from a known source.

1.2.4.2   Flavor conversions in matter

Neutrinos propagating in matter are subject to an effective potential caused by coherent forward elastic scattering with the particles in the medium (electrons and nucleons). This potential, which is equivalent to an index of refraction, modifies the mixing of neutrinos [23]. In the case of two-neutrino mixing, the mixing angle in vacuum is replaced by an effective mixing angle in matter. Flavor conversions in matter are described by the MSW mechanism. In addition to weak Neutral Current (NC) scattering of neutrinos on nucleons and electrons of matter, identical for all flavors of neutrinos, only electronic neutrinos can interact through the Charged Current (CC) weak interaction with electrons (cf. figure 1.5). The CC potential V_{CC} [20] of an
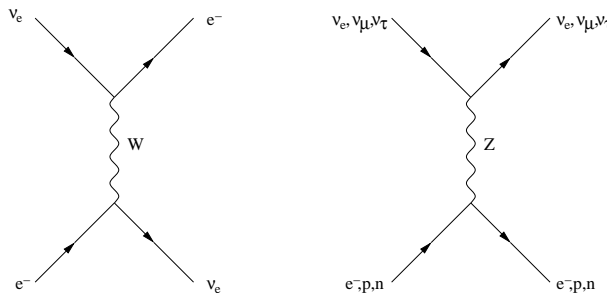
Figure 1.5: Feynman diagrams of the coherent elastic scattering processes that generate the CC potential V_{cc} through $W^\pm$ exchange and the NC potential through Z exchange.

electronic neutrino can be written as:

$$V_{CC} = \sqrt{2}G_F N_e \tag{1.42}$$

G_F being the Fermi constant and N_e the electron volumetric density in the material crossed by the neutrino. In the same way one can write down the V_{NC} potential corresponding to the weak NC scattering for a neutrino of any flavor. However, this interaction being the same for each kind of neutrino, it only adds a common propagation phase to neutrino oscillations in vacuum and therefore has no influence on flavor transitions in matter. So, oscillation probabilities in matter can be determined the same way as in vacuum from the Schrödinger equation, taking

into account the potential from equation (1.42), which adds an energy term to the electronic neutrinos' Hamiltonian. The flavor conversions probabilities depend then not only on the electron density but also on the neutrino energy.

1.3   Phenomenological landscape

Physicists have tried to measure the oscillation parameters for over a decade. Indeed, without any indication on those parameters, a lot of experiments had to take place to explore each and every possible $(\tan^2\theta, \Delta m^2)$ couple. Some experiments were unlucky enough not to observe any phenomenon in relation to neutrino flavor transition because their sensitivity was not good enough, or because they were not at an appropriate distance from the source (see section 1.2.4.1). Neutrino properties, masses and mixing parameters, can be looked for either in a "direct" manner by measuring kinetic parameters in a process producing a neutrino (study of beta decay and the spectrum distortion coming from the neutrino), or in an "indirect" manner by observing the oscillations induced by the fact that neutrinos are massive.

1.3.1   Direct measurement of the neutrino mass

Neutrino flavor transitions depend on the squared mass differences, not on the actual neutrino mass values. In figure 1.6 are shown the neutrino masses values in the cases of normal hierarchy
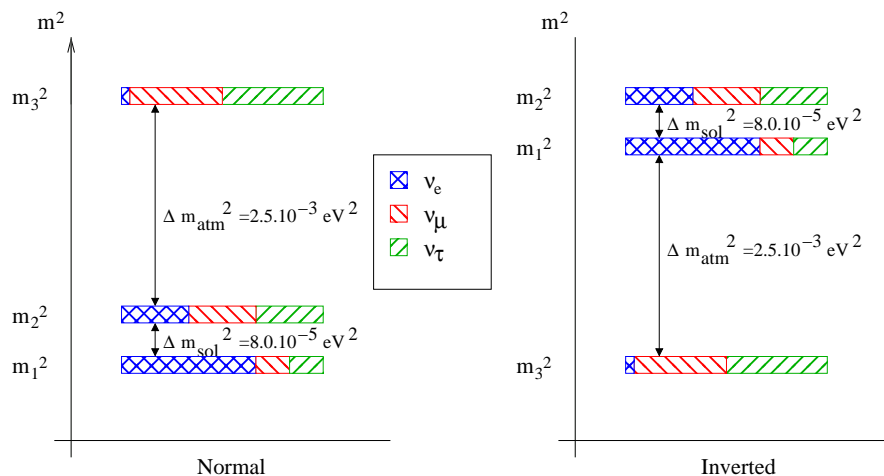
Figure 1.6: Oscillation parameter measurement results in both cases: normal and inverted hierarchy [10].

(m_1 being the lighter mass) and inverted hierarchy (m_3 being the lighter mass). There are some ways (described below) to perform absolute measurements of neutrino masses: through Tritium beta decay, neutrinoless double beta decay and Cosmology.

1.3.1.1 Tritium beta decay

This method is based on kinematic considerations and energy, momentum conservation. Three different techniques are used depending on the neutrino flavor. The first method described here to measure the electron neutrino mass is by studying the electron energy spectrum in nuclear beta decay of light nuclei, as Tritium:

$$^3\text{H} \rightarrow {}^3\text{He} + e^- + \bar{\nu}_e \tag{1.43}$$

The total accessible energy of the reaction Q_β (18.6 keV for tritium) is divided between the electron and the neutrino. Therefore, the end point of the electron spectrum has to be reduced from Q_β to $Q_\beta - m_\beta c^2$ because of the effective neutrino mass m_β in beta decay. The neutrino being extremely light compared to the considered energies, the difference is really small (easier to detect as the nucleus is lighter). This effective neutrino mass comes from neutrino mixing: $m_\beta = \sqrt{\sum_i |U_{ei}|^2 m_i^2}$ [20]. It can be expressed as a function of the parameters accessible thanks to oscillation experiments (equation (1.37)):

$$m_\beta^2 = c_{12}^2 c_{13}^2 m_1^2 + s_{12}^2 c_{13}^2 m_2^2 + s_{13}^2 m_3^2 \tag{1.44}$$

Therefore, to determine the neutrino masses, one has to combine the oscillation and direct measurement experiments results for beta decay. The effective mass m_β is shown figure 1.7 as a function of the lighter neutrino in the normal (m_1) and inverted hierarchy (m_3).
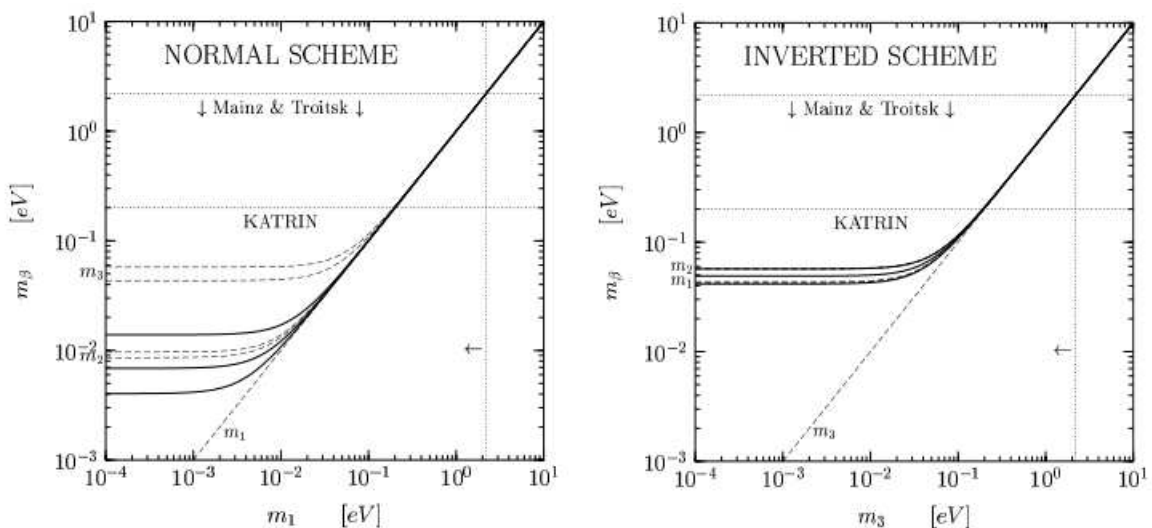
Figure 1.7: Effective mass m_β as function of the lighter neutrino mass in the normal (m_1) and inverted (m_3) hierarchy [20]. The plain line represents the masses best fit, along with their 3σ limits. The best limit as well as the one expected from KATRIN is also indicated.

The best actual limit comes from the Mainz and Troitsk experiments with $m_\beta < 2.2$ eV at 2σ (figure 1.7) [24]. The KATRIN experiment should reach a sensitivity of 0.2 eV [25].

1.3.1.2   Neutrinoless double beta decay

Neutrinoless double beta decay ($0\nu2\beta$ decay) corresponds to the decay of a nucleus into another one with the emission of only two electrons:

$$(A,\ Z) \rightarrow (A,\ Z+2) + 2e^- \tag{1.45}$$

This reaction does not conserve the leptonic number L. To observe such a decay would determine whether neutrinos are Majorana particles and thus their own antiparticles. The main mechanism of the $0\nu2\beta$ decay is the exchange diagram shown in figure 1.8 in which a mass eigenstate ν_i is exchanged. The neutrino-electron-W vertices are those of the SM, which means
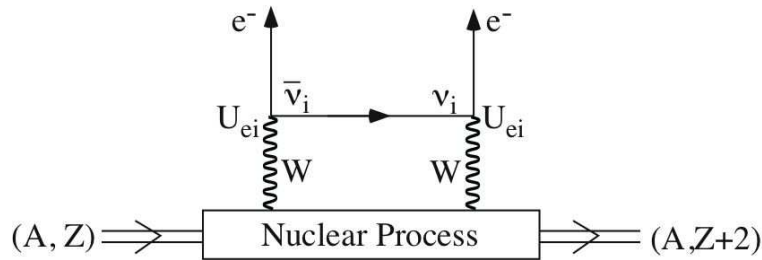
Figure 1.8: Neutrinoless double beta decay diagram. A mass eigenstate ν_i is exchanged. [22].

the vertex on the left has to be a $\overline{\nu_i}$. However, when this particle is absorbed by the vertex on the right, it has to be a ν_i. Therefore, $0\nu2\beta$ decay is only possible if $\overline{\nu_i} = \nu_i$. The necessary amplitude for a ν_i to generate a charged lepton, in our case an electron, is $U_{\alpha i}$, which means there is a U_{ei} factor at each vertex. This leads to a effective Majorana neutrino mass of $m_{\beta\beta} = \left| \sum_i U_{ei}^2 mi \right|$ [20].

1.3.2   Solar neutrinos

Nucleosynthesis reactions happening in stars like the Sun generate electronic neutrinos with energy of order ~ 1 MeV through beta decays. The Sun is powered by two groups of thermonuclear reactions known as the *pp* chain and the CNO cycle. The result of both the *pp* chain and the CNO cycle (1.7 % of the ^{4}He nuclei produced) is the conversion of four protons and two electrons into a ^{4}He nucleus plus two electron neutrinos:

$$4p + 2e^- \rightarrow^4 \text{He} + 2\nu_e + 26.731 \text{ MeV} \tag{1.46}$$

This neutrino source is a very powerful one: the solar neutrino flux on Earth is about 6×10^{10} cm^{-2}s^{-1} [20].

There are two types of solar neutrino experiments. The reaction of interest of the first one is the neutrino capture ($\nu_e + (A,Z) \rightarrow (A,Z+1) + e^-$), only sensitive to electronic neutrinos.

The pioneering Homestake experiment is a radiochemical experiment which detects solar neutrinos through the reaction:

$$\nu_e +^{37} Cl \rightarrow^{37} Ar + e^- \tag{1.47}$$

with neutrino energy threshold 0.814 MeV. The main contribution to the Homestake event rate comes from high-energy ^{8}B neutrinos. The Argon atoms generated by the interaction of the electronic solar neutrinos with the Chlorine target are extracted by chemical means and then counted, giving direct access to the number of solar neutrinos. The first data collected indicated that the solar neutrino flux was well below the rate predicted by the Standard Solar Model (SSM): about one-third of it. This was the discovery of the solar neutrino problem, resulting in the conferring of a Nobel Prize to R. DAVIS JR in 2002!

GALLEX [26] and SAGE [27] were solar neutrino radiochemical experiments based on the interaction of electronic neutrinos with Gallium atoms through the reaction:

$$\nu_e +^{71} Ga \rightarrow^{71} Ge + e^- \tag{1.48}$$

with a neutrino energy threshold of 0.233 MeV. This makes the detection of all sorts of solar neutrinos possible, as shown in figure 1.9. Therefore, Gallium experiments are decisive for
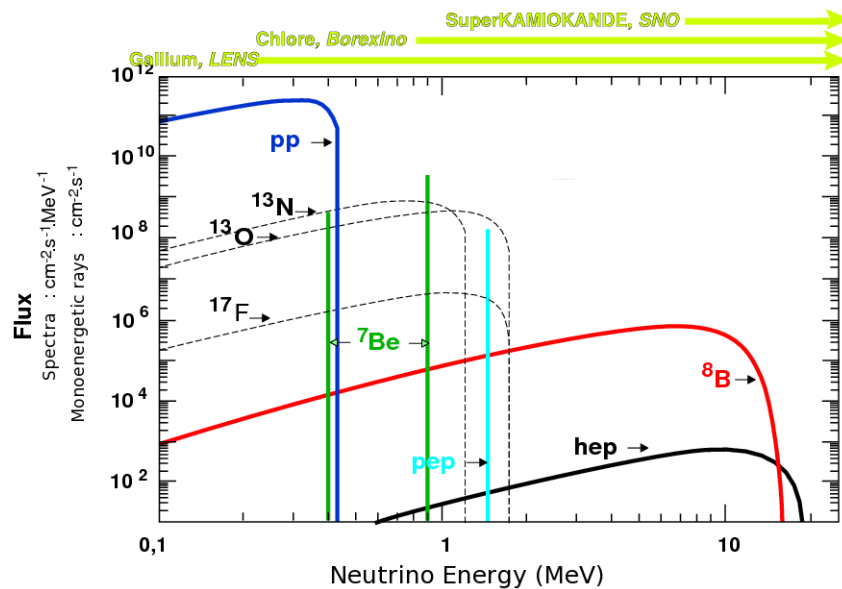
Figure 1.9: Energy spectra of neutrinos produced in the Sun and their chain reaction production. The Gallium experiments' range is large enough to detect all sorts of solar neutrinos. The SNO Neutral Current threshold has lowered down to 2.2 MeV since.

the measurement of the neutrino flux produced in the basic reaction of the *pp* chain, directly related to the luminosity of the Sun. To access the number of electronic neutrinos, Germanium atoms are extracted by chemical methods, and counted afterwards by observing their decay back to ^{71}Ga. The GALLium EXperiment (GALLEX) was located in the Laboratori Nazionali del Gran Sasso (LNGS) in Italy, the Soviet-American Gallium Experiment (SAGE) in the Baksan Neutrino Observatory (BNO) in the northern Caucasus mountains. The two experiments independently reached the same conclusion, that the electronic neutrino rate was half of what was predicted by the SSM.

The second type of experiment (water Cerenkov detectors) uses a water target and detects neutrinos through elastic scattering on electrons. When a charged particle with velocity $v > c/n$ passes through a medium with index of refraction n, the particle emits Cerenkov light. This is

how water Cerenkov detectors observe the tracks of ultra-relativistic charged leptons produced by neutrino interactions. These experiments are mostly sensitive to electronic neutrinos since their cross section is higher and they can interact through weak NC and CC.

The Kamiokande and later Super-Kamiokande detectors were located in the Kamioka mine in Japan. Kamiokande was originally built to search for nucleon decay, and therefore underwent different phases [28]. The successor, the Super-Kamiokande experiment consists of 50 000 m^3 of pure water. The solar neutrino flux was measured through the elastic scattering reaction

$$\nu_e + e^- \rightarrow \nu_e + e^- \tag{1.49}$$

Super-Kamiokande can measure the energy of neutrinos as well as the direction of arrival. It established that solar neutrinos are indeed coming from the Sun, and that the flux of ^{8}B solar electronic neutrinos measured by Super-Kamiokande is about half of the SSM predicted flux.

The Sudbury Neutrino Observatory (SNO) [29] is a heavy-water Cerenkov detector located in Ontario, Canada. The SNO experiment detects solar neutrinos through NC and CC interaction and elastic scattering:

$$
\begin{aligned}
\nu_x + d &\rightarrow p + n + \nu_x & (1.50)\\
\nu_e + d &\rightarrow p + p + e^- & (1.51)\\
\nu_x + e^- &\rightarrow \nu_x + e^- & (1.52)
\end{aligned}
$$

Heavy water allows neutrino detection to be independent from the neutrino flavor through the NC interaction on Deuterium (equation (1.50)) in addition to the interactions used in normal water experiments. The total flux is in agreement with the one predicted by the SSM while the results from the CC reaction (equation (1.51)) confirmed the deficit of electronic solar neutrinos already observed (figure 1.10). Therefore, the solar neutrino enigma is due to the neutrino properties of oscillation.

The neutrino flavor conversion of solar neutrinos is due the MSW effect described in section 1.2.4.2. The mixing happens between ν_e and ν_x (linear combination of ν_μ and ν_τ) [22]. The density in the Sun core is such that ν_e are produced nearly as pure ν_2 mass eigenstate. From the Sun core, neutrinos evolve in a decreasing electron density medium until they reach the star surface. The ν_2 state is then associated with a linear combination of ν_e and ν_x. After that, neutrinos stay associated with ν_2 up to the surface of the Sun, and then in vacuum. Finally, the probability to detect on Earth a ν_e corresponds to the probability for a ν_2 to be a ν_e knowing that $\nu_2 = \nu_e \sin\theta_{12} + \nu_x \cos\theta_{12}$. Solar neutrinos experiments are then sensitive to ν_e disappearance and are able to measure θ_{12} and Δm_{12}^2. The solar parameters are, as we know now [10]:

$$
\begin{aligned}
\sin^2(2\theta_{12}) &= 0.87 \pm 0.03\\
\Delta m_{12}^2 &= (7.59 \pm 0.20) \times 10^{-5} \text{eV}^2
\end{aligned}
\tag{1.53}
$$

1.3.3   Atmospheric neutrinos

Atmospheric neutrinos are created by the interactions of cosmic rays, mostly constituted of protons, alpha particles and heavy nuclei, with nuclei in the atmosphere (N, O). Secondary
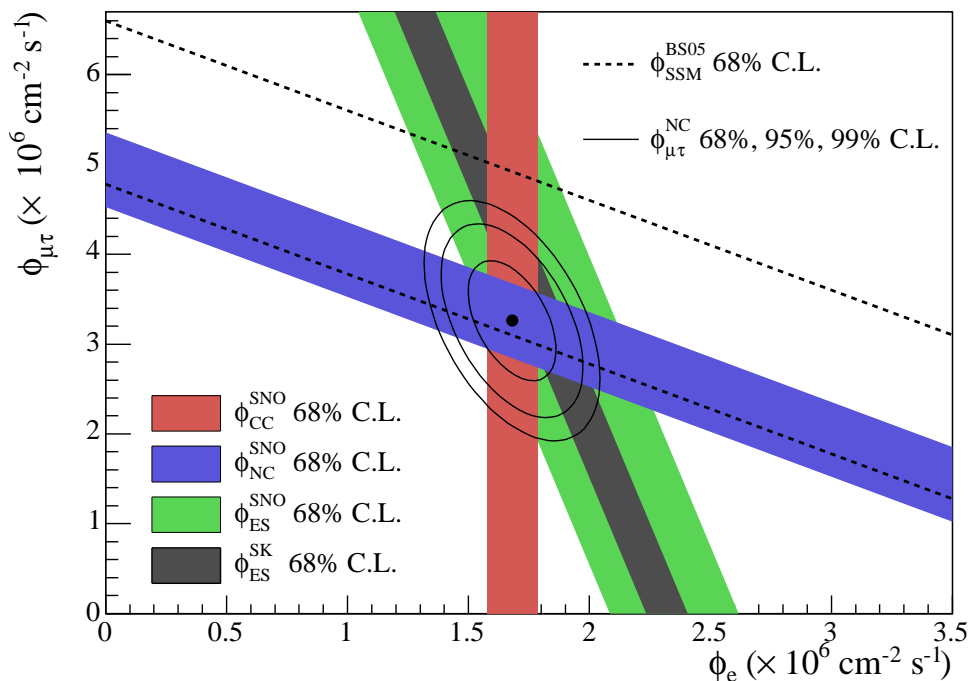
Figure 1.10: $\nu_{\mu\tau}$ flux versus ^{8}B ν_e flux from SNO first analysis of the neutrino elastic scattering, the CC and the NC interactions. The dashed lines define the total ^{8}B solar neutrino flux predicted by SSM, the blue region the total neutrino flux measured from NC interactions by SNO. The two regions are in agreement [10]. The ν_e neutrino flux measured confirmed the lack of ν_e observed by previous experiments. More recent results from SNO confirmed this deficit [29].

particles, mostly pions, muons and kaons, are then generated. These pions decay mainly into muons and muon neutrinos:

$$\pi^+ \rightarrow \mu^+ + \nu_\mu, \qquad \pi^- \rightarrow \mu^- + \overline{\nu_\mu} \tag{1.54}$$

The muons which decay before hitting the ground generate electrons, electron neutrinos, and muon neutrinos through the processes

$$\mu^+ \rightarrow e^+ + \nu_e + \overline{\nu_\mu}, \qquad \mu^- \rightarrow e^- + \overline{\nu_e} + \nu_\mu \tag{1.55}$$

The ratio $R = {}^{(\nu_\mu + \overline{\nu_\mu})}/{}_{(\nu_e + \overline{\nu_e})}$ is well predicted in the sub-GeV region and roughly equal to 2. Current atmospheric neutrinos experiments use water Cherenkov detectors, such as Super-Kamiokande. Since originally, we are dealing with cosmic rays, atmospheric neutrinos have higher energy than the solar ones (peaked in the GeV range), it is possible to produce muons from the muonic neutrino interactions. The flavor ratio measured by the atmospheric neutrino experiments corresponds to only 60 % of the predicted ratio. This difference is due to flavor oscillations.

Irrefutable evidence of atmospheric neutrino oscillation came from the observation of an up-down asymmetry of high energy events generated by atmospheric muon neutrinos in the Super-Kamiokande water Cherenkov detector [30]. In atmospheric neutrino experiments, neutrino

fluxes of different flavors are measured by detection of the charged leptons produced through quasi-elastic neutrino scattering:

$$\nu_l + N \rightarrow l^- + X, \qquad \overline{\nu_l} + N \rightarrow l^+ + X \qquad (l = e,\, \mu,\, \tau) \qquad (1.56)$$

For charged leptons of high momentum, the neutrino and its associated lepton are colinear; therefore the incoming direction of the interacting neutrino is the same as of the detected lepton. Hence, one can compare the downward-going neutrino flux from the atmosphere above the detector to the flux of upward-going neutrinos also produced in the atmosphere and which went through the Earth before being detected. At low energies, the directional flux of atmospheric neutrinos depends on the effect of the geomagnetic field on the cosmic ray. This effect disappears at high energies (> 1 GeV). Hence, the production of high-energy neutrinos in the atmosphere is practically uniform around the globe. This means that, with no oscillations and no interaction of the neutrino in the Earth (very small cross-section), the fluxes of upward- and downward-going neutrinos are to be the same. However, in the Super-Kamiokande experiment, a lack of upward-going ν_μ ($\sim {}^1\!/_2$) is observed (figure 1.11). This phenomenon is explained by the flavor
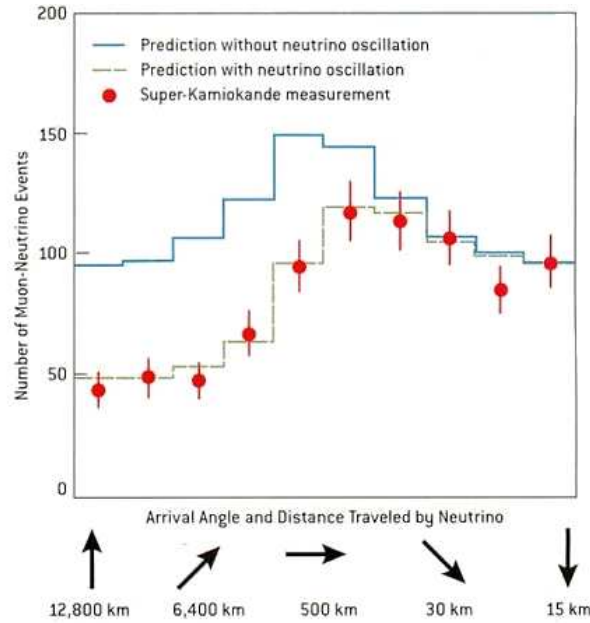
Figure 1.11: Number of muon neutrino events in the Super-Kamiokande detector as a function of the arrival angle and the distance traveled. Upward-going neutrinos are reduced by a factor of 2 whereas the downward-going are not.

oscillation of ν_μ going through the Earth. Indeed, downward-going neutrinos are produced in the atmosphere above the detector and travel a distance of roughly 15 kilometers, which is not enough for them to oscillate. On the other hand, upward-going neutrinos come from the other side of the globe, with traveling distances of about 12,000 kilometers. The larger distances covered by these neutrinos allow them to oscillate into other flavors, leading to a suppression of the upward-going flux with respect to the downward going one.

Atmospheric neutrinos experiments are sensitive to the ν_μ disappearance through muonic neu-

trino, tauic neutrino oscillation and are able to measure the parameters θ_{23} and Δm_{23}^2 [10]:

$$
\begin{aligned}
\sin^2(2\theta_{23}) &> 0.92 \\
\Delta m_{23}^2 &= (2.43 \pm 0.13) \times 10^{-3}\text{eV}^2
\end{aligned}
\tag{1.57}
$$

1.3.4 Accelerator neutrinos

Following a similar production process as for atmospheric neutrinos, it is possible to generate ν_μ beams. An accelerated proton beam on a target produces pions and kaons. These mesons are then focused by magnetic horns towards a decay tunnel of a few hundred meters long, where they decay into antimuons and muon neutrinos (equation (1.54)) with a contamination in electronic neutrinos, intrinsic contamination being an irreducible background. The focusing system can choose between the sign of the mesons and therefore the beam type: neutrinos or antineutrinos. Shielding at the exit of the tunnel stops all particles but neutrinos. Electronic neutrinos coming from muon decays are then not focused on the detector, which reduces the ν_e contamination in the ν_μ beam. Detectors, as for the atmospheric neutrinos studies, are able to see charged leptons of the same flavor of the interacting neutrino. Accelerator neutrino experiments can improve atmospheric neutrino experiments, first by increasing the statistics, then by reducing the systematic uncertainties since the oscillation length is fixed and the neutrino energy is less spread.

Oscillation phenomena with a Δm^2 of the order of 1 eV have been rejected by short-baseline accelerator experiments, except for the LSND one which found a signal in the muonic antineutrino, electronic antineutrino channel. The LSND signal was further investigated by the MiniBooNE experiment [22].

Long-baseline accelerator experiments are sensitive to the atmospheric parameters θ_{23} and Δm_{23}^2 for the muonic neutrino, tauic neutrino oscillations. Two types of experiments can be found: the ones looking for ν_μ disappearance (K2K, MINOS) and the ones looking for the appearance of ν_τ in a ν_μ beam (OPERA). The future neutrino beam experiments (T2K, NOνA) primary objectives are to discover muonic neutrino, electronic neutrino oscillations generated by the atmospheric Δm^2. Such an observation would allow scientists to measure the θ_{13} parameter, as with the reactor neutrino experiments.

1.3.5 Reactor neutrinos

Nuclear reactors are the most important neutrino source on Earth. They emit neutrinos through beta decays of unstable isotopes in the reactor core. As explained later in chapter 3, each fission produces roughly 6 $\overline{\nu_e}$ with energy mainly concentrated around 2 - 3 MeV and extending up to 8 MeV. Hence, reactor neutrino experiments are disappearance experiments since no muons nor taus can be produced at such energies in case of oscillations. Detection happens through the inverse beta decay reaction:

$$
\overline{\nu_e} + p \rightarrow e^+ + n
\tag{1.58}
$$

The energy threshold of the reaction of interest is 1.8 MeV. The experimental technique is the same as the one used in 1956 by F. REINES and C. L. COWAN described in section 1.1.1.

The sensitivity to Δm^2 directly depends on the source-detector distance. This being easy to control in terrestrial experiments, different sets of parameters are accessible. For example, a reactor neutrino experiment with the detector far away from the source such as KamLAND (from 140 km to 210 km) was able to observe the electronic antineutrino disappearance due to the solar Δm_{21}^2 [31], and therefore to study the solar parameters, when experiments closer to the source would not see these oscillations (figures 1.12 and 1.13). However, closer experiments
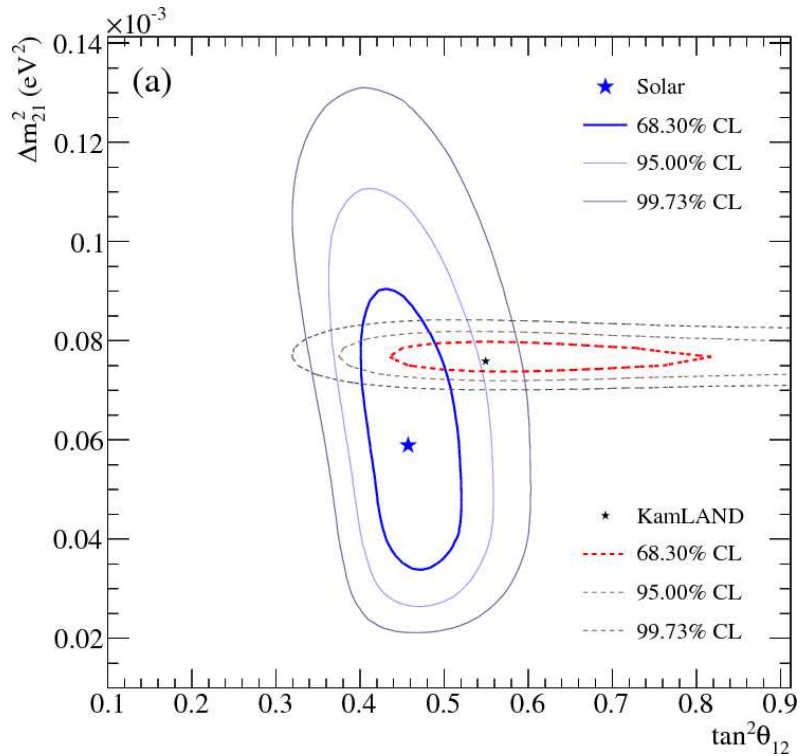
Figure 1.12: Solar and KamLAND oscillation parameter analysis for a two-flavor oscillation hypothesis. The solar data includes SNO, SAGE, GALLEX, Borexino and Super-Kamiokande [29].

(baseline of order 1 km) are sensitive to the last unknown mixing angle θ_{13} and to $\Delta m_{31}^2 \sim \Delta m_{32}^2$. The first generation of reactor neutrino experiments used only one detector to study the electronic antineutrino disappearance and obtained the best sensitivity on θ_{13} (CHOOZ [32], Palo Verde [33], see section 2.1.1).

The main problem for the determination of θ_{13} is the uncertainty on the neutrino flux coming from the nuclear cores . Hence, new generation experiments, like Double Chooz or Daya Bay, will use more than one detector: at least one near detector will be located before the oscillation region in order to directly determine the neutrino flux and at least one far detector, located around the maximum of oscillation, will measure the lack of electronic antineutrinos. These experiments will improve the constraint on θ_{13}, maybe even measure it!
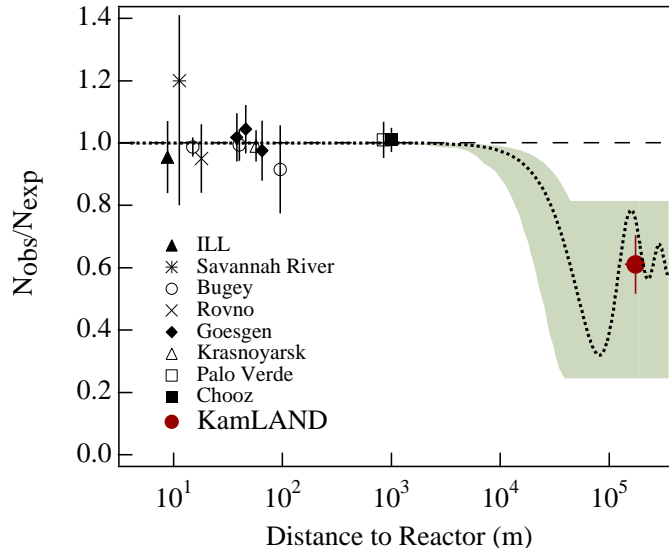
Figure 1.13: Ratio of the observed neutrino signal over the expected one as a function of the distance from the source. Experiments too close to the source are not able to see any oscillations due to the value of Δm_{12}^2 [10].

1.3.6   Flavor transition analysis summary

Thanks to all of the different types of experiments mentioned above values have been given to the three mixing angles (only an upper limit for θ_{13}) and the squared mass differences. The measurements of the oscillation parameters can be summed up as [10]:

$$
\begin{aligned}
\sin^2(2\theta_{12}) &= 0.87 \pm 0.03 \\
\Delta m_{12}^2 &= (7.59 \pm 0.20) \times 10^{-5}\text{eV}^2 \\
\sin^2(2\theta_{23}) &> 0.92 \\
\Delta m_{23}^2 &= (2.43 \pm 0.13) \times 10^{-3}\text{eV}^2 \\
\sin^2(2\theta_{13}) &< 0.19, \ \text{C.L.} = 90\%
\end{aligned}
\tag{1.59}
$$

On figure 1.14 is a map of the different exclusion regions from neutrino experiments. Future neutrino experiments will make precision measurements of the already known parameters but more than anything else try to determine the value of θ_{13}.
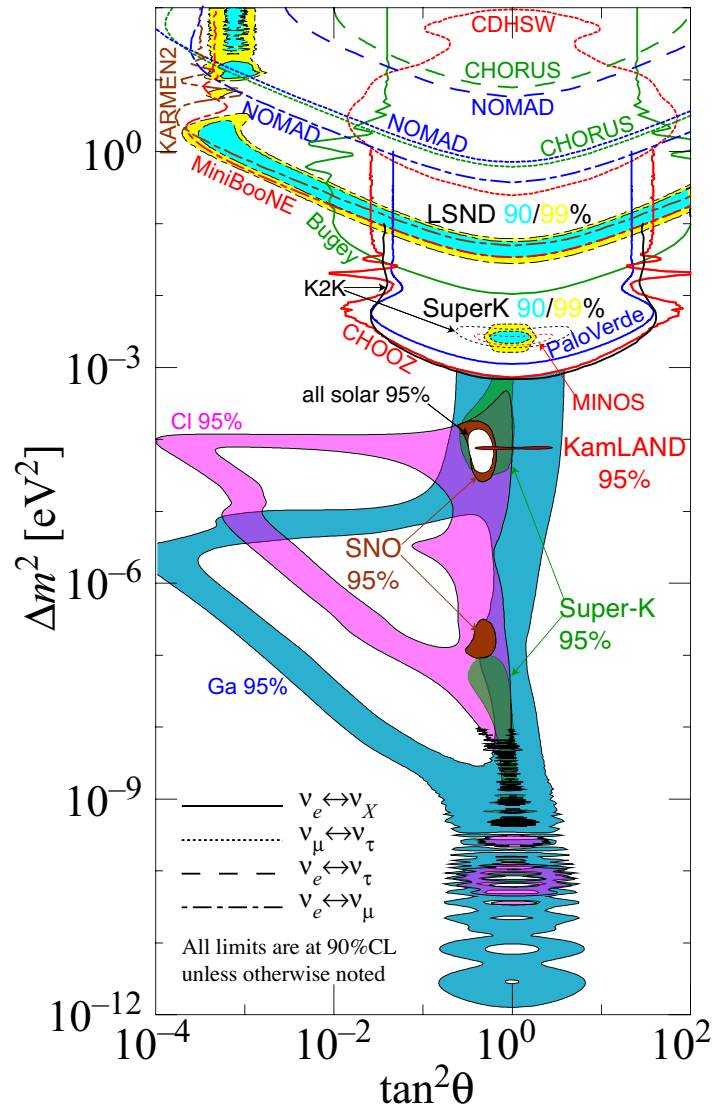
Figure 1.14: Map of the squared mass differences and mixing angles according to various experiments [10].

Chapter 2

θ_{13} or the last unknown mixing angle

It is widely accepted that the next priority of oscillation experiments is to determine the three remaining parameters: the value of θ_{13}, the sign of Δm_{32}^2 and the CP phase δ. The main target is δ since this would give a window into CP violation in the neutrino sector, which may hold the answer to the question of where the matter/antimatter asymmetry in the universe comes from. Indeed, proving CP violation in the neutrino sector is an important step towards giving credit to leptogenesis. Since the effects of δ in oscillations always appear multiplied by $\sin^2(2\theta_{13})$, finding a non-zero value for θ_{13} is a mandatory step in the campaign to measure δ.

2.1 What we know about θ_{13}

2.1.1 From reactor experiments: the limit

At first, middle-baseline (MBL) reactor experiments[1] were carried out to check if $\nu_\mu \leftrightarrows \nu_e$ oscillation could be an explanation for the atmospheric oscillation observed in Super-Kamiokande (see section 1.3.3). In order to reach a Δm^2 sensitivity corresponding to the atmospheric neutrino oscillations mass splitting (of order 10^{-3} eV^2), the CHOOZ and Palo Verde experiments had source-detector distances of about 1 km (cf. equation 1.40). The reaction of interest was the inverse beta decay (see section 1.3.5):

$$\bar{\nu}_e + p \rightarrow n + e^+ \tag{2.1}$$

An electron antineutrino coming from the reactor core interacted with a free proton in the detector target, generating a positron and a neutron. The positron provided a prompt signal (boosted by the two 511 keV annihilation gammas) and the neutron a delayed signal. This was the neutrino signal.

---

[1]Experiments with a distance from the neutrino source to the detector of a few kilometers.

2.1.1.1   CHOOZ

The CHOOZ experiment took place in the French Ardennes between April 1997 and July 1998. It was located next to the Chooz nuclear power plant; the detector was 1.05 km away from the two nuclear cores of 4.2 GW each. Both cores were off at the beginning of data taking in April 1997; they started operation respectively in May and August of 1997. This unique opportunity allowed high accuracy background measurements, reactors being shut off, as well as an independent measurement of each reactor's contribution to the neutrino flux.

The laboratory was set in a preexisting underground cavity under 115 m of rock, equivalent to a shielding of 300 m of water, reducing the external cosmic ray muon flux by a factor of 300, to a value of 0.4 m^{-2}s^{-1} [32]. Thus, background coming from fast neutrons generated by muon-induced spallation in the surrounding materials was reduced. Spallation is a nuclear reaction in which a nucleus is hit by an incoming particle. The target nucleus decomposes into lighter particles, some of which still have enough energy to create new spallation reactions. This leads to a multiplication of emitted neutrons. The fast neutron flux was measured at the CHOOZ experiment site with both nuclear reactors off for energies above 8 MeV (end point of the reactor neutrino energy spectrum) and measured to be roughly one event per day, in agreement with predictions.
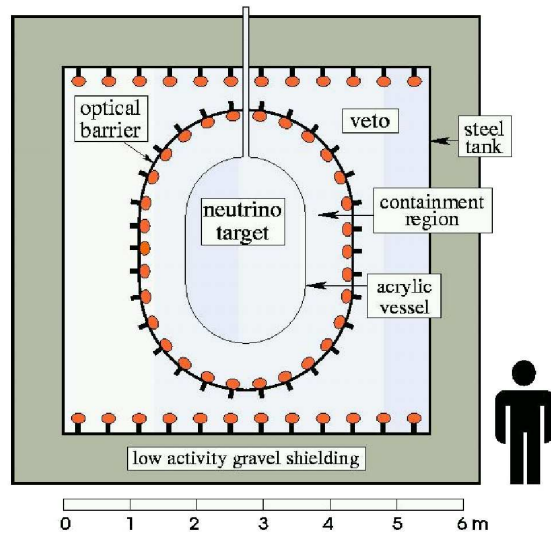
Figure 2.1: Schematic drawing of the CHOOZ experiment. In the center, the neutrino target is an acrylic vessel filled with Gd-doped liquid scintillator. This volume is surrounded by a containment region filled with liquid scintillator, to detect gamma rays coming from the neutron capture on Gd and positron annihilation. On this vessel wall, 192 photomultipliers are installed. This active inner detector is within a muon veto, surrounded itself by a low activity sand shielding.

The detector was located in a 7 m diameter and height cylindrical pit. Its outer vessel was a cylindrical steel vessel, of 5.5 m diameter and height, surrounded by 75 cm of low radioactivity

sand and covered by 14 cm of iron to shield the detector from the natural radioactivity of the rock. The detector comprised three concentric volumes (figure 2.1):

1. A 4.8 ton liquid scintillator target doped with gadolinium (Gd) (0.1 % in mass) within an acrylic vessel, designed to detect neutrinos. The signal that was looked for was the combined detection of the positron and neutron. The latter was to be captured by a Gd nucleus, releasing gammas of a total energy of 8 MeV.

2. A medium region of 70 cm thickness filled with 17 tons of non Gd-doped liquid scintillator, to detect gamma particles coming from the neutron capture on Gd. On the vessel wall were installed 192 photomultipliers tubes (PMTs) used to monitor the two volumes.

3. An 80 cm thick muon veto, filled with 90 tons of the same liquid scintillator as in the previous volume, to shield the detector from cosmic ray muons. It was equipped with with two rings of 24 PMTs.

The Gd-doped liquid scintillator unfortunately showed a loss in transparency with time, which lead to a loss in the amount of light reaching the PMTs (estimated lifetime: 250 days), and shortened the duration of the experiment.

The spectral shape of the events was in agreement with the one expected in the case of no oscillations. The energy averaged ratio between expected (without oscillations) and observed events was measured to be [32]:

$$R = 1.01 \pm 2.8\%(stat.) \pm 2.7\%(sys.) \tag{2.2}$$

Systematic errors were mostly due to the uncertainty on the reactor $\overline{\nu_e}$ flux (2 %), the detection efficiency (1.5 %), the number of free protons, direct target of antineutrinos (0.8 %). The corresponding limit on $\sin^2(2\theta_{13})$ is 0.14 at 90 % C.L. for $\Delta m_{31}^2 = 2.5 \times 10^{-3} \mathrm{eV}^2$.

Figure 2.2 shows the exclusion profiles from CHOOZ in agreement with the allowed regions from Kamiokande for the $\nu_\mu \leftrightarrows \nu_e$ transitions [34]. The area on the right of the curves is excluded. Thanks to the CHOOZ results, it has been established that ν_μ disappearance observed in Kamiokande and then Super-Kamiokande cannot be explained by the oscillation of a muonic neutrino into an electronic neutrino.

2.1.1.2 Palo Verde

The Palo Verde experiment was held near the Palo Verde nuclear generating station in the Arizona desert, the largest nuclear power plant in the United States. The total thermal power of the three reactors in use was roughly of 11.6 $\mathrm{GW_{th}}$. The experiment took data from October 1998 to July 2000. The detector was located at a distance of 890 m from two of the reactors and 750 m from the third one.
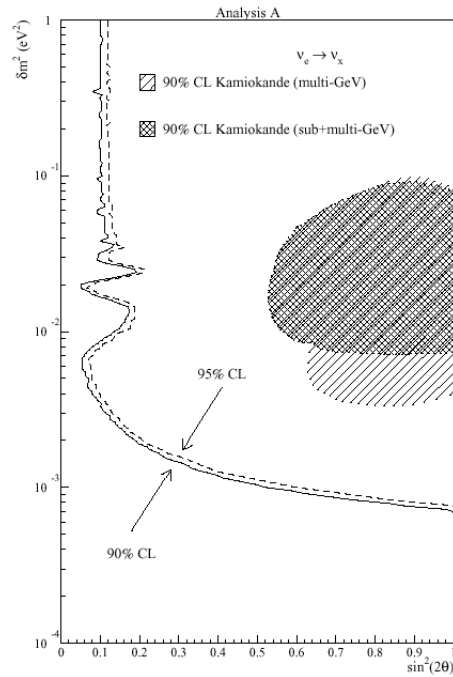
Figure 2.2: CHOOZ exclusion plot for $\overline{\nu_\mu} \leftrightarrows \overline{\nu_e}$ transitions [35]. The excluded regions are on the right of the figure.
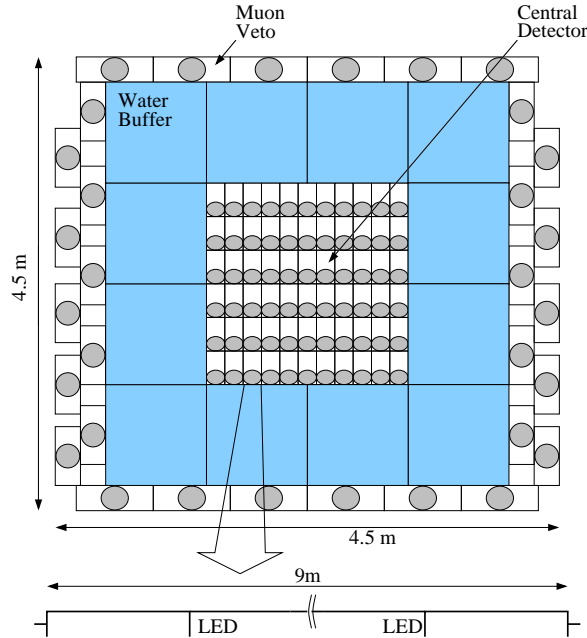
Figure 2.3: Palo Verde detector. The gray circles are photomultipliers. The central detector was made of 66 cells filled with Gd-doped liquid scintillator. It was surrounded by a water buffer to moderate background neutrons. The external layer of the detector was a muon veto. Its detectors were plastic boxes filled with liquid scintillator. At the bottom is a side view of a single scintillator cell. The last half meter on each end of a cell was filled with mineral oil to act as an additional buffer.

The detector was located in an underground bunker 12 m deep, with an overburden of only 32 meter water equivalent (m.w.e.). It consisted of 12 tons of a liquid scintillator loaded with 0.1 % Gd filled in sixty-six 9 m long modules arranged in a 11 × 6 array. It was surrounded by a shield, comprising a 1 m thick water wall to moderate background neutrons and an additional veto system against cosmic muons using 32 large scintillator panels, as shown in figure 2.3. The neutrino signal was defined as the space and time coincidence of three modules activation coming from positron annihilation together with neutron captures.
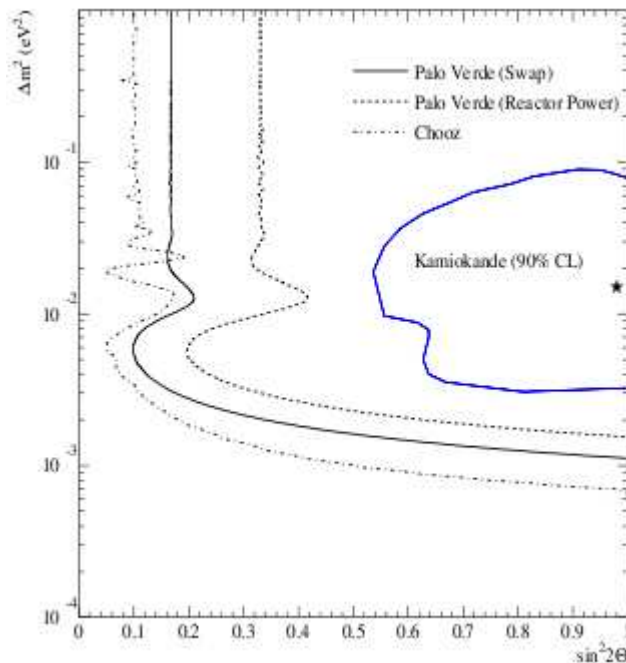
Figure 2.4: Palo Verde exclusion contour. The exclusion frontier is less constraining than CHOOZ's [36].

The data taking of Palo Verde led to the ratio of measured to expected $\overline{\nu_e}$ events [36], showing no evidence for oscillation:

$$R = 1.01 \pm 2.4\%(stat.) \pm 5.3\%(sys.) \tag{2.3}$$

The exclusion plot is shown in figure 2.4. One can see that the results of the Palo Verde experiment were in agreement with those of CHOOZ, though with higher systematic errors.

The observations made by CHOOZ and Palo Verde are fundamental, since they prove that electronic antineutrino oscillations at the Δm^2_{atm} scale are small. There is now intense activity all around the world to develop MBL reactor neutrino and accelerator experiments with improved sensitivities, in order to measure the electronic antineutrino disappearance due to the atmospheric Δm^2 and therefore the last unknown mixing angle θ_{13}.

2.1.2 From neutrino beams: a confirmation

To make a precision measurement of the atmospheric parameters, beam experiments use a particle accelerator for neutrino production (see section 1.3.4). Also, accelerator experiments

can search the appearance of the ν_e flavor in an almost pure ν_μ beam in order to look for θ_{13}.

2.1.2.1   K2K and MINOS, the first long baseline beam experiments.

The K2K experiment was a Japanese accelerator experiment with a source (12 GeV proton accelerator at KEK laboratory)-detector (Super-Kamiokande, see section 1.3.3) distance of 250 km. It was the first long-baseline neutrino experiment to operate at a distance scale of hundreds of kilometers. A near detector complex, comprising a 1 kton water Cherenkov detector, as well as several fine-grained detectors, was located about 300 m from the production target to calibrate the neutrino beam. Its original goal was to be a laboratory check of atmospheric neutrino oscillation. The K2K experiment observed a discrepancy of about 3σ between the observed μ-like events and the expected number without oscillations, indicating muon neutrino disappearance. The energy distribution of K2K events together with the spectrum expected without oscillations and the best fit spectrum with oscillations correspond to the mixing parameters [37]:

$$\sin^2 2\theta = 1.0 \,, \qquad \Delta m^2 = 2.8 \times 10^{-3} \text{eV}^2 \tag{2.4}$$

The energy distribution of the data confirmed the oscillation hypothesis predicted by atmospheric neutrino experiments, even though limited statistics did not permit improvement of confidence limits. It also reduced the allowed region for Δm^2_{atm} [37].

The possibility of $\nu_\mu \to \nu_e$ oscillations has also been investigated by the K2K collaboration through the detection of e-like events in the Super-Kamiokande detector. No events above the expected background were observed; K2K confirmed the results of the Chooz and Palo Verde exclusion of $\nu_\mu \to \nu_e$ oscillations. The 90 % C.L. exclusion curve obtained by the K2K collaboration in February 2004 [38] is compared with the Chooz exclusion curve in figure 2.5. K2K results from 2006 gave the limit on the effective mixing angle $\theta_{\mu e}$ [39]:

$$\sin^2 (2\theta_{\mu e}) < 0.13 \quad (90\% \text{ C.L.}) \quad \text{at} \quad \Delta m^2 = 2.8 \times 10^{-3} \text{eV}^2 \tag{2.5}$$

The Main Injector Neutrino Oscillation Search (MINOS) is a long baseline (LBL) accelerator experiment originally designed to measure the survival probability of muonic neutrinos in order to study atmospheric parameters [40]. The neutrino beam is produced in the NuMI (Neutrinos at the Main Injector) facility at Fermilab by 120 GeV protons hitting a graphite target (cf. figure 2.6). The average neutrino energy is about 3 GeV, therefore no tau particle can be produced. The beam is then mostly made of muonic neutrinos, with an electronic neutrino contamination of roughly 1 % in ν_e. MINOS uses two similar detectors to measure a beam of neutrinos at two different locations: the Fermi National Accelerator Laboratory (Fermilab) and the Soudan Underground Laboratory in northern Minnesota, 735 km from the neutrino source. Both MINOS detectors are tracking-sampling calorimeters with active layers made of plastic scintillators. The 0.98 kton near detector measures the beam energy spectrum and composition close to the neutrino production point while the 5.4 kton far detector measures the beam contents after oscillation. The experiment has begun and is ongoing.

The MINOS detector being optimized for muons, it is rather difficult to identify ν_e CC events since they lead to an electromagnetic shower not very different from a π^0 signal. NC and
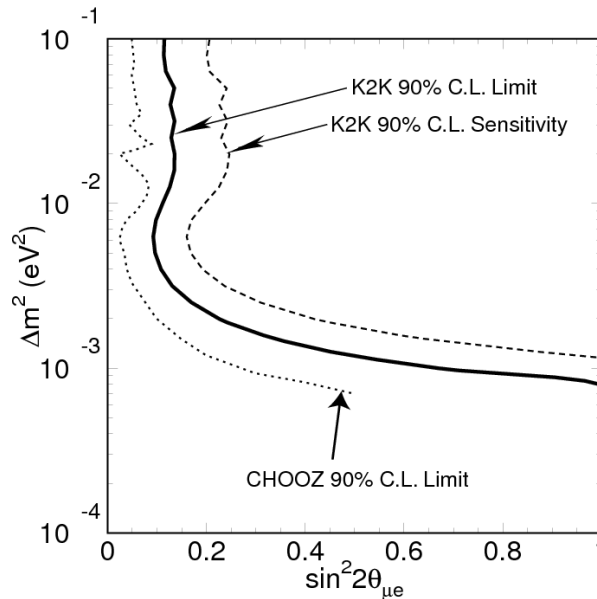
Figure 2.5: Exclusion curve in the $\sin^2 2\theta_{\mu e} - \Delta m^2$ plane for muonic neutrino, elecetronic neutrino oscillations obtained in the K2K experiment [38].The dashed line indicates the sensitivity of the experiment. The dotted line shows the 90 % C.L. exclusion curve of CHOOZ [32].

misidentified ν_μ CC events often have a similar signature, and hence lead to a background for the ν_e appearance search. As of now, the MINOS appearance data shows a slight preference for a non-zero value of θ_{13} with a best fit point of $\sin^2 \theta_{13} = 0.032$ with $\Delta\chi^2 = 1.8$ at $\sin^2 \theta_{13} = 0$ (about 1.3σ) [41].

2.2 The upcoming search for θ_{13}

2.2.1 Reactor neutrino experiments

Reactor experiments see a large signal of electronic antineutrino events and search for a small deviation from the non-oscillation prediction due to θ_{13}-induced electronic antineutrino disappearance. They are disappearance experiments because muonic antineutrinos coming from oscillation do not have enough energy to produce muons through CC processes. The survival probability depends only on θ_{13} and Δm_{31}^2 for a baseline up to a couple kilometers (see section 1.2.4.1). The optimal baseline to measure the value of θ_{13} is in theory at the first minimum in the survival probability near 2 km. Reactor neutrino experiments are precision experiments, whose success relies on statistical as well as systematic errors below the percent level. The CHOOZ experiment concluded with a 2.8 % statistical error and a 2.7 % systematic error. The goals of a follow-up experiment are to improve on CHOOZ's sensitivity, meaning reducing both these errors. The statistics are the easiest to improve. Indeed, CHOOZ ran for 1543.1 hours with the two reactors running and 3245.8 hours with one of the two reactors running [41]. Therefore, with a detector twice as big as CHOOZ's, such as the Double Chooz detector, 3
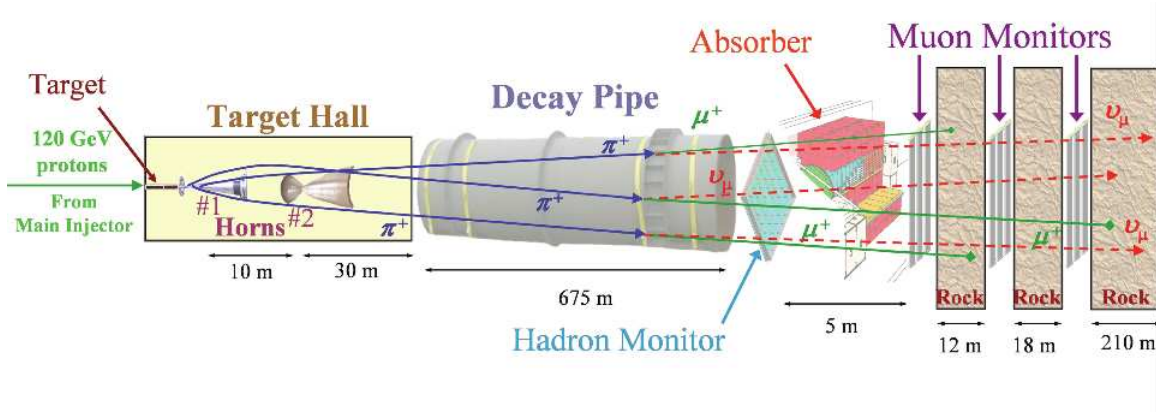
Figure 2.6: NuMI facility sketch. 120 GeV protons hit a graphite target to create mesons These are then focused by magnetic horns towards a decay pipe where they decay into antimuons and muon neutrinos. The focusing system can choose between the sign of the mesons and therefore the beam type: neutrinos or antineutrinos. Absorber at the exit of the tunnel stops all particles but neutrinos.

years of running would be enough to gain a factor 25 in the number of neutrinos in the detector. The systematic uncertainties can be greatly suppressed or totally eliminated in a relative measurement between two identical detectors having the same efficiency positioned at two different baselines. The near detector close to the reactor is used to establish the flux and energy spectrum of the antineutrinos.

The site selection was done in parallel with other similar efforts in Brazil, China, Japan, South-Korea, Russia, Taiwan and the United States, where eleven sites were investigated. This international effort led to five international workshops, from 2002 to 2005, which outlined the challenges and benefits of a new reactor experiment to measure θ_{13} and reviewed the potential of each site [42]. Today, the world wide conditions have changed and only three projects are under construction: Daya Bay (China), Double Chooz (France), and RENO (South Korea). The different layouts of the three experiments are shown in figure 2.7. Double Chooz and
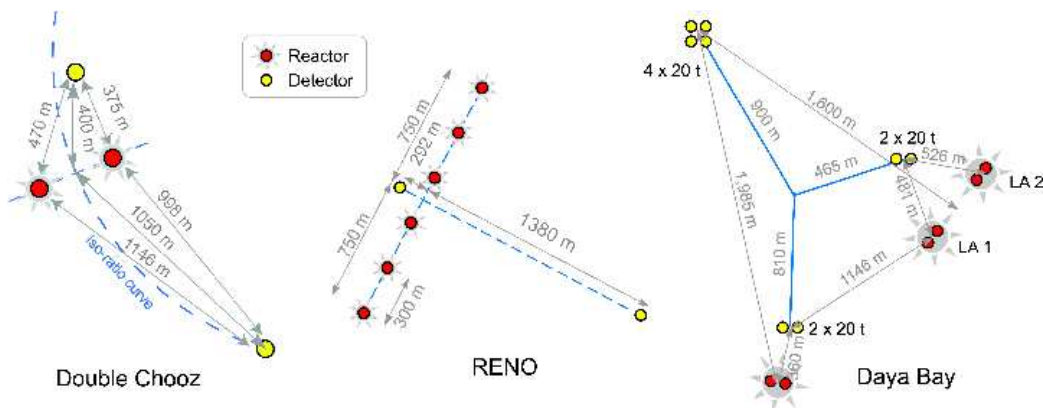
Figure 2.7: Configuration of the experimental layout (reactors, detectors) of Double Chooz, RENO and Daya Bay. Red dots represent the reactor cores, yellow dots the detectors. The dashed line on the Double Chooz plot is the iso-flux corresponding to the far detector [43].

RENO will attempt to probe the value of $\sin^2(2\theta_{13})$ down to 0.02 - 0.03, whereas Daya Bay will endeavor to track $\sin^2(2\theta_{13})$ down to 0.01. A significant Research and Development effort is required since the effective fiducial target mass will be increased by one order of magnitude at the most compared to CHOOZ, and systematic and background uncertainties have to be reduced. Every experimental technique will be pushed to the state of the art.

2.2.1.1 Double Chooz

The Double Chooz experiment is located close to the twin cores of the Chooz nuclear power station [44]. The far detector is located 1.05 km away from the cores, in the laboratory of the CHOOZ experiment, with an overburden of 300 m.w.e. (meters of water equivalent). The near detector is to be an identical replica of the far one, as far as the inner part of the detector is concerned. It will be located 400 m from the cores, as shown in figure 2.7, under 115 m.w.e.
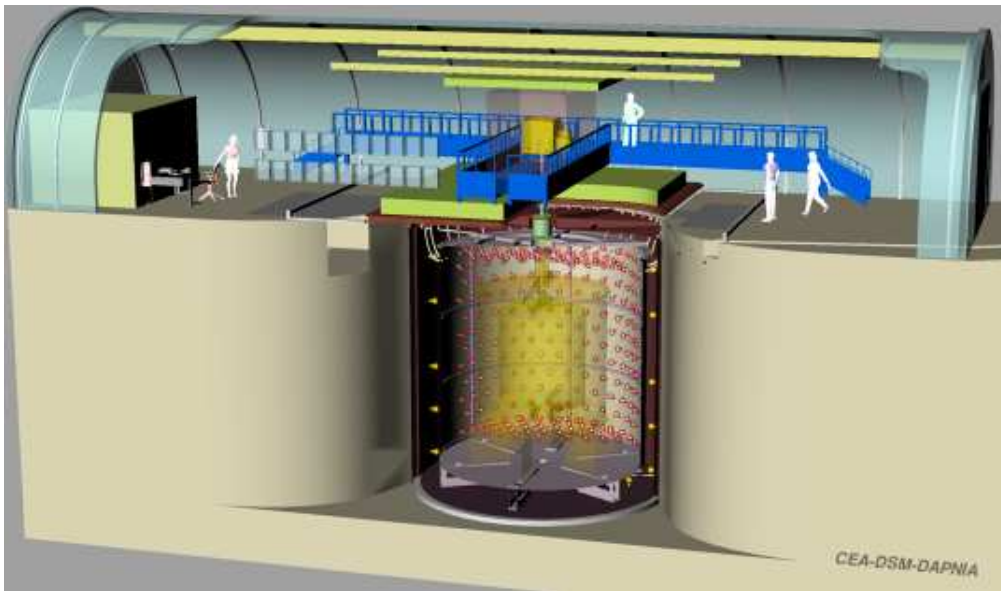
Figure 2.8: Artistic view of the Double Chooz detector and experimental hall (©CEA Imag'In IRFU, L. Scola).

The detector design is an evolution of the CHOOZ detector. On figure 2.8 is shown an artistic view of the detector in the far laboratory. It is based on the concept of Russian nested dolls; on the outside, two veto systems (an outer and an inner one) protect the inner volumes from cosmic muons, interacting in or nearby the detector. Inside these vetos, there is a buffer region in which are installed the photomultipliers (PMTs), to observe and collect light from the active detector center. This volume, filled with mineral oil, also acts as a shielding against external and PMTs radioactivity. Finally, the detector core is composed of two concentric volumes: at the center, an 8.3 ton vessel filled with Gd-doped liquid scintillator (1 gL^{-1}) is the actual target for the neutrino events. Around it, a volume called the Gamma Catcher, filled with unloaded liquid scintillator, collects gammas coming from positron annihilation and/or neutron capture that might escape from the Target. The site and detectors will be described more precisely in the next chapter.

The systematic error is to be about 2.5 % during the first phase of the experiment, without the near detector (instead of 2.7 % in CHOOZ). During phase II, with both detectors running, Double Chooz should reach 0.6 %. The statistical error is to be reduced to 0.47 %, compared to 2.8 % in CHOOZ. Indeed, the number of electronic antineutrinos expected in the far detector is roughly 45,000 (three years of data taking), as opposed to 2,700 in Chooz. One of the main reasons why the experiment can be carried out for so long, as opposed to CHOOZ, is that important progress has been made to improve the stability of Gd-doped liquid scintillators [45]. Indeed, CHOOZ's Gd-doped scintillator degraded enough during the run of the experiment (roughly one year) that the amount of light reaching the PMTs was significantly reduced. Double Chooz's scintillator has to last for at least five years (phase I and phase II) without any noticeable degradation. The sensitivity goal is to reach, with two detectors running:

$$\sin^2(2\theta_{13}) < 0.03 \quad (90\% \text{ C.L.}) \tag{2.6}$$

2.2.1.2 Daya Bay

The Daya Bay experiment is located in the Guang-Dong province of China, close to the Daya Bay nuclear power plant complex producing 11.6 GW$_{\text{th}}$ (Daya Bay and Ling Ao I sites, see figure 2.7), which will increase to 17.4 GW$_{\text{th}}$ by early 2011 when a third pair of reactor cores is put into operation (Ling Ao II). The layout of Daya Bay consists of three underground experimental halls, one far site and two near sites, linked by tunnels (under construction) [46]. Each near detector hall, with an overburden of 100 m, will host two 20 tons detectors (481 m and 363 m from the cores). The far hall, at a depth of 350 m, will host four detectors (1985 m from Daya Bay and 1615 m from Ling Ao's). Table 2.1 summarizes characteristics of the different sites. These eight detectors are designed to be interchangeable, so that near and far detectors

	Daya Bay near	Ling Ao near	Far hall
Baseline (m)	363	481 from Ling Ao I	1985 from Daya Bay
		526 from Ling Ao II	1613 from Ling Ao's
Radioactivity (Hz)	<50	<50	<50
Muon rate (Hz)	36	22	1.2
Antineutrino signal (events/day)	840	740	90
Accidental background/signal (%)	<0.2	<0.2	<0.1
Fast neutron background/signal (%)	0.1	0.1	0.1
^{8}He + ^{9}Li background/signal (%)	0.3	0.2	0.2

Table 2.1: Summary of signal and background rates for each detector module at the different experimental sites [47].

can be swapped for cross calibration. Civil construction began in October 2007.

The design of the detectors is very similar to that of Double Chooz, with a 20 ton target (cf. figure 2.9). The main difference is that the detectors will be immerged in a water pool of
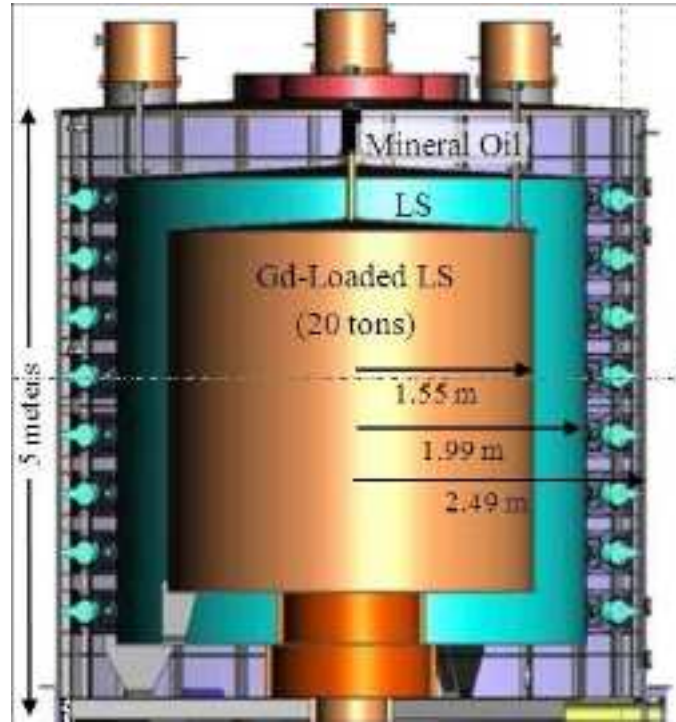
Figure 2.9: Daya Bay detector. It is very similar to Double Chooz, though all detectors will be submerged in a water pool to shield them from ambient radiation and spallation neutrons [46].

2.5 m depth to shield the detectors from ambient radiation and spallation neutrons. Above the pool, a muon veto made of light-weight resistive-plate chambers (RPCs) will be installed. The event rate per year will be about 3×10^4 at the far site. This would lead to a statistical uncertainty around 0.33 %. The final goal in terms of systematics without swapping detector modules is 0.38 %. Swapping could reduce the systematic errors from the desired goal down to 0.18 %. The sensitivity goal is to be, within three to five years of data taking [48]:

$$\sin^2{(2\theta_{13})} < 0.01 \quad (90\% \text{ C.L.}) \tag{2.7}$$

2.2.1.3 RENO

The RENO experiment will be located at the Yonggwang reactor complex in South Korea, which consists of six cores with a total thermal power of 16.4 GW [49]. The six reactors are lined up, at roughly equal distances from each other, and span about 1.3 km (cf. figure 2.7). RENO will use two identical detectors with 16 tons fiducial mass. The near detector will be about 290 m from the detector array (at a depth of 110 m.w.e.) and the far detector 1,380 m from the reactor line, with an overburden of 450 m.w.e.

The design of the detectors is very close to Double Chooz's, with a 16.1 ton target. The outer veto system is a 1.5 m thick layer of water, contained in a 30 cm thick concrete vessel. Event rates will be about 1,280 per day at the near site and 114 per day at the far site [50]. For three years of data taking with 70 % efficiency, this leads to 8.7×10^4 events with a statistical error of
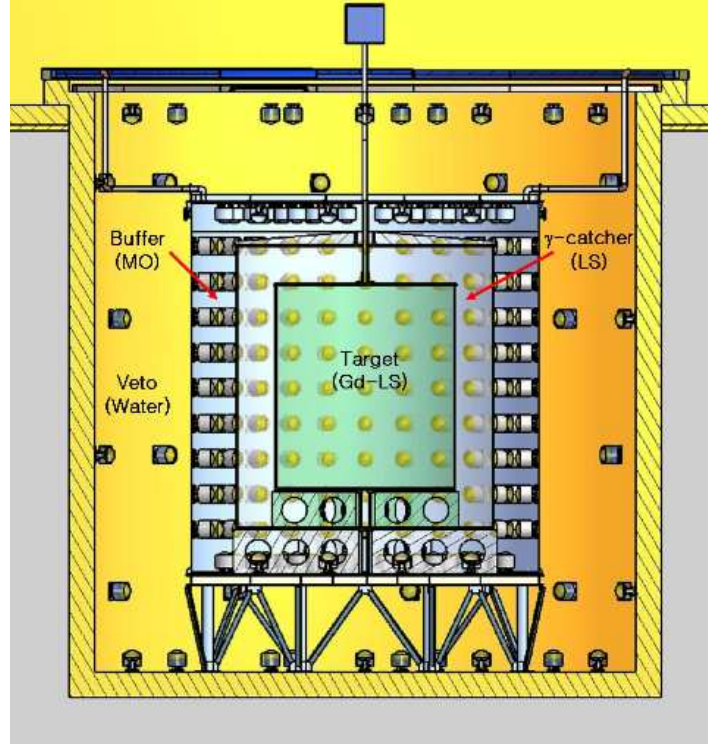
Figure 2.10: The RENO detector, very similar to the Double Chooz detector. The outer veto system is however different, made of a water layer of 1.5 m thickness [49].

0.3 %. The goal is to reach a systematic error of 0.45 %. The sensitivity goal is to be, within three years of data taking

$$\sin^2\left(2\theta_{13}\right) < 0.02 \quad (90\% \text{ C.L.}) \tag{2.8}$$

2.2.1.4   Comparison between the reactor experiments

The new concept of a four-region detector originated from the Double Chooz collaboration, in 2003, and was adopted by Daya Bay and RENO. However, the systematic errors goal are very different for the three experiment: 0.6 % for Double Chooz, 0.45 % for RENO and 0.38 % for Daya Bay (without swapping the detectors).

	Double Chooz	Daya Bay	RENO
Baseline far site (m)	1050	1985 (1613)	1380 in average
Fiducial mass (tons)	8.3	40×2/80	16.1
Thermal power (GW)	8.7	11.6 →17.4	16.4
Relative systematics	0.6 %	0.38 %	0.45 %
Baseline near site (m)	410	360 (500)	292
overburden (m.w.e.)	115/300	260/1140	110/450

Table 2.2: Phenomenological characteristics for all three new generation reactor experiments, Double Chooz, Daya Bay and RENO [44, 46, 49].

Phenomenological characteristics, described below and in table 2.2, give the experiment's sensitivity. For new generation reactor neutrino experiments, the distance from the source is to be considered for both detectors, as well as the fiducial mass, the thermal power of the reactor cores and relative systematic errors.

- According to equation (1.41), the first oscillation maximum for neutrinos of average energy 3 MeV is at a distance of 1.7 km. At this distance, the loss of electronic antineutrinos due to oscillations is maximum and therefore easier to detect in theory. However, the further the far detector is from the neutrino source, the smaller the solid angle is, the larger the statistical error is. Thus, the sensitivity on $\sin^2 2\theta_{13}$ depends not only on the far detector being on the oscillation maximum but also on the statistical and systematic errors. One can then see on figure 2.11 the sensitivity is the same for far detectors between 1 and 2 kilometers for a detector keeping a constant mass away from the source (see table 2.2).
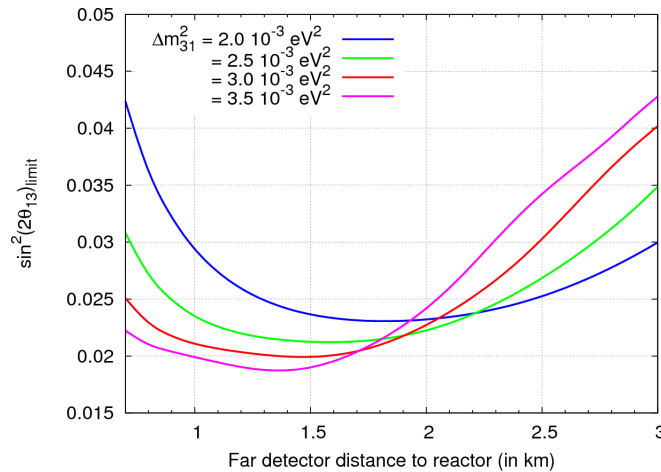
Figure 2.11: $\sin^2 2\theta_{13}$ sensitivity as a function of the far detector distance from the source. Due to statistical errors increasing with the detector-source distance, there is a plateau on the sensitivity for detectors between 1 and 2 kilometers from the source, for $\Delta m^2_{31} = 2.5 \times 10^{-3}$ and three years of data taking.

The far detector of the three experiments are between one and two kilometers from the neutrino source, hence on the plateau of figure 2.11. Double Chooz expects 15,000 events per year at the far site. For a duration of three years, this corresponds to a statistical error of 0.47 %. Daya Bay and RENO both expect 30 000 events at the far site per year, which corresponds to a statistical error of 0.33 % for three years of data taking. Daya Bay and RENO have the lowest statistical errors, with Daya Bay being closer to the oscillation maximum.

- Fiducial masses strongly impact statistical errors. Indeed, if the target mass is increased, then the statistics also increase and therefore the statistical error decreases. Therefore, a bigger far detector will be able to be closer to the distance corresponding to the oscillation maximum for the same sensitivity to $\sin^2 2\theta_{13}$. RENO's fiducial mass (16.1 ton) is twice Double Chooz's (8.3 ton), and Daya Bay's fiducial mass (80 tons) is ten times Double Chooz's! Daya Bay here has a strong advantage; this is why its far detectors are the closest to the oscillation maximum location.

- Related to the thermal power, the parameter to compare the statistical power of the experiments is the luminosity: $\frac{m \times P_{th}}{d^2}$. The luminosity is of 45.85 ton.GW.km^{-2} for Double Chooz, 235.52 ton.GW.km^{-2} for Daya Bay (soon to be 353.28 ton.GW.km^{-2} when the third pair of nuclear cores start) and 138.65 ton.GW.km^{-2} for RENO. The luminosity will be seven times bigger for Daya Bay than for Double Chooz, and two times bigger for Daya Bay than for RENO. This is due to the difference in the reactor power and mostly to the difference in fiducial mass.

- Relative systematic errors are very different (0.6 % for Double Chooz, 0.45 % for RENO, 0.38 % for Daya Bay, see table 2.2) even though the detectors are quite identical. The difference in systematics for the three experiments is a 0.4 % systematic error for RENO compared to Double Chooz, and a 0.5 % systematic error for Daya Bay. One can ask the question: what could be the sensitivity difference under the assumption that systematics are known at the same level [43]. The most significant systematics on the sensitivity of each experimental setup are the power uncertainties, the relative normalization between detectors, the energy scale uncertainties (absolute and relative, between detectors). The Double Chooz and Daya Bay proposals set the power evaluation uncertainty at a conservative value of 2 %. The central value is set to $\sigma_{PWR} = 2.0$ % for all the experiments. The relative normalization between detectors is the most significant systematic. For Double Chooz and Daya Bay, a conservative value on the relative accuracy on the electronic antineutrino rate measurement was taken: $\sigma_{rel} = 0.6$ %. The Daya Bay collaboration plans to reach a relative uncertainty of 0.2 %. The standard central value can be set to $\sigma_{rel} = 0.4$ % for all experiments. Concerning the energy scale uncertainties, the Double Chooz proposal quotes $\sigma_{scl}^{abs} = 0.5$ %. This is taken as the common central values for all the experiments. On figure 2.12, each contribution is assessed separately, as well as the total
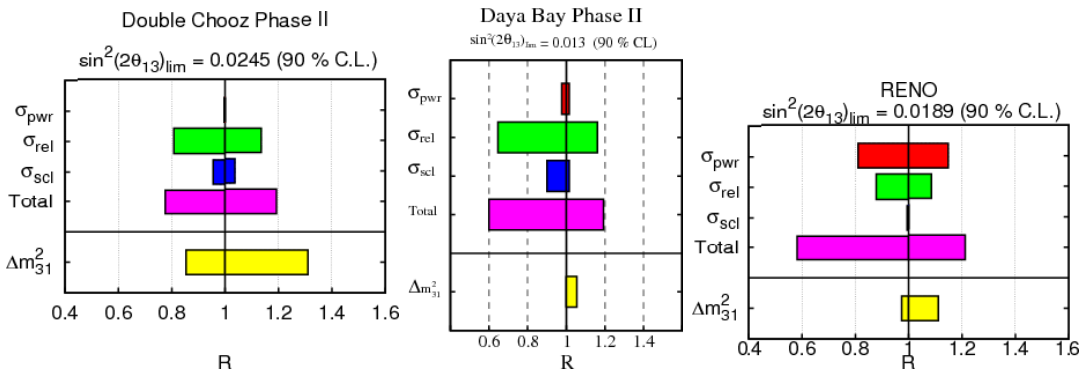
Figure 2.12: Double Chooz, Daya Bay and RENO sensitivities as a function of the size of the main systematics. The common systematic framework is what experimentalists believe to be achievable, without any further R&D. This is used to compute $\sin^2 2\theta_{13}$ sensitivity of each setup (value on top of each graph). Then each systematic impact on sensitivity is separately computed and illustrated as ratio R = $\sin^2 2\theta_{13\text{best or worst}}$ / $\sin^2 2\theta_{13\text{central}}$ on each graph. The overall impact changing all three systematics together is also illustrated with the "Total" label [43].

impact, obtained by summing the three different systematics. The sensitivity to $\sin^2 2\theta_{13}$ is also computed for standard central systematic values. The "Total" bar shows that in Daya Bay and RENO the sensitivity can vary from 0.6 to $1.2 - 1.3$. In the case of Double Chooz, the impact of systematics is less significant, at the level of 20 % on both sides.

• The use of a near detector in new generation experiments partially cancels the systematics. Nevertheless, an experiment has to understand the neutrino flux in the near detector at the best level of precision. The near detector is 410 m from the source in the Double Chooz experiment (see table 2.2). If this detector were on the iso-flux determined by the far site and the reactor cores, the sensitivity would be improved by 20 %. Double Chooz's near detector flux is the simplest to compute since there are only two reactors at the power plant, and therefore two different near baselines. Reno has six different near baselines (distance from 292 m to 700 m between the cores and the near detector). At such baselines, some neutrinos might have already oscillated once they arrive to the near detector. Daya Bay has 12 different near baselines. The distances are from 363 m to 1.347 km between the cores and the near detectors: neutrinos will have oscillated before they reach the detectors. In the three experiments, there is no optimal near detector, which would be a unique near detector that receives the same flux from all cores. The advantage here goes to Double Chooz.

• The rock overburden impacts the backgrounds. It was fixed for Double Chooz since the far site is the CHOOZ site, with no further civil engineering. Concerning the near detector, RENO and Double Chooz are equivalent, Daya Bay slightly better (see table 2.2). For the far detector, RENO has an advantage over Double Chooz, but Daya Bay's far site is under a hill and therefore has a great overburden. The investment in civil engineering is very important in Daya Bay and RENO, as opposed to Double Chooz. Backgrounds induced by cosmic muons are scaled according to the depth scaling factor (DSF), defined by:

$$DSF = \frac{\phi_\mu \times E_\mu^{0.73}}{\left(\phi_\mu \times E_\mu^{0.73}\right)_{\text{Double Chooz far detector}}} \tag{2.9}$$

The Double Chooz far site is taken as the reference. Figure 2.13 features the DSF factor for
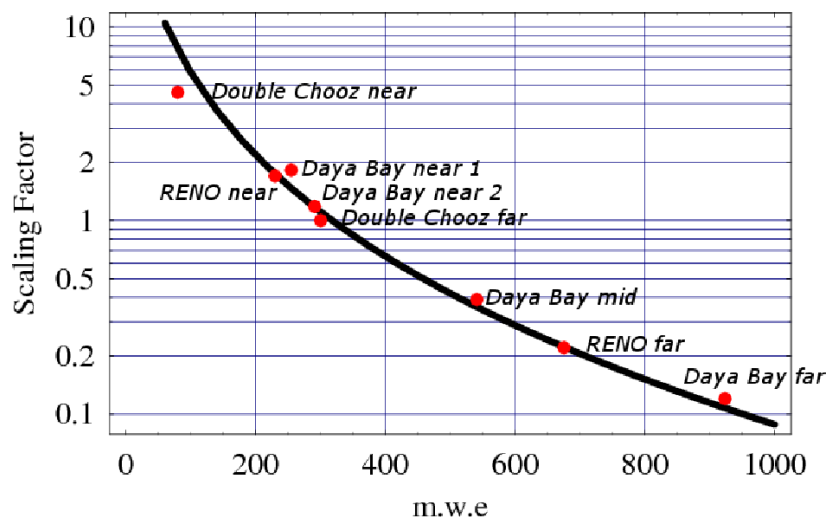
Figure 2.13: Depth scaling factor at the various sites of Double Chooz, RENO and Daya Bay. The Double Chooz far site is taken as a reference. Backgrounds induced by cosmic muons are scaled according to this factor. Daya Bay will then be the experiment with the lowest muon background, Double Chooz the one with the highest.

the different sites of Daya Bay, RENO and Double Chooz. The muon induced background will be more reduced for Daya Bay than for the other experiments.

	Double Chooz	Daya Bay	RENO
Gamma Catcher thickness (mm)	550	445	570
Buffer thickness (mm)	1,000	450	694
Light collection in Buffer	4π	PMTs on the cylinder	4π
Vetos	liquid scintillator (50 cm thickness)	water (1 m thickness)	water (1.50 m thickness)
Acrylic vessels thickness (mm)	Target: 8 Gamma Catcher: 12	Target: 10 Gamma Catcher: 15	Target: 25 Gamma Catcher: 30
Calibration systems	7	3	2

Table 2.3: Experimental details comparison table. This justifies the robustness of our sensitivity predictions [44, 46, 49].

The prediction robustness, justifying the numbers above, is given by a number of experimental details listed in table 2.3.

- The Gamma Catcher thickness acts on the lower part of the energy spectrum. Indeed, the thinner the Gamma Catcher is, the more gammas coming from positron annihilation and neutron capture might escape the active detector. Thus, the events' total energy is measured less often. Therefore, due to light leaks, the energy reconstruction systematic is higher. Since Daya Bay has the smallest Gamma Catcher (see table 2.3), it is a worse calorimeter than the other two.

- In new generation experiments, the background that dominates should be due to PMTs on the buffer wall. In Double Chooz, without the buffer, the background induced by PMTs would be of 500 Bq instead of roughly 3.5 Bq, for a threshold of 0.5 MeV.The Buffer is half as thick in Daya Bay as in Double Chooz: indeed, the radiation from the PMT glass detected in the liquid scintillator is 7.7 Hz in Daya Bay, for a 45 cm thick buffer [46]. The Buffer is a clear advantage for Double Chooz.

- Light collection is performed differently in the three experiments. For Double Chooz (392 PMTs) and RENO (354 PMTs), the collection is done over 4π. In Daya Bay, the collection is only done on the cylinder wall (224 PMTs), with reflective material on the lid and bottom. This is the first time this is done on an experiment this size. Light collection has a direct impact on energy resolution. From the three proposals [44, 46, 49], the light yield (number of photoelectrons per MeV) is 100 pe/MeV for Daya Bay, 150 pe/MeV for Reno and 180 pe/MeV for Double Chooz. Another important parameter is light uniformity in the detector. In Double Chooz, the location of the Buffer PMTs was carefully studied to ensure the best uniformity possible. In Daya Bay, due to the reflective panels on Buffer lid and bottom, the light uniformity in the detector is unknown.

- In Double Chooz, the detector's size was constrained by the size of the already existing pit, therefore the choice was to have an inner muon veto of liquid scintillator (50 cm thick). In RENO and Daya Bay, inner vetos are thicker and made of water (see table 2.3). Three cases are to consider, from which one can tell that different strategies are used in the three experiments and that none is really more efficient than the other:

  - muons: liquid scintillator is more efficient to discriminate muons than water but the veto is thinner in Double Chooz than in the other experiments. Therefore, the detection of muon is somewhat identical for all three detectors.
  - fast neutrons: proton recoils from fast neutrons in matter are visible in liquid scintillator, but not in water. There is a clear advantage for Double Chooz.
  - neutron attenuation: attenuation will be stronger in RENO and Daya Bay since there is more water than there is liquid scintillator in Double Chooz.

- At the center of the detector, to hold the Target and Gamma Catcher liquids, there are two acrylic vessels in all three experiments. RENO's target vessel is three times thicker than Double Chooz's. This decision was probably made to have a more resistant vessel, facilitating transportation, integration and filling. The acrylic vessel is a dead zone inbetween the Target and Gamma Catcher liquid scintillators, as discussed in chapter 6. Antineutrino events interacting in the Target vessel can have an ill-reconstructed energy (some of it is lost in acrylic), or even be lost. I computed the visible energy spectrum for 35,000 neutrino events in the Double Chooz detector with Target vessel thicknesses 8 mm, 10 mm and 25 mm. For a threshold of 0.7 MeV, 1.64 % events are lost in the 8 mm case, 1.71 % in the 10 mm case and 2.88 % in the 25 mm case. Moreover, in order to determine the spectral distortion of the detected positron spectrum due to this dead zone, I computed the previous spectra ratios. On figure 2.14, one can see the ratios of an 8 mm vessel with a 10 mm vessel on the left-hand side, and with a 25 mm vessel on the right-hand side. In the first scenario, mimicking a comparison between Double Chooz and Daya Bay, the spectral distortion is within 2 % higher in the simulated Daya Bay case at energies lower than 5.5 MeV, and about 4 % at higher energies. In the second scenario, mimicking a comparison between Double Chooz and RENO, the spectral distortion is higher by 5 % in the simulated RENO case at energies lower than 5.5 MeV, and up to 10 % at higher energies. Thus, one can see that between the 8 mm and 10 mm cases, the difference is acceptable. However, in the 25 mm case, twice as many events are lost, and the spectral distortion is larger; the acrylic thickness of the different experiments will impact their efficiencies. The cylindrical part of the targets weighs 250 kg, 534 kg and 934 kg for Double Chooz, Daya Bay and RENO respectively. These acrylic vessels have some contamination in Potassium, Uranium and Thorium, which will induce background while decaying. Assuming that Daya Bay's and RENO's acrylic materials have the same radioassay results as Double Chooz's and using the technique of chapter 7, this leads to a contamination from both acrylic vessels of 0.17 Bq for Double Chooz, 0.24 Bq for Daya Bay and 0.35 Bq from RENO, only considering the cylindrical part of the vessels. As an example, the construction goal of Double Chooz was to have an induced contamination below 0.1 Bq for each vessel [44]. Daya Bay and RENO are already above this limit.

- There are more calibration systems in Double Chooz than in RENO and Daya Bay (see table 2.3). The latter have both a light calibration system and a source calibration system
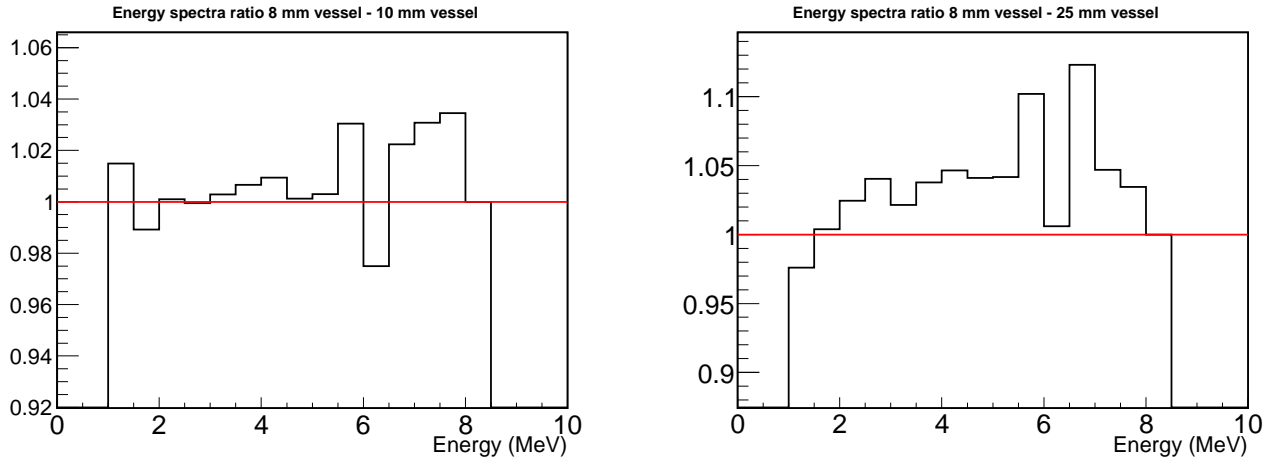
Figure 2.14: Visible energy spectra ratio to compare different Target vessel thicknesses in the Double Chooz detector. On the left-hand side, one can see the ratio between an 8 mm and a 10 mm thick vessel (the thickness of Daya Bay Target vessel); on the right-hand side is the ratio between an 8 mm and a 25 mm thick vessel, the thickness of RENO Target vessel. At energies lower than 5.5 MeV, the spectral distortion is within 2 % larger in the 10 mm case than in Double Chooz, and 5 % in the 25 mm case.

(two for Daya Bay) in both the target and Gamma Catcher. Double Chooz has the same kinds of calibration, in the Target, Gamma Catcher and Inner Veto. Moreover, one of the source calibration systems in the Target is an articulated arm that will allow to reach every corner of the Target. Finally, Double Chooz has a neutron calibration for spill in/out in the Gamma Catcher, that RENO and Daya Bay have not. Spill in takes place when an electronic antineutrino interaction happens in the Gamma Catcher close enough to the Target boundary for the neutron to cross the Target vessel and be captured on Gd, mimicking an electronic antineutrino interaction in the Target. Spill out occurs when an electronic antineutrino interaction happens in the Target close enough to the boundary for the neutron to cross the vessel and by captured on H in the Gamma Catcher. The interaction is thus not detected. Spill in/out is a 1 % systematic.

2.2.2   Neutrino beam experiments

Accelerator experiments look for the appearance of the electronic flavor in an almost pure muonic neutrino beam. A beam configuration to optimize long baseline (LBL) experiments with the goal of measuring θ_{13} is the off-axis configuration. According to the two-body π-decay kinematics, all pions above a given momentum produce neutrinos of similar energy at a given angle $\alpha \neq 0$ with respect to the direction of the parent pion. So, in an off-axis beam the energy of the neutrino depends on the angle, leading to a narrow-band beam, whereas in an on-axis beam the neutrino energy is proportional to the hadron energy. Therefore, an off-axis beam provides more flux in the region of the oscillation than an on-axis beam. Moreover, it also reduces backgrounds due to π^0 generated by NC events since these are caused by higher energy neutrinos and thus are largely absent. Finally, the intrinsic background due to beam electronic

neutrinos is reduced since they are mostly generated by three body meson decays that have different kinematics than the two body pion decays. These advantages overcompensate the smaller total neutrino flux of the off-axis configuration.

In an appearance experiment the influence of systematic errors is very much reduced if compared to reactor experiments. Nevertheless, a near detector is necessary in order to precisely measure the flux of muonic neutrinos that are going to oscillate into electronic neutrinos. The upcoming NOνA experiment is planning to have a replica of the far detector at the near site. The T2K experiment, on the other hand designed a near detector capable of precisely measuring the exclusive neutrino cross section as well as the flux of muonic neutrinos.

2.2.2.1 NOνA

The NOνA experiment [51] will run at an upgraded NuMI neutrino beam expected to deliver $6.5 \cdot 10^{20}$ pot/year generating a neutrino beam with an average energy $E_\nu \sim 2$ GeV and an electronic neutrino contamination less than 0.5 %. The power of the NuMI beam line will be upgraded, first to 700 kW by the end of 2009, then 1.2 MW, which is a factor of 6 compared to its present value. NOνA will run on surface, with an overburden of 3 m of concrete. The far detector will be located in northern Minnesota, 810 km from the neutrino beam source (at the first oscillation peak), 0.7° off the center of the beam line. It is a Totally Active Scintillator Detectors (TASD) of total mass 15 kilotons. It is expected to detect electronic neutrino signals with an efficiency of 26 % and to reduce the detector background rate to a level comparable to the rate from the intrinsic beam electronic neutrino contamination. The near detector will be a 215 ton replica of the far detector, off-axis, at a distance of 1 km from the target.

By observing the $\nu_\mu \rightarrow \nu_e$ oscillation, the expected sensitivity on $\sin^2(2\theta_{13})$ is of one order of magnitude better than the 90 % C.L. limit set by the Chooz experiment:

$$\sin^2(2\theta_{13}) < 0.01 \quad (90\% \text{ C.L.}) \tag{2.10}$$

A second goal of NOνA is to explore the CP phase and neutrino mass hierarchy. Since it has a very long baseline, matter effects are non negligible (30 % effect). Electronic neutrino CC interactions with the electrons in the Earth's crust create a potential that depends on G_F, N_e (electron density on neutrino path), E_ν (-E_ν for antineutrino). It modifies the mass eigenstates values and thus the oscillation probability, reducing Δm_{23}^2 in the case of normal hierarchy and increasing it in the case of inverted hierarchy. Thus, the probability of oscillation is different for neutrinos and for antineutrinos. This matter effect will then mimic a CP phase effect and must be well understood to clearly identify a "CP phase signal". In figure 2.15, one can see that the NOνA experiment will only be able to investigate up to 60 % of the true value of the CP phase, depending on $\sin^2(2\theta_{13})$. Thus, other experiments will be needed to explore the whole range of CP phase values.

The experiment is to start early 2012, while the nominal exposure in the detector is expected to be reached in 2019.
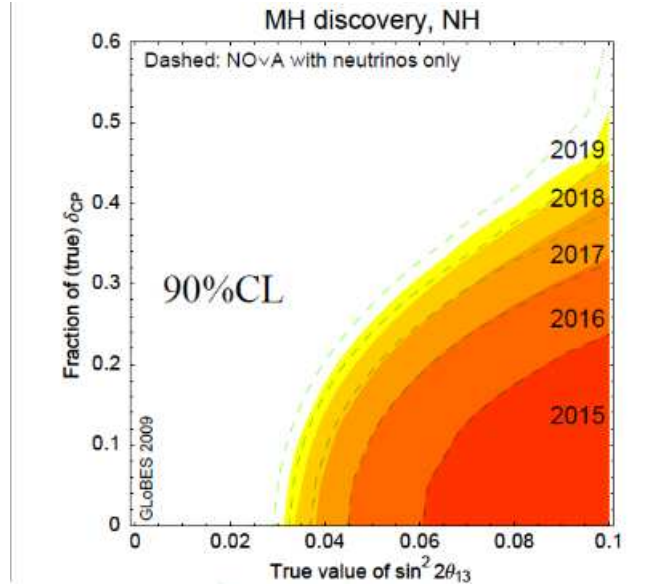
Figure 2.15: Fraction of observable CP phase as a function of $\sin^2 2\theta_{13}$ in NOνA, at 90 % C.L. Even with conducting the experiment until 2019, only a fraction of δ can be investigated.

2.2.2.2   T2K

The T2K experiment is designed to study neutrino oscillations in the atmospheric neutrino regime [52]. The neutrino source will be the J-PARC accelerator in Tokai, on the east coast of Japan. The neutrino beam has an average energy of 0.76 GeV. The properties of the resulting neutrino beam are measured by a near detector 280 m away from the source. It is expected to calibrate the absolute energy scale of the neutrino spectrum with 2 % precision, measure the non-QE/QE ratio at the 5-10 % level and monitor the neutrino flux with better than 5 % accuracy. The electronic neutrino fraction should be measured with an uncertainty better than 10 %. The detector is too close to the decay tunnel to have a neutrino flux identical to the far detector flux. Differences as big as 50 % are expected between the two fluxes, reducing the capability of the close detector to reduce systematic errors independently from any Monte Carlo simulation. The beam then propagates underground for 295 km, nearly across the width of Japan before reaching the Super-Kamiokande detector, a water Cherenkov detector with a fiducial mass of 22.5 kton (see section 1.3.3). Signal events are detected with an efficiency of 45 % and with a detector background contamination smaller than the intrinsic beam electronic neutrino contamination. The Super-Kamiokande detector is off axis by 2.5°.

T2K will make two related measurements of oscillations of the muonic neutrino beam. The first of these will look at the disappearance of muonic neutrinos. For the parameters of T2K, this oscillation is absolutely dominated by the atmospheric oscillation and therefore its measurement will allow the accurate determination of the values of $\sin^2 (2\theta_{23})$ with an uncertainty of 0.01, and Δm^2_{32}, with an uncertainty of 10^{-4} eV^2. The second T2K oscillation measurement is to look for appearance of electronic neutrinos in the beam. If $\theta_{13} = 0$, then the muonic neutrinos would oscillate into tauic neutrinos and we would see no electronic neutrinos in the beam. However if $\theta_{13} \neq 0$, there is an oscillation that would produce electronic neutrinos in the beam, and hence an observation of these would allow a measurement of θ_{13}. The electronic neutrino

contamination coming from muon and kaon decay will be around 1 %. After five years of data taking, the expected sensitivity is:

$$\sin^2\left(2\theta_{13}\right) < 0.006 \quad (90\% \text{ C.L.}) \tag{2.11}$$

The experiment has started, expecting to reach nominal exposure for the desired sensitivity around 2017.

2.2.3 Complementarity of reactor and superbeam experiments

While reactor experiments search for the disappearance of electronic antineutirnos, accelerator experiments look for the appearance of electronic (anti)neutrinos in a beam initially composed mainly of muonic (anti)neutrinos. In reactor experiments, the survival probability neither depends on θ_{23}, nor on the CP phase δ, nor on the sign of Δm_{31}^2. Hence, reactor experiments provide a "clean" measurement of θ_{13}, free of correlations with other parameters, apart from $|\Delta m_{31}^2|$. Figure 2.16 shows typical fits in the $\theta_{13} - \delta$ plane for $\sin^2 2\theta_{13} = 0.03$ and δ close to maximal CP violation ($\delta = \pi/2$). Concerning LBL appearance experiments, for typical
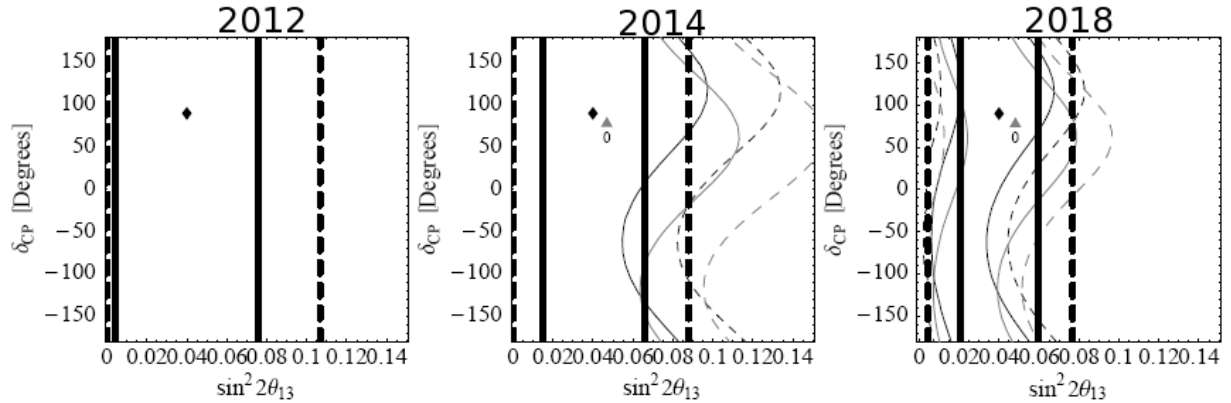
Figure 2.16: Typical fit results for Double Chooz and T2K. The figures represent fits in the $\theta_{13} - \delta$ plane, for $\sin^2 2\theta_{13} = 0.03$ and $\delta = \pi/2$. The contours correspond to 1σ, 2σ and 3σ. The best fit values are marked by diamonds for normal hierarchy and triangles for inverted hierarchy. One can see that, for reactor experiments, there is no dependence on δ and that inverted and normal hierarchy coincides, as opposed to accelerator experiments.

energies in the GeV range and baselines larger than 100 km one cannot neglect matter effects. However, it is a good approximation to assume a constant matter density, given by the average density along the neutrino path. Therefore, a rather useful expression for the $P_{\mu e}$ appearance probability can be [41]:

$$
\begin{aligned}
P_{\mu e} \;=\; & \sin^2 2\theta_{13} \sin^2 2\theta_{23} \frac{\sin^2\left(A-1\right)\Delta}{\left(A-1\right)^2} \\
& + \; \beta \sin 2\theta_{13} \sin 2\theta_{12} \sin 2\theta_{23} \cos\left(\Delta + \delta\right) \frac{\sin A\Delta}{A} \frac{\sin\left(A-1\right)\Delta}{A-1} \\
& + \; \beta^2 \sin^2 2\theta_{12} \cos^2\theta_{23} \frac{\sin^2 A\Delta}{A^2}
\end{aligned}
\tag{2.12}
$$

with:

$$\Delta \equiv \frac{\Delta m_{31}^2 L}{4E}, \qquad A \equiv \frac{2\sqrt{2}EG_F N_e}{\Delta m_{31}^2}, \qquad \beta \equiv \frac{\Delta m_{21}^2}{\Delta m_{31}^2} \qquad (2.13)$$

where N_e is the electron density along neutrino path. Thus, the parameter dependence of the appearance probability is much more complicated than that for disappearance in reactor experiments, as it depends on all six oscillation parameters. In accelerator experiments, correlations between θ_{13}, δ and the sign of Δm_{31}^2 are especially important.

The θ_{13} sensitivity limit is the upper limit on θ_{13} that an experiment would report. The discovery potential is given by the smallest true value of $\theta_{13} > 0$ which cannot be fitted by $\theta_{13} = 0$ at a given confidence level. As expected, the discovery potential for accelerator experiments depends on the CP phase and the mass hierarchy. For reactor experiments, both the sensitivity limit and discovery potential are very similar. In figure 2.17, the θ_{13} sensitivity limit is shown. According
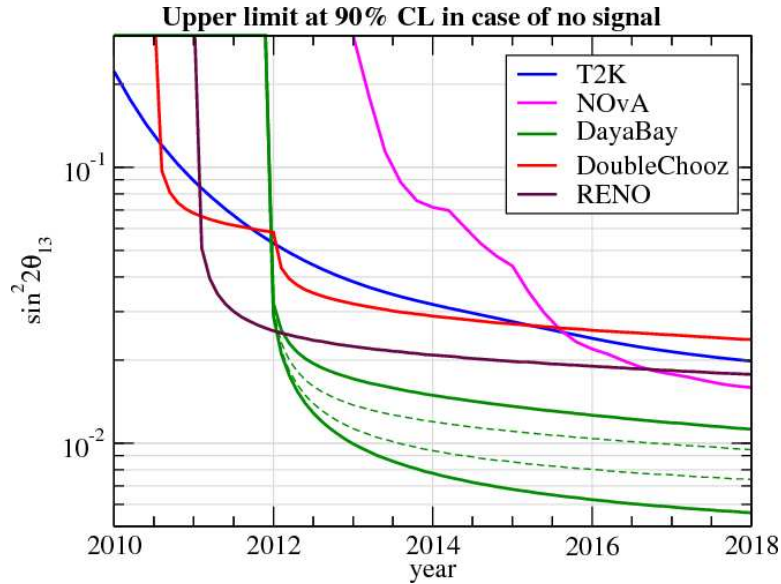
Figure 2.17: θ_{13} sensitivity limit (90 % C.L.) evolution with time, for upcoming experiments [41]. The four curves for Daya Bay represent different assumptions on the systematics. Correlations and degenerescences are not taken into account for accelerator experiments. The global sensitivity will be dominated by reactor experiments.

to it, the global sensitivity limit will be dominated by reactor experiments.

Chapter 3

Double Chooz: Site and detectors

3.1 Nuclear reactors and antineutrinos

3.1.1 Nuclear power plant

The Chooz power plant has two nuclear cores working with pressurized water (PWR), as shown in figure 3.1.
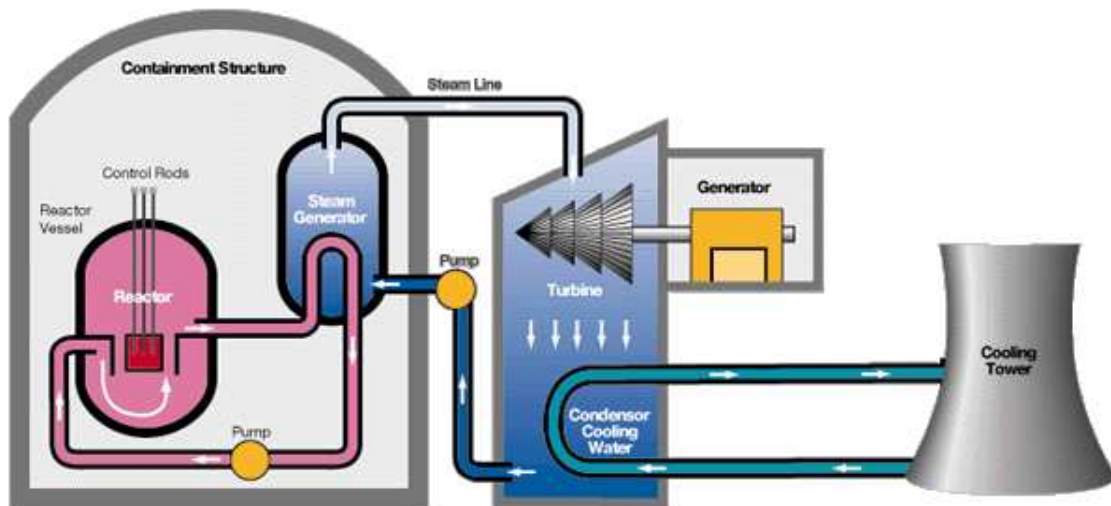
Figure 3.1: Scheme of a Pressurized Water Reactor. The primary circuit is represented in pink, its goal is to prevent the water in the reactor to boil. The secondary circuit, in blue, is where electricity is actually produced. The third circuit, in cyan, evaporates residual heat.

The nuclear fuel is made of hard pellets of enriched uranium dioxide (UO_2). The cylindrical pellets are stacked inside corrosion-resistant zirconium tubes which are backfilled with helium to aid heat conduction and detect leakages. The finished fuel rods are grouped in fuel assemblies,

61

called fuel bundles, that are then used to build the core of the reactor. A typical PWR has fuel assemblies of 200 to 300 rods; they are where the nuclear fission reactions happen. PWRs require the fast fission neutrons to be slowed down (process called moderation or thermalization) in order to interact sufficiently with the nuclear fuel and sustain the chain reaction. In PWRs, the coolant, water, is used as a moderator by letting the neutrons undergo multiple collisions with light hydrogen atoms in the water, losing speed in the process.

As already said, PWRs use ordinary water under high pressure as coolant to remove heat generated by nuclear chain reaction from nuclear fuel. The primary coolant loop is kept under high pressure (155 bar) to prevent the water from boiling; it indeed can reach a temperature of about 315 °C. Pressure in the primary circuit is maintained by a pressurizer; a separate vessel is connected to the primary circuit and partially filled with water heated to the saturation temperature for the desired pressure (here, it is 345 °C) by submerged electrical heaters. The fission chain reactions happening in the nuclear fuel produce heat, heating the water in the primary coolant loop by thermal conduction. The hot primary coolant is pumped into a heat exchanger called the steam generator, where heat is transferred to the lower pressure secondary coolant, which evaporates to become pressurized steam. The transfer of heat is accomplished without mixing the two fluids, which is desirable since the primary coolant might become radioactive.

In a nuclear power station, the pressurized steam of the secondary circuit is fed through a steam turbine which drives an electrical generator connected to the electric grid for distribution. After passing through the turbine the secondary coolant (water-steam mixture) is cooled down and condensed into water before being fed into the steam generator to start a new cycle. A third circuit, independent from the two others, condenses the steam coming out of the turbine. For this, a condenser is used, made of thousands of tubes in which circulates cold water directly from a river nearby, for example. This water is then sent back to where it came from, slightly heated. However, to prevent the river from being too much heated, cooling towers cool down the water (hence their name). Most of the water goes back to the condenser, though a small amount of it evaporates in the atmosphere: these are the white panache typical of nuclear power plants.

3.1.2   Fission reactions and neutrino productions

Nuclear power plants produce energy thanks to the heat produced by fission reactions in their core, made of enriched uranium. Natural uranium is made at 99.28 % of ^{238}U and 0.71 % of ^{235}U, fissile[1], meaning it breaks under the action of thermal neutrons. The uranium pellets are enriched to a level of nearly 3 % of ^{235}U. This isotope breaks into two new nuclei (fission products), and two or three neutrons from which one on average will induce a new fission (cf. figure 3.2), after being thermalized in water. The majority of fission products are unstable with respect to β decay, and emit an electron and an electronic antineutrino. On average, they undergo three β decays before getting to stable nuclei. ^{238}U is transformed by capture of a thermalized neutron into ^{239}U, unstable, which itself transforms into ^{239}Pu after two successive

---

[1] The only fissile products are ^{235}U, ^{233}U, ^{239}Pu and ^{241}Pu
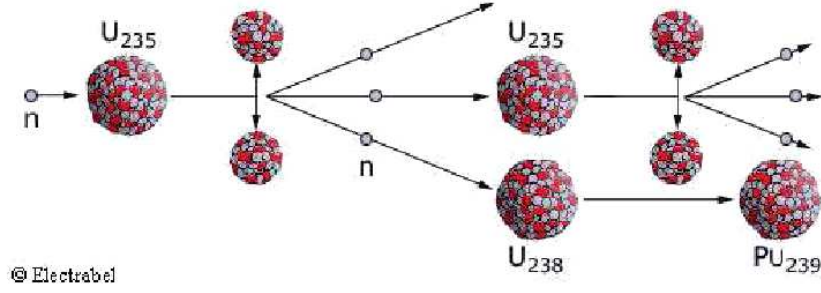
Figure 3.2: Chain reaction of the ^{235}U fission
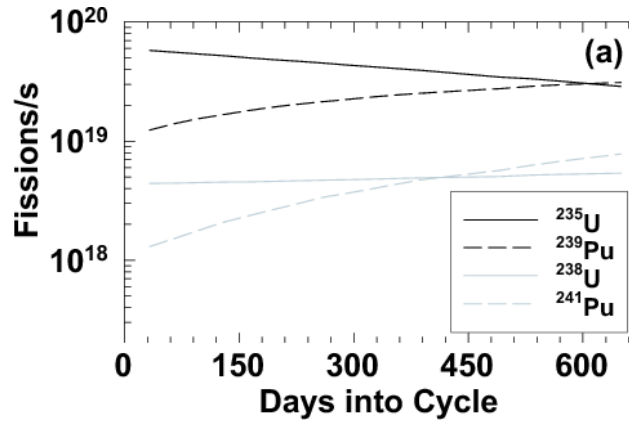
Figure 3.3: The predicted fission rates for the four main fissioning isotopes in a PWR [53].

β decays:

$$n +^{238} U \rightarrow^{239} U \rightarrow^{239} Pu \qquad T_{1/2} = 24000 \, years \qquad (3.1)$$
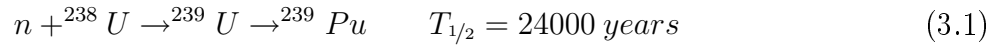
Thanks to two successive neutron captures, ^{239}Pu transforms into ^{241}Pu, fissile also.

$$n +^{239} Pu \rightarrow^{240} Pu + n \rightarrow^{241} Pu \qquad T_{1/2} = 14.4 \, years \qquad (3.2)$$

Beta decays intervening in the processes described above produce on average six electronic antineutrinos per fission. The number of emitted electronic antineutrinos is however correlated with the composition of the fuel; indeed, while the reactor is working, the fuel composition evolves with time. The number of fissions of ^{235}U decreases whereas the one of ^{239}Pu and ^{241}Pu increase. The one of ^{238}U stays practically stable (see figure 3.3). The measured antineutrino energy spectrum, and thus the average number of detectable antineutrinos produced per fission, differ significantly between the two major fissile elements, ^{235}U and ^{239}Pu (1.92 and 1.45 average detectable antineutrinos per fission, respectively). Therefore, the number of electronic antineutrinos produced decreases until the reactor is refueled. This relation between the mass fractions of fissile isotopes and the detectable antineutrino flux is known as the burn up effect. Afterwards, as a new cycle starts, antineutrino production is nominal, as one can see on figure 3.4. The Chooz power plant emits on average 4×10^{20} electronic antineutrinos per second. In figure 3.5 is the average electronic antineutrino spectrum in a detector using inverse β decay as detection reaction, like in Double Chooz, along with the inverse β decay cross section and and the antineutrino flux at the detector.

It was said that the antineutrino energy spectrum evolves also during a cycle. CEA developed a
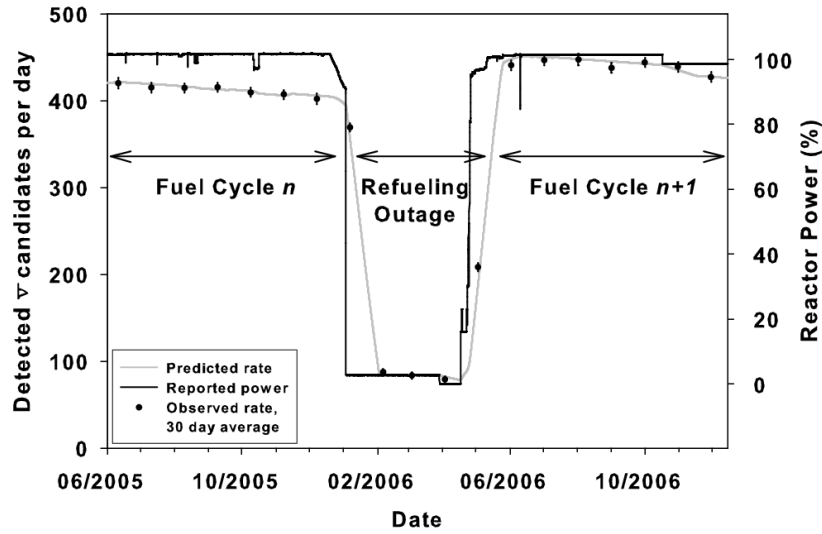
Figure 3.4: Antineutrino rate measurements before, during, and after a reactor refueling. The decrease in detection rate as the fuel evolves can be seen [53].
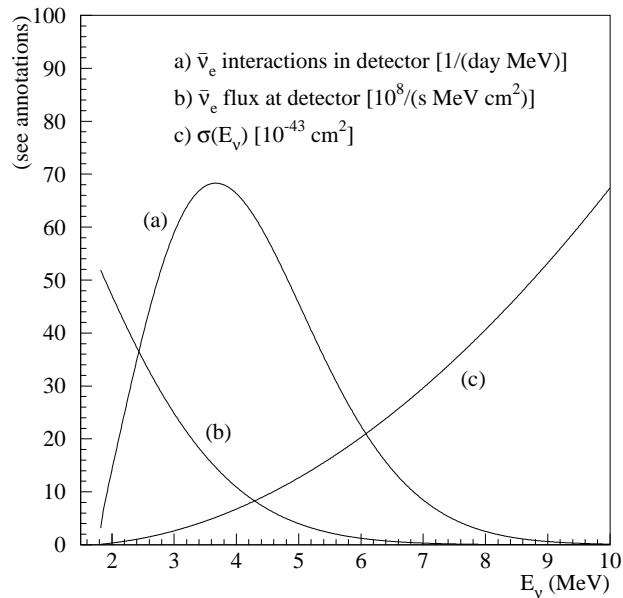
Figure 3.5: Here are represented: (a) the electronic antineutrinos interactions in a detector with inverse β decay as reaction of interest, (b) the electronic antineutirno flux at this detector and (c) the inverse β decay cross section. The electronic antineutrino energy spectrum peaks around 3 - 4 MeV [54].
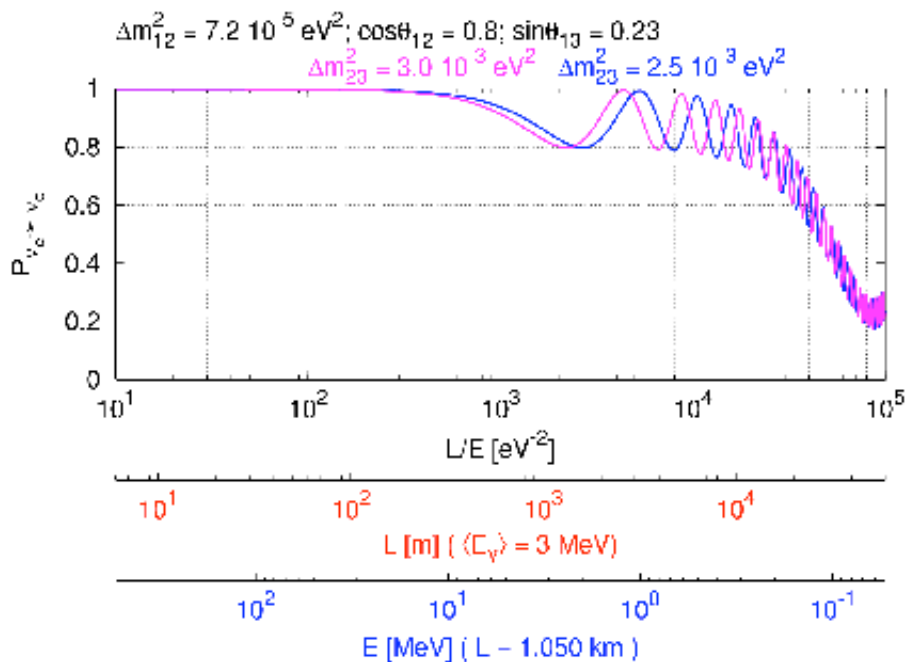
Figure 3.6: Oscillation probability of the electronic antineutrino as a function of L/E.

technique to predict the reactor electronic antineutrino spectrum for a given fuel composition. It is described in [55].

3.2 Double Chooz: site and detectors

In order to improve the CHOOZ sensitivity, at least two identical detectors close to a power station are required. The first one, located at a few hundred meters from the nuclear cores, monitors the neutrino flux and spectrum before neutrinos oscillate. The second, located between 1 and 2 km away from the cores, looks for a departure from the overall $1/L^2$ behavior of the neutrino energy spectrum, the fingerprint of an oscillation. Figure 3.6 represents the oscillation probability of electronic antineutrinos as a function of the L/E ratio. Since the reactor neutrino source led to the largest systematic uncertainties in the CHOOZ experiment, this new set-up provides a great improvement in the search for a small mixing angle. Two identical detectors allow a relative comparison, within one percent precision or less using standard technologies. Of course, the statistical error has also to be decreased by a similar amount, leading to an increase of the exposure by a factor 15 at least.

3.2.1 Experimental site

The Double Chooz experiment was initiated in 2003. Previously, a thorough review of the few French sites suitable to carry out a new reactor neutrino experiment dedicated to θ_{13} was

Figure 3.7: Overview of the Double Chooz experimental site. The two underground laboratories are located at the end of the two 150 m tunnels (in red).

carried out. The Chooz site was selected because of the availability of the underground neutrino laboratory located at 1.05 km from the nuclear cores (figure 3.7), funded and constructed by Electricité de France (EDF) for the first experiment carried out at Chooz [32].This is the main advantage of this site compared with other French locations since it minimizes the civil construction work to be done on site. The site is located in the Ardennes region, in the northeast of France, very close to the Belgian border, in a meander of the Meuse river (figure 3.8). The antineutrinos used in the experiment are those produced by the pair of reactors located at the Chooz-B nuclear power station operated by the French company Electricité de France. Both nuclear cores are the most powerful type reactors, with a thermal power of 4.27 GW each.

The Double Chooz experiment will use two almost identical detectors of 10.3 cubic meter active size. The laboratory located 1.05 km from the two nuclear cores constructed for the first neutrino detector performed at Chooz in the late 90's is being re-used by the new collaboration. The second detector will be installed at about 410 m away from the nuclear cores. Since no high natural hills or underground cavity already exist at this location, a new underground laboratory will be excavated and equipped from November 2010 to end of 2011. The integration of the near detector will be done early 2012. An averaged neutrino rate of 55 (550) events per day are expected to be detected inside the far (near) detector, taking into account the various efficiencies, if no oscillations.
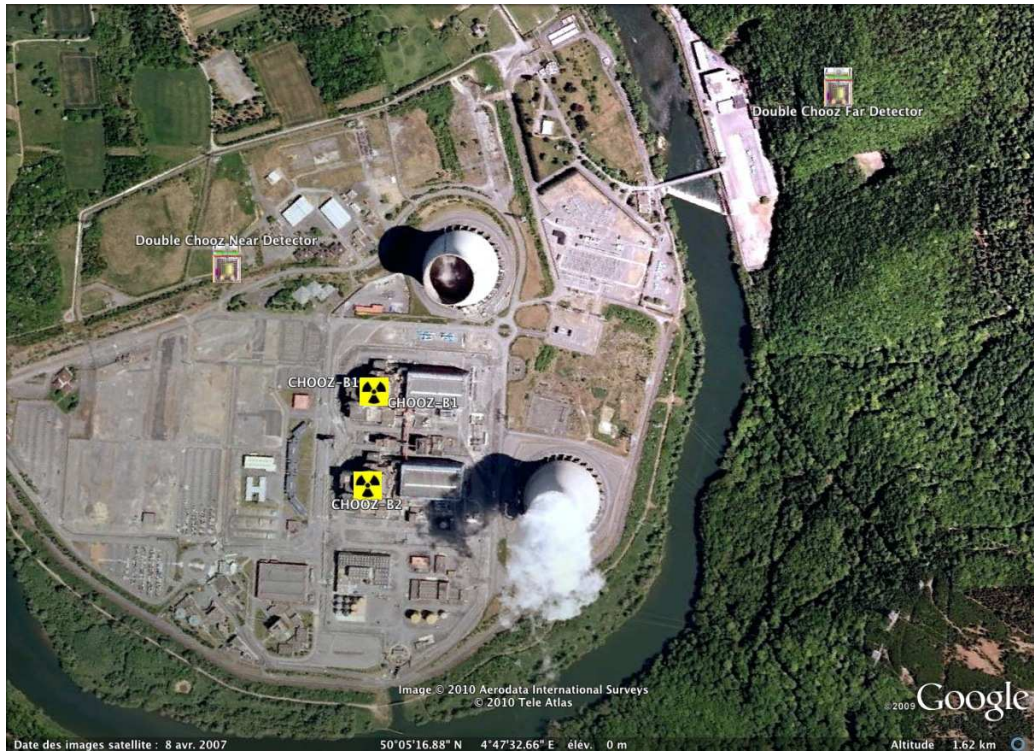
Figure 3.8: Top view of the Double Chooz experimental site. The far detector is located at an average distance of 1.05 km from the cores, and the near detector will be located 410 meters from the core, on average.

3.2.1.1   The Chooz nuclear power station

The Chooz nuclear power station is located 2 km away from the Chooz village, close to the Meuse river. Chooz is located 10 km away from the city of Givet close to the Belgium border, and about 60 km away from the biggest city of the district, Charleville-Mézières. The power station is composed of two 1,500 MW_e units known as the Chooz B site. These units are the latest N4 type PWRs. Their construction started in 1982 and the first reactor (n°1) started operation in 1996 and the second one (n°2) in 1997. In 2008 the Chooz power station produced 24.44 billions kWh representing 5% of the french nuclear energy production. The global load factor reached 91.57%. In addition, in 2008 unit n°1 obtained the world record for nuclear energy production over the year, with 12,839 billion kWh. 30 million euros are invested every year to upgrade facilities. In 2009-10, the first 10-year stop is being conducted for both units. This may provide a unique opportunity to measure background with both reactors off for more than a few days at the end of summer 2010.

On the same site, the EDF Company ran the Chooz A nuclear reactor from 1967 to 1991, which is being dismantled. This was the first PWR built in France, running at 320 MW_e. During its 24 years of operation, the Chooz A reactor produced 38 billion kWh, corresponding roughly to the needs of the city of Paris for three years. The dismantling of the reactor was authorized in 2007 and will be conducted until 2020-2025.

Concerning safety and security, the Chooz nuclear power station is being controlled by ASN (Au-

Figure 3.9: Double Chooz far neutrino laboratory, located in a tunnel of the old Chooz-A power station, at distance 1.05 km in average from the Chooz-B nuclear cores. The laboratory is shielded by 300 m.w.e. of rock. The liquid Storage building, also named liquid Storage area is dedicated to the storage of all four liquids prior to detector filling.

torité de Sureté Nucléaire) on a regular basis. Concerning environmental issues, the Chooz nuclear station is strictly constrained concerning any gaseous emission, and each year about 11,000 analyses are conducted. Results are publicly available at the EDF web site (www.edf.com). From the start of the nuclear operations at Chooz, EDF has been contributing to the economic development of the Champagne-Ardenne region. Currently more than 700 EDF employees are working on site. In addition 200 local employees are contributing to power plant operations. During the 10-year stop, more that 2,000 people were working on site. The Double Chooz experiment added about 200 temporary physicists, technicians, and engineers coming on site for detector integration and shifts.

3.2.1.2   Far site

The Double Chooz far detector is located in the CHOOZ laboratory. It is located at the end of a 200 m long tunnel of the old Chooz-A power station (see figure 3.9). Next to the tunnel entrance is the liquid Storage building, dedicated to the storage of all four liquids, before the detector is filled. In this building, represented on figure 3.10, Buffer oil (115 m^3) as well as Veto liquid scintillator have to be mixed in order to adjust their densities at the 0.1 % level. They have thus to be stored on site a few months for this operation. On the other hand, the Gamma Catcher (24 m^3) and Target (11 m^3) liquids are prepared in Heidelberg and transported on site right before filling because they are more sensitive to temperature induced effects. Beside the liquid tanks, the collaboration has installed a liquid nitrogen plant in order to purge liquids of the dissolved oxygen, as well as to provide the source of nitrogen needed for the tanks and detector flushing prior to the filling of the detector. Indeed, no oxygen is allowed in any liquid scintillator. The laboratory itself is 20 m long, 7 m large and 3.5 m high. These dimensions made the detector integration difficult, which is why the near laboratory will be larger and higher. A sketch of the laboratory and the detector is shown on figure 3.11.
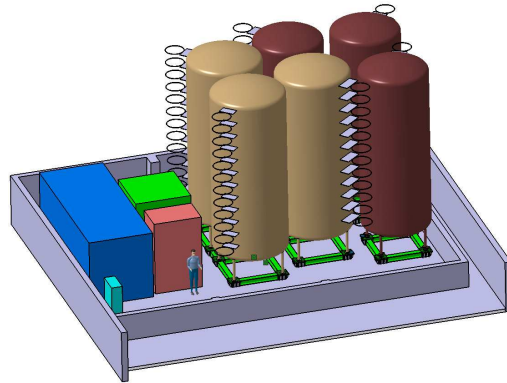
Figure 3.10: Far site liquid Storage area located close to the neutrino laboratory tunnel entrance. This is where all liquids are stored before the detector is filled. The tanks on the right of the graph are dedicated to Buffer oil and Inner Veto liquid; those on the left store Gamma Catcher and Target liquids.
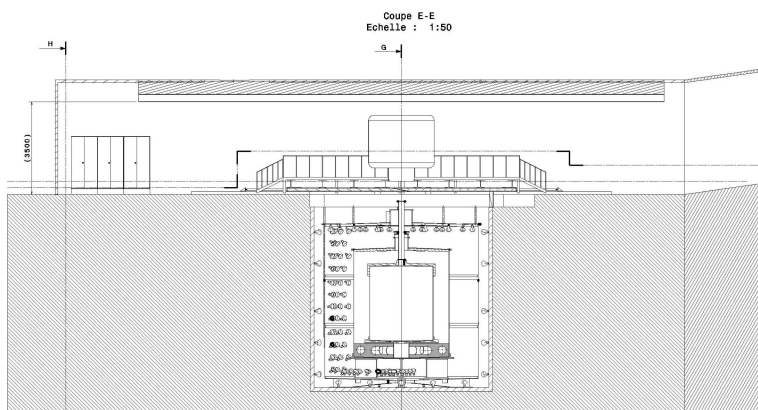
Figure 3.11: Drawing of the far laboratory including a sketch of the detector in the 7 m x 7 m pit. Because of the laboratory dimensions (20 m long and 7 m wide) the integration of large pieces was very challenging. The difficulty was increased by the low laboratory height (3.5 m available) as well as the 5 tons crane moving along the long axis on a centered single rail.
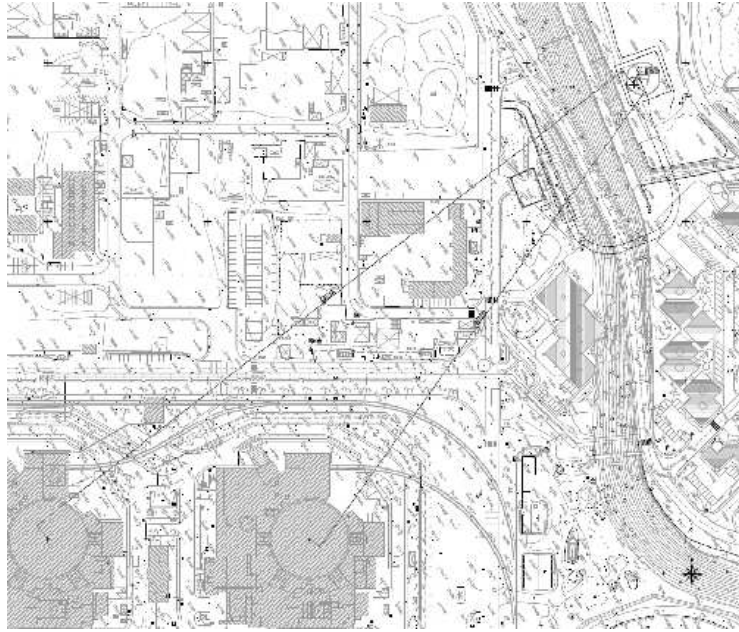
Figure 3.12: Double Chooz near neutrino laboratory, located at 400 m from the Chooz-B nuclear cores, at the end of a 14 % 88 m long open air ramp and a 12 % 155 m long tunnel. Thanks to a 20 m natural hill on top of the new laboratory, it will be shielded by a rock overburden of 120 m.w.e. We expect to detect 550 electronic antineutrinos per day.

3.2.1.3   Near site

As opposed to the far site, no underground near location is available close to the reactor cores. An old tunnel excavated at about 700 m from the cores still exist, but it unfortunately is too far and too shallow to be used as a near site. Negotiation with the EDF Company in order to allocate some space on the power plant site started in 2003 with a direct contact with the power plant director. After a few years of preparation, a first engineering study including boreholes was conducted in 2006 (the so-called APS, "Avant Projet Sommaire" in French). Full funding for the laboratory excavation was obtained in 2009 through an agreement between CEA, CNRS, the Champagne-Ardenne region, EDF, the Ardennes district, the French state, as well as the European commission. A final study to prepare the excavation bid was completed by EDF in 2010. The excavation should start by November 2010.

The location of the near site is shown on figure 3.12, at a distance of 351 m from the west reactor and 466 m from the east reactor. The new laboratory will be 45 m right below the heliport of the power plant. The detailed topology of the site is presented on figure 3.13. In order to reach a depth of 36 m below the level of the reactor cores (level labeled as NGF 120) an 85 m open air ramp (14% slope) as well as a 155 m tunnel (12% slope) have to be excavated with explosives. The site geology is rather similar to the far laboratory site, with a rather hard 'shist-gréseux' rock at an average density of 2.7 g/cm3. The top of the laboratory cavern will be covered by more than 45 meters, corresponding to 120 m.w.e. It is worth noted that the site is located below a small hill which contributes to about 50 m.w.e of the total overburden. This avoids more than 100 m of additional tunneling and was a key element for the choice of the site location compared to closer possibilities (a shaft would have been required however). The
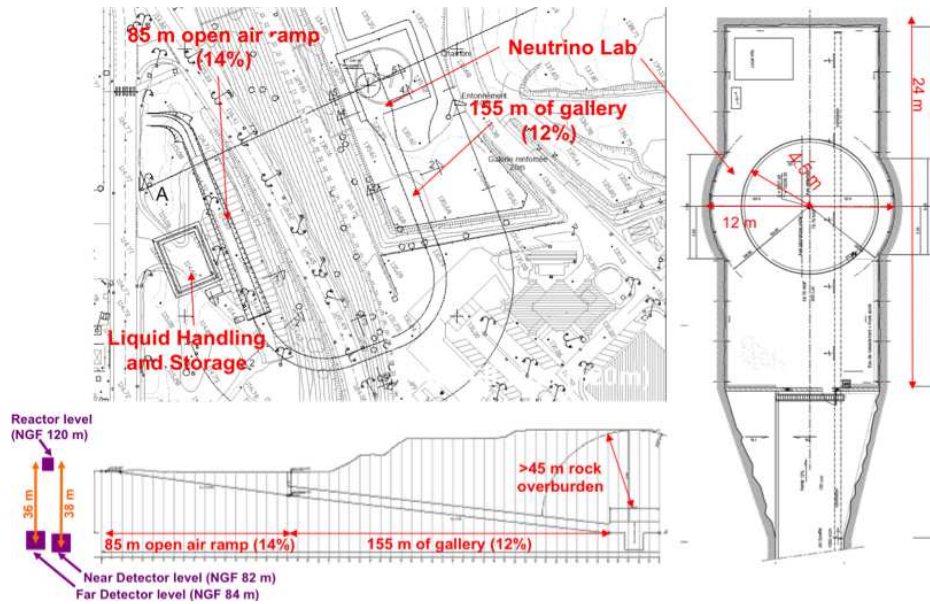
Figure 3.13: Overview of the Double Chooz Near site, located 351 m and 466 m from the Chooz-B nuclear cores (Up left). On the bottom of the figure is a side view of the tunnel and open ramp showing that the laboratory will be shielded by more than 45 m of rocks at an average density of 2.7 g.cm^3 (120 m.w.e); the NGF label indicates the relative vertical position of the laboratories and nuclear cores. On the right is a top view of the near site neutrino laboratory, similar to the far one, but larger in order to facilitate and accelerate the detector integration.

neutrino laboratory depth has been optimized according to sensitivity studies briefly described in figure 3.14.

3.2.2   A new detector design

The basic principle of the multi-detector concept is the cancellation of reactor-induced systematic errors. Though an uncertainty from the neutrino contribution of spent fuel pools remains, it is negligible for Double Chooz. Technically, the two detectors should have a set of very similar parameters to guarantee their conformity for the neutrino oscillation search. For instance, neutrino rates are proportional to the number of free protons inside the target volumes, which thus has to be experimentally determined with a precision of 0.2% (see chapter 9). This constitutes one of the major improvements with respect to CHOOZ. In order to correct for the unavoidable differences between the two detector responses, a comprehensive calibration system is being enforced, consisting of radioactive sources deployed in the different detector regions, laser light flashers, and LED pulses. Meanwhile, a new Double Chooz design has been implemented in order to simplify the analysis and to reduce systematic errors while keeping high statistics and high detection efficiency. Only three selection cuts will be used to tag the neutrino signal instead of seven for the CHOOZ experiment.

The Double Chooz detector design is an evolution of the CHOOZ detector. It is described in figure 3.15. It was first publicly presented at the Reactor Neutrino Meeting for θ_{13} at the
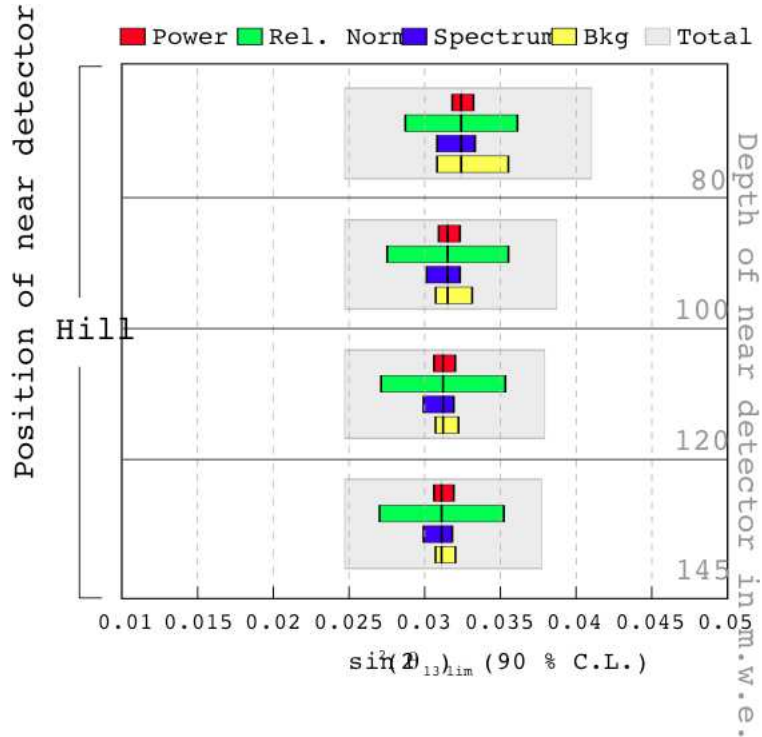
Figure 3.14: Pulls approach computation of the Double Chooz sensitivity with a near detector at four different depths: 80 m.w.e., 100 m.w.e., 120 m.w.e., and 145 m.w.e. (hill profile). An optimum reactor neutrino experiment for θ_{13} should be designed such that its sensitivity is limited by the relative detector comparison systematic uncertainty. Other pulls should be negligible. Backgrounds tend to be negligible if the overburden exceeds 100 m.w.e. We thus decided to excavate a neutrino laboratory at 120 m.w.e in order to account for contingency. We assume 3 years of data taking and a Δm^2_{atm}=2.5×10^{-3} eV^2. Pulls variations correspond to the following triplet of uncertainties: reactor power (1%, 2%, 3%), relative normalization (0,4%, 0,6%, 0,8%), neutrino spectrum shape (1%, 2%, 3%), backgrounds (none, nominal, nominal×2).

University of Alabama in 2004 [56]. It is worth noting that the Double Chooz design has been chosen by both Daya Bay and Reno collaborations to conduct their experiments. The design presented below is described in [44]. The Target is the heart of the detector. It consists of a proton-rich liquid scintillator mixture loaded with gadolinium (Gd) at a concentration of 1gL^{-1}. The solvent is a phenyl-xylylethane/dodecane mixture at a volume ratio of 20:80, so as to improve the chemical compatibility with the acrylic and to increase the number of free protons in the Target. Metal loading of liquid scintillators has been comprehensively studied within the collaboration for a few years, and a new complex has been designed for Double Chooz, based on β-diketonate chemistry. Large scale production of 16 tons of Target scintillator was completed in order to provide identical neutrino Targets for both Double Chooz detectors several years ago. Target and Gamma Catcher vessels have been built from acrylic plastic material, transparent to UV and visible photons for wavelengths above 400 nm. This is the main hardware topic developed in this manuscript. The vessels have been designed to contain the Target and Gamma Catcher aromatic liquids with long-term tightness and stability. The strongest constraint is the chemical compatibility between the vessel and the scintillating liquids of the Target and Gamma Catcher (chemical stability for a period of at least 5 years).
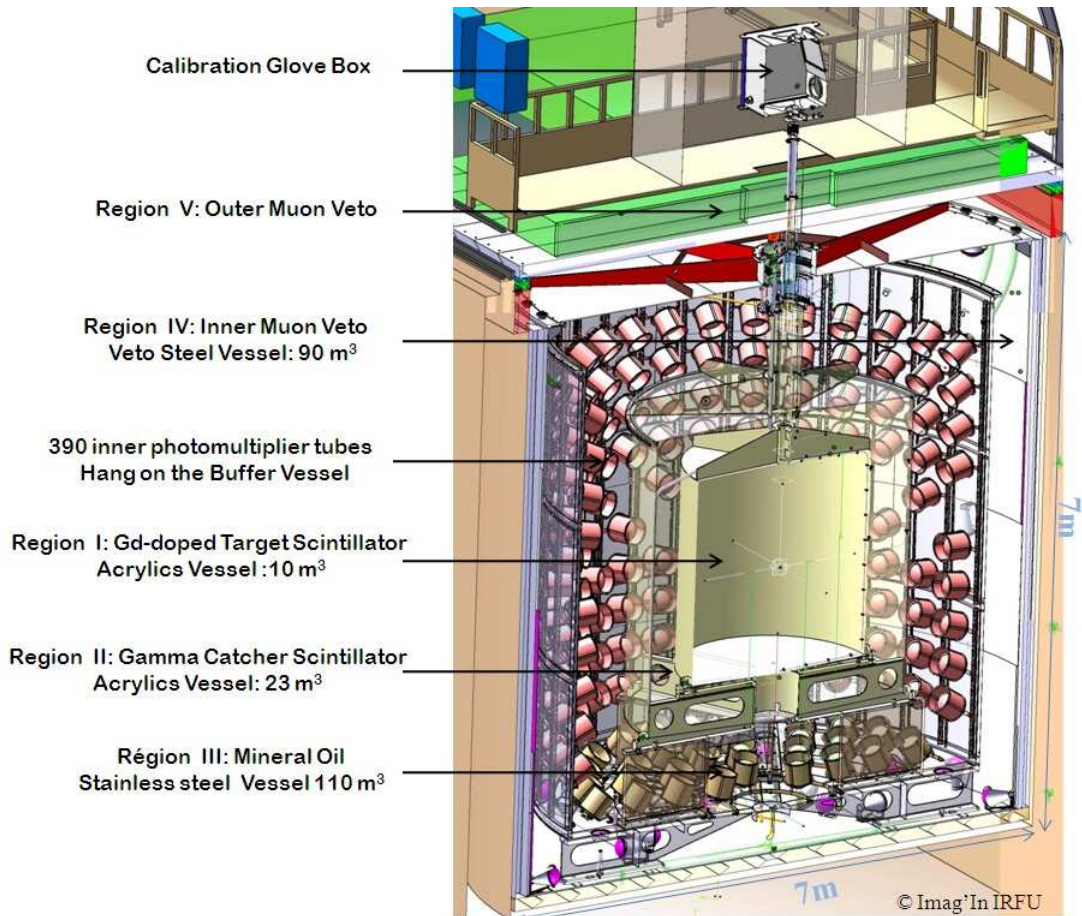
Figure 3.15: Double Chooz detector design.

The Gamma Catcher vessel must also be chemically compatible with the mineral oil of the Buffer region, which is a weaker constraint. The Target vessel is a cylinder of 246 cm height, 230 cm diameter, and 8 mm thickness. It contains a target volume of 10.3 m^3. The Gamma Catcher is a 55 cm thick buffer of non-loaded liquid scintillator (22.6 m^3) with the same light yield as the Target. This scintillating buffer is necessary to fully contain the energy deposition of gamma rays from the neutron capture on gadolinium, as well as the positron annihilation gamma rays in the central region. It also improves the rejection of the fast neutron background.

Surrounding the Gamma Catcher, a 105 cm thick region of non scintillating liquid (114.2 m^3) serves to decrease the level of accidental background by two order of magnitudes (mainly the contribution from photomultiplier-tube radioactivity). This region, called the Buffer, is crucial to keep the singles rate below 10 Bq in the sensitive region (Target and Gamma Catcher). The oil is contained in an opaque 3 mm thick stainless steel vessel maintained with stiffeners. A total of 390 phototubes (10 inch Hamamatsu R7081MOD-ASSY) are distributed almost uniformly on the interior surface of the Buffer vessel, providing a 13 % photocathode coverage. The inner detector presented above is encapsulated within a 50 cm thick region filled with scintillating organic liquid and viewed by about 70 8-inch Hamamatsu R1408 PMTs. It acts as a cosmic muon veto. Finally a 15 cm low level activity iron layer is shielding the detector against gamma rays. Above the detector pit, a highly segmented muon tracker system will identify and locate the muons missed by the inner system, with the purpose of improving the background rejection.

The near and far detectors are planned to be "identical" inside the PMTs supporting structure, allowing a relative normalization error of 0.6 %, or less. Pictures of the integration are shown in figure 3.16.

After light reaches the PMTs, the signal they produce is carried out on the same cable as the high voltage, which is why a high voltage splitter is used. The signal goes afterwards to the front-end electronics, which amplify and sum the signals. These reach the trigger units, designed to send a trigger signal to the Flash ADCs to store the event. The stored events are read out by computers; the analysis work can then begin.

3.2.3   Detection

Neutrinos interact through elastic scattering on electrons, CC on protons, NC on neutrons. The elastic scattering has a small cross section and no real discriminating signature, making it hard to detect. NC on nuclei is even harder to detect: only bolometers can study this reaction characterized by the nucleus recoil, of the order of the keV. The CC on protons, also called inverse beta decay of neutron, is the more practical detection method:

$$\overline{\nu_e} + p \rightarrow e^+ + n \tag{3.3}$$

The energies of the neutrino and the positron are related through the formula:

$$E_{\overline{\nu_e}} = \frac{1}{2} \frac{2 M_p E_{e^+} + M_n^2 - M_p^2 - m_e^2}{M_p - E_{e^+} + \sqrt{E_{e^+}^2 - m_e^2} cos\theta} \tag{3.4}$$

which gives to a good approximation

$$E_{\overline{\nu_e}} = E_{e^+} + M_n - M_p + \mathcal{O}\left(\frac{E_{e^+}}{M_n}\right) \tag{3.5}$$

where the difference between the neutron and proton mass is of 1.293 MeV. The energy actually visible by the detector is the sum of the positron energy and the electron rest mass:

$$E_{\text{vis}} = E_{e+} + m_e = E_{\overline{\nu_e}} - 1.293 + m_e = E_{\overline{\nu_e}} - 0.782 \text{ MeV} \tag{3.6}$$

The threshold of the reaction is $M_n - M_p + m_e = 1.8$ MeV which corresponds to a threshold of the visible energy of $E_{\text{vis}} = 2m_e = 1.022$ MeV. The expected antineutrino spectrum peaks around 2 - 3 MeV.

3.2.4   Conclusion

To conclude, one can state that the experiment will run in two phases: the first phase with only the far detector, the second one with two detectors. The far detector is starting right now; the first phase has begun! The near site construction will start in November 2010. Once the tunnel is excavated and the laboratory constructed, the actual detector integration is to last thirty weeks, whereas the far detector installation took roughly one and a half year. This is explained by the different sizes of the laboratories; indeed, the far detector construction was sometimes very tricky, for example for the Gamma Catcher of height superior to 3.6 m in a 3.5 m high laboratory... Once the second detector is running, the experiment is to reach a 0.03 sensitivity to $\sin^2 2\theta_{13}$ (see figure 3.17).

Figure 3.16: Pictures of the detector integration. On the top left is the integration of the shielding; one can see the bottom of the pit with shielding bars. On the top right is the inner veto, with the PMTs installed. On the middle left is the Buffer, with PMTs installed. On the middle right is the open Gamma Catcher in the Buffer. On the bottom left are the Target and Gamma Catcher, closed. One can see the filling coming out of the detector chimney. On the bottom right is the closing of the buffer, with PMTs under the Buffer lid.
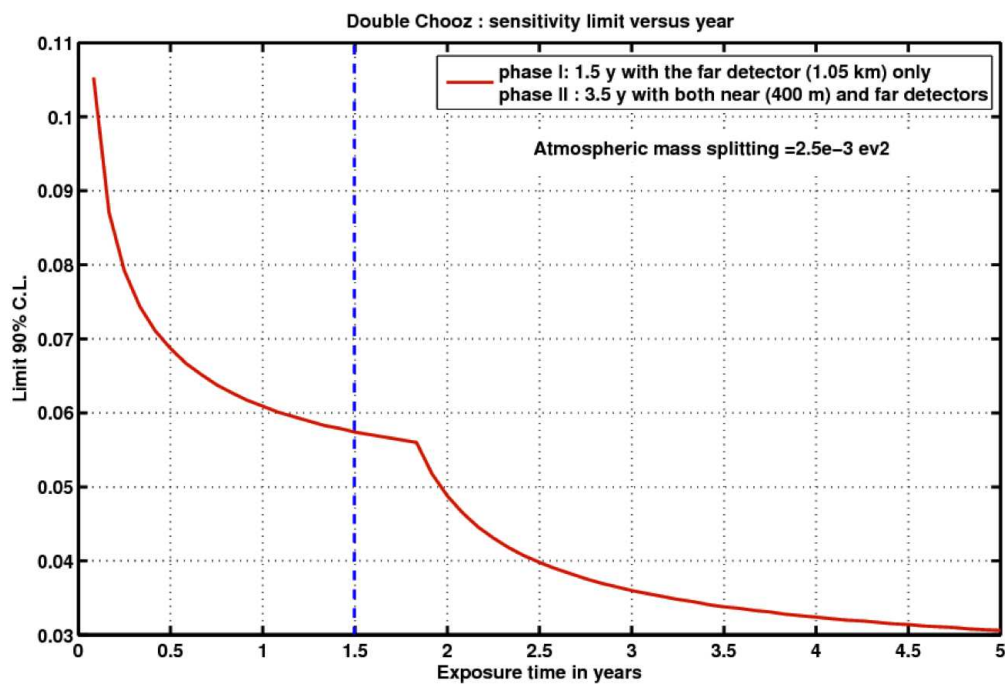
Figure 3.17: Sensitivity limit for the Double Chooz experiment versus time. During the first phase, we are to reach an 0.06 sensitivity to $\sin^2 2\theta_{13}$, while the sensitivity will go down to 0.03 for the second phase.

Chapter 4

Target and Gamma Catcher acrylic vessels

The Double Chooz detector design was motivated by several physics requirements, such as the reduction of background and the increase of statistics. We expose here these requirements, focusing on the acrylic vessels. The mechanics and tolerable constraints on these vessels are also described. Indeed, the filling phase is critical for the vessels' integrity and was studied thoroughly to determine which level difference between two adjacent volumes is tolerable without the risk of damaging the vessels.

4.1 Physics specifications for the Double Chooz detector

4.1.1 The Target volume: proton container and neutron capture

As already said, the Double Chooz experiment's reaction of interest is the inverse beta decay:

$$\overline{\nu_e} + p \rightarrow e^+ + n \tag{4.1}$$

The purpose of the detector is to measure a coincidence between the signal from the positron, prompt, and the neutron, delayed; this is the neutrino signal. Neutrons can be captured on hydrogen within 230 μs, forming Deuterium and releasing a gamma ray with energy 2.2 MeV:

$$n + p \rightarrow d + \gamma \ (2.2 \text{ MeV}) \tag{4.2}$$

In Double Chooz, in order to better identify the neutron signal, the scintillator is loaded with 1 gL^{-1} of Gd. Indeed, this nucleus has a high capture cross section (between 10 and 100 barn at 20 keV energy) for thermal neutrons and improves the neutron probability to be captured. In the CHOOZ experiment, 86.6$\pm$1.0 % of neutrons were captured on Gd [32]. The capture process is faster than on Hydrogen ($\sim$ 30 μs). The Gd nucleus is excited by neutron capture and deexcites by releasing gamma showers of 8 MeV total:

$$n + Gd \rightarrow Gd^* \rightarrow Gd + \Sigma\gamma \ (8 \text{ MeV}) \tag{4.3}$$
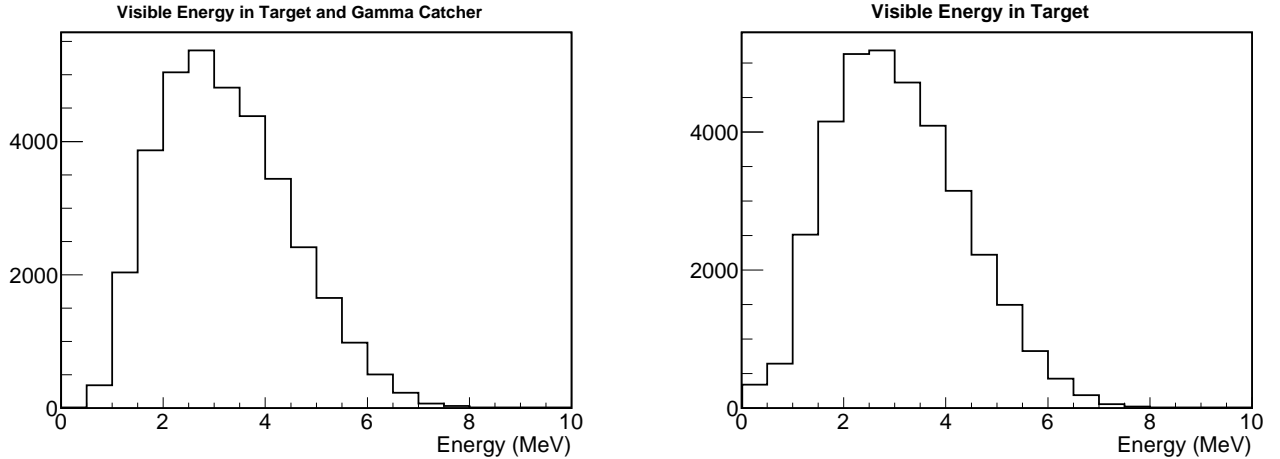
Figure 4.1: Visible energy spectra of the Double Chooz detector, for three years of data taking, with (left-hand side) and without Gamma Catcher (right-hand side). One can see that without Gamma Catcher, about 400 events have energies below 1 MeV, while there are only 150 events below this energy with Gamma Catcher.

The well constrained definition of neutron signals leads to a strong discrimination of inverse beta decay versus backgrounds. This is how the Double Chooz Target (or fiducial volume) is identified: a rigid volume of Gd loaded liquid scintillator in which neutron capture takes place. On the other hand, a neutrino event is defined as a positron energy deposition between 1 and 10 MeV followed by a neutron capture on Gd (energy deposition of 8 MeV) within a time window of 100 μs.

The inverse beta decay reaction takes place on free hydrogen atoms. The number of free protons in the Target liquid and its vessel has then to be well known in order to determine the expected number of antineutrino interactions with no oscillations.

4.1.2   The Gamma Catcher volume: positron energy detection

While the neutron capture on Gd is well defined in the Target volume, the positron full energy needs to be fully contained for all neutrino-like events. Indeed, our goal is to measure the energy spectrum of neutrinos generated in the nuclear cores of the power plant. Therefore, the whole positron energy, that carries the information on the neutrino energy, has to be deposited in an active volume of the detector. In order to allow this, the Target is surrounded with a liquid scintillator volume, with the evocative name of Gamma Catcher. Indeed, not only a positron that leaves the Target does not lose more energy than what it loses in the Target wall, but also the two 511 keV coming from its annihilation are detected in the Gamma Catcher if they escape the Target. It leads to a better energy reconstruction of the antineutrino events. This can be seen on figure 4.1, where one can see the visible energy spectra in the Double Chooz detector with and without the Gamma Catcher for three years of data taking. In the lower part of the spectrum, below 1 MeV, only roughly 150 events can be found in the case with Gamma Catcher, while there are about 400 events without Gamma Catcher. Thus, without Gamma Catcher, the experiment would have a higher systematic on the energy reconstruction. This

Energy spectra ratio with and without Gamma Catcher
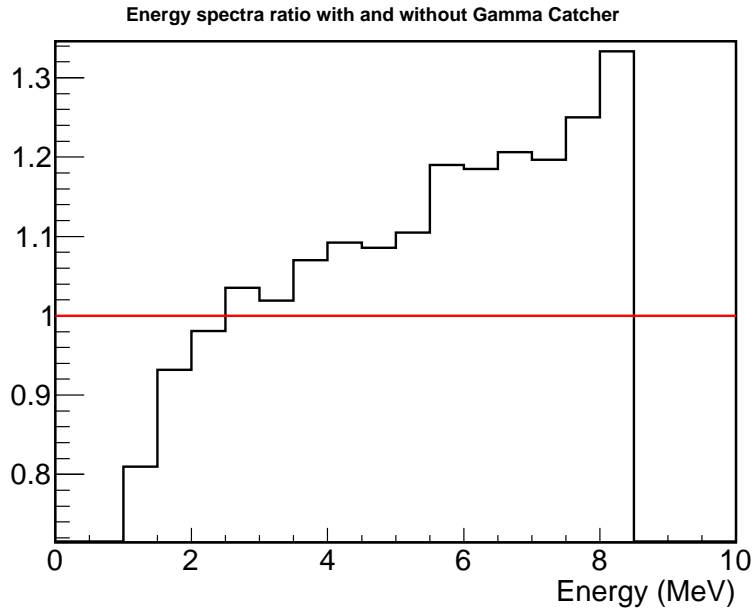
Figure 4.2: Visible energy spectra ratio of the Double Chooz detector with and without Gamma Catcher. Without this volume, the positron energy spectrum would be ill-reconstructed; there would be 20 % events more at 1 MeV and 20 % events less at 7 MeV. The end of the spectrum is better reconstructed with a Gamma Catcher. Between 2 and 4 MeV, the peak of the energy spectrum, the spectral distortion would be roughly 5 %. This is where the oscillation is expected.

can also be seen on figure 4.2, where I computed the ratio of the two previous spectra. With the Gamma Catcher, the end of the spectrum is better reconstructed.

Moreover, around 3 MeV, where the oscillation is expected to be seen, roughly 5 % less events would be seen with no Gamma Catcher. This could simulate an oscillation where there is none to find, leading to a bad estimation of θ_{13}. Moreover, as already said, a neutrino event is seen as so if and only if the neutron is captured on Gd. This leads to several gammas of total energy 8 MeV. These gammas might also escape the Target, and be detected in the Gamma Catcher. There is no Gd in the Gamma Catcher so that the Target volume stays well defined. This reduces a systematic error from 0.8 % in the first Chooz experiment [57].

4.1.3 Acrylic vessels mechanical structure

So, the core of the detector is made of two concentric vessels, the Target and Gamma Catcher, filled with active liquid scintillator. The material for both vessels was chosen to be acrylic, transparent to photons with wavelengths above 400 nm. Acrylic, or Plexiglas, chemical designation is Poly(methyl methacrylate) (PMMA). The material and its properties are described in the following chapter. Both vessels are designed to contain the Target and Gamma Catcher aromatic liquids with a long-term tightness (10 years) and stability. The strongest constraint is the chemical compatibility between the vessel and the scintillating liquids, for at least five years. We tolerate neither a modification of the liquid properties (scintillation, absorbency) nor a degradation of the acrylic material (breaking, crazing of more than a few percent of the

acrylic surface area). The Gamma Catcher vessel also must be compatible with the mineral oil of the Buffer region, which is a weaker constraint. Acrylic materials immersed in liquids have been studied under mechanical stress up to 30 MPa and at different temperatures to accelerate the aging processes. According to theses studies, realized in collaboration with the Degussa company in Germany (Darmstadt), the maximum equivalent stress tolerated in Double Chooz has been set to 5 MPa.

Mechanically, the double vessels have to be strong enough to ensure identical shapes between near and far Target vessels. No deformations of more than 5 mm are allowed during the running phase. This small geometrical difference between the two Target acrylic vessels eliminate any measurable difference of the spill in/out effect between the near and far detectors. We note here that the number of free protons inside the Target vessel has to be measured at better than 0.2 %. Thus, according to the 5 mm geometrical tolerance, the volume difference between the Target vessels could be as large as 0.6 % (60 L). In consequence, a weight-based measurement method has been developed and tested to control the Target content at the required precision (see chapter 9).

Acrylic vessels also have the advantage to be rigid, as opposed to nylon balloons, which ensures that fiducial volumes (Target and Gamma Catcher) to be as stable as possible. Moreover, both the near and far detectors' active volumes have to be identical; the forming process to construct acrylic vessels will quite easily ensure. Furthermore, acrylic material has an elasticity, that glass has not, which gives some latitude to the filling scenario. Finally, glass has a high component in ^{40}K, since it is made from silicate, that acrylic has not.

4.1.4   Cylindrical design of the detector

Now that the need for two vessels has been identified, their shape has to be chosen. In Double Chooz, the best detector is to have two features:

- It has to be highly symmetrical, in order to have a detector response as uniform as possible, i.e. the localization of an event depends on as few parameters as possible. For example, in a spherical detector, the position of an event will only depend on the radius in the sphere. For a cylindrical detector, it will depend on the radius of the cylinder, but also on the height. A cubical detector will be defined spatially by the coordinates on x, y and z.

- Its ratio of surface to volume has to be the lowest possible. This leads to less material used, therefore to a lowest surface radioactivity, a lowest cross section to cosmic rays, and less PMTs, hence, once again, less inner radioactivity for the detector.

For these two reasons, the ideal detector has a spherical design, closely followed by a cylindrical design which has the same surface to volume ratio. Indeed, we have, R being the radius (sphere

and cylinder), h being the cylinder height:

$$
\begin{aligned}
S_S &= 4\pi R^2 \\
V_S &= \frac{4}{3}\pi R^3 \\
R^S_{S/V} &= \frac{3}{R}
\end{aligned}
\tag{4.4}
$$

Whereas

$$
\begin{aligned}
S_C &= 2\pi R\,(h+R) \\
V_C &= \pi R^2 h \\
R^C_{S/V} &= \frac{2\,(h+R)}{Rh} \simeq \frac{3}{R} \qquad \text{with } h \simeq 2R
\end{aligned}
\tag{4.5}
$$

In Double Chooz we are using an already existing laboratory, the one of the first Chooz experiment. This experiment was held in a cylindrical pit of 7 m diameter and 7 m height. Therefore, in order to have the largest target possible, a cylindrical shape for the detector was chosen.

4.1.5 Design optimization

Double Chooz takes place in the CHOOZ laboratory; the detector of the new experiment was installed in the same pit that hosted the previous one, a cylindrical pit of 7 m height and 6.9 m diameter. Therefore, the overall detector size was constrained to fit in this volume. The size of the Target was decided to be twice the one of CHOOZ, to increase the statistics. This corresponds to roughly 10 m^3, a cylindrical Target of 2.3 m diameter. The thickness of the Gamma Catcher was determined by the length necessary to "capture" most of the gammas escaping the Target, to reduce the systematic errors. This lead to a thickness of 55 cm. Another parameter that was set at an early stage was the thickness of the shield, the more external volume of the detector. Due to the lack of space, the shield is made in iron. Its thickness was decided to be 15 cm, which corresponds to a 70 cm sand shielding.

Another improvement compared to the CHOOZ experiment is that PMTs are not located in the Gamma Catcher, but in a third surrounding volume, non scintillating, the Buffer. This way, the liquid scintillator is shielded from PMTs and external radioactivity and the overall background of the experiment is reduced. Concerning backgrounds, most of them come from events associated with cosmic rays. This is reduced by choosing an underground location at 120 m.w.e. depth for the near and 300 m.w.e. for the far detector. Also, the flux of neutrons coming from muon interactions in the detector or the rock close by can be controlled and rejected thanks to detector muon vetos. The first item is an Inner Veto surrounding the Buffer, filled with liquid scintillator to turn off data taking while a muon is going through or nearby the detector active volume. The second item is the Outer Veto, made of plastic scintillator strips on top of the detector. It is placed on top of the pit but is larger, to cover the rock surrounding the pit. Its purpose is to tag neutrons generated by muons passing nearby the detector, which were the principal background of the Chooz experiment.

If one considers the fixed sizes of the Target, Gamma Catcher and shield, one calculates that the Buffer and Inner Veto had to fit within 1.55 m thickness. Simulations were performed to
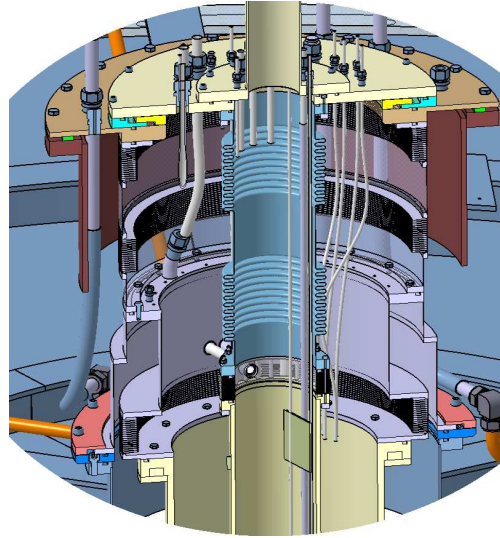
Figure 4.3: Detector chimney. In yellow are the Target and Gamma catcher chimneys; in grey is the Buffer one. On top of the Target are two Teflon bellows, to absorb any shock the chimney might encounter. The tubes that are represented are filling, calibration and sensors tubes. Not all are represented.

determine the thinnest thickness possible for the Inner Veto volume; it was computed to be 50 cm. The Buffer thickness was then decided to be 1.05 m; the Buffer was indeed chosen to be as large as possible since its purpose is to reduce the accidental background.

4.1.6   Chimneys

Acrylic vessels need to have access ports through which the volumes can be filled and also in which radioactive sources and optical calibration devices can be introduced and moved around: this access is the chimneys. The chimney is represented on figure 4.3. Target and Gamma Catcher chimneys stop right above the Buffer. On top of the Target chimney are two Teflon bellows to absorb any shock the chimney might have. Many tubes run down the chimney: filling tubes (one in the Target, three in the Gamma Catcher), calibration tube (such as the guide tube), sensors to monitor the liquid levels in the different vessels during filling.

4.1.7   Material radiopurity

Naturally occurring radioactivity can induce accidental as well as correlated backgrounds (see chapter 7). If a background event is triggered by two signals that come from the same source, such as those induced by the same cosmic muon, it is a correlated background event. On the other hand, if two signals coming from different sources satisfy the "neutrino event" conditions" by chance, the event is an uncorrelated background. Selection of high purity materials for detector construction as well as passive shielding provide an efficient reduction on this type of background.

The accidental background rate, with no spatial cut, is given by:

$$R_{ACC} = R_P R_D \tau \tag{4.6}$$

τ being being the time coincidence window (100 μs), R_P the total prompt rate of positron-like events, R_D the total delayed rate of neutron-like events. The rates are defined by the specific background rates b in Bqm^{-3} and the considered volumes V: $R = bV$. The positron-like events volume is the inner active volume (Target and Gamma Catcher, 32.9 m^3), the neutron-like events volume is the Target (10.3 m^3), where neutrons are captured on Gd. From the first Chooz experiment, the estimated neutron capture rate at the far site is of 88.5 neutrons per hour [32]. Then, a good estimate for the daily accidental background is:

$$R_{ACC} \simeq 0.2 \times \frac{R_P}{1\ s^{-1}} \times \frac{R_D}{88.5\ h^{-1}}\ day^{-1} \tag{4.7}$$

If we require the accidental background rate from all materials but PMTs ("highly" radioactive due to the PMTs' glass) to be less than 1 % of the neutrino signal at full reactor power, we get the constraints R_P^{far}<10 Bq and R_P^{near}<14 Bq [44]. This leads to the maximum allowed concentrations for ^{238}U, ^{232}Th, ^{40}K, and ^{60}Co isotopes described in table 7.1.

	^{40}K (g/g)	^{238}U (g/g)	^{232}Th (g/g)	^{60}Co (mBq/kg)
Target LS	10^{-10}	10^{-13}	10^{-13}	-
Target Acrylics	10^{-8}	10^{-11}	10^{-11}	-
GC LS	10^{-10}	10^{-13}	10^{-13}	-
GC Acrylics	10^{-8}	10^{-11}	10^{-11}	-
Buffer Oil	-	10^{-12}	10^{-12}	-
Buffer Vessel	-	10^{-9}	10^{-9}	15
Veto LS	-	10^{-10}	10^{-10}	-

Table 4.1: Maximum allowed concentrations (g/g) of ^{40}K, ^{238}U, ^{232}Th and ^{60}Co for the main components of the Double Chooz detector: Target liquid scintillator and vessel, Gamma Catcher liquid scintillator and vessel, Buffer oil and vessel, Inner Veto liquid scintillator [44].

4.2 Acrylic vessels mechanical description

4.2.1 Acrylic vessels

In figure 4.4 is shown a technical drawing of the Gamma Catcher and Target vessels. On the left-hand side is a front cut of the two vessels. The Target vessel is 8 mm thick, while the Gamma Catcher is 12 mm. On both vessels, there are stiffeners on the lid, to reinforce the structure and avoid shear stress. The Gamma Catcher is installed in the Buffer on six 60 cm high solid acrylic pieces.The Target feet, on the other hand, have holes, both to let fluids circulate and reduce pressure on the feet and to have as little non-scintillating material in the Gamma Catcher as possible. On the Gamma Catcher are also represented filling tubes and a

Figure 4.4: Acrylic vessels technical drawing.
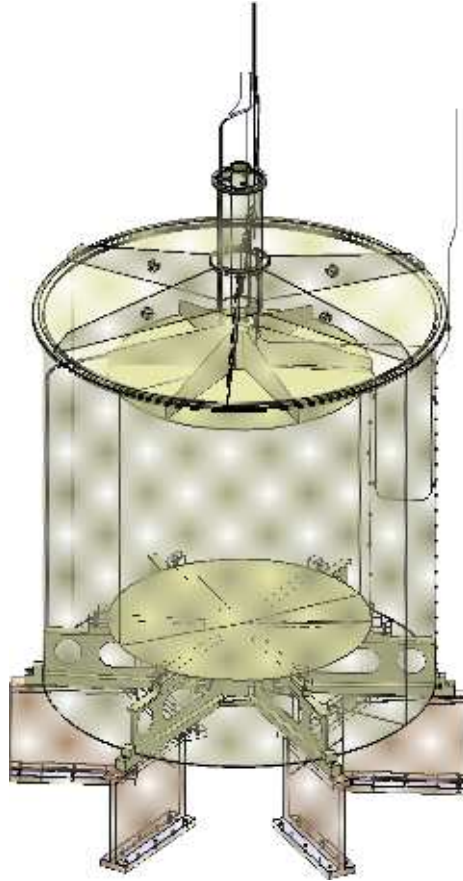
Figure 4.5: Tridimensional view of the acrylic vessels. On this view one can see two calibration devices, the Guide Tube and the Buffer Tube, as well as the chimneys.

calibration device, the Guide Tube. This device is a tube attached to the outside of the Target and the inside of the Gamma Catcher. On figure 4.5 is a tridimensional view of the vessels. On top are the chimneys with all filling tubes and the Guide Tube. On the outside of the Gamma Catcher is another calibration device, the Buffer tube.

4.2.2 Mechanical constraints: analytical check

The dimension constraint on the acrylic thickness is given by the liquid pressure. The integrity of a vessel depends on the the integrity of the gluing of the vessels. The Target vessel, of diameter D 2,300 mm and thickness e 8 mm, can resist a traction at the gluing point of 12 MPa [58]. The admissible constraint in the material is 5 MPa (safety coefficient 2.4).

For a fluid level difference of 15 mm, the pressure on the Target vessel on the cylindrical part is:

$$P = \rho g h \tag{4.8}$$

with ρ the liquid density (800 kg.m^{-3}), g the gravitation constant (9.81 ms^{-2}) and h the level difference (15×10^{-3} m). From this values, equation (4.8) gives a pressure of 117.72 Pa. The

maximal acceptable constraint is given by:

$$C_{max} = \frac{PD}{2e} \tag{4.9}$$

Therefore, the admissible maximal constraint is 1.69×10^{-2} MPa. Therefore, the thickness of the vessel could theoretically be, for a maximal admissible constraint of 5 MPa:

$$e_{th} = \frac{e C_{max}}{5} \tag{4.10}$$

Thus, for a difference level of 15 mm, the Target vessel thickness could be of 2.71×10^{-2} mm. However, such a vessel would of course be impossible to manufacture and to manipulate. In the same way, the admissible level difference would be of $h_{th} = \frac{eh}{e_{th}} = 4.43$ m.

Buckling is a failure mode characterized by a sudden failure of a structural member subjected to high compressive stresses. In the vessel, buckling can ruin the structure before the admissible constraint is reached. Critical pressure, if no reinforcements are on the vessel bottom, is given by [59]:

$$Q_b = \pi^2 \frac{EI}{R^4} \tag{4.11}$$

with E=2,700 MPa the Young modulus, R the Target radius (1,150 mm), I the second moment of inertia. According to the geometry of the vessel, equation (4.11) is equivalent to [59]:

$$Q_b = \pi^3 E \left(\left(\frac{R+e}{R} \right)^4 - 1 \right) \tag{4.12}$$

The critical buckling pressure is then 20.19 MPa. With a maximum admissible constraint of 5 MPa, we have a safety factor of 4.

However, the most constrained areas of the vessel are not on the cylindrical part, but on the bottom and lids during filling (which might because of liquid pressure difference) and on the gluing between the bottom and the cylinder (shear stress). It was then decided to add reinforcements on the gluings of the bottom and lid of both the acrylic vessels, and stiffeners on the lids. Vessels are supported by acrylic feet, which extend practically up to the vessels' bottom center, for this reason. For a liquid level difference of 15 mm, one can compute the effort on the Target bottom due to pressure:

$$F = P \pi R^2 = 489 \, \text{N} \tag{4.13}$$

4.2.3   Mechanical constraints: Finite Element Method

The Finite Element Method (FEM) originated from the need for solving complex elasticity and structural analysis problems in civil and aeronautical engineering. The basic idea is to replace an continuous problem, usually complex, by a finite dimensional version; the considered physical system is meshed into a set of discrete sub-domains, usually called elements. The analysis of these elements leads to a detailed visualization of where structures bend or twist, and indicates the distribution of stresses and displacements.
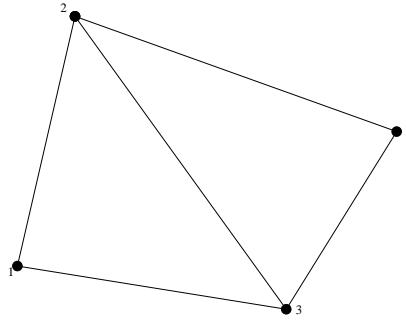
Figure 4.6: System composed by two triangular elements to be studied through FEM analysis. The original form is subdivided into two triangles with nodes (1, 2, 3) and (2, 3, 4) leading to an easier analysis. This pattern can be generalized to more complex systems.

The complete system may be complex and irregularly shaped, but the individual elements are easy to analyze. The behavior of a particular type of element is analyzed in terms of the loads and responses at discrete nodes (figure 4.6). The result of the analysis of an element is a relationship, the stiffness matrix, between the nodal displacements w and the applied nodal forces f. It is the matrix that defines the geometric and material properties of the considered volume. For instance, for triangular elements, we get:

$$\begin{bmatrix} a_{11} & a_{12} & a_{13} \\ a_{21} & a_{22} & a_{23} \\ a_{31} & a_{32} & a_{33} \end{bmatrix} \begin{bmatrix} w_1 \\ w_2 \\ w_3 \end{bmatrix} = \begin{bmatrix} f_1 \\ f_2 \\ f_3 \end{bmatrix} \tag{4.14}$$

The components of the matrix are functions of the shape of the element and properties (rigidity for instance) of the material. Once all the element matrices have been calculated, they are all combined to represent the whole system. Indeed, since the behavior of each element has been described in terms of its behavior at its edges, the assembly of element matrices is simply an expression of the fact that a node shared by two elements must have the same displacement when considered as part of either element. Let's suppose that a system to be studied consists of two triangular elements (figure 4.6). The stiffness matrix for both elements is determined considering the material properties and the element localization; equation (4.14) leads to:

$$\begin{bmatrix} a_{11} & a_{12} & a_{13} \\ a_{21} & a_{22} & a_{23} \\ a_{31} & a_{32} & a_{33} \end{bmatrix} \begin{bmatrix} w_1 \\ w_2 \\ w_3 \end{bmatrix} = \begin{bmatrix} f_1 \\ f_2 \\ f_3 \end{bmatrix} \quad and \quad \begin{bmatrix} b_{11} & b_{12} & b_{13} \\ b_{21} & b_{22} & b_{23} \\ b_{31} & b_{32} & b_{33} \end{bmatrix} \begin{bmatrix} w_2 \\ w_3 \\ w_4 \end{bmatrix} = \begin{bmatrix} g_2 \\ g_3 \\ g_4 \end{bmatrix} \tag{4.15}$$

Since nodes 2 and 3 are common to both elements, we get from equation [4.15] for the whole system

$$\begin{bmatrix} a_{11} & a_{12} & a_{13} & 0 \\ a_{21} & a_{22} + b_{11} & a_{23} + b_{12} & b_{13} \\ a_{31} & a_{32} + b_{21} & a_{33} + b_{22} & b_{23} \\ 0 & b_{31} & b_{32} & b_{33} \end{bmatrix} \begin{bmatrix} w_1 \\ w_2 \\ w_3 \\ w_4 \end{bmatrix} = \begin{bmatrix} f_1 \\ f_2 + g_2 \\ f_3 + g_3 \\ g_4 \end{bmatrix} \tag{4.16}$$

Once this has been computed for the whole system, taking into account boundary conditions, one can determine the displacements of the considered volumes (where the structure bends or twists), and also the distribution of stresses on the element. Indeed, the Von Mises stress or

equivalent tensile stress, σ_ν, is a scalar stress value that can be computed from the stiffness matrix. It determines at which points stress occurring on the x, y and z axis will cause failure. This calculation method is used for measuring stress distributions within a material. The Von Mises stress is also used to predict yielding of materials under any loading condition from results. The yield stress or yield point of a material is defined as the stress at which a material begins to deform plastically. Prior to the yield point the material will deform elastically and will return to its original shape when the applied stress is removed. Once the yield point is passed some fraction of the deformation will be permanent and non-reversible. In FEM analysis, the Von Mises stresses computed correspond to the equivalent stress applied on the material.

4.2.3.1   FEM applied to the acrylic vessels

The acrylic vessels are made of PMMA Plexiglas, which generic mechanical properties are presented in table 4.2. Taking into account the aging of the material in contact with liquid

	Young Modulus (MPa)	Ultimate Strength (MPa)	Poisson's ratio	Density (kg.mm^{-3})
PMMA	2,700	80	0.36	1.19×10^{-6}

Table 4.2: PMMA mechanical properties.

scintillator, possible defects and the gluings, we decided a maximum admissible tensile stress of 5 MPa. The fracture tests showed that shear stress[1] is the most critical solicitation. The rupture occurs in PMMA material, not at the level of a gluing. It is to note that the resistance to shear test is greater than the admissible tensile stress of PMMA.

For all different scenari calculations, we consider the material to be homogeneous and isotropic and displacements and deformations are to be small. In the following study, we place ourselves in a linear inelastic system. First, empty vessels under their own weight, before filling, are studied. Then, a study of the filling scenario was performed to determine which level differences between the vessels are acceptable to stay within the 5 MPa stress limit, and which are the most fragile detector areas.

4.2.3.2   Empty vessels

For the FEM analysis, the considered loading is a dead load (the vessels), and different hydrostatic pressures applied on the walls. These are pressures exerted by a fluid at equilibrium due to the force of gravity. The only force to consider then being the weight of the column, hydrostatic pressure can be described as:

$$p(z) = \int \rho(z) \, g(z) \, dz \qquad (4.17)$$

ρ being the fluid density (0.8×10^{-6} kg.mm^{-3}), g the gravitational acceleration, p the hydrostatic pressure.

---

[1]Shear stress: stress which is applied tangential to a face of a material, as opposed to normal stress
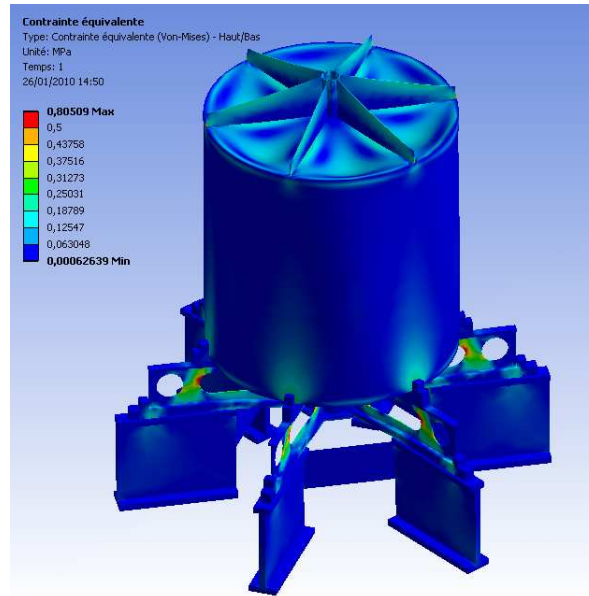
Figure 4.7: Empty Target, Von Mises constraints (MPa).

In the present FEM analysis the boundary condition is to have no displacement imposed on the lower surface of the Gamma Catcher feet. The maximum applied Von Mises stresses are computed: 0.8 MPa on Target feet (see figure 4.7) and 0.8 MPa on the base of the Gamma Catcher chimney. Displacements on the acrylic vessels due to their own weight have also been computed. On the Gamma Catcher, the maximum vertical displacement is of 2 mm on its lid between the stiffeners, towards the center. The maximum horizontal displacement is of 0.2 mm above the feet towards the exterior, 0.2 mm towards the center in between(see figure 4.8). The analysis of empty acrylic vessels integrated in the pit indicates a reaction force on the lower support (Gamma Catcher feet, boundary condition) of 19650 N. This is to relate to equation (4.13).

4.2.3.3 During filling

All vessels have to be filled at the same time to avoid pressure stress and shear, with a height difference on both sides of a vessel wall to be determined in this study. Due to height and volume differences, the filling starts with the Inner Veto, continues with the Buffer, then the Gamma Catcher and finally the Target, this until all vessels are filled. The applied stresses have to be defined in the following areas: bottom, cylindrical tank, lid, chimney. In the present study, since we focus on the acrylic vessels, the Inner Veto is not considered. It was decided to better control the liquid level that all volumes would be "pre-filled", meaning a certain amount of liquid would be present in the volumes before the filling starts. The maximum liquid levels in the vessels in order to stay within the 5 MPa limit were determined (all heights are given from the Gamma Catcher bottom, h_0):

- As the Buffer fills up, it creates a vertical displacement between the Gamma Catcher feet. For a Buffer liquid level (h_1) 30 cm higher than the baseline, the maximum Von Mises
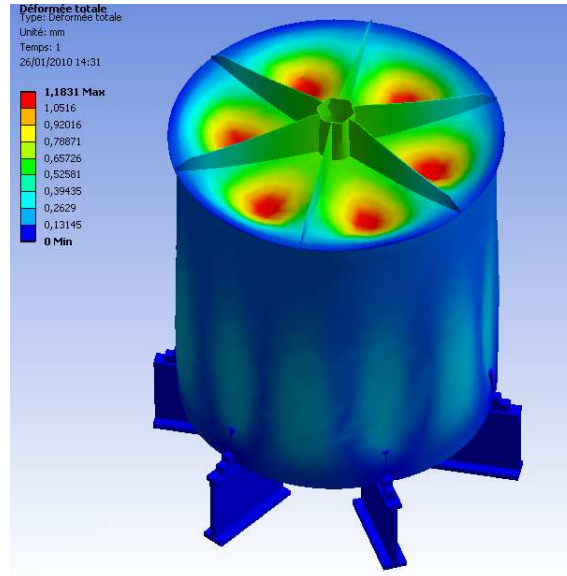
Figure 4.8: Empty Gamma Catcher, total displacement (mm).

stress is of 3.8 MPa on Target feet. Liquid creates a maximum vertical displacement of 9.8 mm. In this scenario, a gap is created between the Target feet and the Gamma Catcher bottom due to the pressure of Archimedes, as shown in figure 4.9. This is due to liquid pressure and Archimedes law on Gamma Catcher feet, transmitted to Target feet since the boundary condition is there is no displacement on the Gamma Catcher feet base.

- In the Gamma Catcher, liquid will also create a vertical displacement between the Gamma Catcher feet, but in the opposite direction (downwards). For a Gamma Catcher liquid level h_2 46 cm above baseline, the maximal Von Mises stress is 4.8 MPa.

- A Target liquid level (h_3) of 86 cm corresponds to a Von Mises stress of 4.8 MPa (cf. figure 4.10). There is a downward displacement between the Target feet.

At the beginning of the filling, only the Buffer and Gamma Catcher volumes are filled. In the following, we assume the Target to be completely empty to consider the worst case scenario. In figure 4.11, Gamma Catcher fills up faster than the Buffer. For h_1=30 cm and h_2=76 cm, the stress on Gamma Catcher reaches 4.6 MPa. The biggest displacement is 14 mm between the Gamma Catcher feet. Target feet also are solicited, with a maximum Von Mises stress of 3 MPa. Another possible scenario is shown on figure 4.12: it is the opposite of the previous situation. The stress on the Gamma Catcher feet reaches 4.3 MPa for h_1=66 cm and h_2=30 cm, with a displacement of 11.2 mm. Though, a gap appears between Target and Gamma Catcher due to pressure. Finally, in the last possibility considered for the beginning of the detector filling, Gamma Catcher and Buffer liquid levels are equal (cf. figure 4.13). For h_1=h_2=86 cm, the maximum total displacement (8 mm) is found on the Target bottom, between the Target feet, with an associated stress of 4.4 MPa. So, in this scenario, there is no stress left on the Gamma Catcher, but some appears on the Target vessel up to the point that the Target moves under the pressure coming from the liquid (a gap is appearing). Therefore, the most suitable
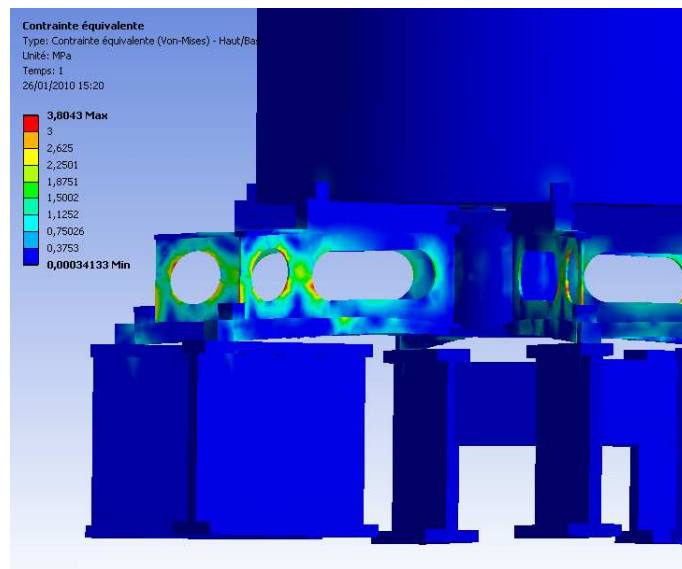
Figure 4.9: Target Feet Von Mises stress (MPa). One can see on the graph the feet displacement due to Archimedes. The maximum stress is of 3.8 MPa on the Target feet.
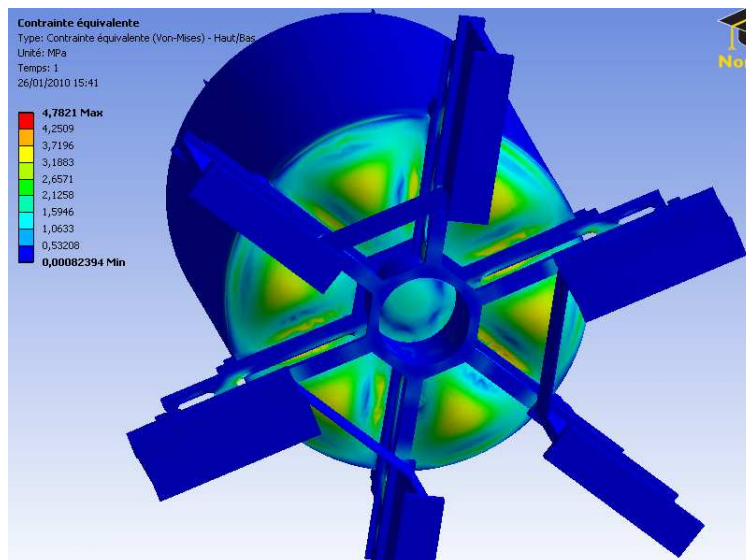
Figure 4.10: Target Von Mises stress (MPa). The maximum stress is of 3.2 MPa between the feet.
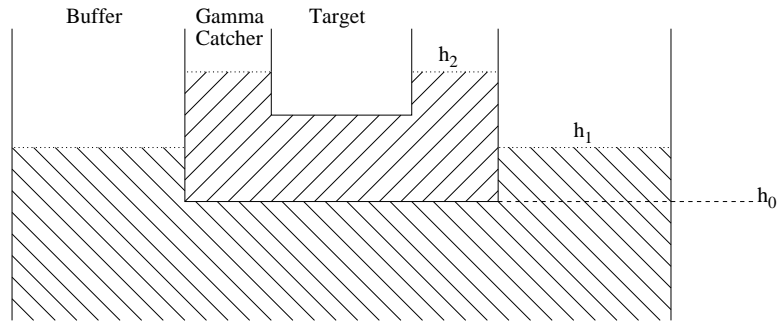
Figure 4.11: In this scenario, only the Gamma Catcher and the Buffer fill up at the beginning of the filling phase. The Buffer liquid level (h_1) is 30 cm above baseline (h_0), the Gamma Catcher liquid level (h_2) is 76 cm above baseline. The biggest displacement is between the Gamma Catcher feet.
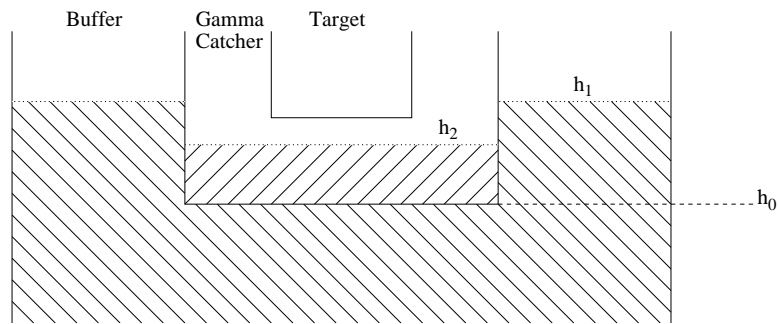
Figure 4.12: In this scenario, as in the previous one, only Buffer and Gamma Catcher fill up but this time, the Buffer liquid level is higher than the Gamma Catcher one: h_1=66 cm, h_2=30 cm.
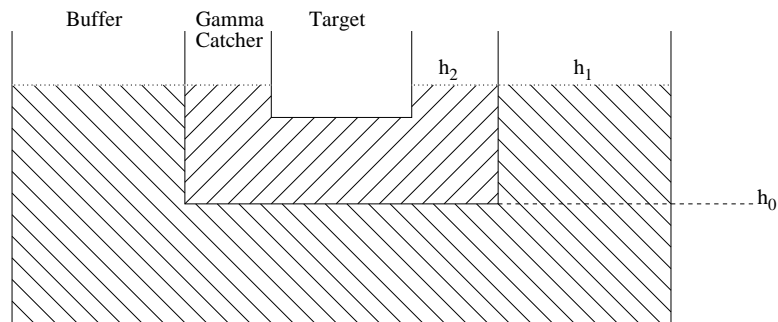
Figure 4.13: Buffer and Gamma Catcher liquid are at the same level (h_1=h_2=86 cm), but the Target stays empty. The pressure here is applied mainly on the Target bottom, which suffers the main displacement.
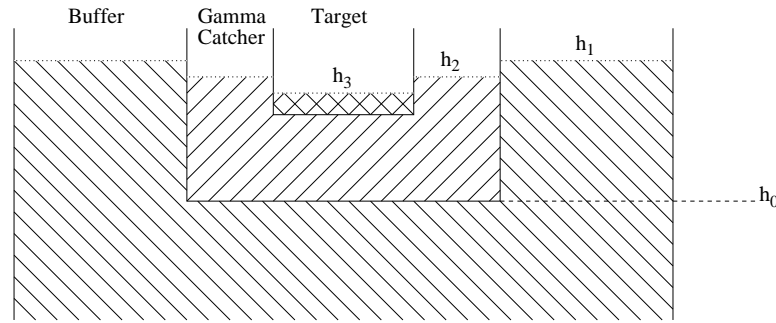
Figure 4.14: The Buffer level (h_1=137 cm) is higher than the Gamma Catcher level (h_2=117 cm) which is higher than the Target level (h_3=86 cm). There is a gap observed between Target feet and Gamma Catcher.
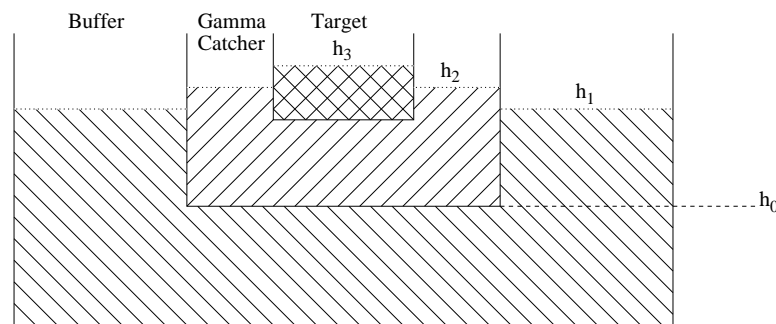
Figure 4.15: Target liquid (h_3=300.5 cm) level is higher than Gamma Catcher level (h_2=270.5 cm) which is higher than Buffer level (h_1=240.5 cm). The maximum stress is between the Target feet.

option for the beginning of filling is the only one with no gap appearing between the Target and Gamma Catcher; Gamma Catcher liquid level is to stay higher than the Buffer's. One might note that liquid level difference can go up to 40 cm.

Once the Target starts to fill up, the best filling scenario would be to keep all liquids at the same level. As an example, with h_1=h_2=h_3=186 cm, the stress on the vessels is at maximum of 0.8 MPa. Though, this is technically very hard to realize and measure. Therefore, at the beginning of the filling, one wants to try and keep the most inner volumes at lowest levels. In figure 4.14, Target liquid level is smaller than Gamma Catcher level which is smaller than Buffer level. With h_1=137 cm, h_2=117 cm and h_3=86 cm, that is to say for a 30 cm liquid level difference, the Von Mises stress reaches 4.46 MPa (corresponding to a total displacement of 8.9 mm). There is a gap between Target and Gamma Catcher due to Archimedes law, it would then be better to reduce the level difference. While the second half of the volume is filling, the filling level of the external vessel has to be higher than the internal one. This way, the lid is relieved by the difference in hydrostatic pressure. As one can see, on figure 4.15, Target liquid level is the highest, right before the Gamma Catcher's and finally the Buffer's. For h_1=240.5 cm, h_2=270.5 cm and h_3=300.5 cm, the highest Von Mises constraint is between Gamma Catcher feet (4.5 MPa for 9.6 mm of displacement). This again is a liquid level difference of 30 cm.

Once the liquid levels reach the Target chimney, the tolerable liquid level difference gets reduced. In figure 4.16, Gamma Catcher and Buffer liquid levels are equal, Target liquid is below. For
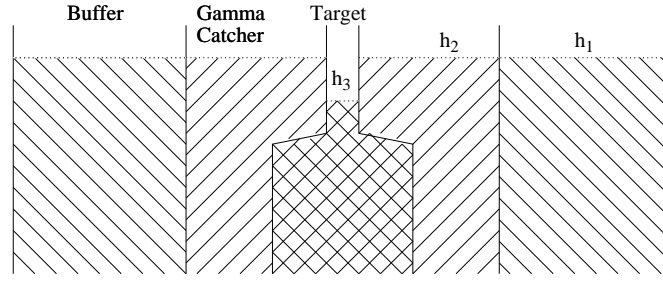
Figure 4.16: Buffer and Gamma Catcher liquid are at equal level (h_1=h_2=358.5 cm), Target level is below (h_3=348.5 cm). In this scenario, the displacements are equal on the Target and Gamma Catcher.

h_1=h_2=358.5 cm and h_3=348.5 cm, the highest observed constraint is between Target stiffeners, of 3.5 MPa, for a total displacement of 4.4 mm. The liquid level difference is 10 cm.

To conclude, by setting a limit of 5 MPa stress on the entire structure, the maximal possible difference in liquid levels for adjacent vessels is 300 mm. This difference is reduced to 100 mm once the liquids reach the chimneys. These are average values.

Simulation has shown that the transportation phase is hazardous for a double acrylic vessel which has been completely assembled by glue. Vibrations generated by the suspension system during ground transportation could be significant if the full double vessel construction was completed at the manufacturer's. Calculation of the structural brittleness of the acrylic gives a maximum acceptable acceleration of 11g. To avoid any resonance problem and completely decouple from the suspension system, the eigen frequency of the system must be higher than 10 Hz. The computation shows that the first eigen frequencies of our double vessel are closed to 8 Hz. A first simple solution is to add stiffeners to the structure. Eigen frequencies are then raised to 13 Hz, above the critical region. This problem is also solved by transporting the Target and Gamma Catcher separately.

4.2.4   Technical characterization

Both vessels are designed to contain the aromatic liquids with a long-term tightness (10 years) and stability. The biggest constraint is the chemical compatibility between the vessels and the scintillating liquids, since we tolerate neither a modification for the liquid properties (scintillation, absorbency) nor a degradation of the acrylic material.

At Degussa, in order to determine the compatibility between the acrylic material and the liquids, many flexural tests were performed. Test specimens horizontally fixed at one end are coated with liquid scintillator and then loaded at their free end in such a way that a maximum tensile stress σ_m of 30 MPa is reached near the grip. This stress decreases linearly to zero at the loading point. A defined tensile stress is attributable to every single point on the upper side of the test specimen in its longitudinal direction. Crazing starts at the point of maximum tensile stress and propagates with the duration of the test in the direction of smaller tensile stresses, i.e. in the direction of the load, up to a certain point. After a test period of 24 hours

	GS2458		
	Target liquid	Gamma Catcher liquid	Buffer oil
Sample Thickness (mm)	8.17 (σ=0.03)	8.18 (σ=0.04)	8.17 (σ=0.04)
Flexural stress limit (MPa)	15.11 (σ=0.42)	19.22 (σ=0.55)	20.68 (σ=0.48)
	GS233		
	Target liquid	Gamma Catcher liquid	Buffer oil
Sample Thickness (mm)	7.88 (σ=0.19)	7.89 (σ=0.22)	7.95 (σ=0.27)
Flexural stress limit (MPa)	19.28 (σ=0.47)	23.33 (σ=0.66)	25.8 (σ=0.48)
	GS0Z18		
	Target liquid	Gamma Catcher liquid	Buffer oil
Sample Thickness (mm)	7.96 (σ=0.02)	7.93 (σ=0.03)	8.04 (σ=0.01)
Flexural stress limit (MPa)	19.17 (σ=0.32)	24.51 (σ=0.52)	23.29 (σ=0.37)

Table 4.3: Flexural stress limit for GS233, GS2458 and GS0Z18 acrylic materials. Samples thicknesses matched the Target vessel thickness. Nine measurements were made for GS233, ten for GS2458 and seven for GS0Z18. The values shown are average values, the dispersion is indicated. GS233 and GS0Z18 crazing stresses are equivalent, while GS2458 is more fragile.

at temperatures of 23 °C the end point of crack formation is visually determined and a flexural stress limit σ_b calculated for this point. Long-term experience at Degussa has taught that products which cause crazing after 24 hours at a stress limit over 25 MPa at 23 °C will not do so either in practical use if handled correctly. Experience has shown that no crazing occurs if the fixed limiting values are observed.

On table 4.3 are represented flexural stress limits (stresses at which crazing occurs in the material) for all three acrylic materials, at 23 °C. GS2458 acrylic is the weakest; in Target liquid scintillator, it starts crazing at about 15.11 MPa. On the other hand, GS233 and GS0Z18 acrylics start crazing at about 19 MPa. Resistance to other liquids is higher. Moreover, to monitor the stresses endured by the vessels during transportation and integration, shock indicators with limit 2, 5 and 10 g were installed on them. Only a 2 g indicator activated on the Gamma Catcher after transportation to the laboratory. Moreover, right before their integration, vessels were checked using a polarizer device. Indeed, acrylic becomes birefringent under stress. No high level stresses were found on either one of the vessels. The test and its result are described in section 10.1.4.

In tables 4.4 and 4.5 are represented the authorized constraints during flushing and filling not to damage the acrylic vessels.

Flushing phase	
Target - GC pressure difference	-5 mbar $< \Delta P_{T-GC} <$ 10 mbar
GC - Buffer pressure difference	-5 mbar $< \Delta P_{GC-B} <$ 10 mbar

Table 4.4: Pressure difference constraints during detector flushing.

Filling phase		
	Prescription	Level constraints
Target pre-filling	H_0 : Target bottom center	H - $H_0 <$ 3 cm
GC pre-filling	H_0 : GC bottom center	H- $H_0 <$ 5 cm
H $<$ Target vessel half height	$H_T < H_{GC} < H_B < H_{IV}$	any ΔH $<$ 3 cm
H $>$ Target vessel half height	$H_T > H_{GC} > H_B > H_{IV}$	any ΔH $<$ 3 cm

Table 4.5: Liquid levels difference constraints during detector filling. During filling, Nitrogen is at equipressure in teh vessels.

Chapter 5

Material choice: GS0Z18 creation

Once the design and type of material was chosen for the Target and Gamma Catcher vessel was decided, it was time to find the most suitable acrylic for the experiment. Two kinds of acrylic commercialized by Degussa, the leading acrylic company in Europe, were studied. Unfortunately, neither of them was adapted to Double Chooz, one for optical reasons, the other for practical reasons. This lead us to create, together with Degussa, a new kind of acrylic material, called GS0Z18. A test batch was realized to check different properties of this material. Once GS0Z18 was accepted, production of the material was launched, enough was ordered to realize three Targets and two Gamma Catchers, all of this in one batch to ensure maximal similitude between near and far Targets. The material was then delivered to Néotec, our manufacturer, for the vessels' construction.

5.1 Existing materials: GS233 & GS2458

GS PLEXIGLAS is a cast acrylic glass with chemical designation Poly(methyl methacrylate) (PMMA), which formula is shown on figure 5.1. Chemically, it is a synthetic polymer of methyl
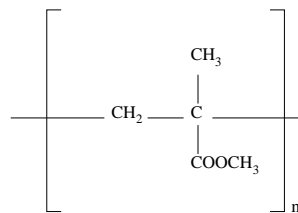
Figure 5.1: Poly(methyl methacrylate), known as PMMA.

methacrylate and is commonly called acrylic or Plexiglas. The material was developed in 1928 in various laboratories and was brought to market in 1933 by Röhm and Haas company. The material has good impact strength and is highly transparent: it transmits up to 92 % of visible light (at 3 mm thickness) and gives a reflection of about 4 % from each of its surfaces. PMMA

polymerizes thanks to radicals[1] that start a chained radical polymerization. Indeed, radical polymerization is a chain reaction whose active species are free radicals. It is a method by which a polymer is formed from the successive addition of free radical building blocks. Three processes exist:

- Emulsion polymerization is a type of radical polymerization that usually starts with an emulsion incorporating water, monomer and surfactant (wetting agent that lowers the surface tension of a liquid, allowing easier spreading). The most common type of emulsion polymerization is oil-in-water emulsion, in which droplets of monomer (the oil) are emulsified (with surfactants) in a continuous phase of water. Solid materials must be isolated from the aqueous phase after polymerization.

- In suspension polymerization, a monomer is dissolved in a non-reactive solvent that contains a catalyst.

- Bulk or mass polymerization is carried out by adding a soluble initiator to pure monomer in a liquid state. It has several advantages over other methods: the system is simple, the polymer is obtained pure, large castings may be prepared directly, very high molecular weights are obtained. This is the method used by the Degussa company, which provided us our acrylic material.

Polymerization is performed in three steps: initiation, propagation and termination. A number of reactions are possible and it is quite difficult to control radical polymerization. During initiation, two distinct mechanisms are involved. The first one is the formation of free radicals, the primary ones, thanks to a substance called the initiator. There are more than one way to produce primary radicals: in thermal decomposition, the initiator is heated until a bond is homolytically cleaved (chemical bond dissociation of a neutral molecule). This method is the one used at Degussa. Photolysis generates free radicals by UV radiation; redox reactions can create radicals...

Only a fraction of the formed radicals will be the active center from which a polymer chain is generated. Generation of radicals must happen throughout the whole polymerization process, that might last several hours. The second mechanism involved in the initiation step is the addition of the primary radical to a monomer to form the first link of the growing polymer chain. Equation (5.1) shows an example of this first polymerization reaction for a monomer of the type $CH_2 = CHR$ and a radical $X^\bullet$:

$$X^\bullet + CH_2 = CHR \rightarrow X - CH_2 - CHR^\bullet \qquad (5.1)$$

Propagation is the main step of radical polymerization. During polymerization, a polymer spends most of its time propagating, that is to say increasing its chain length. The macro-molecular chain grows by successive addition of monomers on the growing "macro-radical". The number of occurrences of the propagating reaction gives the molecular mass of the polymer.

---

[1]A radical is a chemical entity that has one or more free electrons on its external energy shell. This single electron make molecules unstable, which means they are able to interact with many compounds and that their lifetime while in solution is small.

Chain termination connects two growing "macro-radicals" (equation (5.2)). By combination, these radicals re-form a covalent link:

$$X - (CH_2 - CHR)_n - CH_2 - CHR^\bullet +^\bullet - CH_2 - (CHR - CH_2)_m - X \rightarrow X - (CH_2 - CHR)_p - X \tag{5.2}$$
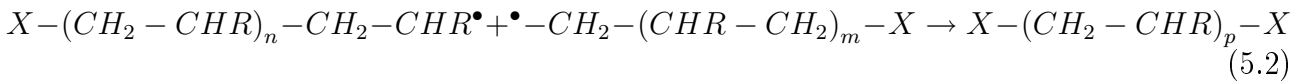
with $p = n + m + 2$. So, polymerization can be summarized in equation (5.3):

$$
\begin{aligned}
A &\rightarrow & 2R^\bullet & \qquad \text{Initation; mechanism 1} \\
R^\bullet + M &\rightarrow & RM^\bullet & \qquad \text{Initation; mechanism 2} \\
RM_n^\bullet + M &\rightarrow & RM_{n+1}^\bullet & \qquad \text{Propagation} \\
RM_p^\bullet + RM_n^\bullet &\rightarrow & RM_{n+p}R & \qquad \text{Termination}
\end{aligned} \tag{5.3}
$$
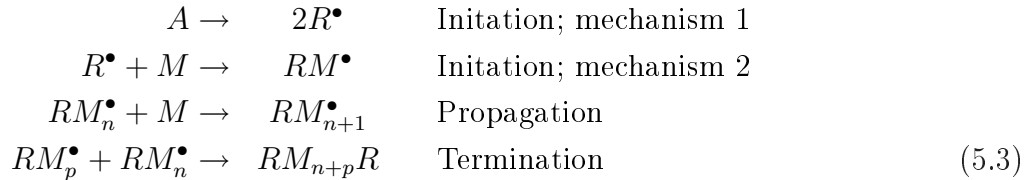
The monomer and the initiator used in the polymerization reaction will determine the polymer physical properties.

The glass transition temperature of PMMA ranges from 85 to 165°C. The forming temperature (temperature at which PMMA can be cast) starts at the glass transition temperature and goes up from there. Any molding procedure can be used on PMMA syrup. The highest quality PMMA sheets are produced by cell casting but in this case, the polymerization and molding steps occur concurrently. Liquid monomer is poured between two flat sheets of toughened glass sealed with a rubber gasket and heated for polymerization. Because the glass sheets may contain surface scratches or sag during the process, PMMA sheets may contain variations in thickness (20 % variation on a 3 m long plate) and surface defects. Still, the strength of the material is higher than with other methods owing to its extremely high molecular mass and the fact that no stress have been applied to the material during forming.

Another production method is extrusion, in which PMMA syrup is cooled and the material is then pushed or drawn through a die of the desired cross-section. This method gives uniform thickness quality and more complex shapes. However, the main disadvantage of such a method is that it generates stress in the material and therefore makes it softer and more fragile. Therefore, we decided that the acrylic material used in Double Chooz would be cast. Main PMMA characteristics are shown in table 5.1.

Properties	Measurements
Density	1.19 g.cm^{-3}
Water absorption (24h, 23°C)	0.3 %
Maximal weight increase during water immersion	2.1 %
Resistance to solvents	Poor
Mollescence zone	100 - 150 °C
Mechanical properties modification	> 50 °C

Table 5.1: Generic PMMA characteristics in terms of density, interaction with water and solvents, reaction to temperature.

Different kinds of cast acrylics are available commercially at Degussa: the GS233 acrylic, which has been the Double Chooz baseline, with an optical transparency cut off near 400 nm, and the GS2458 acrylic, which is UV transparent.

5.1.1   Optical model

In organic scintillators, the absorption of energy by a molecule corresponds to the absorption of kinetic energy from a charged particle depositing part or all of its energy through inelastic collisions with matter electrons, leading to an increase in the energy level structure of a molecule. principal scintillation, or fluorescence light (prompt fluorescence), is emitted during the molecule's de-excitation (transitions between excited state and one of the vibrational states of the electronic ground state). In organic materials, the excitation energy can transfer from molecule to molecule before de-excitation, which is important for scintillators with more than one species of molecules. As an example, a liquid scintillator is composed of a solvent (a liquid substance capable of dissolving other substances, forming a solution) and solutes, the component of the solution present in lesser amount (primary and secondary, usually). The solvent is a chemical substance which converts the kinetic energy of incident particles into excitation energy of liquid molecules. It has to have high transparency to photons emitted by the scintillator molecule. The primary scintillator (or solute) is typically an aromatic hydrocarbon whose molecules contain benzene ring structures which converts molecules excitation energy into photons. The energy deposited by a particle can then be absorbed by a bulk solvent and transferred afterwards to efficient scintillating molecules, whose orbital electron cloud gets disturbed and rise to a state of excitation. The excited orbital electrons of the solute molecule return to the ground state and photons are emitted. Thus, a single particle will cause excitation of many solvent and solute molecules resulting in a number of light sparks. The intensity of the light is proportional to the initial energy of the charged particle. If the fluorescence peak is at too low a wavelength, were the PMT cathode has poor sensitivity, a secondary solute must be added. It acts as a wavelength shifter which absorbs the light produced by the primary scintillant and reradiates it at a longer wavelength. This is useful for closer matching of the fluorescence light to the spectral sensitivity of a PMT photocathode (see figure 5.2).
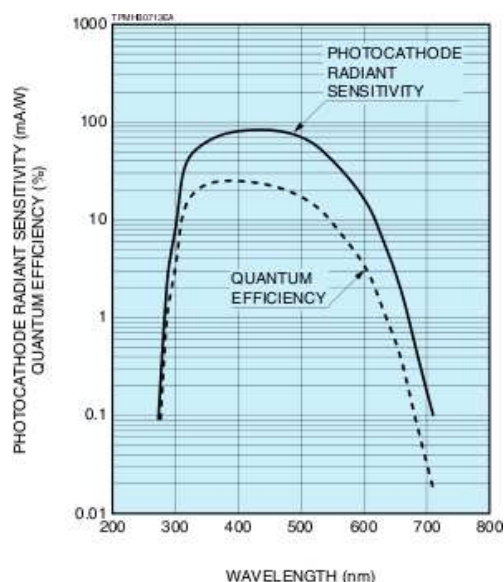
Figure 5.2: Sensitivity of the Double Chooz PMTs (Hamamatsu R7081-20). The photocathode sensitivity is peaked around 430 nm. The scintillation light from the Target has then to be shifted after the primary scintillant ($\sim$ 340 nm) to reach PMTs at their best sensitivity.

Both Target and Gamma Catcher liquid scintillators are composed of n-dodecane (80 % in Target, 30 % in Gamma Catcher), an aromatic, PXE (Phenyl-o-Xylylethan; 20 % in Target, 4 % in Gamma Catcher), a fluor, PPO (2,5-Diphenyloxazol; 7 g.L^{-1} in Target, 2 g.L^{-1} in Gamma Catcher) and a wavelength shifter, Bis-MSB (1,4-bis-(2-Methylstyryl)Benzen; 20 mg.L^{-1} in both Target and Gamma Cather). In addition, the Target liquid has a Gd complex enhancing neutron capture (1 g.L^{-1}), and the Gamma Catcher liquid has Ondina 909 mineral oil (66 %). Thanks to PPO and Bis-MSB, the scintillation photons emitted are wavelength shifted from $\sim$ 290 nm to $\sim$ 430 nm, so that the PMTs can collect them efficiently(see figure 5.3). The
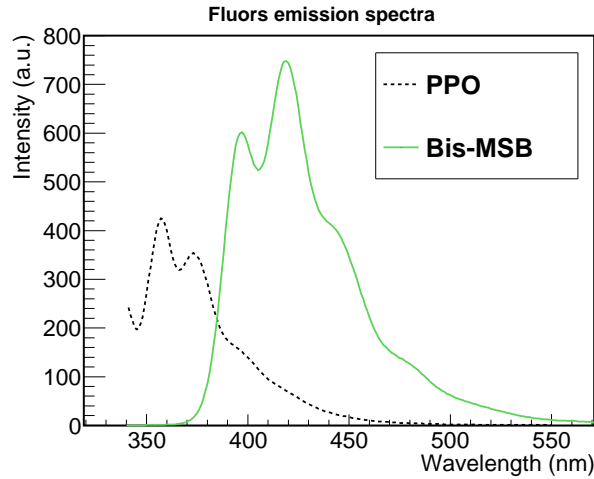
Figure 5.3: Emission spectra of the fluors. The first fluor, PPO, has its first emission peak around 340 nm, and then at 360 nm and 380 nm. Its spectrum overlaps the bis-MSB spectrum from 390 nm to 470 nm. Bis-MSB, the so-called wavelength shifter, peaks around 430 nm, where the PMTs collect light the most efficiently.

wavelength shifting process can be described as follows: first, PXE is excited thanks to energy deposition by a charged particle in the liquid. Then, the energy transfers non-radiatively from PXE to PPO, which means that PXE de-excites while PPO excites without any exchange of real photons (immediate transfer). The energy is then transferred from PPO to Bis-MSB, predominantly radiatively (through emission, absorption, and re-emission of real photons). In order to study the Double Chooz spectra within a few millimeters from the emission of the primary photons, the optical model has to reproduce as accurately as possible the wavelength shifting process, and more precisely the primary emission spectrum (spectrum emitted by molecules that have been fully non-radiatively excited and that de-excite radiatively). In the simulations described in section 5.1.2.2, pure PPO was thus used as the primary emission spectrum, since it corresponds to the fluorescence spectrum of the last non-radiatively excited component.

Acrylic vessels were first proposed to be made of GS233 acrylic (a commercial product), for its better resistance to organic liquids according to preliminary discussions with Degussa. Its optical cut off[2] is at $\sim$ 400 nm, that is to say photons with wavelength smaller than 400 nm will be absorbed by the acrylic material and will not reach the PMTs. This should not be a problem thanks to the wavelength shifting (emitted photons are shifted to wavelength $\sim$ 430

---

[2]In our case, the optical cut off is the wavelength under which photons are absorbed by the acrylic material. In other words, this is the wavelength under which the optical transmission decreases.

nm). However, the wavelength shifting efficiency cannot be measured at a distance shorter than 1 cm from the primary emission. This means we do not know how well the wavelength shifting process occurs within a sphere of 1 cm radius around a primary photon, emitted by PPO (lowest emission at 340 nm). The question is: how much of an optical wall the vessels are if the interaction occurs less than 1 cm away from the acrylics?

5.1.2   Optical transmission

5.1.2.1   Transmission measurement for both acrylics

Both acrylics optical transmission were measured with a spectrophotometer (Perkin Elmer Lambda 19). The first set of measurements used 8 mm thick acrylic GS233 and GS2458 pieces in air compared to a 20 cm thick GS233 acrylic piece (figure 5.4). The transmission measured
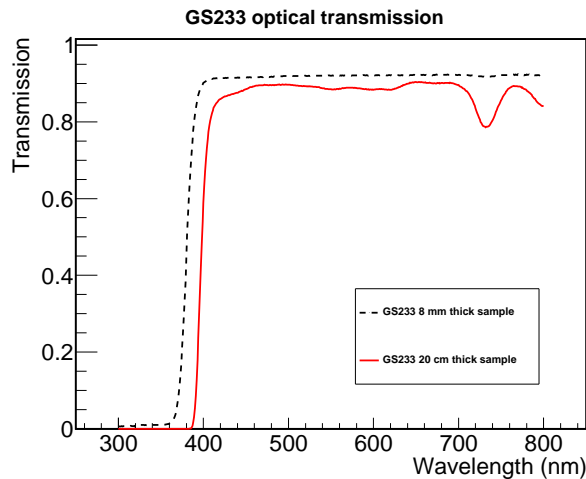
Figure 5.4: GS233 acrylic optical transmission. The optical transmission was measured thanks to a spectrophotometer for a 8 mm thick and a 20 cm thick sample.

for the GS233 acrylic was exactly the same as that of a two year old sample. This shows that this type of acrylic is very stable from one batch to another. On the other hand, the measurements we obtained for GS2458 acrylic were quite different from Degussa data: our transmission decrease start point was around 380 nm, whereas Degussa's was around 300 nm. In order to have reliable data, we ordered from Degussa a new set of transmission data, which were much more consistent with our own data (see figure 5.5).

5.1.2.2   Light transmission through the Double Chooz acrylic vessels

The Target vessel is actually the only one which is critical concerning the wavelength shifting. Indeed, a Double Chooz event is defined as the simultaneity of a positron depositing its energy in the medium and then being annihilated, and the capture of a neutron on Gd. So, if ever an inverse beta decay reaction is to occur near the boundary of the Gamma Catcher vessel, it
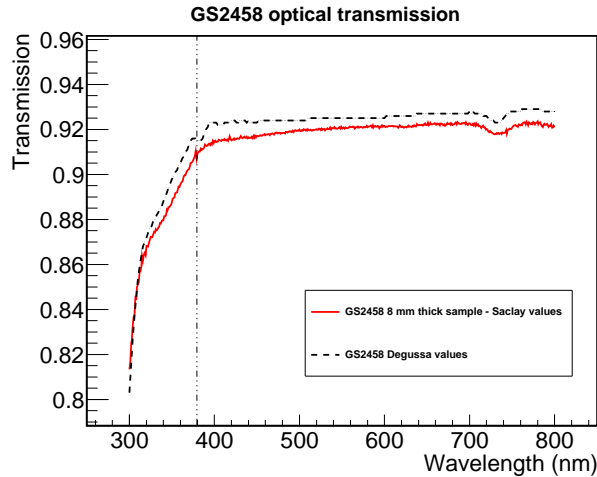
Figure 5.5: GS2458 optical transmission. One can see the measurement made in Saclay (with a spectrophotometer) for a 8 mm thick sample and new measurements from Degussa. The two sets of measurements agree and the decrease start point is around 380 nm (vertical dotted line).

would not be counted as a Double Chooz event, the neutron being too far away to be captured by Gd. Indeed, the mean free path for a 20 keV neutron is 30 mm in the Target, and 40 mm in the Gamma Catcher. However, such an interaction in the Gamma Catcher will create background events.

The simulation of light transmission through the Target vessel has been limited to the interface liquid scintillator with Gd/acrylic material since the studied effect is only dependent on the PPO and Bis-MSB concentration. So, the simulation can be limited to the Target liquid. When PXE molecules are excited, they emit photons with wavelength peaked at 290 nm which are to be wavelength shifted thanks to PPO and Bis-MSB. In order to check light transmission through the acrylic vessel, I performed a scan of 340 nm photons flashes (100 000 photons per flash) in the Target liquid comparing GS233 and GS2458 acrylics, shown in figure 5.6. 340 nm photons are primary photons, since the lowest PPO emission is at this wavelength.

First of all, we see that the number of photoelectrons (electrons produced by the PMT photocathode when hit by a photon) collected far from the acrylic wall when we use GS2458 for the Target vessel is compatible when using either Degussa or Saclay data. This provides a reliable result concerning the GS2458. Then, photons which have not been shifted yet are more easily stopped by GS233 acrylic than by GS2458 acrylic; this is of course due to the different transparencies in the UV region. Indeed, while the number of photoelectrons detected decreases rapidly with a GS233 vessel (we lose $^1/_3$ of them 0.2 mm away from the vessel), we barely lose any photoelectrons with a GS2458 vessel (up to $^1/_{12}$ according to the Degussa data). I also generated some flashes on the edge of the vessel, where photons can be either directly absorbed by the vessel, or head towards the liquid. We then lose as many more photoelectrons than in the liquid ($^2/_3$ of the total amount collectible for a GS233 vessel, $^1/_6$ for a GS2458 vessel). There again, the difference between the two kinds of acrylics is quite clear. However, this effect disappears if photons are 6 mm away (or more) from the acrylic vessel. Therefore, only 1.52 % of the Target volume is affected by this loss of photons.
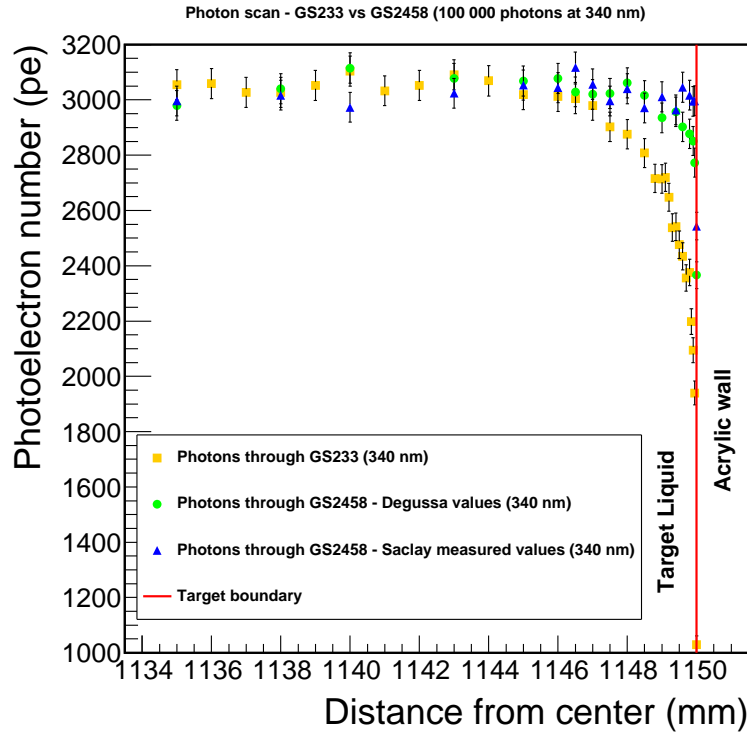
Figure 5.6: Average number of photoelectrons collected by PMTs for a scan of 340 nm photons flashes in the Target liquid, using for the acrylic vessel GS233 and GS2458 material (Saclay and Degussa data). The difference between the two kinds of acrylics is straightforward: photons which have not been shifted above the GS233 acrylic cut off are more easily stopped.

Now that we have studied the impact of the Target acrylic vessel on UV photons, we have to consider what is going to happen in the Double Chooz detector. Indeed, charged particles will excite PXE molecules and then generate UV photons. This implies that this effect will not be as straightforward as it is with photons flashes. In order to study positrons, two things must be taken into account: the way a positron deposits its energy in the liquid (very similar as for an electron) and the two 511 keV gammas coming from its annihilation with an electron. The energy deposition of positrons (or electrons) in the liquid scintillator is a local effect, hence its consequences near the acrylic vessel have to be studied. However, the 511 keV gammas energy deposition is not a local effect, therefore their influence near the Target vessel is negligible; electrons can be simulated instead of positrons. Two effects must be taken into account: the direct energy deposition in the acrylic vessel, as discussed in chapter 6, and UV photons absorbed by the Target acrylic vessel. Figure 5.7 shows an electron scan in the Target liquid near the Target vessel, with 0.2 mm steps really close to the acrylics and 1 mm steps 5 mm away from the acrylics. There are 1,000 electrons per step. Concerning the GS2458 acrylic, one can notice that Saclay and Degussa data are still consistent. The significant optical differences we have for UV photons flashes are leveled up by the energy deposition effect, which dominates. Indeed, if we take into account the whole Target volume, GS233 loses only 0.08 % of photoelectrons with regard to GS2458. Therefore, GS2458 is recommended for the Double Chooz experiment.
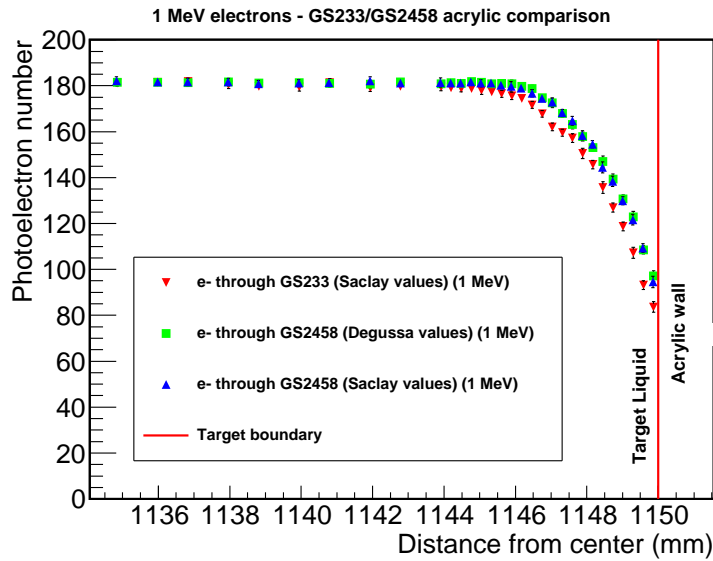
Figure 5.7: Average number of photoelectrons collected by PMTs for a scan of 1 MeV electrons in the Target liquid, using GS233 and GS2458 acrylic materials (Saclay and Degussa data). The optical differences we had for photon flashes are leveled up by the deposited energy in the acrylic vessel.

5.1.2.3 Spectral distortion

Another effect due to the acrylic vessel is the distortion of the detected positron spectrum. Indeed, the Target acrylic vessel absorbs some energy which is therefore not seen by the detector. The distortion is then characterized by the artificial enhancement of low energy events and disappearance of high energy events; the event energy shifts towards the low energy side. The question is: does GS233 induce a spectral distortion with respect to GS2458 (or vice-versa)? In order to quantify this spectral distortion, I simulated the interactions in the far detector Target volume and Target vessel of roughly 35,000 $\overline{\nu_e}$ coming from the nuclear reactors. This corresponds to 1.5 years of exposure, the duration of Double Chooz phase I. I only took into account the positrons coming from the inverse β decay reactions. To clearly identify the effect of the vessel on the optical transparency of the detector, I did the ratio of the GS2458 acrylic spectrum over the GS233 acrylic spectrum (figure 5.8). Over 1,000 photoelectrons, the lack of events gives us ratios with big statistical errors, not really significant. If we look at the zone of interest, between 200 and 1,000 photoelectrons (roughly between 1 MeV and 6 MeV, cf. figure 5.8), the ratio is close to 1 within a few percents. No spectral distortion between the two kinds of acrylics is observed.

5.1.2.4 Simulation robustness

In order to check the robustness of the simulation, I made some of the less well known parameters vary a little to test the consistency of the results. An electron scan similar to the one above was simulated. This allows us to check the response of the liquid when a charged particle goes
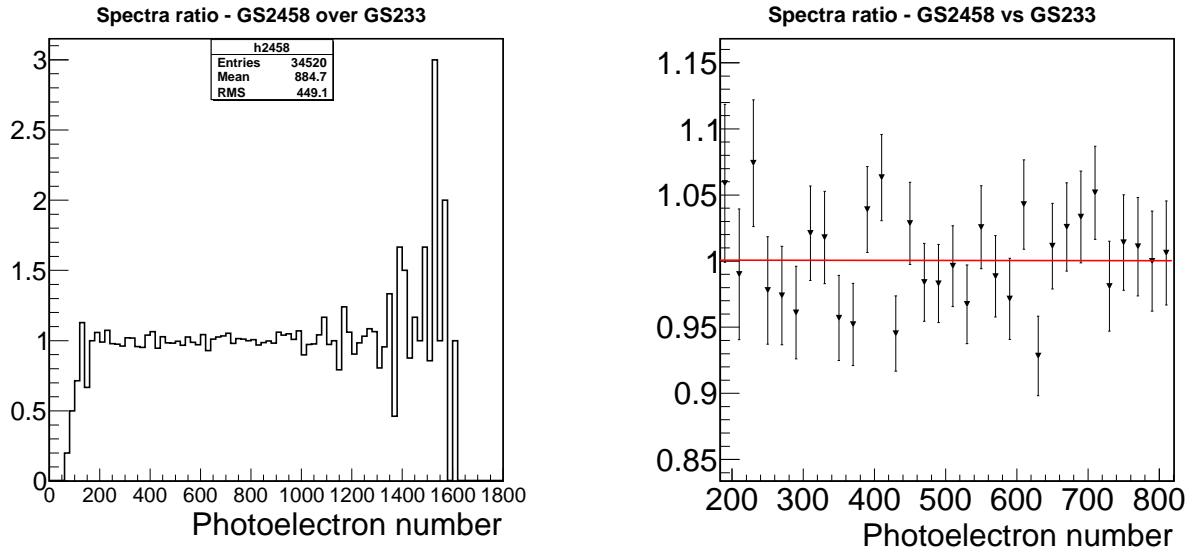
Figure 5.8: On the left hand side: Photoelectron number spectra ratio for positrons generated in the Target volume and the Target vessel, for GS233 and GS2458 acrylics. The high values over 1,000 photoelectrons are poorly significant because of the lack of events in this range. On the right hand side: spectra ratio zoom, between 200 and 800 photoelectrons. There is no spectral distortion induced by the acrylic type.

through it, and is then more relevant than flashes of photons. All simulations were performed using GS2458 acrylic.

One of these parameters is PPO reemission, that is to say the probability that the absorption of a photon by a PPO molecule is followed by reemission of a photon. This is actually the wavelength shifting efficiency of a molecule. The nominal value is 100 % [60], but I tested reemission factors of 95 % and 55 % (extremely unrealistic case). On figure 5.9, one can see there is practically no difference between the 100 % and the 95 % cases; this means that as long as reemission is close to 100 % (which it should be), the results of the acrylic optical comparison will not be affected. When the effect is emphasized, we see that the average number of photoelectrons collected far from the vessel is lower and the slope of the curve approaching the acrylics also changes. This is what was expected: the less efficient the reemission, the less photoelectrons are collected. The normalized curves, in figure 5.9, are in the statistical error of one another, meaning the PPO quantum yield will not affect the optical wall study of the Target acrylic vessel.

The Bis-MSB quantum yield, that is to say the probability that the absorption of a photon by Bis-MSB is followed by reemission, is also to be tested. This coefficient is thought to be 94 % [60]. From literature, it is a quite well known parameter, which can vary by 4 %. Therefore, in order to study small variations of this coefficient, I varied it between 90 % and 98 % (figure 5.10). The average number of photoelectrons collected far from the Target vessel changes; instead of 180 photoelectrons with a 94 % quantum yield, we get 170 and 190 photoelectrons respectively. As we approach the vessel, the curves tend to converge towards one another. Indeed, the photons have less and less chances to be wavelength shifted by PPO and then by Bis-MSB before they get absorbed by the acrylic vessel. As for PPO, the normalized curves on
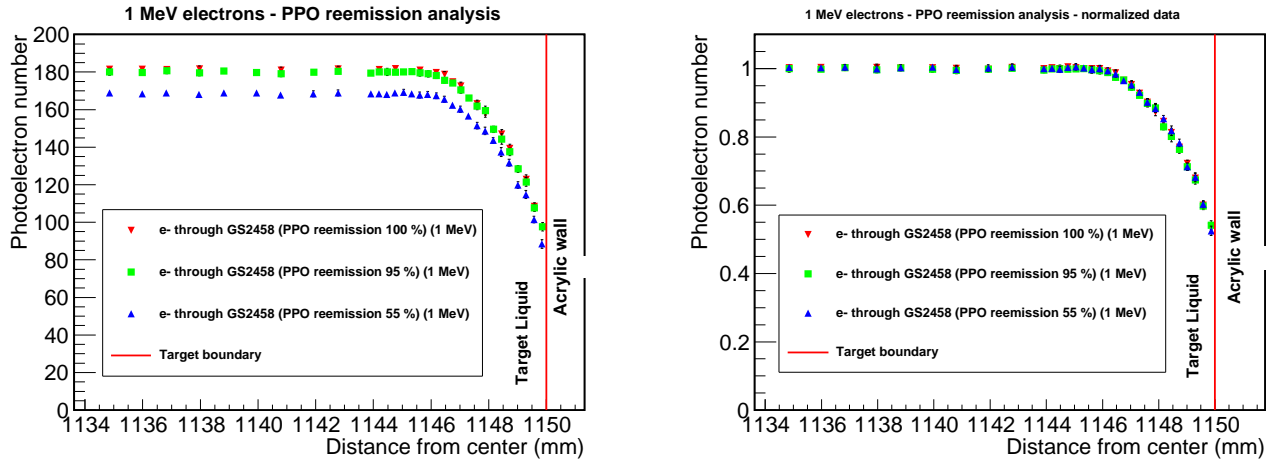
Figure 5.9: PPO reemission analysis. This study was done using a 1 MeV electron scan. The quantum yield implemented in the simulation is 100 %, we tested this coefficient to be 95 % and 55 % in order to check the consistency of the results. On the left-hand side, one can see that for small variations of this parameter, there is no remarkable change in the number of photoelectrons collected. On the right-hand side, one can see the same analysis with normalized data. Whatever the quantum yield is, the spectral shape of the emitted electrons is the same (the three curves have the same shape). This implies that even if this parameter is not exact, it will not affect the optical study.

figure 5.10 are in the statistical errors of one another, meaning this coefficient will not affect the optical study of the acrylics.

The cut offs of Bis-MSB and PPO could also affect this study. The Bis-MSB cut off will not affect the optical study of the acrylic vessel since it happens near 430 nm, where both acrylics are transparent. The PPO cut off (the wavelength at which PPO reemission is of 50 %) is around 390 nm. I forced it to be at 350 nm, 360 nm, 380 nm, 400 nm and 420 nm (figure 5.11). All of the curves are in agreement with one another; this parameter has no impact on the optical study. Such a variation on the parameter was decided to make sure even a strong change in the parameter would not impact the simulation.

To conclude, all parameters of the optical model that are not precisely known were tested, in order to make sure their variation would not impact thee study. From the results, we can ensure the simulation is robust, and its results can be trusted.

5.1.3 Acrylic fluorescence

The fluorescence of the two kinds of acrylics was measured. Acrylic samples were excited at different wavelengths starting from 300 nm up to 430 nm, and reemission was measured. A strong peak at the excitation wavelength was observed, due to the diffusion of this excitation. It turns out that the UV transparent acrylic (GS2458) is practically non fluorescent (figure 5.12). On the other hand, the UV absorbent acrylic does fluoresce (figure 5.13). The strongest reemission corresponds to an excitation at 312 nm. The acrylic is by nature UV-transparent, as GS2458
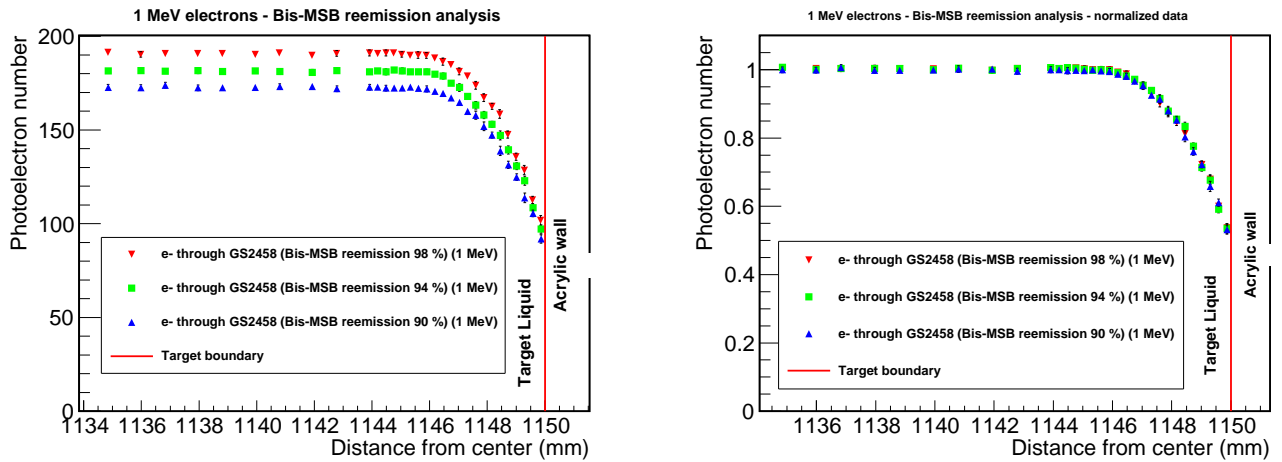
Figure 5.10: Bis-MSB reemission analysis. This study was done using a 1 MeV electron scan. The quantum yield implemented in the simulation is 94 %, we tested this coefficient to be 90 % and 98 % in order to check the consistency of the results. On the right-hand side, one can see the normalized data. Whatever the quantum yield is, the effect on the emitted electrons is the same (the three curves have the same shape). This implies that even if this parameter is not known precisely, it will not affect the optical study.
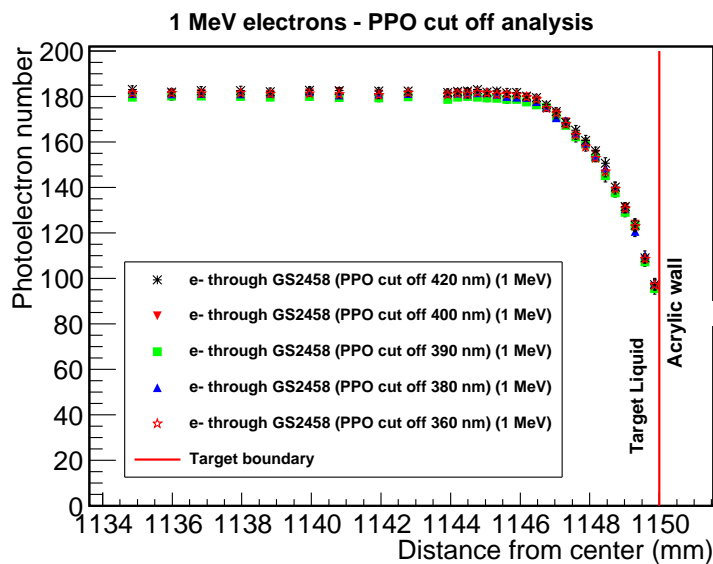
Figure 5.11: PPO cut off analysis. This study was done using a 1 MeV electron scan. The default cut off position coefficient implemented in the simulation is 390 nm, we tested this coefficient to be of 360 nm, 380 nm, 400 nm and 420 nm in order to check the consistency of the results.
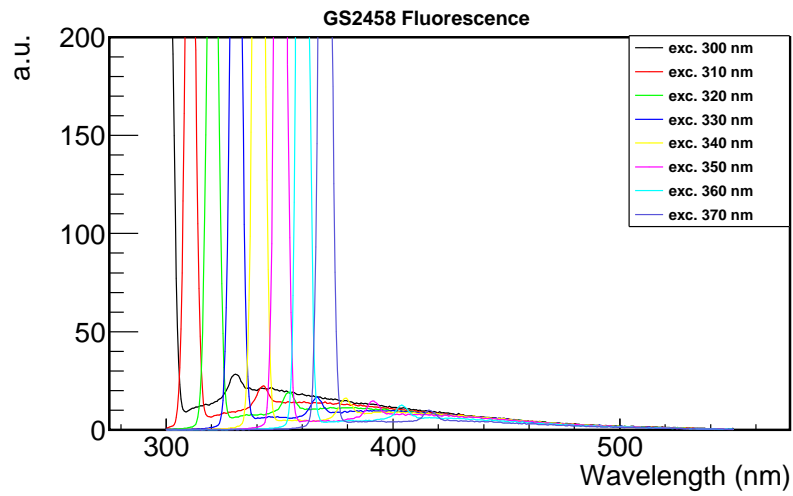
Figure 5.12: Fluorescence data for the GS2458 acrylic. The acrylic sample was excited every 10 nm from 300 nm to 370 nm. There is no emission, which means this acrylic material is not fluorescent.
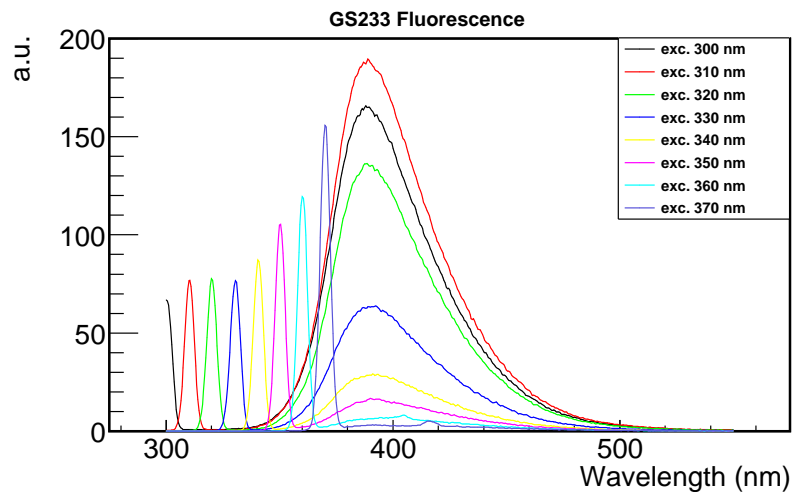
Figure 5.13: Fluorescence data for the GS233 acrylics. The acrylics have been excited every 10 nm from 300 nm to 370 nm. We can see there is a strong emission (fluorescence) peak at 395 nm.

acrylic, and some adjuvant (a UV stabilizer) is added so that the acrylic absorbs UV light (GS233 acrylic). This stabilizer actually is a wavelength shifter (see figure), which causes the fluorescence of the UV absorbent acrylic: the energy is reemitted at some higher wavelength, around 395 nm in our case. The excitation wavelength of GS233 acrylic is between 300 nm
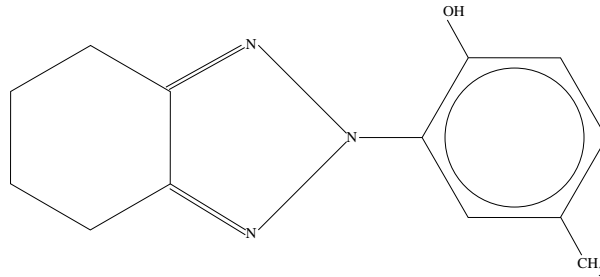
Figure 5.14: UV stabilizer, added up to a few ppm to the GS233 acrylic. The aromatic in the molecule causes the fluorescence of the acrylic.

and 340 nm; one could think this will not be a problem for our experiment since the primary emission spectrum is the PPO's starting at 340 nm. Still, there could be some Cerenkov effect inside the detector activating the fluorescence quality of the acrylic (most Cerenkov radiation is in the UV spectrum), making it possible to detect spurious light. The UV-transparent acrylic, or at least an acrylic without any UV stabilizer is then recommended.

5.1.4 Not the best materials for the experiment

If we look at the number of photoelectrons collected by the PMTs, GS233 is slightly darker than GS2458. Indeed, if we only consider the Target volume, we get 0.08 % less photoelectrons using GS233 with regard to GS2458. Still, this effect is quite small compared to the loss of energy in the acrylic vessel and is therefore not really significant. We also found that no spectral distortion is induced by the kind of acrylic we use. The robustness of the simulation was checked. This confirms the reliability of the optical model and the simulation. GS233 acrylic appears to be fluorescent and emits light at roughly 395 nm when it is excited at 300 nm, up to 340 nm. GS2458, on the contrary, does not fluoresce. Therefore, it has been decided that GS2458 acrylic is more suitable for our experiment, or at least an acrylic without any adjuvant absorbing in the UV and reemitting visible light. However, when we met with Degussa to share the results of this study and our decision to use GS2458 acrylic, we learned that this acrylic is not manufactured in the same plant and cannot be produced in thicknesses larger than 8 mm. Since the Gamma Catcher vessel thickness is of 12 mm, and the feet are as large as a few centimeters, to use GS2458 acrylic we would have to glue several layers of material to obtain the required thicknesses. Such a solution would induce weaknesses in the vessels and was rejected by the CEA team in charge of the acrylic vessels. Thus, the use of the GS2458 acrylic is not possible. Another kind of acrylic must be found.

5.2 New acrylic material developed by CEA Saclay and Degussa

5.2.1 GS233 without UV shifter

As said in the previous section, the two different kinds of acrylic considered were not optimal for the experiment, GS233 because of its optical properties, GS2458 because of the impossibility to manufacture it at the needed thicknesses. GS type acrylics are cast acrylics made from a PMMA monomer syrup. As shown, GS2458 acrylic is UV transparent whereas GS233 is not. The difference in composition between the two is that GS233 has an adjuvant added to the initial syrup that absorbs in the UV range and reemits at shorter frequency, bringing the optical cut off to around 400 nm. This is also the reason why GS233 acrylic is fluorescent and GS2458 is not. With this in mind, the solution foreseen by CEA and Degussa was to produce a new kind of acrylic at Degussa plant, in Darmstadt, in order to get every thickness needed (this is where GS233 acrylic is produced). This new acrylic has the same monomer syrup as GS233 acrylic but without the UV absorber. This customized acrylic was labeled GS0Z18. At first, a small scale production (150 kg) test was performed at Degussa, in order to check the optical properties and radiopurity of the new acrylic. Moreover, according to Degussa engineers, material compatibility with the liquid under constraints is identical as for the other two acrylics, since it has the same basic chemical composition (same monomer syrup).

5.2.2 First production: test batch

150 kg of the new acrylic material, GS0Z18, were produced as a test batch so that we check its optical properties and radiopurity. The optical transparency was checked using a spectrophotometer (see figure). I used the same set up as for the other two acrylic materials. GS0Z18 was measured to be UV transparent, with a cut off around 280 nm as shown in figure 5.15, just like GS2458. This was expected, since GS0Z18 corresponds to GS233 but without the UV absorbant. Fluorescence properties of the new acrylic material were also measured. Once again, I used the same set up as for the previous materials. No fluorescence was found (see figure 5.16); this confirms the theory that the fluorescence in the GS233 was coming from the adjuvant, and not the monomer syrup. As far as the optical properties are concerned, the GS0Z18 acrylic is perfectly suitable for the experiment.

Radiopurity of the material was checked as well. The maximum allowed concentrations in Thorium, Uranium and Potassium was determined so that the resultant contamination would not exceed 0.1 Bq per detector element (Target, Gamma Catcher in our case; see chapter 7 for more details). These concentrations are shown in table 7.1. The test batch radiopurity was measured at the Laboratori Nazionale del Gran Sasso (LNGS) through Germanium spectroscopy. The sample mass was 1 kg, counted for 24 days. Another sample of the same batch was counted by Neutron Activation Analysis (NAA)[3] at the FRM Munich research reactor. A 1 g sample was irradiated for 10 minutes before being measured in a Germanium detector

---

[3]A sample is activated in a research nuclear reactor and is then counted in a Germanium detector.
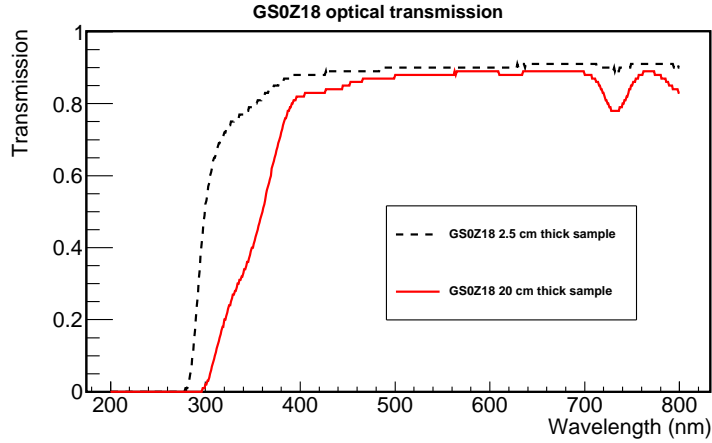
Figure 5.15: GS0Z18 transmission. Its optical cut off is around 280 nm, which was expected since this material corresponds to GS233 acrylic without the UV shifter. The optical transmission was measured with a spectrophotometer for a 20 cm and a 2.5 cm thick sample.

	Target	Gamma Catcher
^{238}U (g/g)	2.30×10^{-11}	2.53×10^{-11}
^{232}Th (g/g)	5.52×10^{-11}	5.98×10^{-11}
^{40}K (g/g)	9.49×10^{-12}	1.01×10^{-11}

Table 5.2: Maximum allowed concentrations in Uranium, Thorium and Potassium in acrylic, in order not to exceed 0.1 Bq in overall contamination. These concentrations were calculated for both Target and Gamma Catcher. See chapter 7 for more details on background contamination.

1h40 later. Only Potassium could be measured due to the sensitivity limitation of the system. Both measurements are summarized in table 5.3. The concentrations in radionuclides were marginally compatible with the specifications; GS0Z18 material was approved as far as the radiopurity was concerned.

GS0Z18 acrylic material was validated concerning optical properties and radiopurity. The production of material for the acrylic vessels was then decided. Since GS0Z18 was produced on the same site as GS233, production within the needed thicknesses was possible and was ordered in order to proceed with the vessels construction.

	Germanium Detector (LNGS); 90 % C.L.	NAA (Munich); 90 % C.L.
^{238}U (g/g)	$< 9.4 \times 10^{-11}$	-
^{232}Th (g/g)	$< 3.0 \times 10^{-10}$	-
^{40}K (g/g)	$\sim 3.1 \times 10^{-11}$	$\sim 7.78 \times 10^{-11}$

Table 5.3: Concentrations in Uranium, Thorium and Potassium measured in a GS0Z18 sample both at LNGS by Germanium detection and at the Munich research reactor by Neutron Activation Analysis.
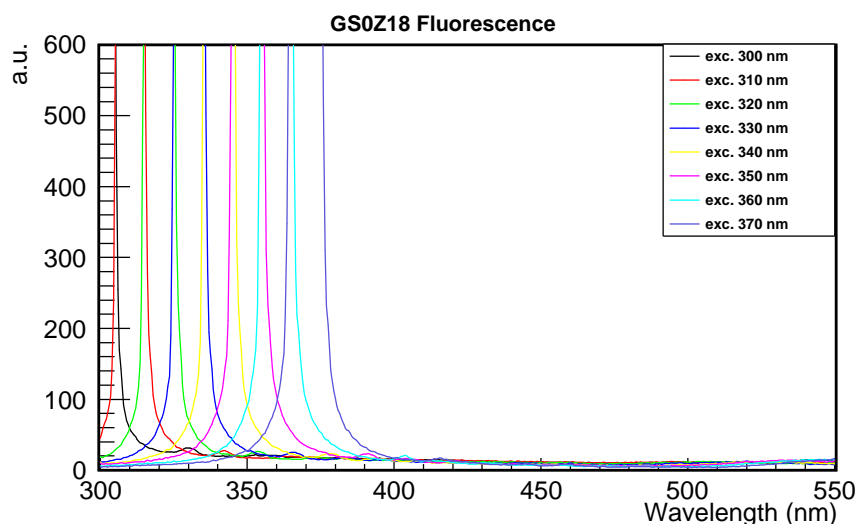
Figure 5.16: GS0Z18 fluorescence. The acrylic sample was excited every 10 nm from 300 nm to 370 nm. No emission was seen, therefore GS0Z18 is not fluorescent.
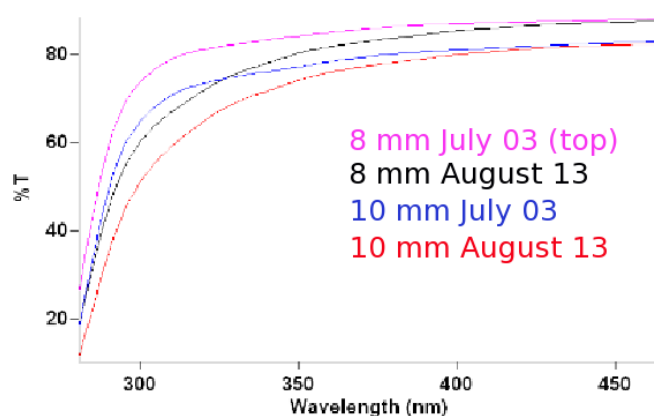
Figure 5.17: Transmittance change (in %) as a function of wavelength for a GS0Z18 sample (8×10 mm) exposed to sunlight. The loss of transmittance is about 1 % in six weeks of average sunlight exposure.

5.2.3   GS0Z18 weakness to UV light

The removal of the UV stabilizer in the acrylic could affect the sensitivity to photochemical reactions in the material. This would be observed as a degradation of the acrylic transparency when exposed to UV radiation, such as sunlight. To quantify the effect of an absorbance change due to photochemical reactions, a GS0Z18 piece (8 × 10 mm) was exposed to sunlight for six weeks. The transparency of the pieces was measured in a spectrophotometer before and after exposure. Measurements were made through the 8 mm path length and the 10 mm path length (cf. figure 5.17). The sample was measured over a course of average days in July and August (40 days of exposure) and no further measurements were made to quantify the effect of solar radiation. The sample was suspended outside a window and protected by a UV transparent polyethylene bag. It faced West and was in the line of the Sun about 25 % of the time. The main change in transmission is in the range between 280 nm and 350 nm. This spectral region
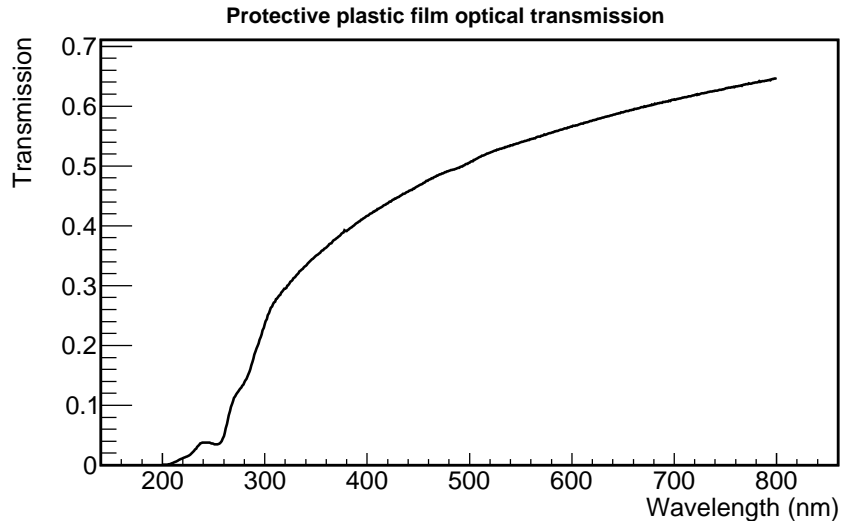
Figure 5.18: Protective blue film optical transmission. At 300 nm, only ⅓ of the light goes through the plastic film. It was on the acrylic material during construction and transportation, to shield the material from UV light.

is well below the scintillator emission region. However, at wavelength between 400 nm and 450 nm (Bis-MSB emission), there is still an observable degradation. In this case, about 1 % of the outgoing scintillation light would be lost in passing through the acrylic vessel. The Daya Bay experiment also performed a study on the consequences of their acrylic material exposed to UV light, leading to similar results [61].

To protect the GS0Z18 acrylic from UV light, from material production to the start of manufacturing, we decided to protect the GS0Z18 acrylic by a blue film cutting the UV light, as shown in figure 5.18. During construction, the material was kept under this blue film. It was only taken off when the acrylic was in a clean room (necessary to avoid external pollution in the vessels, see chapter 8). The clean room walls were UV absorbant, to protect the acrylic material. Finally, in the laboratory, the only light source is Sodium-vapor lamps. The emission spectrum, shown in figure 5.19, peaks between 550 nm and 650 nm; it therefore is not a threat to the acrylic material.

5.2.4   Material acceptance

Once the test batch was characterized (radiopurity, see chapter 7, and optical properties), we decided that GS0Z18 was suitable for Double Chooz, even considering its weakness to UV exposition. However, we required the production of the material to happen in a clean room (see chapter 8), so that no external dust, possibly with radioactive components, might contaminate the material. Moreover, we asked for the material to be stored in an area protected from UV light, in addition to the protecting film.
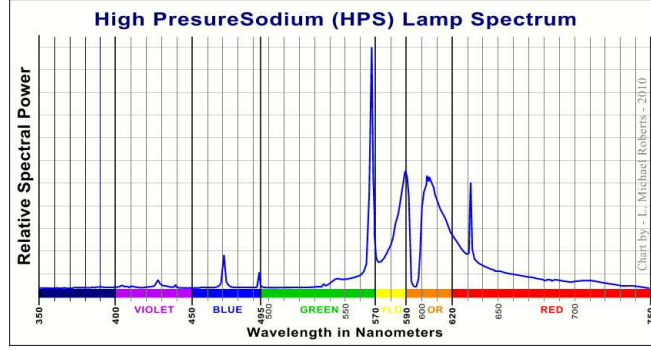
Figure 5.19: High Pressure Sodium (HPS) lamp emission spectrum. The emission is mostly between 550 nm and 650 nm, thus the light in the laboratory is not a threat to the optical transparency of the GS0Z18 material.

5.3   Final material production

Once the material was accepted, we launched the production for the experiment; we need enough material for three Targets (one spare Target was required) and two Gamma Catchers. In the meantime, I implemented the new acrylic properties in the Double Chooz detector simulation.

5.3.1   Implementation in Double Chooz simulation

The simulation of the detector has to be very accurate in terms of geometry, but also in terms of material definition. For example, data such as material opacity in the inner detector is very important to our experiment, since it is based on the ability of the light produced by liquid scintillator to reach the PMTs. Such a quantity can be represented by a material attenuation length, which is the distance at which the probability that a particle has not been absorbed is at $1/e$. This probability comes from the Beer-Lambert law and is given by:

$$P = e^{-\frac{L}{L_{att}}} \tag{5.4}$$

L_{att} being the attenuation length. From this law, one can check that the smaller the attenuation length, the faster the non interaction probability decreases, the more opaque the material is. To compute the attenuation length, one has to measure the absorbance A as a function of the wavelength λ. We have:

$$A = -\log(T) \tag{5.5}$$

T being the optical transmission. From equation (5.4)

$$T = P = \frac{I}{I_0} = e^{-\frac{L}{L_{att}}} \tag{5.6}$$

I being the intensity. Therefore, combining equations (5.5) and (5.6):

$$L_{att} = \frac{\frac{1}{e} \cdot L_{cell}}{A} \tag{5.7}$$

L_{cell} being the sample length. This gives the attenuation length of the sample plus the reflection on the sample. To get the true attenuation length, one has to subtract reflection from equation (5.7) from a reference. We obtain:

$$L_{att}^{true} = \frac{\frac{1}{e} \cdot L_{cell}}{A - A_{ref}} \tag{5.8}$$

which is equivalent to

$$L_{att}^{true} = \left(\frac{1}{L_{att}} - \frac{1}{L_{ref}} \right)^{-1} \tag{5.9}$$

L_{att} being the attenuation length, L_{att}^{true} the true attenuation length, L_{ref} the attenuation length of a reference. This allows us to suppress the reflection component. Therefore, one needs to have a reference when calculating the attenuation length of a material. For example, for the GS233 sample in the air, we took a long and a small sample to get rid of reflections, and moreover we have the long attenuation lengths well defined ($L_{cell} = 20$ cm). We therefore have a reference with which we could determine smaller attenuation lengths for GS233, as well as attenuation lengths for GS2458, with the assumption that for large attenuation lengths, GS233 and GS2458 are equivalent. In mineral oil, one can use the cell as baseline in order to directly have the true absorbance. The difference is that once immersed in oil, the acrylic is optically transparent (same indices), whereas in air, the indices are different and thus there is some transmission and reflection in the acrylic. One then has to differentiate the loss of light due to reflection and the one due to attenuation in material. This is why we need a reference when trying to calculate the attenuation length, to correct for reflections from one sample to another.

5.3.2   GSOZ18 production

More than 9 tons of material were produced. As we requested, not only the cell casting happened in a clean room, but also the application of the UV protecting film. Acrylic materials are produced in plates of different thicknesses. The production for the Double Chooz experiment was: two plates of 3 mm thickness, 30 plates of 8 mm thickness, 30 plates of 12 mm thickness, 3 plates of 20 mm thickness, 10 plates of 30 mm thickness and 2 plates of 50 mm thickness. This represents about 10 tons of material and was enough to manufacture the required Targets and Gamma Catchers. All of the three Targets and one Gamma Catcher were manufactured for the far laboratory. The second Gamma Catcher will be produced for the near detector. The three Targets were produced at the same time in order to choose the closest ones, in terms of volume (see chapter 9).

Chapter 6

Physics and mechanics: design optimization

Acrylic vessels are located around the core of the Double Chooz detector. Antineutrino interaction can happen in or near the vessel material, being either completely lost for detection or ill-detected, which would lead to spectral distortion. Those particular interactions have to be carefully studied since they deposit part of their energy in the non-active acrylic material. The only affected antineutrino interactions are those taking place in (or near) the Target acrylic vessel. Indeed, the Gamma Catcher vessel can be considered as part of the non-scintillating material that protects the scintillator from external background, as Buffer liquid.

The number of antineutrino interactions which can be altered (total loss of the interaction or spectral distortion) is directly related to the number of free protons in the acrylic vessel. After a neutrino interaction within acrylic material, the positron and neutron signals can be influenced by the acrylics. On one hand, the positron loses its kinetic energy mainly by collisions with other electrons in the material (following the Bethe-Bloch law including multiple scattering). For positrons with an energy below 10 MeV, the energy loss through radiation can be neglected with an error of less than 10%. In this range of energy, the positron kinetic energy is absorbed inside a small region of less than a few tens of centimeters. Low energy positrons created inside or near the acrylic vessel could be either missed or poorly reconstructed. Part of the energy coming from the annihilation with an electron could be missed as well, but as a second order effect. On the other hand, the acrylic vessel is too thin to really affect neutron thermalization or photons coming from its capture.

Target vessel thickness optimization

6.1   Antineutrino interactions in acrylics

One can get a fairly good estimate of the nuisance of acrylics by calculating the number of free protons in the Target acrylic vessel. This vessel is actually a cylinder of internal radius

	Acrylic vessel 8 mm	Acrylic vessel 12 mm	Stiffener 12 mm
Volume (m^3)	0.21	0.32	0.13
Mass (kg)	250	376	160

Table 6.1: Volume and mass of the possible Target acrylic vessels (thickness 8 mm or 12 mm) and their stiffeners.

1150 mm, of internal height 2458 mm, and of possible thicknesses 12 mm and 8 mm. It is reinforced in both cases with acrylic pieces of 12 mm width. Table 6.1 summarizes different properties of the possible vessels. The acrylic's monomer formula is $C_5H_8O_2$ and its density is 1.19 g.cm^{-3}. This leads to a number of protons per m^3 of $5.73{\times}10^{28}$ m^{-3}. Then, for a 12 mm width acrylic vessel, we have $2.58{\times}10^{28}$ free protons, and $1.97{\times}10^{28}$ for an 8 mm width acrylic vessel. Combining this to the total number of protons in the Target liquid, we have, in case of a 12 mm width acrylic vessel, 3.71 % of antineutrino events taking place in the Target vessel. This is reduced to 2.86 % in the 8 mm case. This percentage is calculated based on the total number of protons in Target liquid and Target acrylic vessel. This means that nearly 3 % of neutrons and positrons are created inside the acrylic vessel. As already said, the neutron is poorly affected since its thermalization length is about 30 cm. The positron, on the other hand, has a non negligible risk to lose all of its kinetic energy in the acrylic vessel, preventing any detection. The two 511 keV gamma rays coming from its annihilation with an electron might also lose part of their energy through Compton scattering in the acrylic.

6.2   Simulation: design optimization

6.2.1   Systematical errors

In the first CHOOZ experiment or in Double Chooz phase I, only one detector is built; one can only try to minimize systematical errors due to the detector to reduce the overall systematics. One of the strengths of the Double Chooz experiment is that a second detector will be built in phase II. The knowledge of the detectors will then be increased by comparing the two of them, hence detector relative systematical errors will be reduced.

Double Chooz Phase I.   During this phase, we will only have the far detector available. The total systematical error is estimated to be roughly of 2.5%, highly dominated by the uncertainty on the antineutrino flux coming from the reactors. In the worst case scenario (12 mm width acrylic vessel), we have 3.71% of antineutrino interactions inside the Target vessel. The systematical error on this data depends on the characterization of acrylic material: composition and mass. We estimate this information at less than 10%, meaning the systematical error due to the loss of antineutrino events is less than 0.37%. This is negligible against 2.5%.

Double Chooz Phase II   During this phase, our two detectors will be running simultaneously. The relative systematical error is predicted to be 0.6%. This number is mainly coming
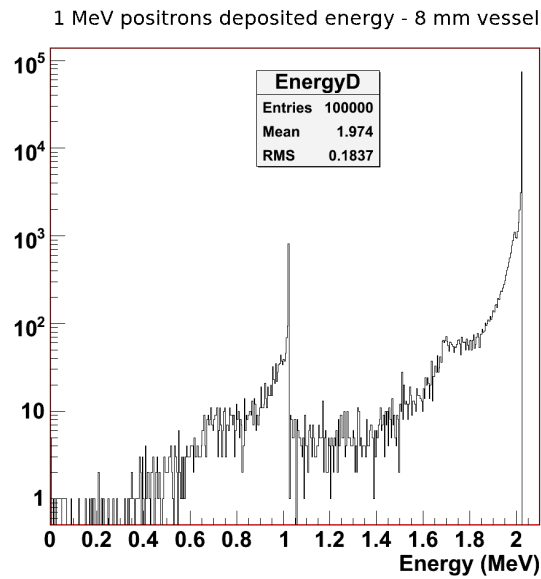
Figure 6.1: Energy spectrum of 1 MeV positrons generated in an 8 mm width acrylic vessel and liquid scintillator. Logarithmic scale. The highest peak, at 2.022 MeV, corresponds to fully detected positrons. The peak at 1.022 MeV corresponds to positrons generated in the acrylic vessel; only the annihilation gammas are detected.

from the combination of detector uncertainties (Target mass, spill in/spill out ...) as well as from the different event selection cuts needed to extract the signal (neutron energy determination...). To be dominated by those effects, we have to guarantee the characterization of our acrylic vessel to be much better. This is possible if we use the same acrylic batch for both detectors. Indeed, this ensures the same composition for both near and far Target vessels. Moreover, as they are manufactured at the same time, same place, by the same people, their form is be as identical as possible. Also, one can compare their two masses: the relative error due to the mass sensors is estimated to be less than 0.5%. Then, in the worst case, the systematical error due to the loss of antineutrino events will be roughly of 0.02%, which is negligible against 0.6%.

6.2.2   Spectral analysis

One can consider that positrons at low energy (1 MeV) will be affected the most by the presence of a dead zone, since they will have the shortest range. Let us consider their energy spectrum in our two cases (8 mm and 12 mm), figures 6.1 and 6.2. Positrons have been generated both in the Target liquid and Target acrylic vessel, keeping in mind the proportions determined in section 6.1. We considered the energy deposited both in Target and Gamma Catcher. One can see 3 main peaks. The highest one corresponds to fully detected positrons: 1 MeV (kinetic energy) + 1.022 MeV (two photons coming from the positron annihilation). The second peak at 1.022 MeV corresponds to positrons generated in the acrylic vessel: we can only detect the two photons of 511 keV each. Finally, the last peak is at roughly 0.685 MeV. This one corresponds to positrons generated in the acrylic vessel: they lose all of their kinetic energy, then one of the 511 keV photon coming from the positron annihilation goes straight into the scintillator liquid
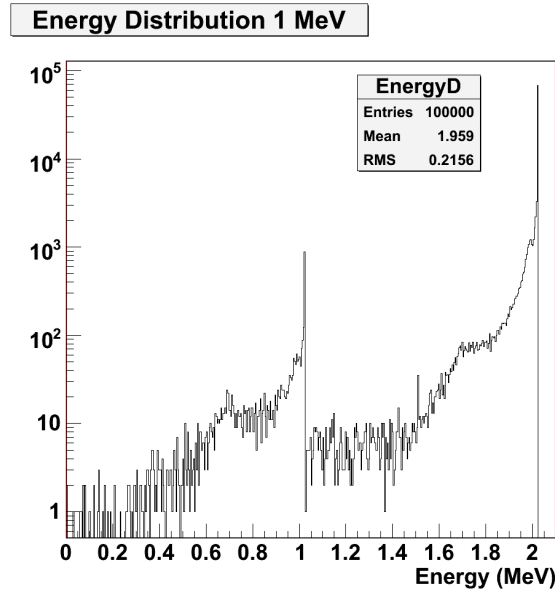
Figure 6.2: Energy spectrum of 1 MeV positrons generated in a 12 mm width acrylic vessel and liquid scintillator. Logarithmic scale. The 2.022 MeV peak corresponds to fully detected positrons, the 1.022 MeV peak corresponds to positrons in the acrylic vessel, with only their annihilation gammas detected. The 0.685 MeV peak; it corresponds to positrons in the vessel. Only one 511 keV gamma is detected, while the other escapes in the buffer to do inverse Compton scattering.

to be fully detected, while the other one goes in the Buffer liquid direction, without interacting, to do an inverse Compton scattering. This photon goes straight back into the scintillator liquid and is detected at 1/3 of 511 keV. The tails we see are mostly due to positrons generated near the acrylic vessel, their kinetic energy being partly absorbed, and to gammas scattering outside of the scintillator liquids. We also notice two rather discrete peaks. The first one at 1.5 MeV corresponds to positrons generated outside the vessel with their kinetic energy fully detected. Then, only one of the annihilation gammas is detected and the other one escapes from the liquid scintillators. Finally, barely visible at 1.7 MeV, we have a tiny peak that corresponds to an inverse Compton scattering with the kinetic energy of the positron fully detected.

To check that what we labeled as the inverse Compton scattering peaks are indeed due to Compton scattering, I generated gammas varying their energies and checked that the resulting peak is shifted according to the Compton scattering prediction (figure 6.3). As an example I generated 700 keV photons in Target acrylic. The resulting inverse scattering peak is expected and observed near 200 keV, as shown in figure 6.3.

6.2.3 Positron study

Two parameters are of utmost importance when studying a positron: its kinetic energy, which evolves quite similarly as an electron's, and the two 511 keV gammas coming from its annihilation with a medium electron. In Double Chooz, a positron is not taken into account as
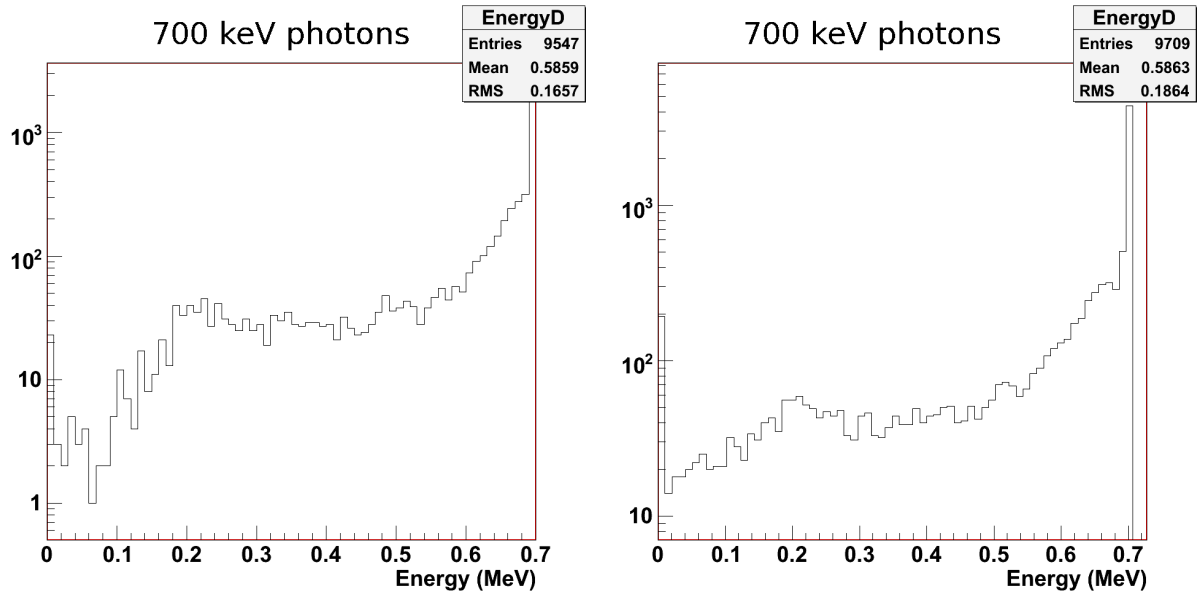
Figure 6.3: Left hand side: Energy spectrum of 700 keV photons in a 12 mm width acrylic vessel. We can see the inverse Compton scattering peak at 200 keV. Right hand side: Energy spectrum of 700 keV photons in a 12 mm width acrylic vessel. The Gamma Catcher thickness has been reduced from 55 cm to 25 cm, in order to allow more photons to backscatter. We can clearly identify the inverse Compton scattering peak at 200 keV.

an antineutrino event unless it is coupled with a neutron captured on a Gd nucleus. So, to determine the effective counting rate of positrons associated to antineutrino interactions, I had to consider neutron capture too. The top and bottom acrylic lids are reinforced with acrylic pieces of 12 mm width. In this first stage study I focused on the vessel sides. This gives us the acrylics response, given a certain width, when it is immerged in liquid scintillator. The counting rate of positrons has been determined considering the whole acrylic vessel, except for the chimney.

Kinetic energy study: electrons The first thing to study in a positron analysis is its kinetic energy since this is the parameter which will be affected the most by any absorbing material. Indeed, the positron mass is the same as that of electrons in a medium. This means that the interaction of a positron in a medium is characterized by a tortuous path, large fraction of energy transfer per interaction, scattering and/or back scattering. Hence, before it stops and annihilates, a positron will travel on a path length that can be rather long, though its range can be pretty small. For positrons generated inside or near the acrylic vessel, we have to determine this range in order to evaluate the loss of energy of those particles. One can consider the electron and positron behaviors to be quite the same[1]. Thus, the study has been done simulating electrons, so as to blind the annihilation gammas component. I did an electron generation scan in position in the acrylic vessel and the two liquids. It appears that a few millimeters away from the vessel, all of the electron energy is detected. As one approaches the

---

[1]In the Bethe Bloch Formula, positrons and electrons behave slightly differently because Target and matter electrons have similar quantum particle states.
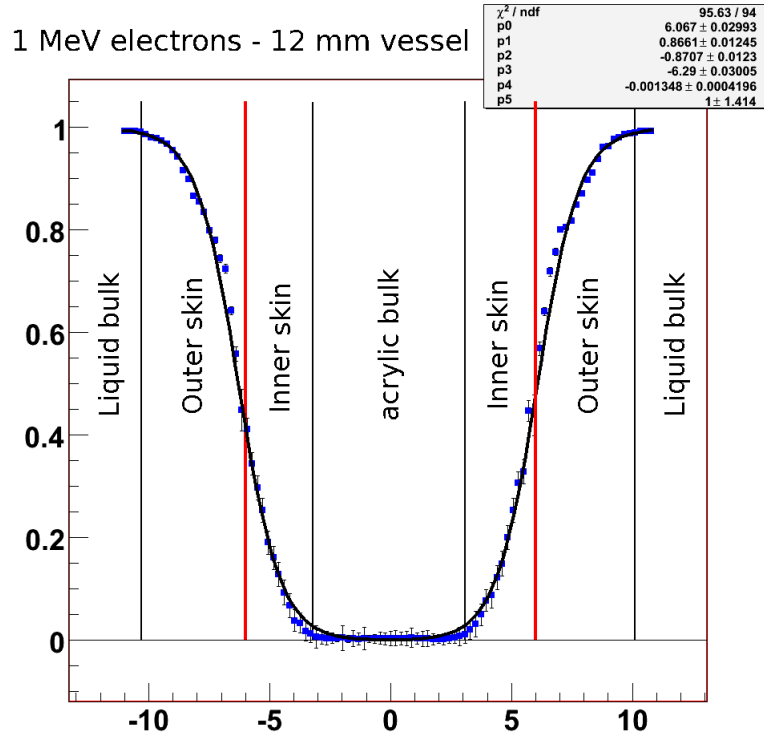
Figure 6.4: Average energy of a scan of 1 MeV electrons throughout the 12 mm width acrylic vessel. Different zones are defined: the acrylic bulk, where electrons lose all of their energy, the liquid bulk, where electrons are fully detected, and in between are the inner skin (in the acrylic vessel) and the outer skin (in the liquid scintillator).

acrylic vessel, the deposited energy slowly begins to decrease and decreases still as one enters the acrylic material. If the latter is thick enough, then the electron visible energy reaches zero: the electron is not detected at all (cf. figure 6.4). I chose to define the part where we detect 100 ± 1 % of the energy as the liquid bulk, the one where we detect no energy at all $\pm\,1$ % as the acrylic bulk, and the parts where the energy decreases (or increases) as the outer skin (in the liquid) and the inner skin (in the acrylic vessel). The scan has been performed from -11 mm to +11 mm with a step of 0.2 mm. I generated 1,000 electrons per step. The errors were calculated using the standard deviation:

$$\sigma = \sqrt{\frac{1}{N} \sum_{i=1}^{N} (x_i - \overline{x})^2} \tag{6.1}$$

N being the number of electrons per bin. The error simply is the standard deviation divided by the number of electrons per bin. Outer skin in the Target liquid scintillator and the Gamma Catcher liquid scintillator are roughly the same. This is what we expected since liquids do not differ that much in composition. Concerning electrons with energy 3 MeV and 7 MeV, the vessel is thin enough not to reach the acrylic bulk. Still, by extending the vessel width, we can determine the inner skin length. Data are given in table 6.2. Exact calculation of the range of electrons (or positrons) in a medium is not possible due to multiple scattering. Though, empirical range energy relationships were proposed; the more accurate one is Katz

	1 MeV	3 MeV	7 MeV
Inner skin (mm)	3.5	11.5	30.0
Outer skin (mm)	5.0	17.0	45.0

Table 6.2: From simulation: Inner skin and outer skin lengths for electrons of 1 MeV, 3 MeV and 7 MeV.
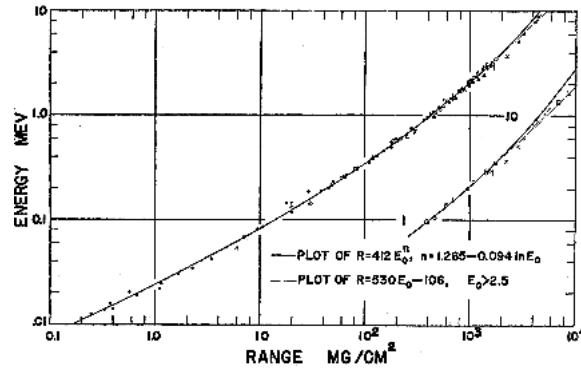
Figure 6.5: Katz and Penfold's range energy empirical formula.

and Penfold's [66], shown in figure 6.5:

$$\text{For energies from 0.01 MeV to 2.5 MeV:}$$
$$R = 412E^n; \; n = 1.265 - 0;0954 \ln E \; (\text{in mg.cm}^{-2})$$
$$\text{For energies above 2.5 MeV:}$$
$$R = 530E - 106 \; (\text{in mg.cm}^{-2}) \tag{6.2}$$

The resulting ranges, corresponding to our inner and outer skins, can be calculated using the liquid and acrylic density (0.8 g.cm^3 and 1.19 g.cm^3 respectively) and are given in table 6.3. Empirical statements and simulation agrees at nearly 1 % at high and low energy. At 3 MeV, however, the difference is roughly of 9 %, which is worst but still acceptable. One can see that the higher the energy, the thicker the skin: the effect of the acrylic will spread farther for more energetic particles. One may also notice that for 3 MeV electrons, which is the most probable energy in Double Chooz for positrons, the inner skin is nearly 12 mm. This is one of the possible widths of acrylic vessel and might have a stronger impact on the analysis. Indeed, if the range of a particle lies between the two possible acrylic vessel widths, then particles might get out of the thinner vessel nearly all the time, while a non negligible part of them will stay stuck in the thicker vessel.

Let us now compare the width acrylic vessel effect. Obviously, since the inner skin length only depends on the acrylic density, the larger the vessel, the thicker the acrylic bulk, the more

	1 MeV	3 MeV	7 MeV
Inner skin (mm)	3.46	12.47	30.29
Outer skin (mm)	5.15	18.55	45.55

Table 6.3: From empirical statements: Inner skin and outer skin lengths for electrons of 1 MeV, 3 MeV and 7 MeV.
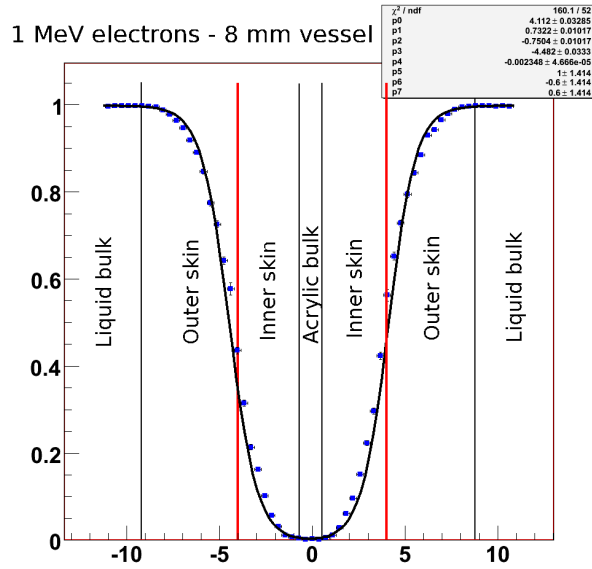
Figure 6.6: Average energy of a scan of 1 MeV electrons throughout the 8 mm width acrylic vessel. The red lines represent the acrylic wall, on its left is the Target liquid, on its left the Gamma Catcher's.

important the energy loss. This can be easily seen if you compare for two different Target widths the average deposited energy for 1 MeV electrons generated inside and near the vessel (cf. figures 6.4 and 6.6). The acrylic bulk is much longer in the 12 mm case, leading to a complete blinding of 41.5 % of electrons generated in the vessel, whereas only 12.5 % of these electrons are unseen in the 8 mm case.

The fitting has been performed by two Saxon-Woods functions, $f^-(x)$ for x negative and $f^+(x)$ for x positive, having three parameters each. A Saxon-Woods function is of the form:

$$f(x) = \frac{h}{1 + \exp\left(\frac{a-x}{r}\right)} \tag{6.3}$$

h corresponds to parameters 4 and 5, it represents the height of the fitting curve; a represents the point where $f(x) = h/2$ and corresponds to parameters 0 and 3, we can see it corresponds to the boundaries of the vessel; r represents the "velocity" with which the curve is increasing or decreasing, it corresponds to parameters 1 and 2. Actually, parameters 0, 1 and 4 correspond to $f^+(x)$ and parameters 2, 3 and 5 to $f^-(x)$.

The same analysis was done at different energies (3 MeV and 7 MeV). The fitting is worst and worst as the energy increases. Indeed, the Saxon-Woods function only remains a mathematical model and does not reflect exactly the physics taking place inside the vessels. This leads to non-significant χ^2. We can see that, for 3 MeV electrons, the lower average energy (at the center of the vessel wall) is half less in the 12 mm case than in the 8 mm case.

Gamma ray study : positrons Now that we have studied the kinetic energy dissipation in the Target vessel, we have to determine its blinding of annihilation gammas. These gammas'
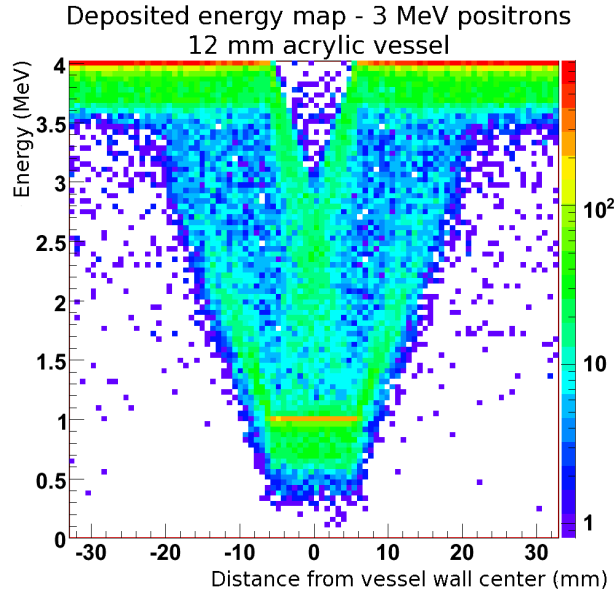
Figure 6.7: Map of the energy repartition; scan of 3 MeV positrons in the 12 mm width acrylic vessel and the liquids.

	1 MeV	3 MeV	7 MeV
8 mm	76 %	26 %	10 %
12 mm	83 %	43 %	10 %

Table 6.4: Percentage of positron events generated inside the Target vessel which energy is below 1.022 MeV

range is such that they will almost not be affected by the vessel. So, one expects a huge proportion of events generated outside the acrylic vessel to deposit all of their energy + 1.022 MeV, and a huge proportion of events generated inside the vessel to only deposit 1.022 MeV. One also expects, in both cases, a non negligible proportion of gammas escaping from the Target and Gamma Catcher liquid scintillators, resulting in a distribution of the gammas energy. This is clearly seen in figures 6.7 and 6.8: There are sharp peaks at 1.022 MeV and 4.022 MeV, and a distribution tail of roughly 300 keV following those two. Then, the shape of the average energy of positron events will not change, it will only be shifted and/or distorted by factors that will depend on the initial energy (cf. figure 6.9).

Another parameter of interest is the number of positrons which energy fits the theoretical reactor positron spectrum range (from 1.022 MeV to 10 MeV). This can be given by calculating the percentage of positrons depositing more than 1.022 MeV in Target and Gamma Catcher. The same technique as before was used. Figures 6.10 and 6.11 show us these percentages for 1 MeV positrons. The curve of percentage outside the acrylics is the same whatever the positron energy or the vessel width is: it corresponds to the liquid skin. The fitting was also done with a Saxon-Woods function; it determines the percentage of events which would be out of the theoretical spectrum if all of the events were to be counted. This information is summarized in table 6.4. At high energies, acrylic width is not that important since the positron range (30 mm) is three times higher than the possible widths. Then, the percentage of "unseen" events is rather low and there is no difference between our two cases of acrylic widths. For
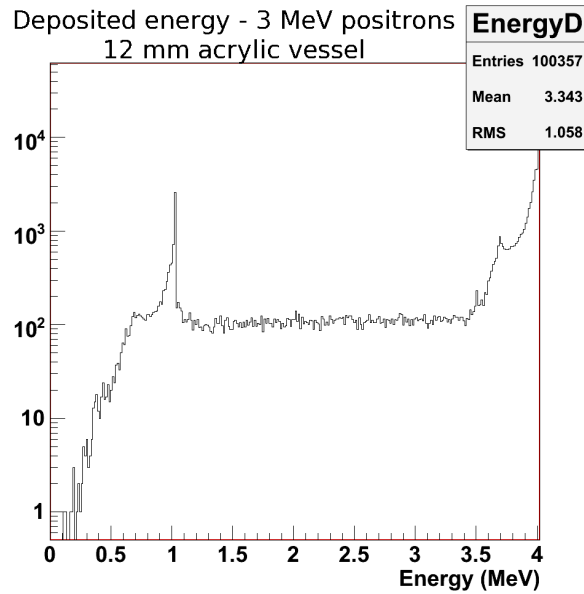
Figure 6.8: Energy spectrum of a scan of 3 MeV positrons in the 12 mm width acrylic vessel and the liquids. We can identify the five peaks we talked about previously: we identify positrons generated outside the acrylic vessel with their annihilation gammas fully detected (peak at 4.022 MeV), with an inverse scattered gamma and a right scattered gamma (peak at nearly 3.7 MeV) and with only one fully detected gamma (peak at 3.5 MeV). We also identify positrons generated inside the vessel with their annihilation gammas fully detected (peak at 1.022 MeV) and with an inverse scattered gamma (peak at nearly 0.7 MeV)
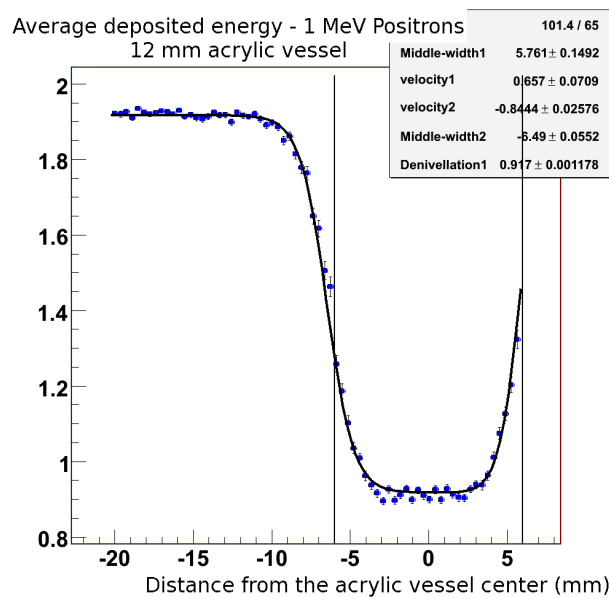
Figure 6.9: Average energy of a scan of 3 MeV positrons throughout the 12 mm width acrylic vessel. The curve has been shifted by nearly 1 MeV, comparing to the electrons curve.
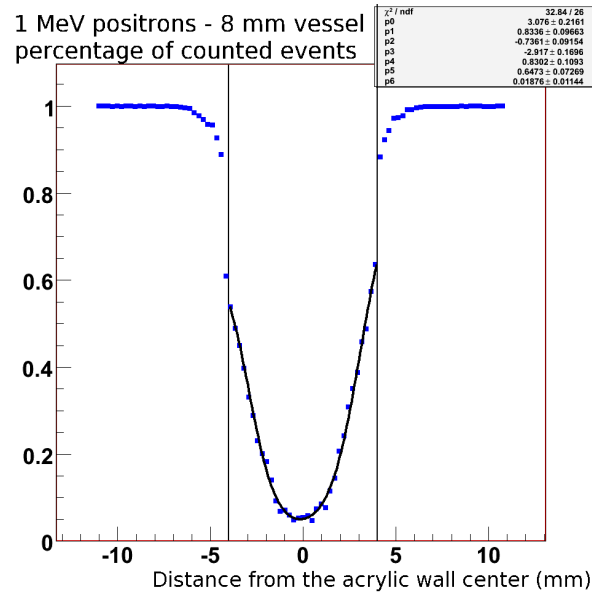
Figure 6.10: Scan of 1 MeV positrons throughout the 8 mm width acrylic vessel. Percentage of events whose energy is of 1.022 MeV at least.
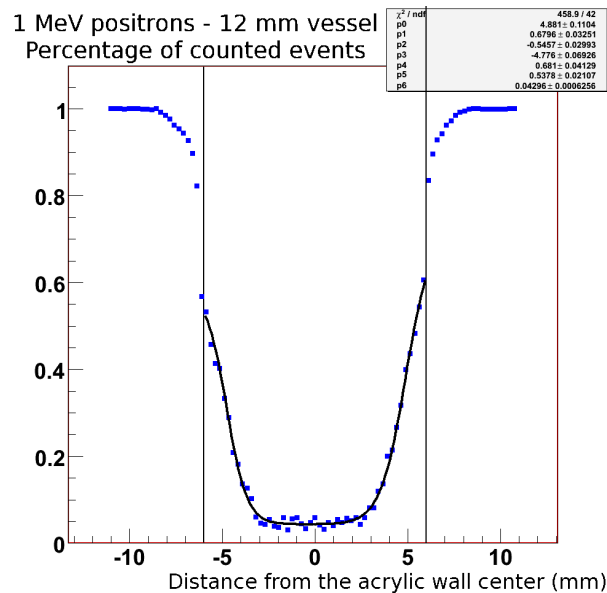
Figure 6.11: Scan of 1 MeV positrons throughout the 12 mm width acrylic vessel. Percentage of events whose energy is of 1.022 MeV at least.

low energies (1 MeV), the positron range is 3 − 4 mm, shorter than 8 mm; then, in both cases, there is a huge proportion of "unseen" events. This proportion is a little higher in the 12 mm case, since there is more distance to travel as far as the positron is concerned to get out of the vessel. In the 3 MeV case, which corresponds to the most probable energy for reactor positrons, the difference is quite large. This is because the positron range is nearly 11.5 mm, as we saw in section 6.2.3. Indeed, this range being lower than 12 mm but higher than 8 mm, positrons generated inside the vessel get away most of the time in the 8 mm case, whereas in the 12 mm case a larger fraction of them stays trapped.

The next step in the analysis is to consider the coupling of the positron event with a neutron event.

6.2.4   Neutrons

In Double Chooz, in order to detect an antineutrino event, we have to detect a positron event and a neutron event within 30 μs. A neutron event is defined as a neutron being captured by a Gd nucleus. Neutron physics is rather complicated to simulate with Geant4. So, we chose not to simulate neutrons, but to consider that positron events have to be given weights representing the neutron event probability. On the simplest point of view, this probability is represented by a sort of step function (figure 6.12). The 50 % domain is of 8 mm between Target and Gamma
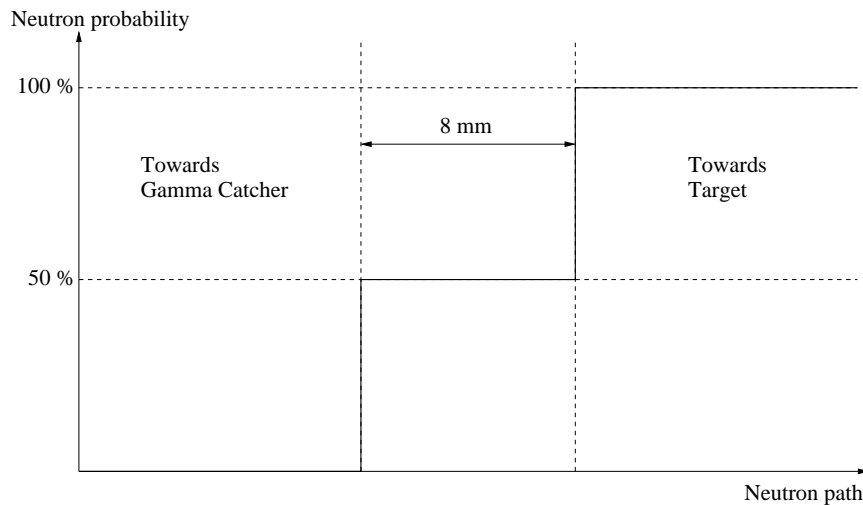
Figure 6.12: Scale function corresponding to the neutron event probability. The 50 % domain is of 8 mm.

Catcher, corresponding thus exactly to the 8 mm thick acrylic vessel. The average energy of events is strictly the same as when we did not consider neutrons, except the affected weight changes (figure 6.13). Indeed, positrons in the "100 % volume" a weight of 1, meaning they will be totally taken into account; positrons in the "50 % volume" are affected by a weight of $^1/_2$, so that it is as if one only considers half of them. Positrons in the rest of the detector are not taken into account at all. The main changes concern the percentage of events with energy higher than 1.022 MeV, as shown in figure 6.13.
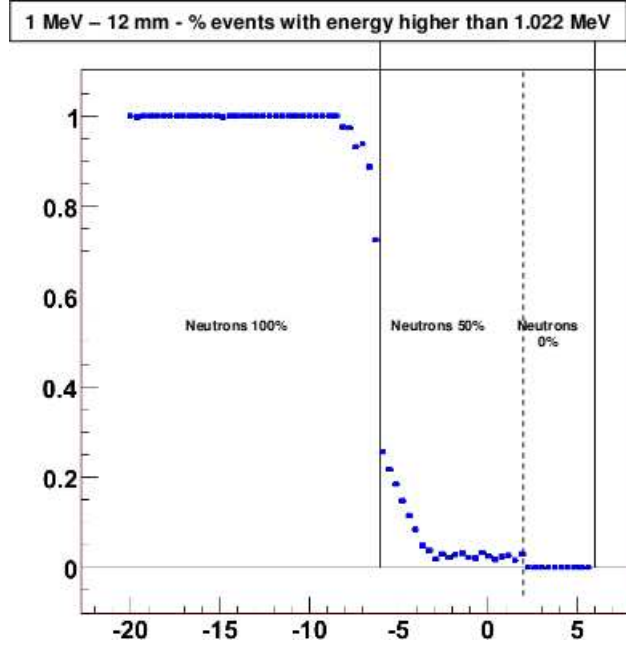
Figure 6.13: 1 MeV positrons have been generated in the liquid scintillator and throughout the 12 mm width acrylics. This graph represents the percentage of events with energy higher than 1.022MeV. The neutron probabilities domains have been added.

500,000 positrons were generated in the Target liquid scintillator and vessel in the 8 mm and 12 mm cases. In order to determine the percentage of events that would be inside the theoretical energy spectrum, we have to normalize both cases. To do that, we consider the Hydrogen atoms total mass in the Target (the "100 % volume") and the "50 % volume", of width 8mm. Then, the number of detected events will be, if by detected we mean events with energy above 1.022 MeV:

$$N_{DET} = N \left(M_H^{100\%} P_{E>1.022}^{100\%} + 0.5 \times M_H^{50\%} P_{E>1.022}^{50\%} \right) \tag{6.4}$$

with $M_H^{x\%}$ the hydrogen mass of the "x % volume", $P_{E>1.022}^{x\%}$ the probability to have the positron deposited energy higher than 1.022 MeV in the "x % volume", N the total number of generated events. We determine N_{DET} in the 8 mm, the 12 mm and the perfect cases, the perfect case being when every event is detected ($P_{E>1.022}^x$=1). Table 6.5 gives us the different probabilities we are interested in. $P_{E>1.022}$ represents the 8 mm or 12 mm case compared to the perfect case. We may notice that the difference between both cases is the highest at 3 MeV, as expected. This is a problem since this is where oscillation are to happen.

6.2.5 Spectral distortion

Another problem due to the acrylic vessel is the distortion of the detected positron spectrum. Indeed, as we already described, the Target acrylic vessel absorbs some energy which is therefore not seen by the detector. The distortion is then characterized by the "appearing" of low energy events and "disappearing" of high energy events. In order to quantify this spectral distortion, I simulated using DCNuGen the interactions in the far detector Target volume and Target vessel of roughly 35,000 $\overline{\nu}_e$ coming from the nuclear reactors. This corresponds to 1.5 years

		1 MeV	3 MeV	7 MeV
8 mm	$100 \cdot P^{100\%}_{E>1.022}$	99.97	99.97	99.98
8 mm	$100 \cdot P^{50\%}_{E>1.022}$	23.69	74.45	95.70
8 mm	$100 \cdot P_{E>1.022}$	98.90	99.62	99.94
12 mm	$100 \cdot P^{100\%}_{E>1.022}$	99.96	99.96	99.98
12 mm	$100 \cdot P^{50\%}_{E>1.022}$	13.94	57.17	89.68
12 mm	$100 \cdot P_{E>1.022}$	98.75	99.38	99.85
12/8	N^{8}_{DET}/N^{12}_{DET}	1.0015	1.0025	1.0009

Table 6.5: Probabilities of the 100 % and 50 % volumes and compared to the perfect case in each case (8 mm and 12 mm). The last line of the table represents the ratio of the two acrylic width cases.

of exposure, the duration of Double Chooz phase I. I only took into account the positrons coming from the inverse β decay reactions, and then used the normalization described in the neutron section. Figure 6.14 represents the positron spectra we obtained first in the virtual case, meaning without an acrylic vessel, and then in the case of an 8 mm thick Target acrylic vessel. Let's specify that the ideal case is non realistic... By observing figure 6.14, we can say that even if at high energy these spectra are hardly different, the appearance of low energy positrons in the 8 mm case is clearly visible.

In order to clearly identify the effect of the Target acrylic vessel on the detector, I did the ratio of the 8 mm thick spectrum over the ideal spectrum. At first, we identify really high ratios at low energy. This is simply due to the lack of events with energy below 1 MeV in the ideal case. These ratios are significant only in the way that they indicate the appearance of low energy events. If we consider positrons with energy higher than 1 MeV, the spectra ratio is quite close to 1 (within a few percents). However, since the effects we are looking for are of nearly that order of magnitude, we still have to focus. Finally, the lack of events at high energy (8 MeV and more) gives us ratios with big statistical errors, not really significant using those statistics. If we zoom in the interesting zone, from 1 MeV to 6 MeV, we can study more precisely the spectral distortion due to the presence of the acrylic vessel (figure 6.15). We see that we have an increase of roughly 5 % of low energy positrons (1 MeV) whereas we have a decrease of roughly 5 % of high energy positrons (6 MeV). This effect might hide the oscillations we are looking for if we do not know enough how our acrylics affect the energy spectrum.

In order to determine if we can identify an oscillation by perfectly modeling our acrylics, I compared two different positron energy spectra in the 8 mm case. One of the spectra represents an oscillation with the following parameters:

$$\Delta m^2 = 2.5 \times 10^{-3} eV^2 \ ; \ \sin^2{(2\theta_{13})} = 0.1 \tag{6.5}$$

The other stands for the case where no oscillation has occurred. Figure 6.16 shows the ratio of these two spectra. If we perform a χ^2 test on those spectra to check their compatibility, we get a χ^2 of 1.75 for 39 degrees of freedom. When we enter these data in the graph presented figure 6.17, we see that the histograms are compatible at less than 1 %. This implies we can discriminate an oscillated spectrum from a non oscillated spectrum with more than 99 % C.L.
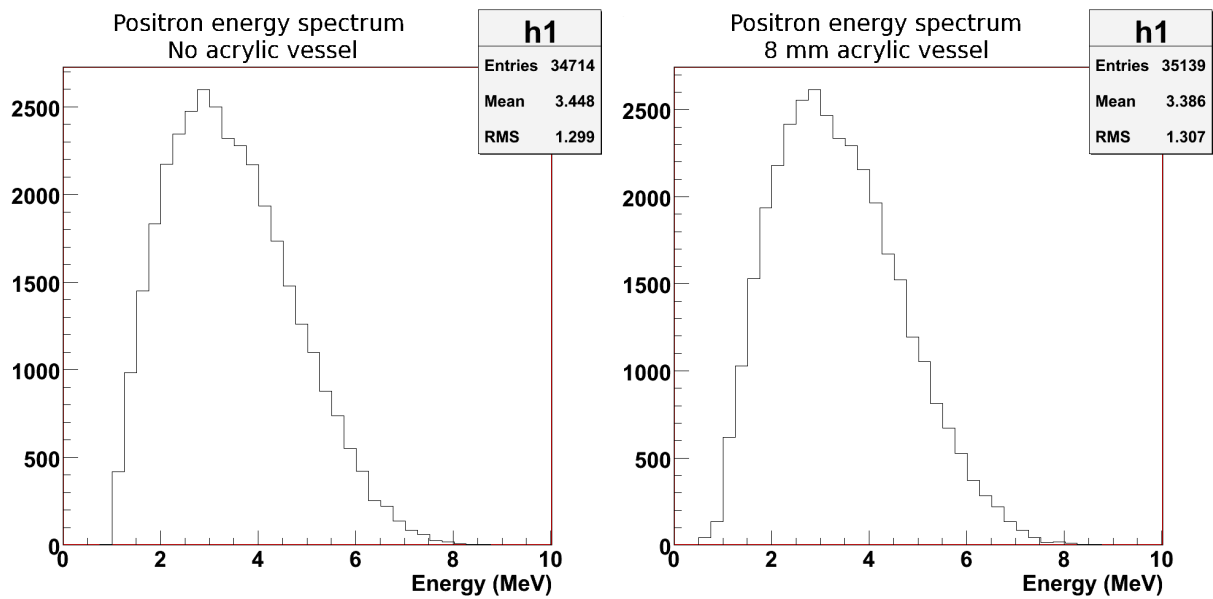
Figure 6.14: Energy spectrum of positrons generated in the 100% volume and the 50% volume without the acrylic vessel (left hand side) and with an 8 mm thick acrylic vessel (right hand side). It corresponds to 1.5 y of data taking in the far detector (roughly 35,000 events). One can see that with no vessel, there is hardly no low energy positrons (below 1 MeV), while they appear with an acrylic vessel.
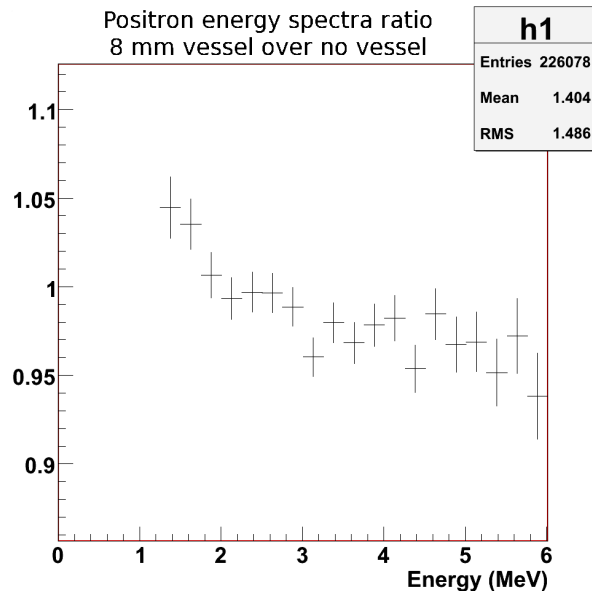
Figure 6.15: Positron energy spectra ratio for the Target volume with an 8 mm thick vessel over a volume without vessel. I took the spectra from figure 6.14. One can see that there is an increase of roughly 5 % of low energy positrons (1 MeV) whereas we have a decrease of roughly 5 % of high energy positrons (6 MeV). This effect might hide the oscillations we are looking for if we do not know enough how our acrylics affect the energy spectrum.
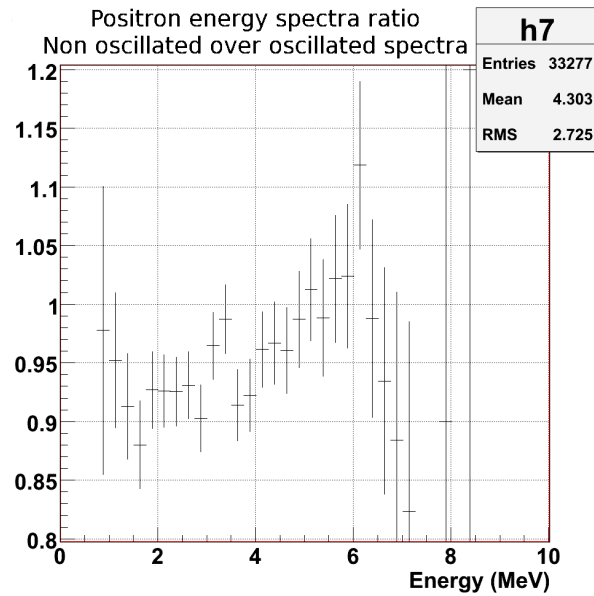
Figure 6.16: Spectra ratio considering an 8 mm thick acrylic vessel for an oscillated spectrum $(\sin^2(2\theta_{13}) = 0.1)$ and a non oscillated spectrum. We can detect the oscillation with a 99 % C.L.
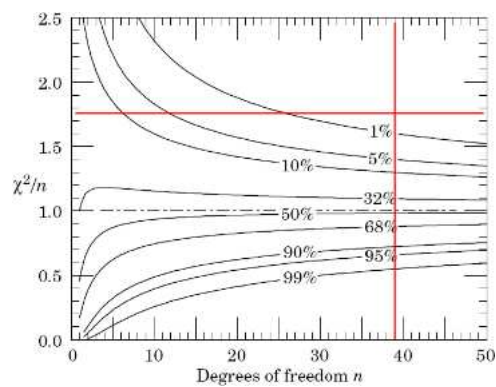
Figure 6.17: Reduced χ^2 compared to the number of degrees of freedom n. The curves represent the compatibility between two spectra with the associated confidence level. The red lines stand for the determined values in our case [10].

6.2.6 Conclusion

The uncertainty on the composition and mass of the Target acrylic vessel will not affect the overall systematical errors of Double Chooz. Though, it has an effect both on the positron spectrum shape and the counting rate. Indeed, even if the counting is poorly affected by the vessel thickness, there is still a significant difference between 8 mm width acrylics and 12 mm width acrylics. The width of the acrylic vessel has an incidence on its effect, obviously. Actually, even though a positron is more affected as energy decreases, the most important difference between the two cases (8 mm or 12 mm acrylics width) is for positrons of energy around 3 MeV. Indeed, the positron range at these energies lies between 8 mm and 12 mm; as a consequence, many more positrons can escape from the thinner vessel. Since these are the most probable energies, it seems important to reduce as much as possible the clouding effect of the acrylics, and then to take the 8 mm width vessel. Finally, the acrylic vessel induces a spectral distortion of roughly 5 % in our energy range reported to the ideal, yet unrealistic case, where we don't have any Target vessel. This number is validated only for an 8 mm thick acrylic vessel and would be even worse for the thicker vessel. This tends to prove too that the 8 mm thick vessel is more suitable for the experiment. However, still considering the thinner vessel and thanks to our perfect knowledge of the acrylics, we can discriminate with a 99 % C.L. an oscillation with $\sin^2{(2\theta_{13})} = 0.1$.

Chapter 7

Radiopurity and background

Naturally occurring radioactivity mostly creates accidental, or uncorrelated, background, defined as a random coincidence of a prompt energy deposition similar to the true prompt positron signal, followed by a delayed neutron-like event in the fiducial volume within a one hundred microsecond interval. Selection of high purity materials for detector construction and passive shielding around the active region provide an efficient protection against this type of background. Furthermore, accidentals can be accurately measured in situ. Cosmic ray muons dominate the trigger rate at the detector sites, and they induce the main source of background.

Correlated backgrounds are the ones where the two mimicking signals come from the same source, such as a cosmic muon. Muon-induced production of the radioactive isotopes ^{8}He, ^{9}Li and ^{11}Li cannot be correlated to the primary muon interaction since their lifetimes are much longer than the characteristic time between two subsequent muon interactions. These neutron-rich radioisotopes β-decay, mimicking the prompt signal, and later evaporate a neutron. This cascade fakes the neutrino signal, and the few events produced each day in the Target volume have to be correctly subtracted to give the number of true neutrino events. Another background comes from neutrons that are produced in the surrounding rocks by radioactivity and in cosmic ray muon induced hadronic cascades. In the latter case, dominant at shallow depth, the primary cosmic ray muon may not penetrate the detector, being thus invisible. Fast neutrons may then enter the detector, create recoil protons mimicking the prompt signal and be captured by Gd nuclei after thermalization. Such a sequence can be misidentified as a neutrino event. Fortunately this background can be fairly well estimated to one to two counts per day at the far site, from measurements of the CHOOZ experiment during reactor off periods.

7.1 Accidental background

7.1.1 Brief introduction on singles

Natural radioactivity detection can be reduced in a detector thanks to a careful selection of the construction materials and self-shielding (the Buffer region, the lead shielding). The expected

rate and spectrum of single events can be well determined by radioassays of the different materials used in the detectors and by a characterization of the surrounding rock.The radioactive sources to consider are then ^{40}K, ^{238}U and ^{232}Th from the laboratory rock, but also from the PMT glass, the scintillators, the acrylic; ^{40}K, ^{238}U, ^{232}Th and ^{60}Co in the metallic construction pieces, large as the Buffer vessel and small as the screws fixing the Target, ^{222}Rn in the air, various isotopes in the dust.

7.1.2   Neutrons

The delayed background (neutron-like) comes mainly from neutron capture on Gd in the Target. However, part of those neutron-like events could be due to Bremsstrahlung photons radiated from cosmic muons which cross the rock surrounding the detector. The neutron-like background rate was measured at the far site by the CHOOZ experiment, at the level of 45 ± 2 h^{-1} (after cuts)[32]. Based on that measurement and our Target volume, we assume a neutron rate of 88.5 h^{-1} in the Double Chooz far detector. Such a big rate remained unexplained in CHOOZ.

7.1.3   Accidental background rate expected and detector radiopurity constraints

As already explained in section 4.1.7, the accidental background rate:

$$R_{ACC} \simeq 0.2 \times \frac{R_P}{1 \ s^{-1}} \times \frac{R_D}{88.5 \ h^{-1}} \ day^{-1} \qquad (7.1)$$

If we require the accidental background rate from all materials but PMTs (highly radioactive due to the PMTs glass) to be less than 1 % of the neutrino signal, we get the constraints R_P^{far} < 10 Hz and R_P^{near} < 14 Hz. As a guideline, we require each detector element (Target liquid, Gamma Catcher vessel...) contribution to be less than 0.1 Bq. To determine the maximum allowed concentrations in radionuclides, the latters were generated uniformly in several parts of the inner detector, PMTs were simulated separately. The result of the simulation is the spectra of the deposited energy in the sensitive volumes, that is to say Target and Gamma Catcher liquids. The maximum concentration allowed for each detector component have been calculated here for a threshold of 0.5 MeV. PMTs' contribution to the singles rate is expected to dominate, at the level of a few Hz. The expected singles rate above 0.5 MeV is expected to be between 9 and 14 Hz for the PMTs, possibly to be lowered down to 4-10 Hz. This translates to 1-1.4 and 0.4-1 accidental events per day respectively.

The Double Chooz inert steel shield was designed to minimize the incidence of gamma rays coming from the rock surrounding the detector into the active volumes (Target and Gamma Catcher). This component grants Double Chooz with a critical reduction on the uncorrelated background, compared to the CHOOZ experiment. Simulations have been performed to determine the optimal thickness of the shield. The goal is to reduce the rate of rock gammas with energy deposition above the considered threshold lower than the expected activity from the PMTs. This study showed that a 15 cm shield would suffice. This way, the overall rate of rock

gammas is expected to be smaller than 2 Bq, dominated by ^{208}Tl (from the Thorium chain) and ^{40}K. To check this simulation, we characterized the radioactivity of the laboratory rock.To perform this characterization, we made some measurements a portable Germanium counter, inside the pit right after the 15 cm lead shielding installation (with and without extra shielding to simulate the top lid), and in the laboratory outside the pit. Several measurements were made, inside the pit with and without extra shielding, outside of the pit. This last measurement was made to tune the Monte Carlo simulation as far as the radioactivity from the surrounding rock is concerned. For this measurement, the rate in the Ge counter was of 111.74 Hz, 9.61 Hz with a threshold of 0.7 MeV. The main contamination come from ^{238}U, ^{232}Th and ^{40}K. Inside the pit, without any extra shielding, the rate was 17.87 Hz, 0.92 Hz with an 0.7 MeV threshold. This measurement gives us and upper limit on what we expect to measure in the Double Chooz far detector once the shielding is completed. Therefore, to simulate the missing top lid, we installed an extra shielding with thickness 5 cm on top of the Germanium counter. The rate was of 6.08 Hz, 0.15 Hz with a 0.7 MeV threshold.

Maximum allowed concentrations for ^{238}U, ^{232}Th, ^{40}K, and ^{60}Co isotopes in detector components are described in table 7.1.

	^{40}K (g/g)	^{238}U (g/g)	^{232}Th (g/g)	^{60}Co (mBq/kg)
Target LS	10^{-10}	10^{-13}	10^{-13}	-
Target Acrylics	10^{-8}	10^{-11}	10^{-11}	-
GC LS	10^{-10}	10^{-13}	10^{-13}	-
GC Acrylics	10^{-8}	10^{-11}	10^{-11}	-
Buffer Oil	-	10^{-12}	10^{-12}	-
Buffer Vessel	-	10^{-9}	10^{-9}	15
Veto LS	-	10^{-10}	10^{-10}	-

Table 7.1: Maximum allowed concentrations (g/g) of ^{40}K, ^{238}U, ^{232}Th and ^{60}Co for the main components of the Double Chooz detector: Target liquid scintillator and vessel, Gamma Catcher liquid scintillator and vessel, Buffer oil and vessel, Inner Veto liquid scintillator. [44]

7.2 Constraints on the acrylic vessels

7.2.1 Main critical isotopes: Uranium, Thorium and Potassium

The three nuclides ^{40}K, ^{238}U and ^{232}Th were simulated in the acrylic vessels. The emitted particles (alphas, betas, gammas) could deposit energy in any detector components (acrylics, liquid scintillator, calibration systems...), but only the energy fraction deposited in the liquid scintillator was considered. These simulations allow us to determine the acceptable limits on the concentration of each nuclide based on its position in the detector and its mass. The background induced by ^{238}U and ^{232}Th was simulated in the hypothesis of secular equilibrium. If this condition does not hold, the final background could be estimated based on the direct measurement of the gamma lines activity obtained by gamma ray spectroscopy (Ge counters). Note that the final result could change significantly.

For each nuclide considered (^{40}K, ^{238}U or ^{232}Th), we compute an "efficiency" parameter to account for the amount of energy deposition of a given radionuclide at given location in the detector above a certain threshold. This parameter is determined in different ways depending on if we have a decaying chain of isotopes (as for Uranium and Thorium) or a radioelement (as for Potassium):

- Considering ^{40}K, the efficiency parameter is the probability to have an energy deposition greater than a given threshold (0.7 MeV for instance) inside the Target and Gamma Catcher. This number is less than 1 by construction, since one radioisotope decay induces at most one decaying particle in an event time window.

- Both ^{238}U and ^{232}Th decay in a long chain providing many particles; the decay chains are shown in figures 7.2 and 7.3. Thus, for a single decay of ^{238}U and ^{232}Th, the number of energy deposition above a given threshold (0.7 MeV for instance) could be greater than 1. It corresponds to the decay of several particles produced along the chain that could induce several event depositions over threshold. The efficiency parameter is then taken as the multiplicity of energy deposition greater than the threshold considered.

The singles rate above a given threshold is thus given by equation [7.2]:

$$Bkg\,(\text{Bq}) = A_N\,(\text{Bq/g}) \cdot P\,(N) \cdot C_N\,(\text{g/g}) \cdot M_D(\text{g}) \qquad (7.2)$$

Bkg being the induced single rate in Bq, A_N the specific activity of the nuclide in Bq/g, $P(N)$ the efficiency relative to the nuclide defined as above, C_N the nuclide concentration in the considered detector component in g/g, M_D the mass of this detector component (Target feet for instance).

7.2.2   Acrylic vessels

Let us focus on the background induced by the acrylic tanks, the Target and the Gamma Catcher. Each of these vessels has been divided in three parts: the cylindrical vessel, feet and stiffeners. This allows us to determine more accurately the background in relation with location in the detector and acrylic thickness. The masses of the different parts have been determined, along with the relative importance of each component (cf. table 7.2).

The background rate of single events coming from all detector sub-regions is to remain small compared to the PMTs induced background ($\sim$5 Bq). This implies that each detector component (Target tank, Gamma Catcher liquid, etc.) has to contribute to the singles background up to a certain rate for each of the radioelements considered. An interesting goal to reach for the acrylics would be a rate of $\sim$0.1 Bq coming from ^{40}K, ^{238}U and ^{232}Th (considering that they are the most probable elements contained in the acrylics). Measurements of ^{235}U and ^{137}Cs have also been performed.

		Mass (kg)	% of total mass
T	Vessel	250	57.8
T	Stiffeners	16	3.7
T	Feet	166	38.5
GC	Vessel	814	56.3
GC	Stiffeners	37	2.5
GC	Feet	596	41.2

Table 7.2: Mass and relative importance of the different parts of the acrylic vessels. The feet and stiffeners of the Target vessel are in the Gamma Catcher liquid scintillator. The feet and stiffeners of the Gamma Catcher vessel are in the Buffer oil.
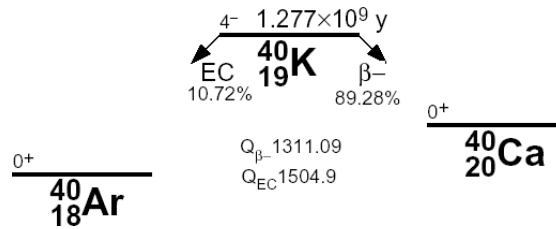
Figure 7.1: ^{40}K nuclear decay scheme

7.2.2.1 ^{40}K

^{40}K represents 0,0117% of natural Potassium. Its specific activity is 30.3 Bq.g^{-1}. If one looks at figure 7.1, one can see that it has 89.28 % of probability to decay through β^- (Q_β=1.311 MeV), and 10.72% through β^+ (Q_{EC}=1.505 MeV), transiting in 10.67 % of the cases by the 1.461 MeV excited state responsible of the main gamma emission. We computed the "efficiency" parameter setting the threshold at 0.7 MeV. Results are given in table 7.3. Beta decays within a few

	Target			Gamma Catcher		
	Vessel	Stiffener	Feet	Vessel	Stiffener	Feet
Efficiency	0.10	0.10	0.08	0.04	0.02	3.0×10^{-3}

Table 7.3: Efficiency of the detector relative to ^{40}K above 0.7 MeV

millimeters away from the acrylics surface lead to a visible energy deposition in the Target and Gamma Catcher that could exceed the threshold, though the external part of the Gamma Catcher vessel induces less background thanks to the non active Buffer oil. Beta decays within the Gamma Catcher feet and stiffeners barely deposit significant energy in the Gamma Catcher. Concerning the 1.4 MeV gammas, one can see that the efficiency for an energy deposition from the Target vessel is twice larger than from the Gamma Catcher vessel. This is explained by the solid angle seen in both cases: the two sides of the Target vessel are surrounded by liquid scintillator, whereas only the internal surface of the Gamma Catcher vessel is in contact with some. This effect also explains the low efficiencies obtained for the Gamma Catcher feet and stiffeners, dipped into non active oil.

In conclusion, the background goal of 0.1 Bq induced by ^{40}K in the Target acrylic lead to a maximum allowed concentration of 9.49×10^{-12} g/g. The same calculation for the Gamma

	Target			Gamma Catcher		
	Vessel	Stiffener	Feet	Vessel	Stiffener	Feet
Efficiency	0.87	0.88	0.73	0.37	0.14	0.02

Table 7.4: Efficiency of the detector relative to ^{238}U above 0.7 MeV

Catcher gives us a maximum allowed concentration of 1.01×10^{-11} g/g. The fact that the constraint in the Gamma Catcher is roughly the same as in the Target is due to the mass difference between the two vessels. Indeed, most of the Gamma Catcher contribution comes from its cylindrical tank, whereas all of the Target parts are to be considered (similar efficiency parameters). This gives us a mass ratio between active Gamma Catcher and Target of 1.96. At the same time, the Gamma Catcher efficiency parameter is half the Target one, which gives us a contribution ratio for these vessels of one.

7.2.2.2　^{238}U

^{238}U represents nearly 100% of natural Uranium. Its specific activity is of 12.44 kBq.g^{-1}. All the way down its decay chain, we have alpha, beta and gamma emissions (cf. figure 7.2). The
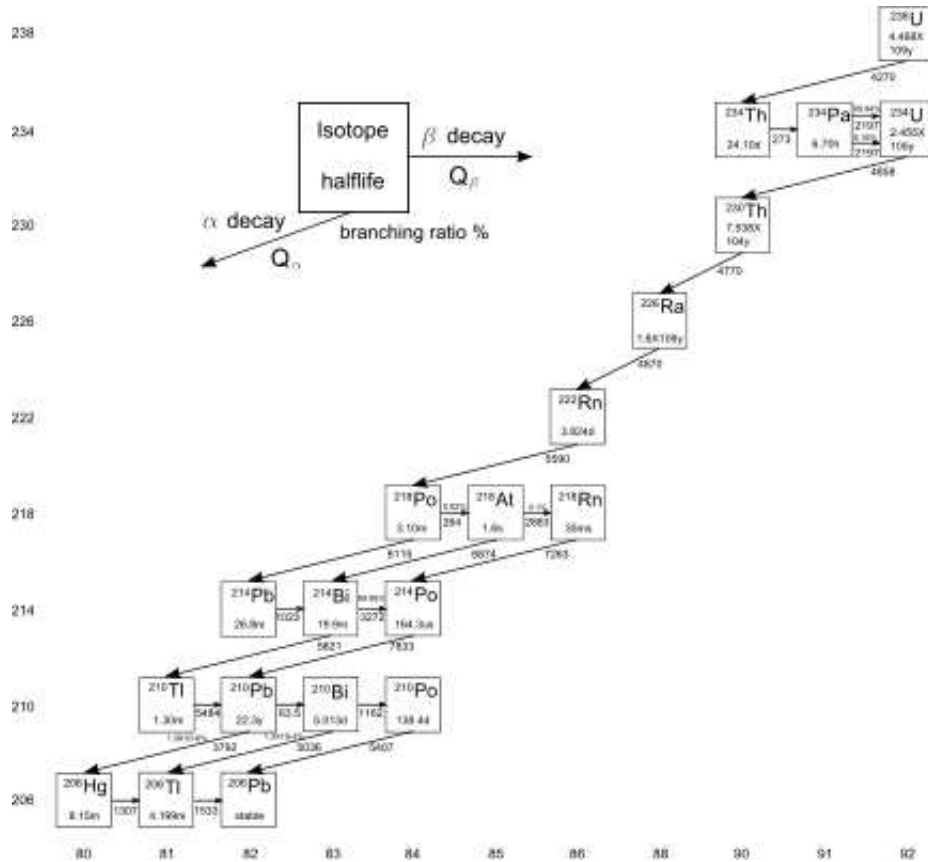
Figure 7.2: ^{238}U nuclear decay scheme.

efficiency of the detector above 0.7 MeV concerning ^{238}U is given in table 7.4. In the Uranium

(and Thorium) case, due to alpha emissions, the quenched energy has to be considered and not directly the deposited one. The consequence of a change of the quenching factor is discussed in section 7.2.2.4. Betas travel typically a distance of a few millimeters within acrylic and liquid scintillator. This implies that Gamma Catcher feet and stiffeners have a less important impact, being in the Buffer oil. Concerning the alpha particles, most of those are trapped in the acrylics Only alphas lying on the surfaces of Target (internal and external) and Gamma Catcher (internal) are potential contributors. Concerning the gamma emission, both Target and Gamma Catcher are affected in a similar way, though the solid angle from which the Target vessel sees the liquid scintillator active volume is twice that of the Gamma Catcher.

To conclude, the background goal of 0.1 Bq induced by ^{238}U leads to a maximum concentration of 2.30×10^{-11} g/g for the Target acrylics and of 2.53×10^{-11} g/g for the Gamma Catcher acrylics. The active masses ratio is of 1.96 in favor of the Gamma Catcher. However, the efficiency parameter ratio of Gamma Catcher and Target is of 0.45, which gives us a contribution ratio of 1.1 in favor of the Gamma Catcher.

7.2.2.3 ^{232}Th

^{232}Th represents 100% of natural Thorium. Its specific activity is of 4.06 kBq.g^{-1}. As for Uranium, we encounter alpha, beta and gamma ray emissions all along the decay chain of Thorium (cf figure 7.3). Then, since these are similar cases, the method applied on Uranium
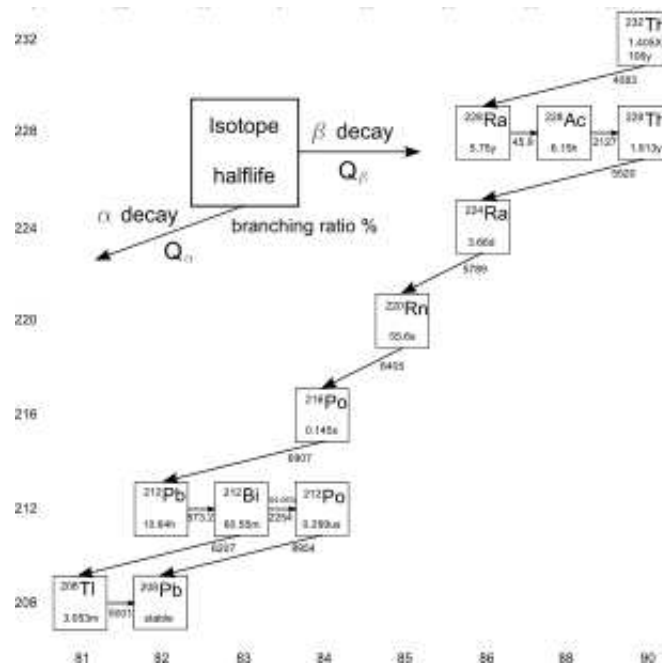
Figure 7.3: ^{2322}Th nuclear decay scheme.

was strictly applied to Thorium: the quenched energy was looked at, and not the energy deposition in the liquid scintillator; the multiplicity of the response lead to high efficiency parameters, possibly greater than one. These parameters are listed on table 7.5. Concerning alpha, beta and gamma emissions, the understanding is strictly the same as for Uranium

		Target		Gamma Catcher		
	Vessel	Stiffener	Feet	Vessel	Stiffener	Feet
Efficiency	1.10	1.10	0.90	0.47	0.19	0.03

Table 7.5: Efficiency of the detector relative to ^{232}Th above 0.7 MeV

To conclude, to get 0.1 Bq of background induced by Thorium, we get a maximum allowed concentration of ^{232}Th in the acrylics of 5.52×10^{-11} g/g for the Target and of 5.98×10^{-11} g/g for the Gamma Catcher. The active masses ratio is of 1.96 in favor of the Gamma Catcher. However, the efficiency parameter ratio of Gamma Catcher and Target is of 0.46, which gives us a contribution ratio of 1.1 in favor of the Gamma Catcher.

7.2.2.4   Impact of the quenching factor

Alpha particles lose most of their energy through ionization and/or excitation of the matter atoms. The kinetic energy of an alpha particle is gradually dissipated by such interactions until it captures two electrons and settles down as Helium. Matter ionization leads to atomic recombination, exchange of energy which cannot be detected. This is quenching: some of the alpha energy is lost through atomic recombination and therefore the visible energy is much smaller than the actual deposited energy. The quenching depends on matter. Because of large quenching effect in the liquid scintillator, the visible energy of alpha particles is considerably reduced compared to its energy deposition, at around $^1/_{10}$.

7.3   Focus on Target and Gamma Catcher vessels

The radiopurity checks on the GS0Z18 material happened in three steps. Indeed, since this material was created especially for Double Chooz, a laboratory batch of 150 kg was first produced, for us to validate the material optically, its resistance, its radiopurity, an its compatibility with the liquids (see chapter 5). Once the material was approved, the production of the ten tons of material was launched. This unique batch monomer syrup radiopurity was checked before the vessels construction started, in case it was contaminated somehow. Finally, the radiopurity was also checked after construction. Moreover, several small elements are included in the vessels; their radiopurity was checked as well.

7.3.1   GS0Z18 acrylic material

7.3.1.1   Laboratory batch

Neutron Activation analysis (NAA) is a technique used to accurately determine the concentration of trace elements in a sample. The sample is introduced in a reactor core (or any neutron source), being thus irradiated by an intense thermal and epithermal neutron flux. Element

^{41}K reactions	Half-life (s)	Gamma ray energy (MeV)	Cross section (barns)	Branching ratio	Interferences
(n,γ) ^{42}K	45,000	1,524.7	1.45	17.9 %	Other $^A_Z X$ with similar decay time?
(n,p) ^{41}Ar	6,480	1,293.6	0.39	99.2 %	^{41}Ar reactor production
(n,α) ^{38}Cl	2,238	2,167.5	0.21	44.0 %	(n,α) ^{37}Cl

Table 7.6: ^{41}K reactions and parameters.

traces of the sample are activated and decay, emitting gamma rays. The sample is then transported to a NaI or HPGe detector to be analyzed. The radionuclides produced decay with characteristic half-lives and emit gammas with well defined energies. Note that since the mean free path of the neutrons is large compared to the sample size, as is the mean free path of the emitted gammas, this method can be used to probe the bulk concentration of trace elements.

During the exposure to neutron, the concentration of the produced isotope i+1 is given by:

$$\frac{dN_{i+1}}{dt} = (\sigma \varphi_{th} + I_{res} \varphi_{epi}) N_i - \lambda N_{i+1} \tag{7.3}$$

N_i being the concentration of the radionuclide i, N_{i+1} the concentration of the radionuclide i+1, φ_{th} the thermal neutron flux in neutrons.cm^{-2}, σ the thermal neutron capture cross section in cm^2, φ_{epi} the epithermal neutron flux in neutrons.cm^{-2}, I_{res} the resonance integral, and λ the decay constant of the radionuclide i+1 (T$_{1/2}$=$0.693/\lambda$). The quantity of gamma rays detected in a detector can be written as:

$$N_\gamma = \frac{1}{100\lambda} N f I_\gamma \varepsilon_\gamma \left(\sigma \varphi_{th} + I_{res} \varphi_{epi}\right) \left(1 - e^{-\lambda t_i}\right) \left(1 - e^{-\lambda t_c}\right) e^{-\lambda t_w} \tag{7.4}$$

f being the isotopic abundance of the radionuclide i, I_γ the gamma ray intensity, ε_γ the full energy gamma ray detection efficiency, N the number of target nuclei, t_i the irradiation time, t_c the counting time, and t_w the waiting time.

with this method, we get a robust measurement of ^{40}K that we can compare to the Germanium measurement performed at Gran Sasso and allows us to identify if the background produced by the acrylics is acceptable. Several nuclear reactions could be considered to get measurable gamma emissions. Natural Potassium isotopes are ^{39}K, ^{40}K, ^{41}K, but only the activation of ^{41}K (isotopic abundance of 6.8%) has to be considered, since the other isotopes do not give exploitable gamma ray emissions (their lines are lost in background). The ^{41}K reactions and parameters are given in table 7.6. The second and third reactions are difficult to use due to interferences and lower cross sections. The first reaction seems to be more useful, though the detection sensitivity depends on the presence of other nuclides with similar decay time.

To better constraint the ^{40}K, a neutron activation analysis has been performed in Munich on a solid piece of GS0Z18 of roughly 1g. The sample was irradiated at the FHM Munich research reactor for 10 minutes and put into the germanium detector seven hours later; the counting time was 1.3 hours. The acrylic sample turned yellow after irradiation. The measurement of

the Potassium concentration is $(7.78 \pm 0.8) \times 10^{-11}$ g/g in the GS0Z18 acrylic, which is a factor between two and ten above the allowed concentration to reach the 0.1 Bq. Considering the different masses and the efficiency of the detector for ^{40}K concerning the different parts, we get an estimate of the Potassium background in the detector, of 0.82 Bq from the Target acrylic and 0.77 Bq from the Gamma Catcher vessel. This is higher than expected. Though, it remains small with respect to the PMTs induced gammas (less than 5 Bq), and is thus acceptable for the experiment.

7.3.1.2   Monomer syrup

A measurement of GS0Z18 syrup has been done using GeMPI, a highly sensitive germanium gamma-spectrometer operated at the Gran Sasso underground laboratory [62]. The sample was of 1 kg, the live time of 2,883,581.35 s, 2,046,081.26 s for Radon daughters. Indeed, there was a small Radon contamination at the beginning of the measurement, so the beginning of the measurement was not taken into account for Radon daughters. The results are displayed below in table 7.7. The upper limits are given at 90% CL and the uncertainties at 68% CL.

	GS0Z18 monomer syrup
^{238}U: ^{226}Ra(*)	$< 9.4 \times 10^{-11}$ g/g
^{238}U: ^{234}Pa	$< 2.3 \times 10^{-9}$ g/g
^{232}Th: ^{228}Th	$< 2.4 \times 10^{-10}$ g/g
^{232}Th: ^{228}Ra	$< 3.0 \times 10^{-10}$ g/g
^{40}K	$(3.1 \pm 1.5) \times 10^{-11}$ g/g
^{137}Cs	< 0.75 mBq.kg^{-1}
^{235}U	$< 2.0 \times 10^{-9}$ g/g

Table 7.7: GS0Z18 monomer syrup measurement. It was a 1 kg sample, with live time 2,883,581.35 s, 2,046,081.26 s for Radon daughters(*). Upper limits are given at 90 % C.L., actual measurements at 68 % C.L.

The measured radionuclide concentrations either come directly from the radionuclide gamma emission (^{234}Pa) or from other gamma emissions further in the decaying chain. For the latter case, the secular equilibrium is supposed to be respected in order to determine the different chain elements concentration. For example, the ^{228}Ra concentration comes from the ^{228}Ac line; the ^{228}Th from ^{212}Pb, ^{212}Bi and ^{208}Tl; ^{226}Ra from ^{214}Pb and ^{214}Bi and ^{235}U is a mix between a direct gamma emission and the ^{226}Ra, ^{214}Pb and ^{214}Bi concentrations.

With those concentrations, we get upper limits and or estimates for the singles background coming from the Target and Gamma Catcher acrylics, as shown in table 7.8. No Uranium or Thorium impurities have been detected. Unfortunately, the sensitivity needed to ensure the 0.1 Bq goal could not be reached due to the combination of the small amount of material tested, the exposition time and the background. However, the upper limits given for the uranium and thorium concentrations ensure a single induced background coming from both Target and Gamma Catcher smaller than the Bq. Considering potassium, a signal has been detected, which also gives a single induced background around 1 Bq. Even though those values are higher than the targeted goal, they still remain small compared to the PMTs induced gammas (less than 5 Bq) and are thus acceptable for our experiment. The results are lower than for the test batch.

	Target	Gamma Catcher
^{40}K	0.35 ± 0.18 Bq	0.33 ± 0.17 Bq
^{238}U	< 0.41 Bq	< 0.37 Bq
^{232}Th	< 0.54 Bq	< 0.50 Bq

Table 7.8: Estimates of the singles background induced by the Target and Gamma Catcher acrylics.

7.3.1.3 After construction check

Both methods were used to determine the contamination in the final material. As for the test batch, NAA allowed us to quantify the background contamination in Potassium, but not in Thorium and Uranium. The acrylic sample mass was 2 g, it was irradiated for 20 minutes and was measured in a Germanium counter two hours after irradiation. The estimated Potassium concentration is $(5.04 \pm 0.8) \times 10^{-11}$ g. This is roughly five times higher than the specifications from section 7.2.2.

At Gran Sasso, 13.82 kg of the final GS0Z18 material were measured during 52 days. The results are displayed in table 7.9. With these measurements, we would be in the specifications

	GS0Z18 final material
^{238}U: ^{226}Ra	$< 4.1 \times 10^{-12}$ g/g
^{238}U: ^{234}Pa	$< 3.3 \times 10^{-10}$ g/g
^{232}Th: ^{228}Th	$< 1.3 \times 10^{-11}$ g/g
^{232}Th: ^{228}Ra	$< 2.5 \times 10^{-11}$ g/g
^{40}K	$< 1.9 \times 10^{-12}$ g/g
^{137}Cs	< 26 mBq.kg^{-1}
^{235}U	$< 1.8 \times 10^{-10}$ g/g

Table 7.9: Final GS0Z18 acrylic material measurement. It was a 13.82 kg sample, with live time 4,483,664 s. Upper limits are given at 90 % C.L. The sensitivity is about one order of magnitude better compared to the monomer syrup measurement.

to reach 0.1 Bq of contamination induced by Potassium, Uranium and Thorium described in section 7.2.2. However, some other elements are to consider in the Target and Gamma Catcher vessels. They are described in the next section.

The two measurements are in disagreement by a factor 26. Up to this day, we still do not know where this disagreement come from. However, the acrylic contamination stays acceptable for the experiment which ever measurement we take into consideration.

7.3.2 Other elements

In the acrylic vessels are several small elements added to hold the structure, such as the glue used to form the vessels, the screws to attach the Target to the Gamma Catcher and the Gamma Catcher to the Buffer...

	Acryfix 190	Acryfix 194
^{238}U: ^{226}Ra	$< 4.5{\times}10^{-9}$ g/g	$< 2.2{\times}10^{-9}$ g/g
^{238}U: ^{234}Pa	$< 2.2{\times}10^{-7}$ g/g	$< 1.5{\times}10^{-7}$ g/g
^{232}Th: ^{228}Th	$< 2.4{\times}10^{-8}$ g/g	$< 1.6{\times}10^{-8}$ g/g
^{232}Th: ^{228}Ra	$< 2.9{\times}10^{-8}$ g/g	$< 1.5{\times}10^{-8}$ g/g
^{40}K	$< 2.4{\times}10^{-5}$ g/g	$< 1.7{\times}10^{-5}$ g/g
^{60}Co	-	< 27 mBq.kg^{-1}
^{137}Cs	-	< 21 mBq.kg^{-1}

Table 7.10: Glue Ge measurement

	Acryfix 190	Acryfix 194
Target	< 0.39 Bq	< 0.29 Bq
Gamma Catcher	< 0.73 Bq	< 0.54 Bq

Table 7.11: Upper limits to the potassium background induced by the glue in the acrylic tanks. They are given for ^{40}K, with 90 % C.L. on the measurements.

7.3.2.1   Glue

The assembly of the vessels is done by gluing together acrylic sheets, like for example different plates of the cylindrical vessel, the chimney to the lid, the different parts of the feet, etc. As any other detector component inserted within the active detector Target, it has been checked for radiopurity concerns. We estimated that up to 5.41 kg of glue is needed for the Target, that is to say 1.51 % of the total Target mass, and 22.31 kg for the Gamma Catcher (1.36 % of the total Gamma Catcher mass). These are high estimates, based on the assumption that the glue skin is 2 mm thick. According to the manufacturer, less than 40 kg were used for the construction of three Targets and one Gamma Catcher.

Two different glues, Acryfix 190 (137 g with a counting time of 600,985 s) and Acryfix 194 (138 g and live time 603,126 s), have been measured by Ge detectors in Heidelberg. Unfortunately, these will not be the final glues, since the components are to be mixed at the very last moment, supposedly at the fabrication company. Any dust, radioactive possibly, can pollute the glue. Hence, the measurements given here are to be taken carefully. Therefore, these first measurements were not meant to reach a really high sensitivity and we only have upper limits (see table 7.10). Considering the glue mass in the detector, this gives us upper limits on the induced background. For example, the ones for ^{40}K are shown table 7.11. In these calculations, safety factors have been taken. Indeed, these limits are calculated considering that all of the glue is in the actual vessel, meaning this suppose the highest "efficiency" of the detector (the location is not taken into account). Also, we have to recall that the estimates of glue masses are pretty high. The glue represents less than 2 % of the mass of each tank. This implies that even with the actual limits on the glue activity, we will not be taking any risk using it in terms of radiopurity of the vessels.

7.3.2.2 Inserts and screws

To fix the Gamma Catcher to the Buffer and the Target to the Gamma Catcher, the feet of the smaller vessel were screwed in the larger vessel. However, it is impossible to screw stainless still in acrylic; it would start to grip and break the acrylic piece. Therefore, inserts (stainless steel rods with a screw thread) were glued on the large vessel. These two pieces were measured. The twelve needed screws were measured at Heidelberg. They weighed 4 kg and the live time was 758,207 s. The results are displayed in table 7.12.We measured the inserts at CEA. The results are displayed in table 7.13.

	Screws
^{238}U: ^{226}Ra	$< 9.6 \times 10^{-10}$ g/g
^{238}U: ^{234}Pa	$< 5.1 \times 10^{-8}$ g/g
^{232}Th: ^{228}Th	$< 3.3 \times 10^{-9}$ g/g
^{232}Th: ^{228}Ra	$< 4.4 \times 10^{-9}$ g/g
^{40}K	$< 7.2 \times 10^{-7}$ g/g
^{137}Cs	< 4.6 mBq/kg
^{60}Co	4.52 ± 1.8 mBq/kg

Table 7.12: Screws used to attach the vessels. It was a 4 kg sample, with live time 758,207 s. Upper limits are given at 90 % C.L.

	Inserts
^{238}U	$< 8.4 \times 10^{-8}$ g/g
^{232}Th	$< 2.6 \times 10^{-7}$ g/g
^{40}K	$< 3.4 \times 10^{-5}$ g/g
^{235}U	< 2.5 Bq/kg
^{60}Co	< 0.1 Bq/kg

Table 7.13: Inserts used to attach the vessels. Six of them are needed for the Gamma Catcher, and six more for the Target.

7.3.2.3 Pressure sensor

One of the liquid level monitoring systems is a pressure sensor located at the bottom of the Gamma Catcher. It weighs 200 g, so it will not contribute too much to the background. However, since it is located in liquid scintillator, its radiopurity was checked (see table 7.14). The measurement was done in Munich, with the same Germanium counter that was used for NAA.

7.3.2.4 Dust from the laboratory

Cleanliness was a high requirement throughout the whole construction and integration of the detector, as explained in chapter 8. Even though we took great care in reducing the amount of

	Pressure sensor
^{238}U	$1.0 \times 10^{-8} \pm 7.5 \times 10^{-10}$ g/g
^{232}Th	$3.2 \times 10^{-8} \pm 3.8 \times 10^{-9}$ g/g
^{40}K	$(8.8 \pm 1.5) \times 10^{-6}$ g/g
^{60}Co	< 3.0 mBq/kg
^{137}Cs	< 5.1 mBq/kg

Table 7.14: Pressure sensor. The sensor weighs 200 g. Upper limits are given at 90 % C.L.

dust in the laboratory, some probably fell in the vessels. The exact amount is hard to determine; a Gamma Catcher and Buffer cleaning right before closing the Gamma Catcher collected 4 ± 2 g of dust. We collected 15 g of dust from the vacuum cleaner in the laboratory and counted it for roughly one day. These are high levels compared to the materials we used, especially in Cesium. Results are in table 7.15.

	Dust
^{238}U	$(4.6 \pm 1.3) \times 10^{-6}$ g/g
^{232}Th	$4.3 \times 10^{-6} \pm 2.7 \times 10^{-7}$ g/g
^{40}K	$3.4 \times 10^{-3} \pm 2.8 \times 10^{-4}$ g/g
^{60}Co	< 1.27 Bq/kg
^{137}Cs	3.4 ± 0.7 Bq/kg

Table 7.15: Dust collected from the laboratory. 15 g were counted for roughly a day. Upper limits are given at 90 % C.L. These are high levels compared to the materials we used, especially in Cesium.

7.3.2.5   Dehydrating bags

Water in the Target liquid scintillator degrades Gd encapsulation; the Target vessel had to be dried intensely before the filling phase (see section 10.2.3). In order to lower the humidity in the Target vessel with respect to the ambient laboratory air ($\sim$ 90 % relative humidity), not only did we flush the vessel right before filling with clean and dry Nitrogen gas, but also we deployed some dehydrating bags in the Target (dry clay bags, see section 10.2.3.2). In order to determine the possible contamination coming from these bags, we counted them first in a Germanium counter, then in a Radon chamber (both at the Heidelberg MPIK institute). Results are displayed in table 7.16.

From figure 7.2, the parent of ^{222}Rn is ^{226}Ra. If we consider N_{Ra} to be the number of Radium atoms, N_{Rn} to be the number of Radon atoms, τ_{ra} and τ_{Rn} time constants for Radium and Radon respectively:

$$\begin{cases} \frac{dN_{Ra}}{dt} & = -\frac{N_{ra}}{\tau_{Ra}} \\ \frac{dN_{Rn}}{dt} & = -0.2\frac{dN_{Ra}}{dt} - \frac{N_{Rn}}{\tau_{Rn}} \end{cases} \tag{7.5}$$

The 0.2 factor comes from the measurement: 20 % of Radon emanated. By combining the two

	Gamma Spectroscopy			Radon emanation
	^{238}U	^{232}Th	^{40}K	^{222}Rn
Contamination	~ 9	~ 25	~ 170	1.8 ± 0.2
(Bq.kg^{-1})	($7.2{\times}10^{-7}$ g/g)	($6.2{\times}10^{-6}$ g/g)	($5.6{\times}10^{-3}$ g/g)	

Table 7.16: Dehydrating bags gamma spectroscopy and Radon emanation measurement. Roughly 20 % of the produced ^{222}Rn is emanated, while this fraction is usually lower.

lines of equation (7.5), we get:

$$\frac{dN_{Rn}}{dt} - 0.2\frac{N_{Ra}}{\tau_{Ra}} + \frac{N_{Rn}}{\tau_{Rn}} = 0 \tag{7.6}$$

The number of atoms follow:

$$\begin{cases} N_{Ra} & = N_{Ra}^0 e^{-t/\tau_{Ra}} \\ N_{Rn} & = N_{Rn}^0 e^{-t/\tau_{Rn}} \end{cases} \tag{7.7}$$

N_{Ra}^0 and N_{Rn}^0 being the number of Radium and Radon atoms, respectively, at $t = 0$. Equation (7.7) gives:

$$\frac{dN_{Rn}}{dt} + \frac{N_{Rn}}{\tau_{Rn}} = 0.2\frac{N_{Ra}^0}{\tau_{Ra}}e^{-t/\tau_{Ra}} \tag{7.8}$$

This is equivalent to:

$$\frac{dN_{Rn}^0}{dt} = 0.2\frac{N_{Ra}^0}{\tau_{Ra}}e^{-tB} \tag{7.9}$$

with $B = \frac{1}{\tau_{Ra}} - \frac{1}{\tau_{Rn}}$. Therefore, we get for the initial number of Radon atoms:

$$N_{Rn}^0 = -0.2\frac{N}{B\tau_{Ra}}e^{-tB} \tag{7.10}$$

By combining equations (7.7) and (7.10), one gets:

$$N_{Rn} = 0.2\frac{N_{Ra}^0}{\frac{\tau_{Ra}}{\tau_{Rn}} - 1}e^{-t/\tau_{Ra}} \tag{7.11}$$

Radium half-life $\tau_{Ra}^{1/2}$ is 1,600 years whereas Radon $\tau_{Rn}^{1/2}$ is 3.8 days. By approximation and for an initial Radium concentration of 10 Bq.kg^{-1}, one gets from equation (7.11):

$$N_{Rn} \approx \frac{0.2N_{Ra}^0}{\frac{\tau_{Ra}}{\tau_{Rn}}} \tag{7.12}$$

Therefore, considering the long half life of Radium compared to the one of Radon, the concentration of Radon gas in the Target is considered constant. A dehydrating bag is weighing roughly 150 g, so the initial number of radium atoms is:

$$N_{Ra}^0 = \frac{10 \cdot 0.15}{3.7e10} \times \frac{\mathcal{N}_A}{226} \approx 1.08 \times 10^{11} \text{ atoms} \tag{7.13}$$

$\mathcal{N}_A$ being the Avogadro number. By combining equations (7.12) and (7.13), we get:

$$N_{Rn} \approx 1.40 \times 10^5 \text{ atoms} \tag{7.14}$$

Thus, the contamination induced by Radon gas coming from the dehydrating bags in the Target vessel is:

$$\frac{1}{\tau_{Rn}} = \frac{N_{Rn}\ln 2}{\tau_{Rn}^{1/2}} = 0.29 \, \text{Bq} \tag{7.15}$$

This confirms the results from MPIK, which stand a contamination for Radon gas of 0.3 Bq at infinity. The contamination from the bags is acceptable compared to the one coming from the PMTs (~ 5 Bq). Moreover, the detector will be flushed with Nitrogen before filling, starting from the vessels bottom. This will push the Radon gas up and out of the detector, implying that the dehydrating bags can be used safely.

After the Radon gas is pushed out of the detector, there still is a possibility that some Radon daughters are stuck on the acrylic walls of the Target, and keep decaying inside the detector. From figure 7.2, one can see that the first daughter with a considerable half-life is ^{210}Pb (22.3 years). This isotope decays into ^{210}Bi, releasing in the process a 63.50 keV beta particle. Then Bismuth decays into ^{210}Po, producing then a 1.16 MeV beta particle. The chain stops afterwards with the decay of Polonium into ^{206}Pb, stable, with the emission of a 5.30 MeV alpha particle. The beta and alpha emissions coming from this decay chain will happen on the acrylic wall and therefore, roughly half of the particles will be stopped and will not get to the liquid (see section **6**). The rest of them will be a background that we will have to take into account. The associated gamma emissions are not a problem to the Double Chooz experiment (43.5 keV for the ^{210}Pb, 803 keV with 0.001 % ratio for the ^{210}Po). However, the beta particle coming from ^{210}Bi decay might generate some Bremsstrahlung effect, leading to high energy gammas in a small fraction. This also applies to Radon gas in the laboratory air. Due to technical difficulties, the dehydrating bags were not used; the drying of the vessel was realized by Nitrogen flushing.

7.4   Impact: singles rate and spectra

7.4.1   Singles rate

The singles rate is determined thanks to equation (7.2), with detection in Target and Gamma Cacther. All the probabilities (or multiplicities) were simulated for Potassium, Uranium and Thorium thanks to Geant4 (see table 7.17) in different part of the acrylic vessels (feet, cylinders and stiffeners), to take into account their location in the detector. No new probabilities were computed for the smaller elements; we used the acrylic ones.

The singles rate prediction depends on radioassays of the materials and the geometrical factors (probabilities or multiplicities) from simulation. Two possibilities are to consider: either we have an actual measurement or a limit on the material radioactivity. In the first case, we get the singles rate measured for a definite isotope and detector element. This corresponds to the minimum expected rate in the detector. In the second case, we get the maximum expected singles rate in the detector; this is constrained by the radioassays' sensitivities. The observed singles rate, when we switch the detector on, is then to be comprised between these two values.

	Probabilities		
	^{40}K	^{238}U	^{232}Th
Target liquid	0.32	2.71	1.90
Target cylinder	0.10	0.86	1.09
Target feet	0.08	0.73	0.89
Target stiffeners	0.10	0.88	1.08
Gamma Catcher liquid	0.29	1.62	1.78
Gamma Catcher cylinder	0.04	0.37	0.45
Gamma Catcher feet	2.85×10^{-3}	0.02	0.03
Gamma Catcher stiffeners	3.66×10^{-3}	0.02	0.04
Buffer oil	2.88×10^{-3}	0.03	0.03
Buffer tank	9.00×10^{-5}	8.55×10^{-4}	1.04×10^{-3}

Table 7.17: Probabilities and multiplicities of Potassium, Uranium and Thorium for the Target, Gamma Catcher and Buffer tanks and liquids. This was computed for an 0.7 MeV threshold.

	Singles rate (Bq)		
	^{40}K	^{238}U	^{232}Th
Target cylinder	$< 1.31 \times 10^{-2}$	$< 1.09 \times 10^{-2}$	$< 4.40 \times 10^{-2}$
Target feet	$< 7.16 \times 10^{-3}$	$< 6.17 \times 10^{-3}$	$< 2.39 \times 10^{-2}$
Target stiffeners	$< 8.66 \times 10^{-4}$	$< 7.18 \times 10^{-4}$	$< 2.81 \times 10^{-2}$
Gamma Catcher cylinder	$< 1.81 \times 10^{-2}$	$< 1.53 \times 10^{-2}$	$< 5.89 \times 10^{-2}$
Gamma Catcher feet	$< 8.76 \times 10^{-4}$	$< 7.34 \times 10^{-4}$	$< 2.64 \times 10^{-3}$
Gamma Catcher stiffeners	$< 6.93 \times 10^{-5}$	$< 4.57 \times 10^{-5}$	$< 2.31 \times 10^{-4}$
Buffer tank	$< 3.31 \times 10^{-3}$	1.15×10^{-2}	6.38×10^{-2}
TOTAL	< 0.043	< 0.045	< 0.196

Table 7.18: Singles rate from the acrylic vessels and the Buffer tank. This is given for a threshold of 0.7 MeV, with detection in Target and Gamma Catcher. for Potassium, the rate would be 1.13 Bq with NAA results. From this are missing the rates coming from the liquids, for which we did not have the final radioassay results at the moment this report was written.

This will be the first check of the detector; indeed, if the singles rate is what we expect, this will mean that we understood the detector correctly on one hand, on the other hand that the detector is working properly. The singles rate for an 0.7 MeV threshold, from the acrylic vessels and the Buffer tank, are displayed in table 7.18. The results are a rate of 0.043 Bq for Potassium (1.131 Bq with NAA results), 0.045 Bq for Uranium and 0.196 Bq for Thorium.

7.4.2 Singles spectral shape

The singles spectral shape is first determined from radiopurity measurements and simulation (including all isotopes and detector elements). Once the data arrive, we will have the singles spectrum with reconstructed charge, vertex and energy. Visible energy spectra for Uranium, Potassium and Thorium are shown in figures. These are spectra directly from simulation, with no charge or energy reconstruction. For the three liquids, the spectra shown were determined taking into account the radiopurity goals, of 10^{-12} g/g for the Buffer oil in Uranium and
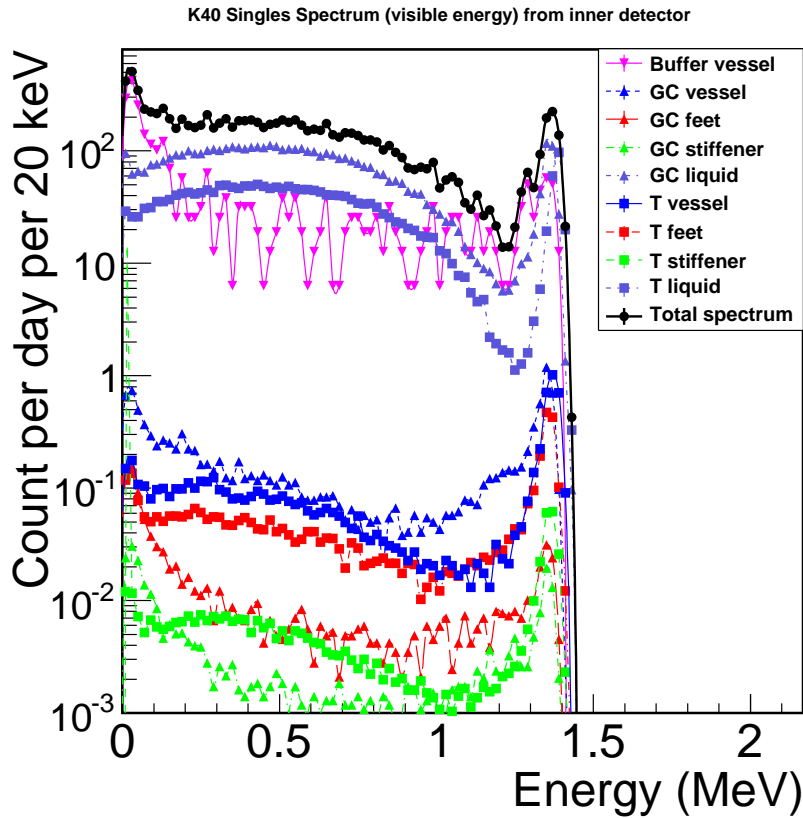
Figure 7.4: Potassium visible energy spectrum. One can see the various detector components contributions; the highest are the Gamma Catcher liquid, Target liquid and Buffer tank.

Thorium and 10^{-13} g/g for Target and Gamma Catcher liquids in Uranium and Thorium, 10^{-10} g/g in Potassium.

The total visible energy singles spectrum is being computed by the collaboration. This will give us an idea of what we will see once the detector is turned on.

7.4.3   Towards accidental background

An accidental background is the coincidence of a prompt signal (energy deposition above threshold in Target and Gamma Catcher), a delayed signal (energy deposition above 6 MeV in Target) within $\tau = 100$ μs. The accidental rate is defined by:

$$R_{acc} = (A_p V_p) (A_d V_d) \tau \tag{7.16}$$

with A_p the prompt activity in Bq.m^{-3}, given by radioisotopes from the materials singles rate. V_p is the volume where a prompt signal can deposit energy, it corresponds to the inner active volume (Target and Gamma Catcher). A_d is the delayed activity in Bq.m^{-3} and corresponds to neutrons captured on Gd. It is estimated thanks to the Chooz neutron rate; since the Target volume is 10.3 m^3 instead of 5.5 m^3 in CHOOZ, this rate is of 88.5$\pm$4 neutrons per hour instead of 45$\pm$2 [32]. Finally, V_d is the volume where a delayed signal can deposit energy, that is to say
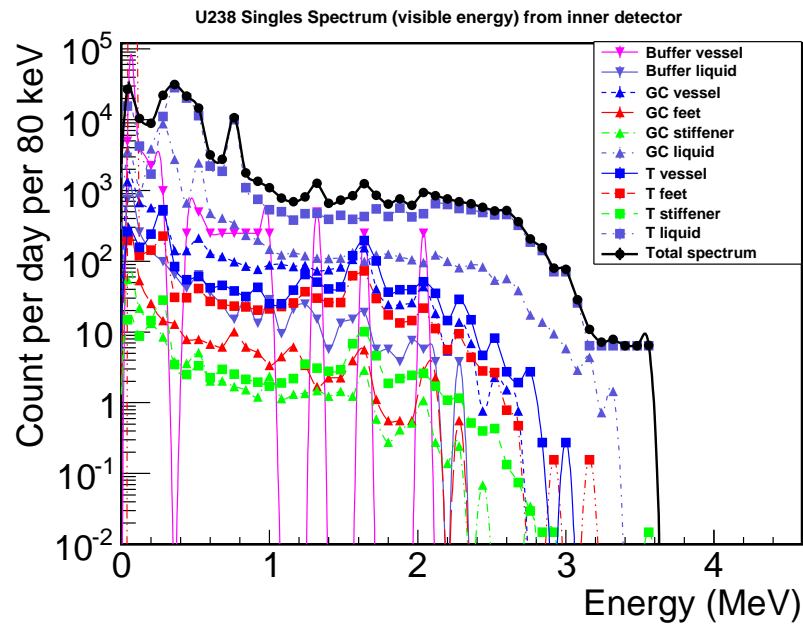
Figure 7.5: Uranium visible energy spectrum and various detector components contributions. The highest comes from the liquids, though the radiopurity data are the goals to achieve, not actual radioassays.
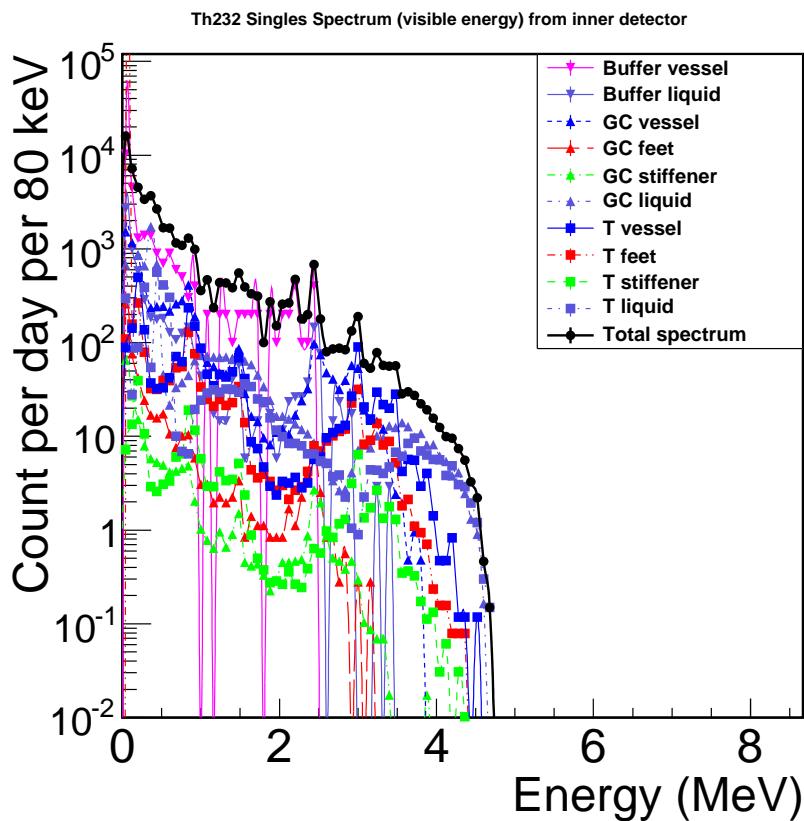
Figure 7.6: Thorium visible energy spectrum, with various detector contributions.

the Target. Although, to be mistaken for a neutrino signal, an accidental background delayed signal has to be captured close to the prompt signal (within 1 m). This would give a volume ten times smaller, hence the accidental rate would be ten times smaller. However, the systematical error of a spatial reconstruction would have to be considered.

7.4.4   Conclusion: towards data analysis

To understand the first data and the reconstructed energy spectrum, one will have to guess what the major contributions are (heavy components and/or components close to the detector core). We could then simulate their spectral shape but let their adjustment α_D free:

$$\sum_{Isotope} \sum_{Detector\ Element} \sum_{E_{bin}} \alpha_D N_D(E) \tag{7.17}$$

$N_D(E)$ being the number of event per bin. We will then attempt to adjust the normalization to the first data. A priori, the main contributions are coming from the Target, Gamma Catcher and Buffer liquids, both acrylic vessels and the Buffer tank. The single rates expected are already computed, and the liquids are to come soon. The expected spectral shape is identified, waiting for the data to arrive to adjust the normalization.

Chapter 8

Cleanliness

When we studied radiopurity, we learned that dust is a source of background. Moreover, too much dust in a volume might cloud the liquid scintillator, reducing the detector efficiency. To fight this, cleanliness during the whole fabrication and integration phases was carefully controlled and monitored. Indeed, cleanliness levels were set for all the integration phases, getting harder as we got closer to the detector core. Acrylic vessels cleanliness was then particularly followed during material production, fabrication and integration. We defined cleaning protocols, set the cleanliness levels to reach during the different phases.

8.1 Cleanliness in the lab

8.1.1 Why is cleanliness important?

Two problems due to the presence of dust in the detector have been identified. On one hand, dust in the liquid scintillator might degrade its optical transparency. On the other hand, dust in the vessels might induce a non negligible accidental background. The radiopurity of the rock was determined by the original Chooz experiment to be of 2,000 ppb in ^{238}U, 5,000 ppb in ^{232}Th and 14,000 ppm in ^{nat}K. Our design goal was that the dust contamination in the detector is not to contribute more than 0.1 Bq to the singles rate in the Gamma Catcher and Target above 0.7 MeV per detector vessel[44]. Simulations were made (using Geant3 and Geant4) to estimate the amount of dust this would correspond to (see table 8.1). Both concluded that for a threshold of 700 keV, 0.05 g of rock dust in the acrylic vessels gives 0.01 + 0.01 Bq of contamination. Therefore, a maximum of 0.5 g of dust is allowed per detector vessel.

8.1.2 Site cleanliness

8.1.2.1 Particle Fallout Photometer (PFO)

The particle fallout (PFO) photometer is a device to measure particulate contamination on surfaces. During the measurement, the precipitating particles are collected on sample plates

	^{40}K	^{238}U	^{232}Th	Total		
	Rate (Bq)	Rate (Bq)	Rate (Bq)	Total Rate (Bq)	Dust mass (g) per Bq	Volume (cm^3) per Bq
Target liquid scintillator	0.13	0.06	0.04	0.22	4.5	1.6
Gamma Catcher liquid scintillator	0.12	0.05	0.03	0.20	5.0	1.8
Buffer oil	0.002	0.002	0.001	0.004	221	79.0
Veto liquid scintillator	1.9×10^{-5}	2×10^{-7}	8×10^{-8}	2×10^{-5}	52,700	18.8

Table 8.1: Contamination, threshold 0.7 MeV, energy deposition in Target and Gamma Catcher. dust density 2.8 g.cm^{-3}

allocated to the areas which have to be monitored. After exposure, they are collected and the degree of contamination of the sample plates is measured with the PFO-photometer (the measurement gives the obscuration ratio in ppm).

Measurements were done in the Double Chooz far laboratory at the end of January 2008; there was no ventilation in the laboratory at the time. The first measurement was made without any activity in the laboratory and the obscuration ratio was of 3,196 ppm. A second measurement was made with worker activity in the laboratory; there was an overflow, meaning the obscuration was so important that the measurement could not be made. These results are due to big dust grains, settling on the floor; some "particles" were visible to the naked eye. The obscuration ratio gets higher when there is activity in the laboratory since people walking move particles around. Solutions to this problem were cleaning during all integration phases and ventilation.

8.1.2.2   Radon monitoring

There are two main different techniques for measuring radon activity: integrative, passive radon sampling and continuous active radon sampling. Alpha track detectors are integrative, passive radon sampling devices that do not require power. They contain a thin piece of plastic or film mounted in the detector. Radon flows into the detector through a filtered opening. As the radon inside the detector decays, the emitted alpha particles hit the film, forming tracks. These tracks are counted to determine radon concentration. The Algade device uses this method to determine the dust radiopurity in the far laboratory and the Radon concentration in the air, by detecting Radon and its daughters. Indeed, long-life elements are collected on a filter to then be counted in a scintillator by a PMT. Short-life elements (from ^{222}Rn and ^{220}Rn) are counted *in situ* by a cellulose detector. The equivalent doses from the ambient gamma rays are counted *in situ* by a thermoluminescent detector. The results of the measurements are the alphapotential energies per Bq that are to be summed according to the appropriate decay chains. To obtain the alphapotential energy of ^{222}Rn, one has to sum these of ^{218}Po (5.8×10^{-10} J.Bq^{-1}), ^{214}Pb (28.6×10^{-10} J.Bq^{-1}), ^{214}Bi (21×10^{-10} J.Bq^{-1}) and ^{214}Po (55.4×10^{-10} J.Bq^{-1}) [64]. ^{214}Po being the only one whose alphapotential energy is determined by considering ^{222}Rn is in secular equilibrium with its daughters (equilibrium factor 0.4), one gets an alphapotential

energy for ^{222}Rn of 7.76×10^{-9} J.Bq^{-1}, which leads to a conversion factor of:

$$7.76\,\text{nJ} \leftrightarrow 1\,\text{Bq} \tag{8.1}$$

The same method can be applied to ^{220}Rn. The alphapotential energies to consider are those of ^{212}Pb (6.91×10^{-10} J.Bq^{-1}) and ^{212}Bi (65.6×10^{-10} J.Bq^{-1}), which leads to a conversion factor of:

$$7.25\,\text{nJ} \leftrightarrow 1\,\text{Bq} \tag{8.2}$$

Combined with the measurements, the conversion factors from equations [8.1] and [8.2] lead to the radon contamination in table 8.2. Our measurements are in agreement with that of the

	^{222}Rn	^{220}Rn
Liquid storage building (Dec. 2007)	5.41 ± 1.3 Bq.m^{-3}	1.79 ± 0.4 Bq.m^{-3}
Liquid storage building (Jan. 2008)	6.70 ± 1.6 Bq.m^{-3}	1.52 ± 0.3 Bq.m^{-3}
Far Laboratory (From beginning of Feb. to mid-March 2008)	27.32 ± 8.9 Bq.m^{-3}	19.17 ± 4.6 Bq.m^{-3}
Far Laboratory (From mid-March to end of April 2008)	13.66 ± 4.1 Bq.m^{-3}	

Table 8.2: ^{222}Rn and ^{220}Rn contamination in the liquid storage building and the far laboratory (with no ventilation), from beginning of December, 2007 to end of April, 2008. The contamination is higher in the far laboratory, which is explained by the fact that there is less ventilation.

first Chooz experiment, which showed an average of 20 Bq.m^{-3} in the far laboratory without any ventilation.

Our second radon monitoring device, the AlphaGUARD, is a continuous active radon sampling sensor, allowing to measure radon concentration in the air and its variation over time. The air
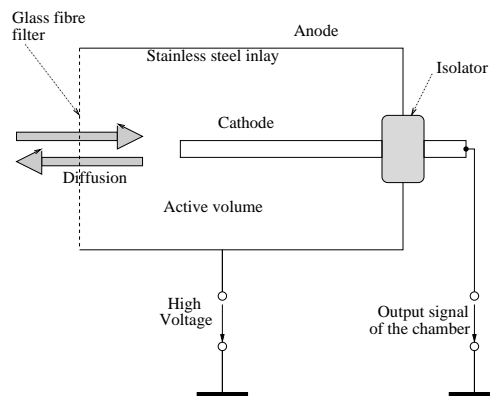
Figure 8.1: AlphaGUARD scheme. Radon gas enters the ionization chamber through a particle filter to decay there. Each decay product is converted into an electric impulsion. The different radon isotopes are identified by alpha spectroscopy.

goes into the device through a filter, so that only gas is being analyzed (see figure 8.1). Radon gas can then decay in the ionization chamber and every decay product is converted into an electric impulsion. The two common isotopes of radon, ^{220}Rn and ^{222}Rn, are identified through

	^{222}Rn
Liquid storage building (Jan. 2008)	< 13 Bq.m^{-3}
Far laboratory (Jan. 2008)	21.5 ± 8.6 Bq.m^{-3}
Far Laboratory (From mid-March to end of April 2008)	31.9 ± 24.1 Bq.m^{-3}

Table 8.3: ^{222}Rn contamination in the liquid storage building and the far laboratory. These measurements were made in January 2008 and are in agreement with the ones of the Algade device.

their respective energies from the alpha decays. The signal generated from the alpha detection is converted into a digital output.

Two measurements were made with the AlphaGUARD. The first one was made in January 2008, in the liquid storage building, to compare the measurements with those of the Algade device. The measurement gave a limit of 13 Bq.m^{-3} on radon contamination (see table 8.3); this is in agreement with the Algade device. The second one was made the same month in the far laboratory, during 16h. The average was of 21.5 ± 8.6 Bq.m^3 (see table 8.3), which is also in agreement with Algade and the first Chooz experiment measurements. A larger measurement campaign was then organized from mid-March to the end of April 2008, which gave results consistent with the previous ones.

8.1.2.3   Particle counter

To have a better estimate of the environment, airborne dust concentration has also been measured with a particle counter. The device is able to count dust particles thanks to light diffusion of a laser, per unit of volume and diameter (0.3 μm, 0.5 μm, 1 μm, 2.5 μm, 5 μm, 10 μm). Measurements were made on the 30th and 31st of January 2008 to determine the airborne dust concentration in the laboratory without ventilation, with and without activity. In figures 8.2 and 8.4, one can see the airborne dust concentration in the laboratory, for particles with diameter 1 μm and 0.3 μm. Larger diameter particles settle down faster than smaller diameter particles. Therefore, the activity in the laboratory will affect their concentration in the air more: once the particles have settled down, workers walking around will raise the dust up in the air, quickly increasing the airborne dust level. This can be observed on figure 8.2; the first peak observed in the dust concentration was actually a test run; there had been no activity in the laboratory for some time, to give dust time to settle. After a peak of intense activity in the laboratory, the dust concentration in the air rose by a factor of 10. Figure 8.3 shows the evolution of the airborne dust concentration for 1 μm diameter particles after this activity simulation. It shows that their falling time is of 188 minutes, and that they go up to 0.94 m. The other activity peak on that same day was caused by the use of the crane. Finally, on the second measurement day, the arrival of the workers in the laboratory can be clearly identified by an augmentation of the dust concentration of nearly a factor 50. On the other hand, smaller diameter particles, as in figure 8.4 do not settle down very fast, and therefore the amount of activity in the laboratory does not affect much their concentration in the air. The conclusion to these measurements was that to remove 'big' dust particles, the solution would be to limit the amount of workers int he laboratory and to clean it as often as possible. For smaller diameter
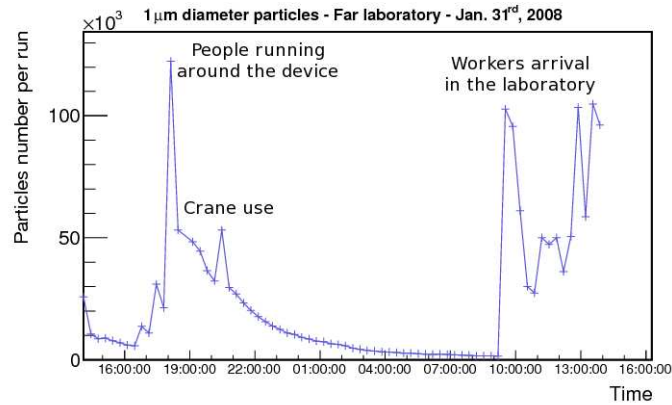
Figure 8.2: Dust measurement in the far laboratory, 1 μm diameter particles. The measurement was performed without and with activity. The first peak one can identify was a test run with a lot of activity around the device, to check that the airborne dust concentration was rising. The second peak, still on the first day of measurement, was induced by the use of the crane. Finally, on the second measurement day, one can see that the dust concentration is rising when workers arrived in the laboratory. This is because all of the dust that settled during the night was raised from the floor by people walking.

particles, the solution would be to filter the air getting in the laboratory. This is now done thanks to the ventilation system installed in the laboratory in April, 2008.

8.1.3   Cleanliness plan

A cleanliness committee has been created, composed of a convener, two deputies, and a representative for each phase of the integration. Its responsibilities are to define off-site cleaning protocols for detector components, cleaning protocols for each phase of the integration, to ensure the coordination between the different working groups and the required equipment (clean tents, HEPA filters, consumable supplies, counters). A cleanliness plan [63] has been written, defining the goals and purpose of the cleanliness group, the means to achieve the required cleanliness levels and to control that such levels are respected.

8.1.4   Clean room calculations

There were two different approaches to determine the dust deposition rates tolerable in the different vessels of the detector during integration. Both of them are based on the particle size distribution in typical airborne dust and radioassays of the Chooz rock (in Uranium, Potassium, Thorium). The first method relies on experience gained during the SNO experiment and the mass deposition rates they measured. The second one is a pure fluid mechanics approach, the dust flow being a non viscous fluid following Stokes' law for deposition. These studies lead to estimates of the amount of dust deposited in Target, Gamma Catcher, Buffer and Inner Veto, leading to a singles rate of 0.3 Bq in the first method and 0.1 Bq in the second one. Then,
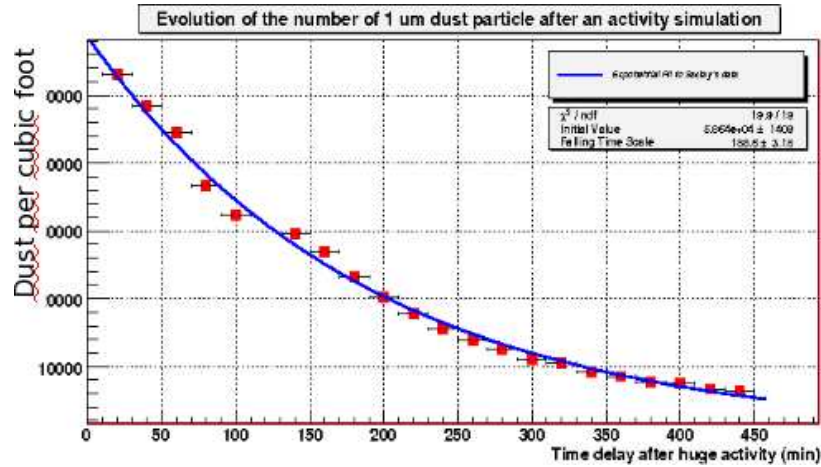
Figure 8.3: Evolution of the airborne dust concentration for 1 μm diameter particles after a peak of high activity in the laboratory. The settling time of the particles is of 188 minutes; according to fluid mechanics, the particles went up to 0.94 m.

Class	0.1 μm	0.2 μm	0.3 μm	0.5 μm	01 μm	5 μm
ISO 1	10	2				
ISO 2	100	24	10	4		
ISO 3	1,000	237	102	35	8	
ISO 4	10,000	2,370	1,020	352	83	
ISO 5	100,000	23,700	10,200	3,520	832	29
ISO 6	1,000,000	237,000	102,000	35,200	8,320	293
ISO 7				352,000	83,200	2,930
ISO 8				3,520,000	832,000	29,300
ISO 9				35,200,000	8,320,000	293,000

Table 8.4: ISO classes for clean room standards. Within this standard, clean room are classified according to the number and size of particles per m^3. The numbers represent the maximum number of particles allowed per m^3.

considering the time each volume would stay open, the maximum allowed dust concentration in the laboratory air is determined. This determines the clean room class required for each phase of the integration, and therefore the goal to reach for each cleanliness representative. Indeed, clean rooms (areas with a low, controlled level of environmental pollutants such as dust) are classified according to the number and size of particles permitted per volume of air. The standard used are the ISO 14644-1 standards, given in table 8.4. For example, an ISO class 5 clean room has at most $10^5 = 100{,}000$ particles per m^3; the ambient air outside in a typical urban environment corresponds to an ISO 9 clean room, ISO 8 with no activity (cf. figure 8.5).

8.1.4.1   SNO based calculation

SNO has unofficially reported a mass deposition rate of 1 μg.cm^{-2}.month^{-1} in areas of "high activity" in a mine laboratory. The reported rate for "low activity" is a factor of 10 less, or 0.1 μg.cm^{-2}.month^{-1}. This deposition corresponded to an ISO 7 class in the "high activity" region.
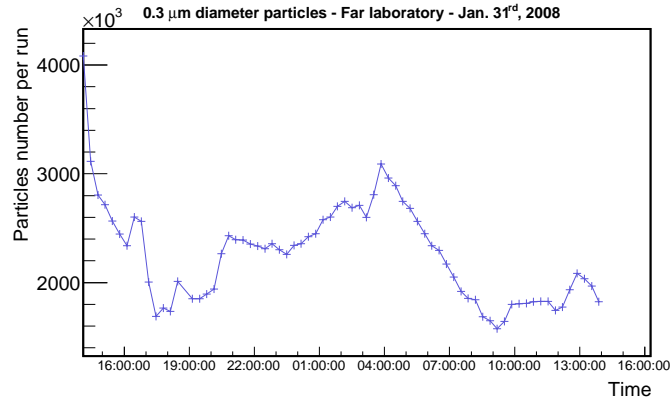
Figure 8.4: Dust measurement in the far laboratory, 0.3 μm diameter particles. One can observe that the airborne dust level stays quite constant compared to larger diameter particles. This is due to the fact that smaller particles do not settle as fast as bigger ones, and therefore the activity in the laboratory does not affect the airborne level as much.

Assuming the deposition rate is proportional to the airborne dust density, one can evaluate the mass density, activity density, and activity deposition rate as a function of ISO clean room class, as shown in table 8.5.

8.1.4.2 Fluid mechanics calculation: an example, the acrylic vessels

The acrylics have been entirely protected from dust until the plastic protections were removed. We assume that the plastic protections were cleaned before being taken off so there will not be any sudden dust deposition on the vessels, but a settling process will begin. Dust deposition will happen practically only on the horizontal surfaces (weak electrostatic effect). I assumed 120 h (4.32×10^5 s) of air exposition for all of the acrylics. Actually, the Target was completely assembled when delivered (except for the chimney) and the chimney neck was covered until the last moment. It seems therefore reasonable to assume the bottom lid of the Target not exposed, the bottom lid of the Gamma Catcher exposed the most, the top lid of the Gamma Catcher the least. For my calculations I took into account one Target lid and both of the Gamma Catcher lids for dust deposition.

There are two effects to take into account: continuous dust deposition on the acrylics surfaces and the dust trapped when the Gamma Catcher and Buffer lids will be closed. In order to determine the amount of dust deposited on the lids, we first have to know in which dynamic regime we are evolving. This is given by the Reynolds number Re, which is the ratio of the inertial to viscous forces.

$$R_e = \frac{v_d L}{\nu_d} \tag{8.3}$$

with v_d being the speed of the fluid, ν_d being the fluid kinematic viscosity and L a characteristic length. In our case, the fluid is practically still and non viscous, the Reynolds number is small, which means our environment is ruled by inertial forces and therefore we can apply Stokes' law. This determines the friction affecting small objects ruled by inertial forces in a fluid. If our
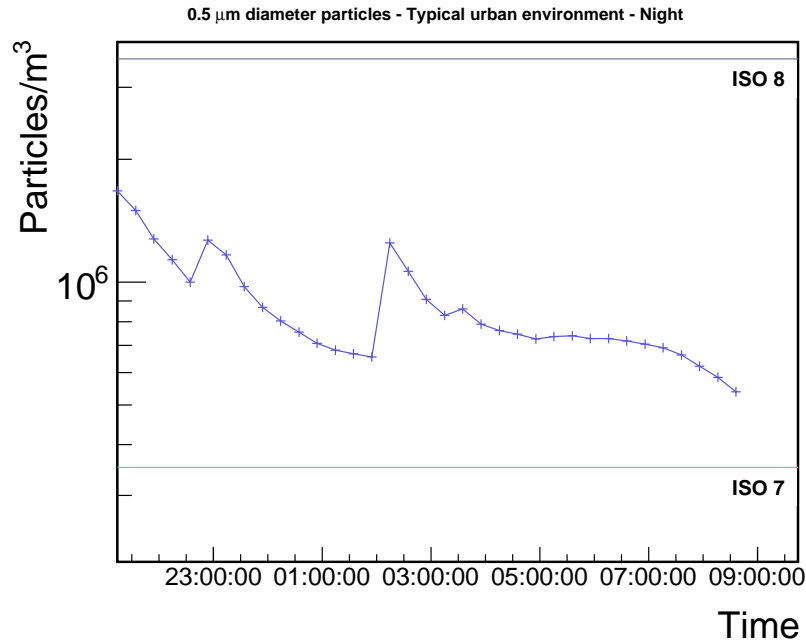
Figure 8.5: Airborne dust concentration in an urban environment, in terms of ISO class. The measurement was done at night, with no activity in the surroundings. This is an ISO class 8 environment.

ISO class	Deposition rate $(\mathrm{Bq.m}^{-2}.\mathrm{day}^{-1})$	Activity density $(\mathrm{Bq.m}^{-3})$	Mass deposition $(\mu\mathrm{g.cm}^{-2}.\mathrm{day}^{-1})$
1	$1.68{\times}10^{-9}$	$7.81{\times}10^{-13}$	$1.68{\times}10^{-7}$
2	$1.69{\times}10^{-8}$	$7.86{\times}10^{-12}$	$1.69{\times}10^{-6}$
3	$1.67{\times}10^{-7}$	$7.77{\times}10^{-11}$	$1.67{\times}10^{-5}$
4	$1.68{\times}10^{-6}$	$7.82{\times}10^{-10}$	$1.68{\times}10^{-4}$
5	$1.64{\times}10^{-5}$	$7.65{\times}10^{-9}$	$1.64{\times}10^{-3}$
6	$1.65{\times}10^{-4}$	$7.70{\times}10^{-8}$	$1.65{\times}10^{-2}$
7	$1.65{\times}10^{-3}$	$7.70{\times}10^{-7}$	$1.65{\times}10^{-1}$
8	$1.65{\times}10^{-2}$	$7.70{\times}10^{-6}$	1.65
9	$1.65{\times}10^{-1}$	$7.70{\times}10^{-5}$	16.5

Table 8.5: Based on ISO size spectrum and SNO "high activity" deposition rate, the mass and activity deposition rates are calculated assuming 1 Bq.g^{-1} of specific activity for rock dust. The third column shows the airborne activity. This table can be scaled to the appropriate specific activity, exposure time, and surface area for the various construction phases.
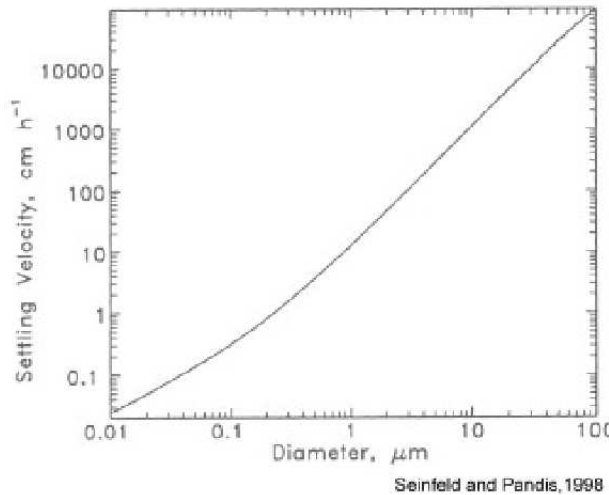
Figure 8.6: The expected settling velocity versus particle diameter from Seinfeld and Pandis. For 1 μm diameter particles, the settling velocity is 4.17×10^{-5} m.s^{-1}. This is consistent with our calculations.

dust particles "fall" in the fluid (air) only because of gravity, then a settling velocity is reached when an equilibrium is reached between gravity and Stokes' friction. The settling velocity is:

$$\omega = \frac{2\left(\rho_d - \rho_f\right)gR^2}{9\mu} \tag{8.4}$$

ω being the settling velocity, ρ_d and ρ_f being respectively the density of the dust and of the air, R being the dust particle radius and μ the dynamic viscosity of the fluid[1]. For 1 μm diameter particles and using our hypothesis, we determine the settling velocity to be $\omega = 8.37 \times 10^{-5}$ m.s^{-1} from equation [8.4]. This is consistent with the literature [65], as one can see in figure 8.6.

Dust deposition happens on a surface of 22.47 m^2 (two Gamma Catcher lids and one Target lid). Three detector elements have to be taken into account: obviously the Target and the Gamma Catcher, but also the Buffer since some of the dust in it might stick to the Gamma Catcher walls. This leads to a maximum of dust amount allowed of 1.5 g. This is actually a stringent and conservative assumption: first of all, the possibility that all of the Buffer dust will stick on the Gamma Catcher is pretty thin, second of all we could tolerate in that case 2.3 g of dust in the Buffer instead of 0.5 g. Let's assume arbitrarily that continuous deposition of dust in the vessels must lead to a maximum of 0.5 g, which means 1 g of trapped dust are allowed. Then, the maximal deposition per square meter is of 2.22×10^{-2} g.m^{-2}; the maximum flow will be of 5.15×10^{-8} g.m^{-2}.s^{-1}. In order to determine the particle flow, we need the mass of one particle:

$$m_d = V_d \rho_d = 5.23 \times 10^{-19} \cdot 2.80 \times 10^6 \simeq 1.47 \times 10^{-12} \text{ g} \tag{8.5}$$

for 1 μm diameter particles. Hence the particle flow:

$$D = 3.51 \times 10^4 \text{ part.m}^{-2}.\text{s}^{-1} \tag{8.6}$$

---

[1]Air kinematic viscosity: $\nu_{air} = 1.51 \times 10^{-5}$ m².s^{-1}; air density: $\rho_{air} = 1.21 \times 10^3$ g.m^{-3}; air dynamic viscosity: $\mu_{air} = 1.82 \times 10^{-2}$ g.m^{-1}.s^{-1}.

Diameter (µm)	0.1	0.3	0.5	1	5
Mass (g)	$1,47{\times}10^{-15}$	$3,96{\times}10^{-14}$	$1,83{\times}10^{-13}$	$1,47{\times}10^{-12}$	$1,83{\times}10^{-10}$
Max number /m³ (deposition)	$4,20{\times}10^{13}$	$1,73{\times}10^{11}$	$1,34{\times}10^{10}$	$4,20{\times}10^{8}$	$1,34{\times}10^{5}$
Max number /m³ (trapped dust)	$5,04{\times}10^{12}$	$1,87{\times}10^{11}$	$4,03{\times}10^{10}$	$5,04{\times}10^{9}$	$4,03{\times}10^{7}$

Table 8.6: Maximum number of particles allowed per m³ for 0.1, 0.3, 0.5, 1 and 5 μm diameter particles. The two possibilities (dust trapped in the vessels or deposited on the vessels during integration) are considered. These numbers allow us to determine the ISO level for each integration phase.

If we now take into account the settling velocity, we have a maximal number of particles per cubic meter:

$$N_d = 4.20 \times 10^8 \text{ part.m}^{-3} \tag{8.7}$$

The maximum amount of trapped dust is 1 g, that is to say $6.82{\times}10^{11}$ particles. We are considering three detector elements (Target, Gamma Catcher and Buffer), which represent 135.5 m³. Hence, the maximal number of particles per cubic meter is:

$$N_e = 5.04 \times 10^9 \text{ part.m}^{-3} \tag{8.8}$$

The limiting factor is then the continuous dust deposition during the integration. We have to have less than 420,000,000 1 μm diameter particles per cubic meter, which corresponds to an ISO class 9.

In order to take into account the limiting factor (continuous dust deposition during the integration), we have to choose the corresponding ISO class. Concerning 1 μm diameter particles, this would be ISO class 9 ($<$ 8,320,000 particles per cubic meter), as shown in table 8.4. We then have to do this calculation (from equation [8.4] to [8.8]) for different particle sizes; this is presented in table 8.6.

The most limiting size particle is 5 μm diameter, which gives us an ISO class 8. We decide to take one extra ISO class as a safety margin because of human activity, so the whole lab has to be in an ISO class 7 state. One can object that some dust might stick on the acrylic walls because of the electrostatic effect. I then did the same calculation but this time taking into account the three lids already considered and the outer wall of the Target, the inside and the outside of the Gamma Catcher walls, but giving this surface a factor ¹/₂ because electrostatic sticking will be less "efficient" than when standing still on an horizontal surface. Let's consider 5 μm particles; we get a maximal number of particles of 44,500 per cubic meter (with no safety margin). This still corresponds to an ISO class 8.

We already have some results concerning the population of dust particles at the far lab. This tends to prove that Stokes' law is used correctly. Indeed, if we simulate intense activity around a particle counter, calculate the settling time and combine it to the settling velocity, we find that the highest point reached by 1 μm diameter particles was 0.94 m above the ground. This has the right order of magnitude.

ISO class	Deposition rate $(\mathrm{Bq.m^{-2}.day^{-1}})$	Activity density $(\mathrm{Bq.m^{-3}})$
1	10^{-8}	8.18×10^{-13}
2	10^{-7}	8.22×10^{-12}
3	10^{-6}	8.14×10^{-11}
4	10^{-5}	8.18×10^{-10}
5	9.71×10^{-5}	8.00×10^{-9}
6	9.81×10^{-4}	8.06×10^{-8}
7	9.81×10^{-3}	8.06×10^{-7}
8	9.81×10^{-2}	8.06×10^{-6}
9	9.81×10^{-1}	8.06×10^{-5}

Table 8.7: Deposition rate and activity density based on Stokes' law analysis and the ISO class clean room standards. The computation has been made for a dust specific activity of 1 Bq.g^{-1}

A similar analysis as the one performed with SNO data (table 8.5) leads to the calculation of the suspended mass, activity, and deposition rate based on a Stokes analysis. This is given in table 8.7.

8.1.4.3 Conclusion

The mass deposition rates from SNO "high activity" are about a factor 20 higher than for the Stokes-based analysis. This is actually within a factor of two of the SNO "low activity" data. Thus, both approaches are consistent, and results will depend on assumptions such as "high" versus "low" activity, exposed area, and exposure times. The ISO levels that were set in the cleanliness plan were ISO 8 for the Inner Veto PMTs and the Buffer integration, ISO 7 for the Buffer PMTs and ISO 6 for the acrylic vessels, the Gamma Catcher and the Target.

8.1.5 Personal contribution to the cleanliness working group

As part of the cleanliness group, I was responsible for the acrylics vessels integration and also one of the deputies of the committee. As deputy, one of my duties was to determine the cleanliness level required for the different phases of integration, as done in sub-section 8.1.4.2, as well as keep supplies available and help with technical difficulties (clean tent...). I also did some shifts on site to get the laboratory to the appropriate cleanliness level for the Inner Veto PMTs (two weeks) and Buffer PMTS (two weeks) integration, and also of course for the acrylic vessels, during manufacturing and integration, to monitor and keep the required cleanliness level, during four months.

Moreover, as deputy, I have been responsible for the particle counter data. Indeed, even though each cleanliness representative is responsible to ensure the cleanliness level required during the considered integration phase thanks to the particle counter, I collect the data and make a global log, for post-integration analysis. Plots of airborne dust concentration for the different integration phases are shown in the next section.
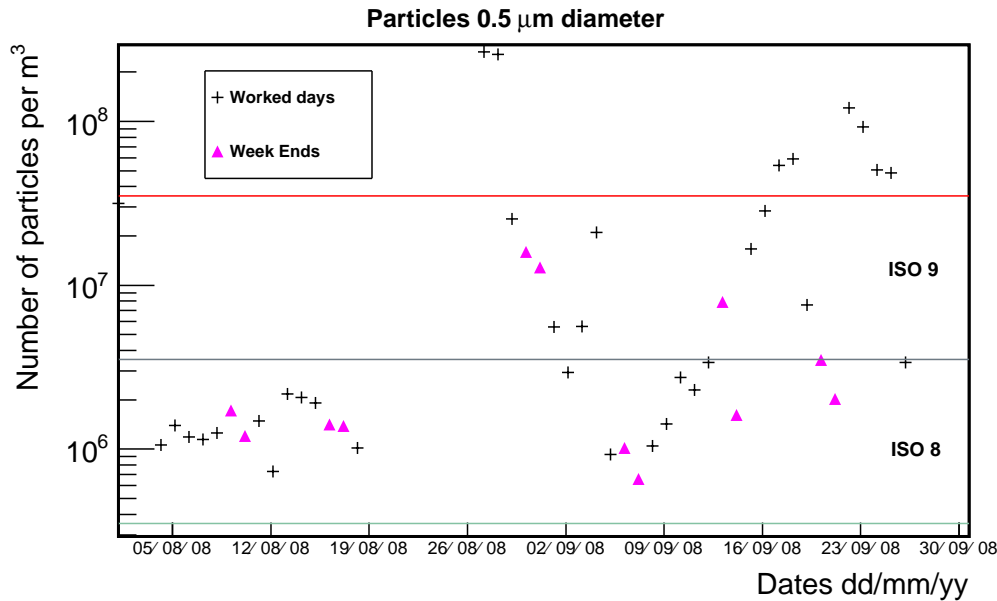
Figure 8.7: Shielding integration phase, August and September 2008, 0.5 μm diameter particles. At best an ISO 8 cleanliness level was reached, even though no cleanliness goal was set. No noticeable difference can be seen between the worked days and the week ends.

8.1.6   Integration from the cleanliness point of view

To determine cleanliness during integration, the particle counter described in section 8.1.2.3 was used. The particle counter was used during all integration phases, taking 10 minutes run every 20 minutes. This leads to 72 runs (i.e. 72 measurements per particle size) per day.

During Shielding and Inner Veto vessel integration, no cleanliness goals were set. Prior to the installation of the Inner Veto PMTs, an initial clean up of the laboratory was performed. After washing, the laboratory floor was painted in order to cover concrete and stick as most of the remaining dust to the ground. The interior of the Veto tank was sandblasted, vacuumed and painted. Even though no cleanliness goal were set, at best an ISO 8 class was reached during Shielding integration, as shown in figure 8.7, and a decrease of the cleanliness level was observed throughout the Inner Veto vessel integration phase (see figure 8.8). The cleanliness work really began with the Inner Veto PMTs installation. A thorough cleaning of the laboratory was performed, as well as of the necessary tooling (scaffolding, etc.). The cleanliness level of the laboratory was at ISO 9 level, thanks to the vinyl sheets at the entrance of the laboratory to protect it from the dust and dirt coming from the tunnel. The aimed cleanliness level (ISO 8, see figure 8.9) in the working area was reached thanks to a clean tent, set up on top of the pit, and the additional ISO 4 High Efficiency Particulate air (HEPA) filter[2] fanjet inside it. The PMTs were brought to the laboratory pre-cleaned and bagged, first to a preparation area, then to the pit to be mounted on the Inner Veto vessel. A sketch of the laboratory during the Inner Veto PMTs integration is shown in figure 8.10.

---

[2]An HEPA filter is a type of high efficiency air filter, composed of a mat of randomly arranged fibers. The fibers are typically composed of fiberglass and possess diameters between 0.5 and 2 micrometers. Key factors affecting function are fiber diameter, filter thickness and air velocity.
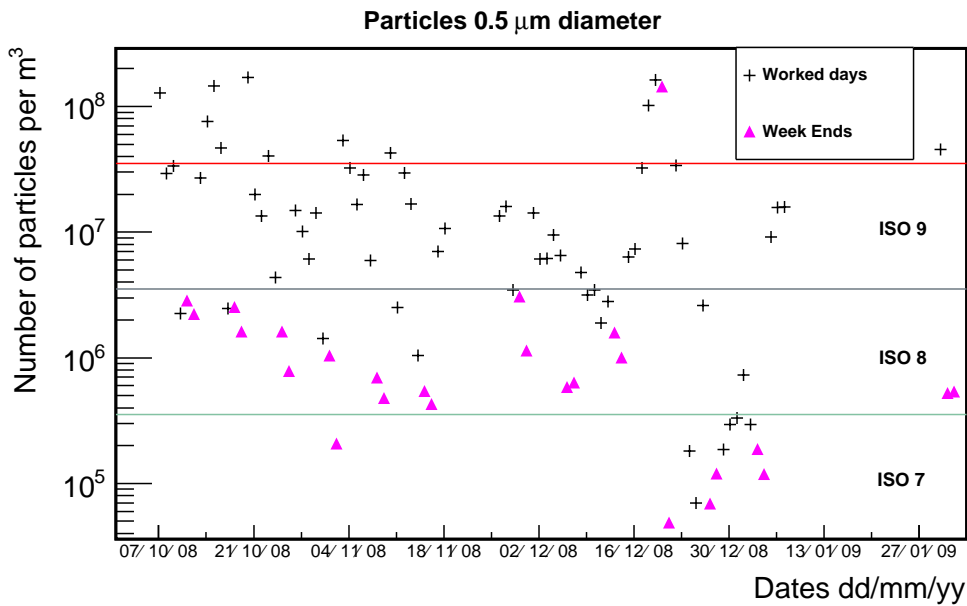
Figure 8.8: Inner Veto integration phase, October 2008 to January 2009, 0.5 μm diameter particles. At best an ISO 7 cleanliness level was reached. The cleanliness level was lowest on the week ends; indeed, since there was no activity, airborne dust could settle on the ground, lowering the number of particles per cubic meter in the air. On worked days, people's activity dirtied the laboratory and raised dust from the floor.
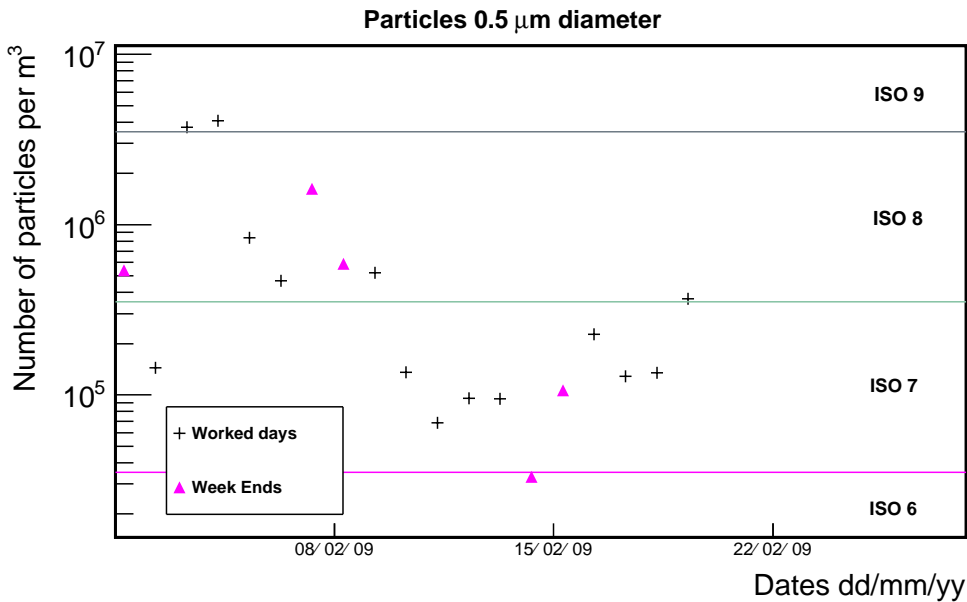
Figure 8.9: Inner Veto PMTs integration phase, February 2009, 0.5 μm diameter particles. The cleanliness goal was an ISO 8 level, which was reached and overcome as soon as the clean tent was set up, around February, 10th. To improve the cleanliness pit level, not only did we use a clean room on top of the pit, but also all the tools and PMTs used during integration were cleaned before entering the pit area.

Neutrino Laboratory – ISO 9

Clean Tent – ISO 8

Entrance of the lab
Vynil sheets

Fanjet
ISO 4

Air Lock

Tunnel

PIT
PMTs integration

ISO 8

PMTs Preparation
and Testing

Figure 8.10: Neutrino laboratory during the Inner Veto PMTs integration. The means to reach the desired cleanliness goals are represented in red. Vinyl sheets at the entrance of the laboratory to protect it against dust coming from the tunnel helped to lower the cleanliness level of the laboratory to ISO 9. The additional ISO 4 fanjet (HEPA filter) inside the clean tent helped to go down to ISO 8, this being the integration goal. The PMTs were brought to the preparation area through an air lock in the laboratory, to be then mounted on the Inner Veto vessel in the pit, inside the clean tent.

During the Buffer tank integration, the laboratory had to be wide open for some time to allow Buffer pieces to enter the laboratory. The pit was always covered thanks to the Veto lid as the pieces were brought across it. These pieces were then pickled, passivated and cleaned with isopropanol before being welded to each other. The Buffer tank was divided into three "layers", three rings that were lowered in the pit and welded to each other one after the other. Veto PMTs were protected throughout the whole integration phase thanks to a ring of plastic attached to one of the Buffer layers on one side, and to the edge of the pit on the other side. Thus, no welding residue could dirty the pit and therefore the Inner Veto. Cleanliness during this phase was not such an issue since Veto PMTs were protected and a thorough cleaning after Buffer integration was scheduled to prepare the laboratory and pit for the Buffer PMTs integration. Therefore, this time was used to send the particle counter for its yearly calibration, and then to measure the cleanliness level at acrylic vessels integration site, as discussed in section 8.2.1.3. Keeping in mind the preparation of the working area for the Buffer PMTs integration, an adjustable wall was installed right in front of the pit, the front pit wall. This wall separated the entrance of the laboratory from the back and the integration area, the pit. Basically, it set in the laboratory a clean room environment around the pit, and a semi-clean environment that would be a Buffer between the outside world, the tunnel, and the clean working area. Also, ISO 5 ventilation was installed in the laboratory.

The Buffer PMTs integration phase cleanliness goal to reach was ISO 7. As one can see on figure 8.11, an air lock was installed at the end of the tunnel, right before the laboratory entrance. This air lock had a double purpose: first to act as a Buffer between the dirt of the tunnel and the laboratory, second as cleaning area for the PMTs boxes coming from the storage area outside the tunnel. In addition, " sheets were hung at the entrance of the tunnel, and the front pit wall was in place. The semi-clean area, at the beginning of the laboratory was kept at an ISO 9 level, which corresponds to a typical urban environment. In the clean area, one could find the air outlet of the ISO 5 ventilation and an ISO 4 HEPA filter fanjet. These two devices lowered the cleanliness level down to ISO 8. Finally, a clean tent was set up above the pit with a second ISO 4 fanjet, reducing once more the ISO level down to ISO 7, which was the integration goal, as shown in figure 8.12. As for the Inner Veto, PMTs were pre-cleaned and bagged before being brought to the laboratory. They transited through the airlock for cleaning of the outer bag, then a preparation area in the semi-clean area, before being cleaned again in the clean area and being installed on the Buffer vessel walls and bottom. Before the next integration phase, the pit was covered by the Buffer and Inner Veto lids and the clean tent was removed, since Target and Gamma Catcher were transported fully assembled to the laboratory and therefore neither one of them would have fit in a clean tent. The acrylic vessels integration is described in the next section.

After the acrylic vessels integration, Buffer PMTs were installed underneath the Buffer lid, which was held at the time at the back of the laboratory inside a clean room. Once this operation was completed, the Buffer lid was installed in the pit, closing then the inner detector. Inner Veto PMTs were then integrated on the top of the Buffer lid. As one can see on figure 8.13, these operations happened in an ISO 6 environment. The Inner Veto lid could then be put on the corresponding vessel. The final closing of the Inner Veto happened in May 2010, in order to keep access to the detector. This is when the electronics installation started, as well as the filling system installation in the laboratory. The goal was to keep an ISO 6 environment in the clean area of the laboratory, since the access to both Target and Gamma Catcher was
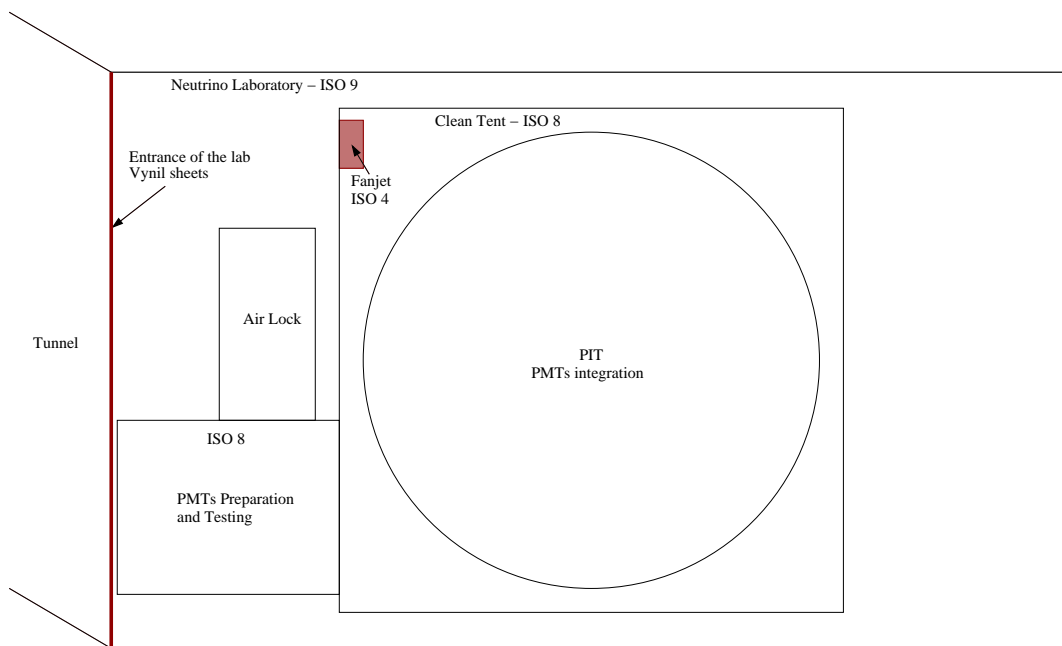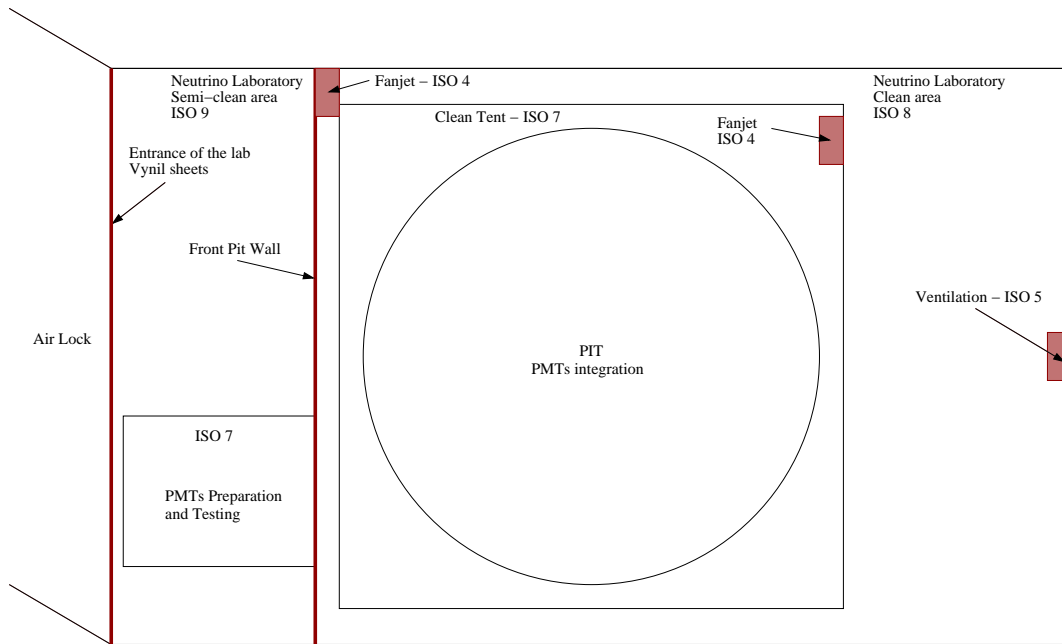
Figure 8.11: Neutrino laboratory during the Buffer PMTs integration. The means to reach the desired cleanliness goals are represented in red. An air lock was installed at the end of the tunnel, right before the laboratory, to shield it from outside pollution. Vinyl sheets at the entrance of the laboratory are an additional protection against such pollution. The neutrino laboratory was separated in two areas thanks to the front pit wall, an adjustable wall in front of the pit. The semi-clean area, between the vinyl sheets and the front pit wall, was kept at an ISO 9 level. The clean area (after the front pit wall), was lowered to an ISO 8 level, thanks to the ISO 5 ventilation and an ISO 4 fanjet (HEPA filter). A clean tent was mounted above the pit with an additional ISO 4 fanjet, the working areas were then an ISO 7 environment, this being the integration goal.
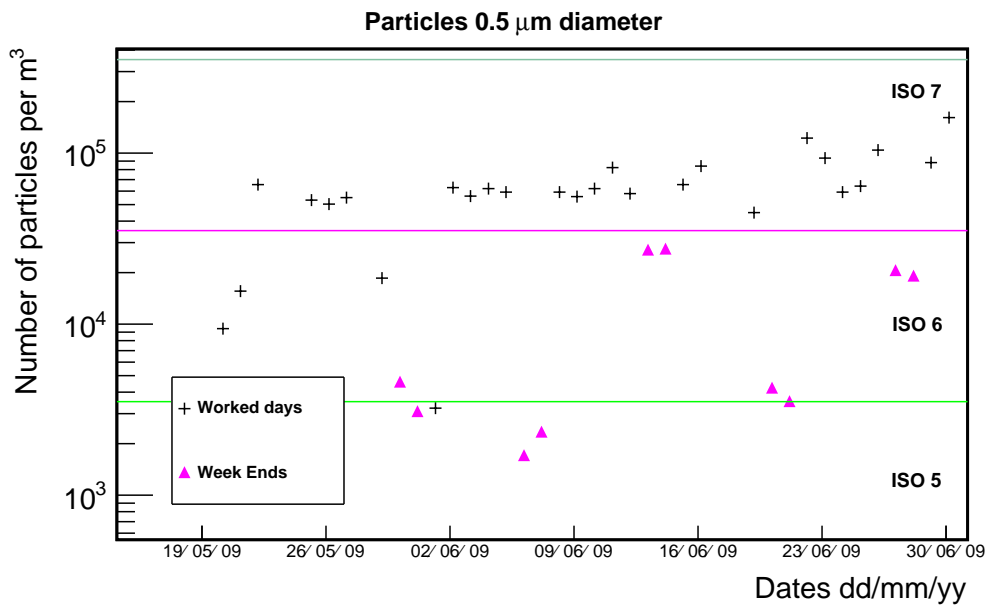
Figure 8.12: Buffer PMTs integration phase, Mid-May to June 2009, 0.5 μm diameter particles. The cleanliness goal of ISO 7 was reached throughout the whole integration thanks to the use of a clean tent and ISO 5 HEPA filters fan jets. On the week ends, the level went down to ISO 6, even ISO 5.
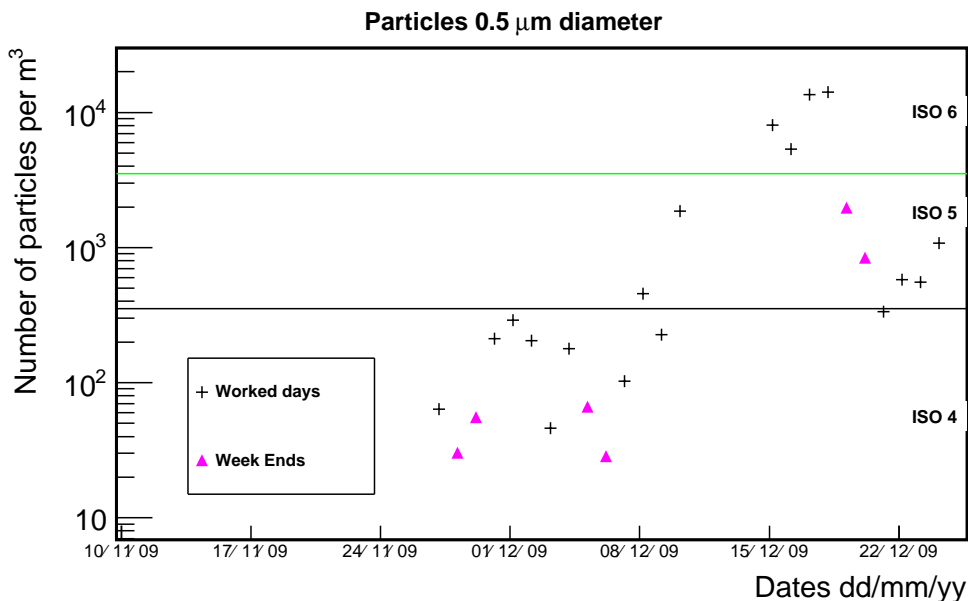
Figure 8.13: Detector closing, November and December 2009, 0.5 μm diameter particles. During this phase, Buffer PMTs were installed underneath the Buffer lid, then the Buffer was hermetically closed. Afterwards, Inner Veto PMTs were installed under the Inner Veto lid, then this lid was put on top of the detector. This happened in an ISO 6 environment. The final closing of the Inner Veto happened in May 2010.
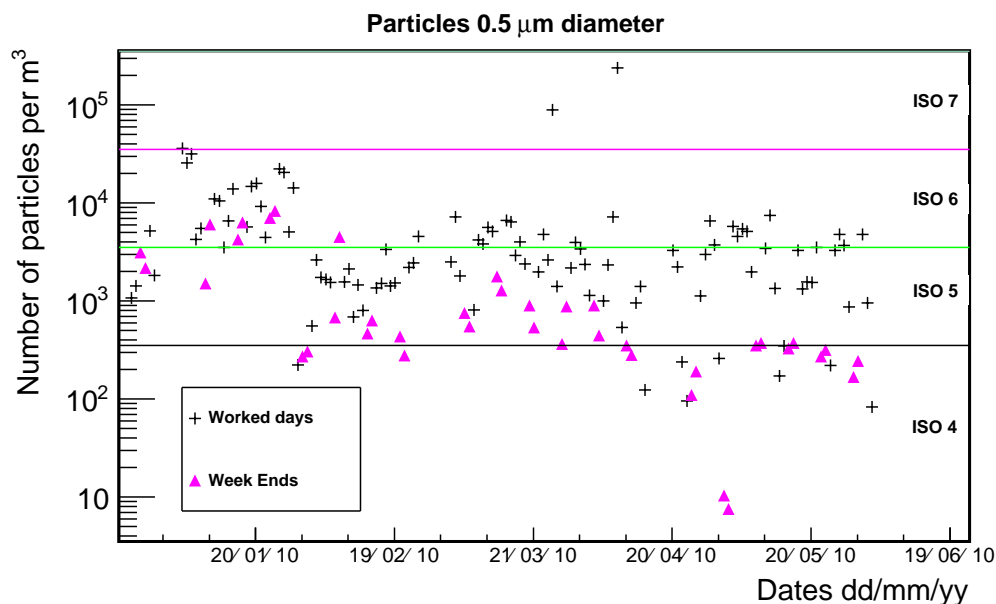
Figure 8.14: Laboratory cleanliness level, from January 2010 to beginning of June 2010, 0.5 μm diameter particles. The goal was to keep an ISO 6 level, since access to the acrylic vessels was opened through the chimneys. The goal was overall reached, though some peaks to an ISO 7 level were reached due to heavy mechanical work in the laboratory.

open through the chimneys; indeed, at the time the detector was flushed with nitrogen in order to prepare for the liquid scintillator filling. Overall, the goal was reached, though some specific actions raised the ISO level up to 7, even 8, on small time periods (see figure 8.14).

8.2   Cleanliness and the acrylic vessels

8.2.1   Cleanliness during construction and production

8.2.1.1   Cleaning protocol

In order to determine which is the better way to clean the acrylic vessels, three cleaning solutions have been tested: mild soap with deionized (DI) water, and two cleaning solutions called Alconox and Liquinox. Alconox is an anionic detergent. It cleans contaminants from glassware, metals, plastic, ceramic, porcelain, rubber and fiberglass. It can replace corrosive acids, which are not to be used with acrylic. It is available as a powder which has to be diluted at 1:100 and its pH is 9.5. Liquinox is an anionic detergent which is extremely mild and completely soluble in soft and hard water. It is a liquid detergent which has to be diluted at 1:100 also, and has a pH of 8.5. These three possible cleaners have to be used with water and rinsed afterwards, which means they will not be used to clean the inside of the Target. Indeed, if some water were absorbed in the acrylics and then released in the Target liquid, then it might destabilize the Gd complex and deteriorate the liquid properties. Anyway, we could use the cleaning solutions on

	Earth			Grease		
	Liquinox	Alconox	Soap	Liquinox	Alconox	Soap
Preparation	Easy to dilute	The powder does not dissolve easily	No problem	Easy to dilute	The powder does not dissolve easily	No problem
pH	6 - 7	9	5	6 - 7	9	5
Dirt mass	0,04 g	0,42 g	0,55 g	0,20 g	0,19 g	0,29 g
% of dirt mass removed	25 %	100 %	71 %	60 %	100 %	42 %
Rinsing	No problem	Hard to rinse; risk to leave some product	No problem	No problem	Hard to rinse; risk to leave some product	No problem

Table 8.8: Analysis for the different acrylic pieces

the outside of the Target and for the Gamma Catcher, but the vessels would have to be dried (nitrogen flux) afterwards.

In order to test and compare the cleaning options, several parameters have been considered: the ease of preparation, the percentage of dirt that has been removed. Two different kinds of dirt have been used, that might enter in contact with the acrylics: soil and mechanical grease. The corrosive action of the cleaners: a blank sample was exposed to check if the cleaners might affect the acrylics. Also, two different types of samples were used: a simple piece of acrylic, and a gluing of two pieces of acrylic. Then, the effect of the cleaning solutions was checked on every piece of acrylic that would be in contact with them.

The same protocol was followed for every sample. First, samples were dirtied with soil or grease, then immersed in the cleaning solution. Afterwards, samples were scrubbed with a sponge and rinsed with DI water. Table 8.8 shows the analysis for the different acrylic pieces. In conclusion, Alconox is the more efficient by far, but it presents some flaws, such as difficulty dissolving the powder, which might be a big issue if we consider the huge amount of solution we need. Also, it is really hard to rinse, which would have been a problem considering the shape of the cylinder and the chimney: some spots would have been really hard to get, and we do not really know the effect of the solution on the liquids. Liquinox seems to be reasonable on grease and terrible on earth, but that might just be because so little earth was put on the sample. Finally, soap is more efficient on earth than on grease; it seems to be more efficient overall than Liquinox if we only consider percentages. Table 8.9 gives the analysis for the different acrylic pieces. The results for Liquinox are better than before, which seems to confirm the fact that the previous results were biased. Still, it has less good results than Alconox. In both cases, traces of grease were left on the gluing, they did not seem possible to remove even after thorough scrubbing. The samples were examined using a UV lamp and a microscope, to search for possible deterioration due to the cleaning agents. None were found. To conclude, Alconox is the cleaning solution giving the best results. However, it is not user-friendly: the powder is hard to dissolve, which will be a real problem when used in huge quantities, and the final liquid is hard to rinse, leaving a film of soapy water on the acrylics. I would then recommend to use Liquinox instead, which gives better results than just mild soap with DI water.

	Earth		Grease	
	Liquinox	Alconox	Liquinox	Alconox
Preparation	Easy to dilute	The powder does not dissolve easily	Easy to dilute	The powder does not dissolve easily
pH	6 - 7	9	6 - 7	9
Dirt mass	0,56 g	0,40 g	0,21 g	0,26 g
% of dirt mass removed	100 %	100 %	95 %	100 %
Rinsing	No problem	Hard to rinse; risk to leave some product	No problem	Hard to rinse; risk to leave some product

Table 8.9: Analysis for the glued pieces

Afterwards, in order to be sure not to contaminate the acrylic vessels with their cleaning products, we checked the Liquinox radiopurity thanks to a Germanium counter. The measurement lasted for five days, in order to have good statistics. The results, shown in figure 8.15, are that the Liquinox has some contamination in ^{238}U (between 0.1 and 0.2 Bq/kg), and a large contamination in ^{40}K: 23.5 ± 0.1 Bq.kg^{-1}. Acrylic being hydrophilic, Liquinox dissolved in water might be absorbed by PMMA. Thus, once the filling phase is complete, ^{40}K might be released in the liquid scintillators and generate background events in the Target and Gamma Catcher. So, in order not to contaminate the vessels, the decision was made not to use Liquinox on the vessels. The cleaning protocol was re-thought: no cleaning products were to be used. Therefore, the vessels were cleaned first with a deionizing air gun, to neutralize electrostatic charges on and at the same time to clean them from dirtiness and dust. Then, the vessels were cleaned with deionized water and clean room compatible rags (see section 8.2.1.3).

8.2.1.2   Degussa

The production of the acrylic material was realized in a clean room. The polimerization itself happens in a room saled during the process. The monomer syrup is poured between two clean glass sheets and heated to polymerize. The acrylic plate is then transported in an ISO 4 clean room, where the blue protecting film is applied. The acrylic plate is then ready to leav the clean environment.

8.2.1.3   Néotec

The Gamma Catcher parts were thermoformed at the Néotec factory, in Bussang (France), our manufacturer. These parts were then shipped to the Chooz site, where the Gamma Catcher was assembled without its lid at "la déminée"[3] on the power plant site (figure 8.16). It was transported to the neutrino laboratory and cleaned on site, thanks to a duster removing static

---

[3]"La déminée" is a hall lent to us by EDF so that we could assemble Gamma Catcher parts. A clean tent was set up there in order to perform the gluing in a clean environment.
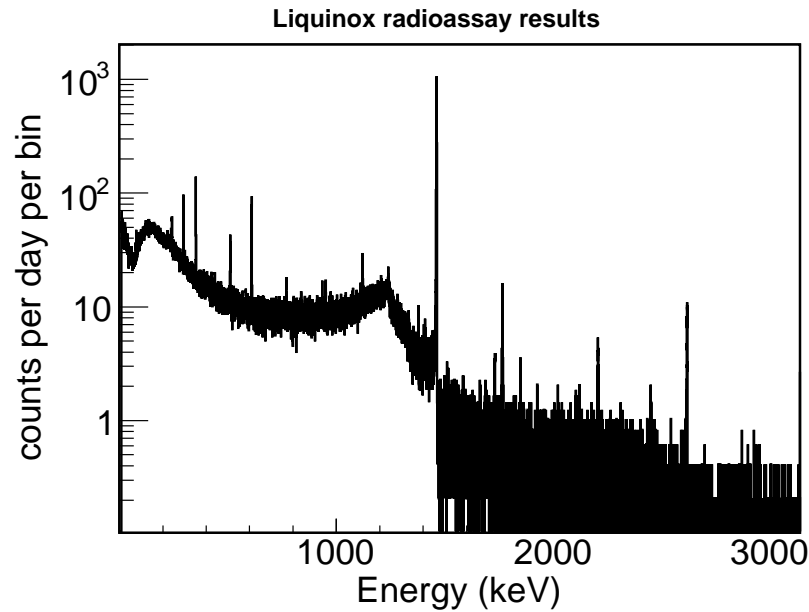
Figure 8.15: Liquinox radioassay results. The peak at 1460 keV is due to the contamination in Potassium. The concentration of ^{40}K is of 23.5 ± 0.1 Bq/kg. Therefore, we decided not to use Liquinox to clean the acrylic vessels, in order not to contaminate them.

electricity first to remove the biggest grain dust and avoid scratches during a more thorough cleaning. The inside and outside of the vessel were cleaned thanks to deionized water and ISO 4 compatible rags.

Targets cleaning was carried out at Néotec before final gluing in an ISO 7 clean room, as shown in figures 8.17 and 8.18. The inside of the vessels was first cleaned thanks to a deionizing gun in order to suppress static electricity from the acrylic material and to remove the biggest dust grains that might scratch the material during dusting. Afterwards a second cleaning was performed with ISO 4 compatible rags and deionized water. Drying was performed thanks to the deionizing gun. The outside of the vessels was cleaned thanks to the deionizing gun and ISO 4 compatible rags and deionized water. The Targets were assembled in an ISO 7 clean room (cf. figure 8.19) and the hole left for the chimney covered with a hair cover, hermetic enough to protect the inside of the vessel from dust but letting air through to avoid any pressure differences between the outside and the inside of the vessel. The outside was cleaned again before integration, since the vessels were stored outside of a clean room before bagging and moving.

8.2.2   Cleanliness during integration

From the opening of the pit to the end of the Gamma Catcher integration, the neutrino laboratory reached an ISO 6 cleanliness level during the day (people working in the laboratory), ISO 5 at night. The ISO 6 goal was reached during integration. During this time, the laboratory was vacuumed two or three times a day, and cleaned with deionized water (floor and walls) once before Gamma Catcher integration, once before Target integration. The pit was covered by

Néotec factory – No ISO class

Clean Room – ISO 7–6

Air Lock

Fanjet – ISO 4

Gamma Catcher Parts

Cleaning
Gluings(lid and bottom)

Gamma Catcher parts

Thermoforming
ofGamma Catcher parts
(lid parts,
cylinder parts)

Gamma Catcher Parts

Bagging and storage

Transportation Chooz
Choc detectors

Chooz

Déminée

Clean Room – ISO 7–6

Fanjet – ISO 4

Gamma Catcher

Gamma Catcher

Gamma Cacther parts
Reception

Gluings

Gamma Catcher

Gamma Catcher vessel rotation
Bagging

Transportation to
Neutrino Laboratory
Gamma Catcher cylinde
and bottom; lid parts

Choc detectors

Neutrino Laboratory
Semi–clean area
ISO 8

Fanjet – ISO 4

Neutrino Laboratory
Clean area
ISO 6

Fanjet
ISO 4

Entrance of the lab
Vynil sheets

Front Pit Wall

PIT

Integration
Lid gluing

Ventilation
ISO 5

Gamma Catcher

Gamma Catcher

Tunnel

Gamma Catcher

Gamma Catcher Parts
Reception

Final cleaning
Lid parts gluing

Fanjet
ISO 4

Figure 8.16: Gamma Catcher construction and integration. Gamma Catcher parts were thermoformed at Néotec, in addition the bottom and two half lids were glued in an ISO 7-6 clean room. The Gamma Catcher parts, bottom and half lids were then bagged and stored before being sent to the Chooz power plant, at 'La Déminée' (storage area lent by EDF). An ISO 7-6 clean tent was set there to glue vessel parts together and to the bottom. The Gamma Catcher without its lid was then sent to the neutrino laboratory to be integrated in an ISO 6 environment. After Target integration, Gamma Catcher lid parts were brought to the neutrino laboratory. The Gamma Catcher was glued and installed in an ISO 6 environment.

Néotec factory – No ISO class

Clean Room – ISO 7–6

Air Lock

Fanjet – ISO 4

Target 1,2,3

Internal cleaning
Gluings

Target 1,2,3

Thermoforming
of target parts
(lid parts,
cylinder parts)

Target 1,2,3

Bagging and storage
Helium leak test

Transportation to Chooz
Targets bagged
Choc detectors

Neutrino Laboratory
Semi–clean area
ISO 8

Fanjet – ISO 4

Neutrino Laboratory
Clean area
ISO 6

Fanjet
ISO 4

Entrance of the lab
Vynil sheets

PIT

Integration

Ventilation
ISO 5

Front Pit Wall

Tunnel

Target

Target

Target

Target Reception
Debagging

Final external cleaning

Fanjet
ISO 4

Figure 8.17: Targets 1, 2 and 3 construction and integration. Targets construction was performed at the Néotec factory. Targets parts were thermoformed before being cleaned and glued inside an ISO 7-6 clean room. In this clean room was also performed the internal cleaning and sealing of the chimney hole. Targets were then taken out of the clean room to be bagged and stored. A Helium leak test was performed (see section 10.1.3). Prior to integration, the bagged Target designed for the far laboratory was transported to Chooz. A final external cleaning was performed in the clean area (ISO 6 level) of the laboratory, before integration into the pit.
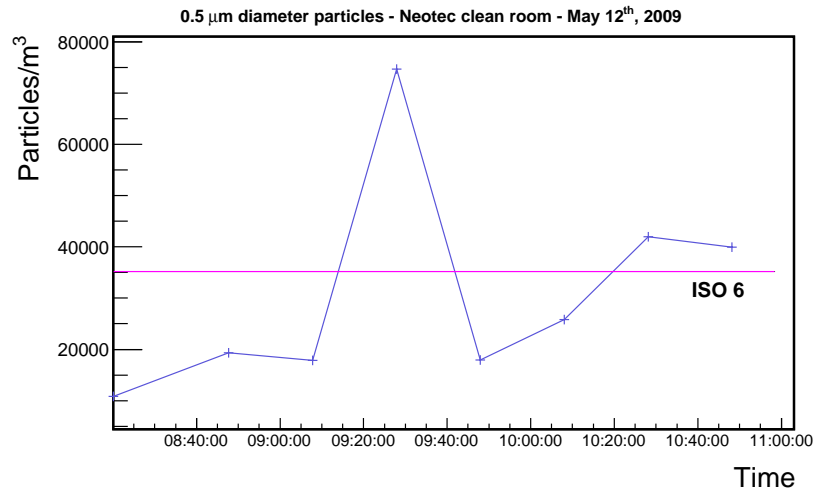
Figure 8.18: Cleanliness conditions during one of the Targets cleaning, performed on May, 12th 2009. This is representative of the other two cleanings. The requirement was to perform the cleaning in an ISO 7 clean room, which from the figure was reached. The peak around 9:30 was due to intensive cleaning next to the particle counter. Most of the dust inside the tent was acrylic dust, coming from cutting and polishing of the pieces.This dust therefore had the same radioactivity contamination as the material itself and is no threat to the experiment.
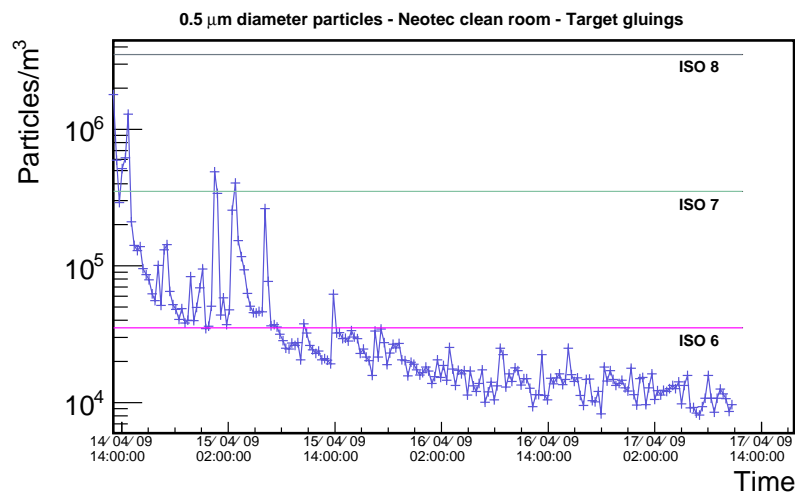
Figure 8.19: Cleanliness conditions in the Néotec clean room during Target gluons. One can identify two anomalies: the first one when the pieces enter the clean room, the second one for short and repeated opening of unknown reasons. Apart from these anomalies, gluings were done in an ISO 7, which was the requirement, sometimes ISO 6 environment.
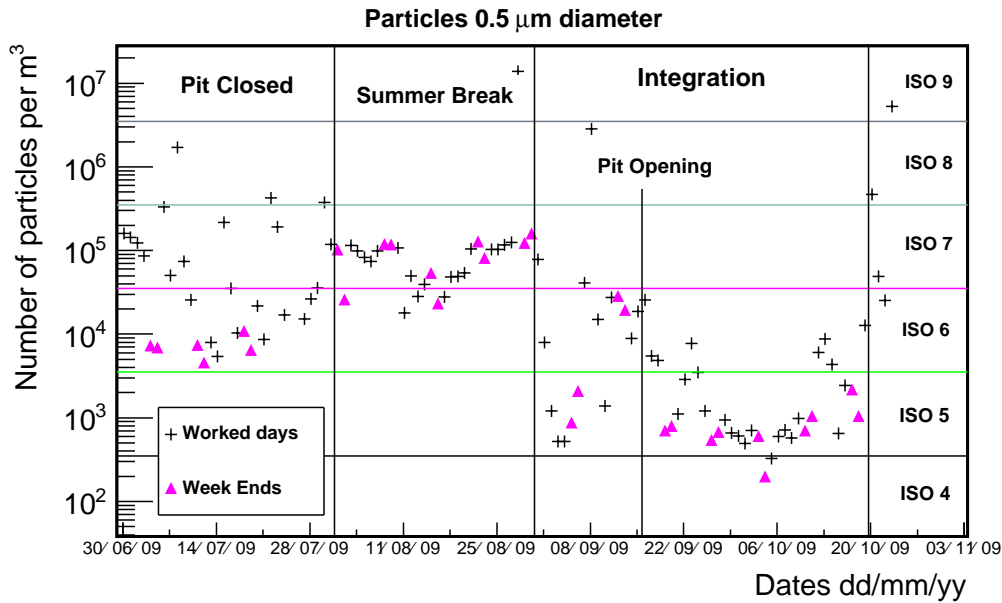
Figure 8.20: Target and Gamma Catcher integration phase, July 2009 to October 2009, 0.5 μm diameter particles. On July, the pit was closed while the vessels were brought to the laboratory. After the August break, once an ISO 6 level was reached, the pit was opened so that the Gamma Catcher (ISO 6 level) and Target (ISO 5 level) integration could happen. Afterwards, the pit was closed and the cleanliness level went up again, at the end of October.

Buffer and veto lids after Gamma Catcher integration, to protect the inner detector from dust contamination and to allow heavy transportation in the laboratory. The lids were removed only when ISO 6 level was reached, and this level was kept throughout the whole Target integration. The cleanliness levels are shown in figure 8.20.

8.2.2.1   Temperature and humidity monitoring

During the acrylic vessels integration several gluing needed to be done, such as the Gamma Catcher lid gluing. Good conditions for gluing acrylic are 20 °C and 40 % relative humidity, when the nominal conditions in the laboratory where 100 % relative humidity and 14 °C. One can note that during the summer break, on figure 8.21, we were at these nominal conditions. In order to reduce the relative humidity and increase the temperature, several devices were set once we returned to the laboratory, described in section 10.2. Temperature and humidity were monitored during integration. We reached about 21 °C and 60 % relative humidity during the integration phase; these conditions were sufficient to glu.

8.2.2.2   Special cleanliness rules for the acrylic vessels integration

In order to improve as much as possible the cleanliness level, it was important to limit the number of people in the laboratory to the strict minimum. Every cleaning session in the laboratory had to be performed with deionized water only. Alcohol was totally prohibited from
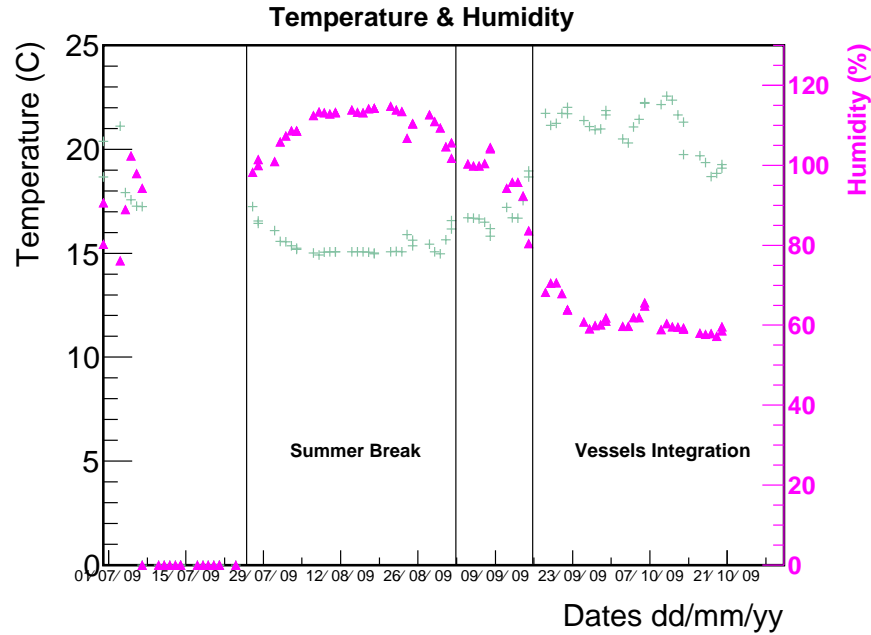
Figure 8.21: Temperature and relative humidity in the far laboratory during Target and Gamma Catcher integration. During teh summer break, nominal conditions were restored (100 % relative humidity and 14 °C). We managed to reach 21 °C and 60 % relative humidity during integration, which was sufficient to perform gluing.

the laboratory since it might alter the acrylic material. Every cleaning session requiring alcohol would have to be done outside of the laboratory and the pieces would only be authorized to enter the laboratory after a complete evaporation of alcohol.

8.3   Conclusion

Throughout the whole detector integration, the cleanliness imrpoved as we got closer to the detector core. The various cleanliness goals (from Inner Veto PMTs to Target vessel integration) were reached. After the Target vessel integration and Gamma Catcher lid gluing, even though the constraints were softer, cleanliness stayed at a high ISO level (ISO 6 most of the time). This ensured that dust could not contaminate the acrylic vessels through the filling system. Monitoring of the laboratory is still ongoing.

Chapter 9

Near and Far Targets similitude

In Reactor neutrino experiments, systematics can be divided in three categories: reactor induced, detector induced and analysis induced. In table 9.1 is shown a comparison systematics between CHOOZ and Double Chooz. As one can see, the great advantage of a near-far detector consideration is that systematic errors in knowledge of antineutrino flux and antineutrino interaction cross-section are absent or greatly reduced, and that detector-related systematics reduce to those due to differences in detectors. Since the Double Chooz reaction of interest is the inverse beta decay, the number of free protons in the Target volume is a key parameter. Indeed, if this number is too different between near and far detector, the comparison of the antineutrino flux will be harder to make.

9.1   Two identical Targets

The success of the Double Chooz experiment relies on the ability to construct two identical detectors in order to reduce as much as possible systematic errors, which limit the sensitivity to θ_{13}. In this context, the number of target protons, i.e. the detectors normalization, is a key parameter. The goal of the Double Chooz collaboration is to reach a total systematic error of 0.6 %. To reach this level, the number of target protons has to be known within 0.2 % [44]. This systematic is checked thanks to the weighting measurement of the Target liquid scintillator, made during the filling phase. However, the three Targets were thermo-formed around the same wooden mold, and therefore ought to be very close in volume. The idea is then to find the most similar Targets possible, in terms of volume, in order to reach a volume difference as close to 0.2 % as possible.

The number of free protons in the most inner vessel as well as detection efficiencies have to be calibrated precisely between both detectors, but only in relative. Indeed, in Double Chooz, the absolute calibration is not necessary for the measurement of θ_{13}. In CHOOZ, the uncertainty on the number of free protons in the Target came essentially from the knowledge of the chemical composition of the liquid scintillator. However, using two identical detectors with the same liquid cancels the uncertainty on this chemical composition. The systematic uncertainty to reach is 0.2 % on the relative determination of the free proton number between both near and far Targets.

		CHOOZ	Double Chooz (relative)	
Reactor induced	Antineutrino flux	1.9 %	< 0.1 %	Two identical detectors, low background
	Reactor Power	0.7 %	< 0.1 %	
	energy per fission	0.6 %	< 0.1 %	
Detector induced	Solid angle	0.3 %	< 0.1 %	Distance measure at 10 cm
	Target mass	0.3 %	< 0.2 %	Relative mass measurement
	Density	0.3 %	< 0.1 %	Near/Far Temperature control
	Liquid chemical composition	0.8 %	< 0.2 %	Same scintillator batch
	Spatial effects	1.0 %	< 0.1 %	Identical Target geometry and liquid
	Live time	few %	< 0.2 %	Measured with several methods
Analysis	From 7 to 3 cuts	1.5 %	0.2 - 0.3 %	Few cuts
	Total	2.7 %	< 0.6 %	

Table 9.1: Systematics comparison between CHOOZ and Double Chooz. The main systematics in CHOOZ came from the antineutrino flux, the liquid composition knowledge, spatial effects and analysis. Three of these systematics are almost canceled out by having two similar detectors [44].

9.2   Targets construction

9.2.1   Same material and construction methods

Ten tons of material are necessary for three Targets and two Gamma Catcher. Even though the second Gamma Catcher is not built yet, the material was bought anyway, to have as few different batches as possible. Indeed, for these ten tons, only three batches were necessary. The plates were made in such way that the same batch was used for the three Targets, at least as far as the cylinder is concerned (all 8 mm thick sheets come from the same batch). This ensures the same radiopurity for all three Targets on one hand, but also the same number of free protons.

In order to have as similar a Target volume as possible, all three vessels were constructed using the same methods. There are construction tolerances, but also tolerances on the acrylic plates thickness... This is why Targets were constructed on a mold, to ensure the inside of the vessels is identical, since the Target liquid proton number is what need to be controlled.

9.2.2   Target vessels similarity

In order to determine which Targets were the closest in volume, we measured the cylinders before lids and bottoms were glued. One could directly measure the inner diameter of a Target

Heights (mm)	Measurements average
Cylinder 1	2458
Cylinder 2	2455
Cylinder 3	2458

Table 9.2: 2009, April 22nd measurements, heights. All three cylinders could be measured.

Diameters (mm)	D_1: Horizontal	D_2: Vertical	D_3: Diagonal 1	D_4: Diagonal 2
Cylinder 1 - Face A	2317	2281	2305	2313
Cylinder 1 - Face B	2319	2281	2318	2298
Cylinder 2 - Face A	2320	2276	2310	2307
Cylinder 2 - Face B	2320	2264	2289	2330
Cylinder 3 - Face A	2321	2280	2307	2310
Cylinder 3 - Face B	2319	2280	2295	2320

Table 9.3: 2009, April 22nd measurements, diameters. All three cylinders could be measured.

and thus compute the Target liquid volume. However, cylinders alone are very elastic and deformable. They were measured while being horizontal (under their own weight), on supports made of wood; the cylinders stuck to the support form and their exact form is not known. This needs to be investigated.

Two sets of measurements were done on the cylinders, in order to define the inner diameter and height. The first set measured the three cylinders; cylinders 1 and 2 were on their support, horizontally, while cylinder 3 was vertical and therefore harder to measure. Five measurements were made on cylinder 3, the last after the cylinder was put back horizontally on its support. This last one is therefore the most easily comparable to measurements of the others cylinders. The second set of measurements could only characterize cylinders 2 and 3 , since n°1 was in the clean room, getting ready for gluing. It is therefore complicated to use the second set of measurements, since it is not independent of the first one.

Concerning the measurements precision, the height measurement is the easiest to perform and the most reproducible (5 measurements on Target n°3): we could reach the millimeter precision. Is measuring the inside of the Targets the best way to determine the Target liquid scintillator quantity? Measuring the outside of the vessels would be a very precise measurement since, once the vessels are complete, no deformation would happen on the vessels, their forms would be fixed and precisely known. Therefore, we could obtain a millimeter precision on the Target perimeter. However, the wall thickness tolerance is 30 %, i.e. 2.4 mm for a 8 mm thick acrylic wall. Thus, one gets an 0.4 % precision on the liquid volume, once we would like to reach 0.2 % precision.

Three different methods were used to compare the measurements.

Heights (mm)	Measurements average
Cylinder 2	2455
Cylinder 3	2457

Table 9.4: 2009, May 12th measurements, heights. Only cylinders 1 and 2 could be measured.

Diameters (mm)	D_1: Horizontal	D_2: Vertical	D_3: Diagonal 1	D_4: Diagonal 2
Cylinder 2 - Face A	2320	2276	2311	2305
Cylinder 2 - Face B	2328	2267	2292	2330
Cylinder 3 - Face A	2324	2271	2301	2316
Cylinder 3 - Face B	2313	2274	2300	2315

Table 9.5: 2009, May 12th measurements, diameters. Only cylinders 1 and 2 could be measured.

The first one simply is to consider the measurements average, assuming cylinders kept their cylindrical form. For the first measurement set (cf. tables 9.2 and 9.3), we got a diameter of 2,304 mm and a height of 2,458 mm for cylinders 1 and 3. This corresponds to a liquid volume of 10.24 m^3. Cylinder 2 has an average diameter of 2,302 mm and an average height of 2,455 mm; this leads to a volume of 10.21 m^3. This first method conclusion is that Targets 1 and 3 are the ones to use. If we consider, for the same method, that all three cylinders took the form of an ellipse, we get a volume of 10.20 m^3 for cylinder 1, 10.17 m^3 for cylinder 2 and 10.21 m^3 for cylinder 3. Cylinders 1 and 3 still are the closest. If we now consider the second set of measurements, cylinder 2 has a diameter of of 2,303.6 mm and a height of 2,455 mm (volume of 10.23 m^3). Cylinder 3's diameter is 2,301.8 mm, its height is 2,458 mm (volume of 10.22 m^3). If we consider the vessels to be elliptic, than Target 2 has a volume of 10.17 m^3, Target 3 a volume of 10.16 m^3. This confirms the fact that the two cylinders are very close in volume (10 L difference on average). Of course, with this second set of measurements, we cannot tell which Targets to chose, since n°1 could not be measured.

The second method is similar to the first one. It considers every possible couple (diameter, height) in order to compute the corresponding volumes. Thus, for one cylinder, we got 32 estimations. For thee first set of measurements, we have:

- cylinder 1: average volume 10.25 m^3 (minimum 10.04 m^3, maximum 10.38 m^3), standard deviation 0.13 m^3.

- cylinder 2: average volume 10.22 m^3 (minimum 9.88 m^3, maximum 10.47 m^3), standard deviation 0.19 m^3.

- cylinder 3: average volume 10.25 m^3 (minimum 10.03 m^3, maximum 10.40 m^3), standard deviation 0.14 m^3.

This method gives once again Targets 1 and 3 to be the closest.

Finally, since the main errors come from cylinder form and the accuracy of the measurements, the last method is a statistical one determining the most probable form taken by the vessel (cylindrical or elliptic). In this method, we also applied errors on the measurements, depending on their location (diagonal, vertical or horizontal). In the following, D_i are the four diameter measurements, d is the generic diameter of the circles, a the long axis of the ellipses, b the small axis, h the height of the vessel. The angles corresponding to the diameters are $\theta_1 = 0$, $\theta_2 = \pi/2$,

First set of measurement	d (mm)	a (mm)	b (mm)	Circle (χ^2/dof)	Ellipse (χ^2/dof)
Cylinder 1 - face A	2,304.00	2,313.00	2,295.00	1.02	0.89
Cylinder 1 - face B	2,304.00	2,313.50	2,294.50	1.28	1.22
Cylinder 2 - face A	2,303.25	2,314.25	2,292.25	1.41	1.17
Cylinder 2 - face B	2,300.75	2,314.75	2,286.75	3.53	3.77
Cylinder 3 - face A	2,304.50	2,314.75	2,294.25	1.18	0.95
Cylinder 3 - face B	2,303.50	2,313.25	2,293.75	1.48	1.48

Table 9.6: First shape fit (error of $\pm$ 8 mm on diameters) of the vessels with the first set of measurements.

$\theta_3 = \pi/4$, $\theta_4 = 3\pi/4$. A vessel can be fitted to a circle according to:

$$
\begin{aligned}
\chi^2(d) &= \sum_i \left\{ \frac{(D_i \cos\theta_i - d\cos\theta_i)^2}{4\sigma_i^2} + \frac{(D_i \sin\theta_i - d\sin\theta_i)^2}{4\sigma_i^2} \right\} \\
&= \sum_i \frac{(D_i - d)^2}{4\sigma_i^2}
\end{aligned}
\tag{9.1}
$$

By minimizing the χ^2, we find:

$$
d = \frac{\sum_i \frac{D_i}{\sigma_i^2}}{\sum_i \frac{1}{\sigma_i^2}}
\tag{9.2}
$$

The same thinking applies if we want to fit the vessels by an ellipse:

$$
\chi^2(a,b) = \sum_i \left\{ \frac{(D_i \cos\theta_i - a\cos\theta_i)^2}{4\sigma_i^2} + \frac{(D_i \sin\theta_i - b\sin\theta_i)^2}{4\sigma_i^2} \right\}
\tag{9.3}
$$

By minimizing the χ^2, we get:

$$
\begin{aligned}
a &= \frac{\sum_i \frac{D_i \cos^2\theta_i}{\sigma_i^2}}{\sum_i \frac{\cos^2\theta_i}{\sigma_i^2}} \\
b &= \frac{\sum_i \frac{D_i \sin^2\theta_i}{\sigma_i^2}}{\sum_i \frac{\sin^2\theta_i}{\sigma_i^2}}
\end{aligned}
\tag{9.4}
$$

First, we assumed all errors to be identical on all diameters for all cylinders, at $\pm$ 8 mm (renormalization of the estimated errors to obtain a χ^2 of 1 per degrees of freedom in order to get the best fit). The results are given in tables 9.6 and 9.7. In a second hypothesis, we take all errors to be the same on the horizontal and vertical diameters, of 2 mm. The errors on the diagonals are set to 10 mm; indeed, these measurements are harder to make since the diagonals are harder to locate. Results are shown in tables 9.8 and 9.9.

Let us now compute the Target volumes. For a circular vessel, with a linear interpolation between faces A and B:

$$
V_C = \frac{\pi h}{12}\left(d_A^2 + d_A d_B + d_B^2\right)
\tag{9.5}
$$

Second set of measurement	d (mm)	a (mm)	b (mm)	Circle (χ^2/dof)	Ellipse (χ^2/dof)
Cylinder 2 - face A	2,303.00	2,314.00	2,292.00	1.41	1.18
Cylinder 2 - face B	2,304.25	2,319.50	2,289.00	3.60	3.58
Cylinder 3 - face A	2,303.00	2,316.25	2,289.75	2.13	1.83
Cylinder 3 - face B	2,300.50	2,310.25	2,290.75	1.39	1.35

Table 9.7: First shape fit (error of $\pm$ 8 mm on diameters) of the vessels with the second set of measurements.

First set of measurement	d (mm)	a (mm)	b (mm)	Circle (χ^2/dof)	Ellipse (χ^2/dof)
Cylinder 1 - face A	2,299.38	2,316.69	2,282.08	13.69	1.06
Cylinder 1 - face B	2,300.31	2,318.58	2,282.04	15.31	1.27
Cylinder 2 - face A	2,298.40	2,319.56	2,277.25	20.35	1.43
Cylinder 2 - face B	2,292.67	2,319.60	2,265.75	33.86	3.67
Cylinder 3 - face A	2,300.81	2,320.52	2,281.10	17.62	1.17
Cylinder 3 - face B	2,299.81	2,318.56	2,281.06	16.21	1.46

Table 9.8: Second shape fit (errors larger on the diagonals) of the vessels with the first set of measurements.

Second set of measurement	d (mm)	a (mm)	b (mm)	Circle (χ^2/dof)	Ellipse (χ^2/dof)
Cylinder 2 - face A	2,298.38	2,319.54	2,277.23	20.34	1.43
Cylinder 2 - face B	2,298.02	2,327.35	2,268.69	39.65	3.58
Cylinder 3 - face A	2,297.92	2,323.40	2,272.44	29.55	2.12
Cylinder 3 - face B	2,294.04	2,312.79	2,275.29	16.25	1.53

Table 9.9: Second shape fit (errors larger on the diagonals) of the vessels with the second set of measurements.

	V_C (m³)	δV_C (%)	V_E (m³)	δV_E (%)
Cylinder 1	10.25	0.49	10.25	0.49
Cylinder 2	10.23	0.49	10.23	0.49
Cylinder 3	10.25	0.49	10.25	0.49

Table 9.10: First shape fit, cylindric and elliptic volumes with their uncertainties.

	V_C (m³)	δV_C (%)	V_E (m³)	δV_E (%)
Cylinder 1	10.21	0.28	10.21	0.38
Cylinder 2	10.17	0.28	10.17	0.38
Cylinder 3	10.22	0.28	10.21	0.38

Table 9.11: Second shape fit, cylindric and elliptic volumes with their uncertainties.

The volume is also computed for an elliptic Target:

$$V_E = \frac{\pi h}{12}\left(a_A b_A + a_B b_B + \frac{a_A b_B + a_B b_A}{2} \right) \tag{9.6}$$

When we apply the first hypothesis, with a quadratic propagation of measurements uncertainties, we obtain what is shown in table 9.10. Thus, we have a global uncertainty of 50 L on the Target volumes. All vessels are close to another. Target 2 is slightly different from the other two vessels. When we apply the second hypothesis, with linear propagation of measurement uncertainties, we get the volumes on table 9.11. Thus, a global uncertainty of 30 to 40 L on the volumes. Target 2 is slightly smaller, though non significantly. Finally, with the second hypothesis and quadratic propagation of measurement uncertainties, we get the results of table 9.12. Thus, with this computation, we have a global uncertainty of 18 L. The volumes calculations do not change, but the errors on the volumes are smaller. Target 2 shows then a larger deviation, considering the uncertainties.

Considering the two sets of measurements, all vessels are comparable. The optimal choice is Target 1 and 3, the closest in terms of dimensions and volumes according to this statistical method. By favoring the vertical and horizontal diameters (2 mm error) to diagonal measurements (10 mm error), the volume computation has an uncertainty of the order of 0.2 % ($\sim$20 L). These results are very good, of the same order of magnitude of the weighing measurement, performed to determine the number of free protons in the Target. Thus, we already have by construction the required systematical error, a first check of the similarity of the detectors.

Weighing   After we discovered the crack on Target n°3, we decided to use Target n°1 in the far detector. Between the 20th and the 27th of October, 2009, we then had the opportunity

	V_C (m³)	δV_C (%)	V_E (m³)	δV_E (%)
Cylinder 1	10.21	0.18	10.21	0.38
Cylinder 2	10.17	0.18	10.17	0.38
Cylinder 3	10.22	0.18	10.21	0.18

Table 9.12: Second shape fit with quadratic errors propagation, cylindric and elliptic volumes with their uncertainties.

	Target n°1	Target n°3
Target vessel	323	322 - 323
Target vessel + 0.5 kg	323	323

Table 9.13: Target n°1 and 3 weighing measurement. Target n°1 weighs 322.75 ± 0.25 kg and Target n°3 weighs 322.25 ± 0.25 kg.

in the laboratory to weigh these two Targets to determine the acrylic mass that is going to be in the detector. For this measurement, we used the weighing sensors in the laboratory, being particularly careful about their leveling: each sensor was set separately so that the measurement axis is vertical (uncertainty < 1 mrad). Then, all sensors were leveled together to have a horizontal measurement plan (uncertainty < 1 mrad).

Since the sensors are sensible to the kilogram, we performed two measurements; one with only the Target vessel, one with the Target vessel and a 500 g weigh to get the sensitivity down to a half of kilogram. In table 9.13 are the measurements for Targets 1 and 3. From these, one can conclude that Target n°1 has a mass comprised between 322.5 kg and 323 kg; Target n°3 has a mass comprised between 322 and 322.5 kg. Thus the mass difference between the two Targets is 0.5 kg, which corresponds to 0.16 %.

This confirms the metrology measurement; the difference between Target 1 and 3 is of order 0.2 %. Therefore, from construction, the systematic goal is reached.

9.3   Target volume proton number

The Target proton number determination relies on an exact knowledge of the chemical composition of the liquid and the Target mass. The first phase of the experiment starts with only the far detector running. Therefore, uncertainties on the chemical composition and on the liquid mass determination have to be taken into account. The real number of atoms per gram is quantity difficult to measure at better than 1 % precision. In order to eliminate the uncertainty on the liquid chemical composition, the same liquid, from a single batch, will be used in both detectors. The same systematic effect should then be in both detectors and will not contribute to the uncertainty on the relative normalization, that is to say in phase II. However, in phase I, this effect has to be taken into account to determine the global uncertainty.

After testing different systems to determine the Target liquid mass, CEA chose to rely on a weighing measurement [55]. To ensure an 0.2 % systematic, the idea is to fill an intermediate vessel with Target liquid before filling the actual vessel. We weigh this intermediate vessel before and after filling the Target. The difference between the two measurements gives the weight of the Target liquid in the detector. Since the determination of the liquid mass in the detector is based on a difference, most systematics related to the weighing measurement cancel. In order to reduce systematics, the same intermediate vessel is to be used for the near and far detectors. We performed tests on the weight sensors; a 1.5 ton mass was weighed 20 times with a standard deviation of 0.15 kg. Also, a cross-check was performed between a flowmeter and the weight sensor filling a 2 m^3 stainless steel vessel. The flowmeter data sheet indicates a global

accuracy of 0.5 % which can be reduced to 0.3 % with local calibration. After the calibration of the flowmeter and several trials with both sensors, compatible values were obtained with a dispersion of 0.12 % (1σ).

The Target liquid total mass M_{tot} can be decomposed into the contribution of all atoms intervening in the liquid composition:

$$M_{tot} = M_H N_H + M_C N_C + M_N N_N + M_O N_O + M_{Gd} N_{Gd} \tag{9.7}$$

where M_i is the atomic mass and N_i the number of atoms [55]. We thus have a direct relationship between the measured liquid mass and the number of free protons as long as we know the liquid composition:

$$N_H = \left(M_H + M_C \frac{N_C}{N_H} + M_N \frac{N_N}{N_H} + M_O \frac{N_O}{N_H} + M_{Gd} \frac{N_{Gd}}{N_H} \right)^{-1} \times M_{tot} \tag{9.8}$$

The estimated uncertainty on $^{N_C}/_{N_H} = 0.53$ is estimated to be 0.1 % by our German colleagues. However, in equation (9.8), it is the preponderant uncertainty since the other ratios are at least three orders of magnitude lower. The uncertainty on the liquid composition can be summarized as an uncertainty on the proportionality coefficient between N_H and M_{tot}. If we take the only uncertainty to be on the one on the $^{N_C}/_{N_H}$ ratio, we get:

$$N_H = M_{tot} \, (8.12 \pm 0.06) \times 10^{22} \tag{9.9}$$

with M_{tot} the total liquid mass in grams.

9.4 Conclusion

An 0.2 % systematic on the Target proton number is to be reached. This will be achievable thanks to a carefully controlled Target vessel construction and a Target liquid weighting measurement. By construction, an 0.2 % error in the Target volume is already reached. The weighting system will allow to constrain the Target mass and cross-check this result.

The Target vessel proton number is also to be determined, since neutrinos will be interacting with them too. We were able to perform a measurement in Heidelberg. An acrylic piece was vaporized, for its atoms number to be counted by chromatography afterwards. The proton concentration in the GS0Z18 acrylic was measured to be 7.94 %, with an absolute error about 0.1 %.

Chapter 10

Acrylic vessels fabrication and integration

In this last chapter is the detailed description of the fabrication and integration of the Target and Gamma Catcher vessels, the main subject of this manuscript. The fabrication happened part at the manufacturer, Néotec, part on the power plant site, in a hall lent by EDF, part directly in the laboratory. The integration happened successfully, even though many steps were necessary for the Gamma Catcher, such as two rotations due to the tightness of the tunnel. The near laboratory will be constructed such that the whole integration is simplified. We are also studying the possibility to construct the Gamma Catcher directly in the laboratory.

10.1 Vessels fabrication

10.1.1 Target, Gamma Catcher and chimneys construction and transportation.

The Target vessels were entirely built and checked for tightness at the manufacturer. The Gamma Catcher was built without the top lid, to be glued at the Chooz far laboratory, in the pit, after Target integration. Both chimneys were constructed at Néotec, and transported to Chooz for installation. All acrylic pieces were bagged during transportation, so that they were protected from external dust. For us to detect any possible weakness of the vessels, shock indicators were installed on the vessels. Only a 5G one was set on, on the Gamma Catcher. This did not impact the vessel integrity.

10.1.1.1 Gamma Catcher

Gamma Catcher feet are acrylic blocks designed to raise the vessel at the right distance from the Gamma Catcher. They are I-shaped GS0Z18 beams, 110 cm long, 92 cm high. The base is 26 cm large, the middle 6 cm, the top 16 cm. All six feet were made by gluing layers of acrylic together, to reach the desired thicknesses. No bubbles were seen in these gluings. The

shapes were cut by laser. Once they were fully assembled, they were bagged and transported to Chooz.

The Gamma Catcher parts were thermoformed at the Néotec factory. For this operation, an acrylic plate is disposed on a mold, protected on both sides by a clean white drape to avoid any external particle incrustation. At Néotec were also prepared the lid and bottom. Then, all Gamma Catcher parts were sent to Chooz. EDF put at our disposition a hall, called "la Déminée" on the power plant site. Néotec set up a clean tent there to finalize the Gamma Catcher construction. The cylinder was glued horizontally, around a mold. It then had to be put on the vertical position, to remove the mold and glue the bottom. Since the Gamma Catcher was transported to the far laboratory (less than 1 km away) without its top lid, its open side was stabilized to avoid stresses. The idea was to use three metal rods as diameters to make the open side rigid.

While handling the Gamma Catcher, a crack of roughly 20 cm long appeared right underneath the lip designed to support the lid. We detected it and came out with a solution with Néotec: they stopped the crack by perforating the vessel with a drill and glued on each side of the vessel a GS0Z18 plate (30 × 15 cm) with the exact same curving radius as the vessel. This happened before transportation in the laboratory.

10.1.1.2   Targets

All three Targets were thermoformed and constructed at Néotec. As for the Gamma Catcher, first the cylinders were formed, then glued on the bottoms. Finally, the lids were glued on. All gluings happened in a clean room. No glue was left on the inside of the Target. Indeed, Target liquid scintillator is damaging to the glue, and we do not want to endanger the integrity of the vessel. From the previous chapter, we learned that Target n°1 and 3 were chosen for the far and near detectors. Target n°3 was sent to Chooz, while the other two stayed in Néotec. However, once it arrived in the laboratory, we discovered one of the gluings was weakened (see section 10.2.1). We therefore decided to switch for Target n°1 while Target n°3 was sent for repairs. In the meantime, a new mechanic shop opened up next to Néotec, with an oven large enough for the Targets to be annealed. Target n°1 was then annealed before being sent to Chooz, and Target n°3 was sent to Saclay for long-term storage after restoration, along with Target n°2.

10.1.2   Annealing

Annealing is a process of heating and cooling the material to relieve internal stresses after it was formed. For a long term usage, the admissible stresses are 5 MPa. Internal stresses are annihilated very quickly at high temperature (80 °C), but it takes several months at usual temperature. Annealing is then advised, at least on the Targets which might endure more stresses due to liquids. Indeed, the Buffer liquid is not aggressive and the Gamma Catcher liquid less aggressive than the Target one. Therefore, Gamma Catcher annealing is less necessary than

in the Target vessel. Moreover, we did not have at hand an oven large enough to contain the Gamma Catcher.

To anneal Plexiglas, the material is heated until the temperature reaches a stress-relief point, that is, the annealing temperature (also called annealing point) at which the material is still too hard to deform, but is soft enough for the stresses to relax. The piece is then allowed to heat-soak until its temperature is even throughout. It is then slowly cooled at a predetermined rate. Indeed, as acrylic is cooled, the inside does not cool off as fast as the outside. The inside stays molten and expanded while the outside is starting to get stiff and begins to contract. If acrylic is cooled off too fast, this expansion and contraction are frozen into place and this creates stress in the piece. For our Targets, the annealing temperature sequence that was followed was: 20 °C, 40 °C, 50 °C, 80 °C, 20 °C, 80 °C, 50 °C, 40 °C, 20 °C.

10.1.3   Leakage tests

We performed a leakage test with Helium on the three Double Chooz Targets at the Néotec factory, before being transported on site.The test concept is that the vessel endures a tiny pressure difference: there is slightly more pressure in the vessel, where the Helium is inserted, than outside of the vessel. To get back to equilibrium, gas in the vessel diffuses through the possible leaks. Helium is used for two different reasons: not only it is a light gas that diffuses easily, more easily than water or oil for example, but also it is hard to find in nature which ensures that its detection is in fact due to a leak in the vessel, not to a hazardous coincidence.

Helium was introduced in each of the three vessels once construction was completed. These were then hermetically sealed, with a plastic bag and some tape on the chimney neck. Every gluing, as well as the sealed chimney were then checked with a Helium "sniffer". The first vessel we checked was Target n°1, which was in a vertical position. The test did not show any leakage at the gluings. The last two Targets were on a horizontal position and bagged, ready for transportation. We then had to de-bag the vessels before performing the test, which concluded that these vessels did not have any leak.

10.1.4   Stress check

Stresses in Double Chooz acrylic vessels were checked by photoelasticimetry. This is an optical method based on birefringence of materials under stresses, i.e. stresses induce a local change in the refractive index of the material and light propagates anisotropically in the material. The birefringence is analyzed through the way light polarization is changed (linear, elliptic or circular polarization) after crossing the material: the two wave components of light get out of phase with one another because of the stresses in the material. The phase difference depends on the wavelength, and therefore on the color. So, if we use a white light for this stress check, we will have an iridescence of color as a result. The more colors we have, the more important the phase difference is, the more important the stresses are. Experimentally, a white light is illuminating a polarizing film, the polarizer, which is aligned with the sample to characterize. Then, behind the sample, one can find another polarizing film, the analyzer (see figure 10.1).
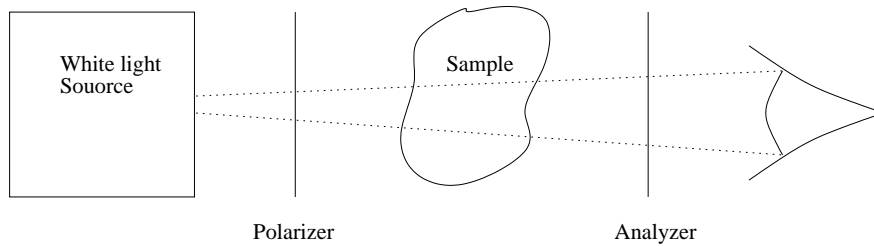
Figure 10.1: Polarizer scheme. A white light is illuminating the sample. Polarizing films in front (polarizer) and behind (analyzer) the sample make stresses appear by revealing local changes in the refractive index of the sample material (acrylic becomes birefringent under stress).

Target n°3, transported to Chooz, as well as the Gamma Catcher without its lid were checked for stress, in the far laboratory. Despite the Target anomaly, we did not find any area with important stresses. On the Gamma Catcher, no gluing showed any stress. However, the ring designed for the lid gluing showed many light iridescence, which means the gluing ring is stressed. Also, on the Gamma Catcher vessel, we found a small deformation in the acrylic material, but no stress was attached.

10.2   Integration

10.2.1   How it happened

Gamma Catcher feet were installed in the Buffer (phototubes were already mounted) two by two, thanks to a special tooling especially designed. Stainless steel shims were inserted underneath to level them. Indeed, considering the chimneys, a non horizontal Gamma Catcher would induce a large angle on the chimneys with respect to vertical. The Gamma Catcher feet were horizontally leveled within 1.5 mm. This leads to a deviation of 2.5 mm at the top of the chimney, which is acceptable.

The first vessel to be brought in the laboratory was the Target, to be stored at the very end of the laboratory so that we could bring the Gamma Catcher. The latter arrived mounted on a supporting system used to minimize the deformations, on a truck, from "La Déminée". It was vertical; but, the only way the Gamma Catcher could fit in the tunnel leading to the laboratory was horizontally. We thus had to rotate the Gamma Catcher in front of the tunnel entrance. A picture is shown on figure 10.2. We then put the Gamma Catcher on a trolley and drove it down the tunnel, towards the laboratory. This was a very tricky operation, as shown in figure 10.3. Finally, the Gamma Catcher arrived in the laboratory. This was time for the summer break.

When we came back to the laboratory, the first thing we did was restoring the cleanliness level to ISO 6. Once this was done, we unpacked the Gamma Catcher and rotated above the pit prior to its insertion in the Buffer vessel. One of the main difficulties was not to damage any PMTs during the operation, and we succeeded. We used a camera to place the Gamma Catcher exactly on its feet. We then unpacked the Target, Target n°3. One of the gluings on the top of

Figure 10.2: Gamma Catcher rotation, prior to enter in the tunnel leading to the laboratory. Special tooling was designed by Saclay. Two cranes were necessary to realize the operation safely.

Figure 10.3: Gamma Catcher going down the tunnel. A crane secured the vessel from behind. The tunnel dimensions were very tight; we even had to break some rocks in order to let the Gamma Catcher go through. Two fake runs were performed before the real one.

Angle from x-axis	Distance (mm)
0	540
$\pi/2$	550
π	535
$3\pi/2$	565

Table 10.1: Distance between the outside of the Target wall and the inside of the Gamma Catcher one, after integration but before Target lid gluing. We discovered that the Gamma Catcher was elliptic at tits top.

the cylindrical part of the vessel, on the outside, was damaged, probably during transportation. On the gluing and the two adjacent plates, one could see some scratches, in the form of a square. The glue on the Gamma Catcher side slightly dried and crackled. However, we did not see any crazing with the polarizer device when we inspected it. We decided nonetheless together with Néotec to exchange this Target against the other one we chose to use (Target n°1), to send Target n°3 to repair at the Néotec factory. This is when we also decided to anneal the vessels. The Target was then inserted in the Gamma Catcher, before the latter was closed. When we tried to install its lid on the Gamma Catcher, we realized that the top of the Gamma Catcher was slightly elliptic. Table 10.1 show measurements that were made of the distance between the outside of the Target wall and the inside of the Gamma Catcher one. The consequence of this elliptic shape is that the Gamma Catcher lid did not fit during construction, and a solution had to be found for the gluing. The considered solution was to add a ring of acrylic material at the top of the Gamma Catcher to make the match between the elliptic shape of the vessel and the cylindrical shape of the lid. This added an extra 14 mm to the height of the vessel. The theoretical volume of the Target (liquid and acrylic vessel) is 10.58 m^3 (feet and reinforcement not considered). Hence, the volume of the Gamma Catcher liquid would be 22.39 m^3, for a cylindrical vessel of 3416 mm diameter and 3542 mm height. Let us compute the new Gamma Catcher volume:

$$V = \frac{h_{new}}{3}\left(S + s + \sqrt{Ss}\right) \tag{10.1}$$

S and s being the "two bases" of the truncated cone that the Gamma Catcher is. This gives:

$$V = \frac{\pi h_{new}}{3}\left(R^2 + ab + R\sqrt{ab}\right) \tag{10.2}$$

Considering the theoretical Target volume, this gives a Gamma Catcher liquid volume of 22.47 m^3; the fixing of the elliptic shape of the Gamma Catcher vessel added an extra 74 L.

Once the extra acrylic ring was installed, the top lid of the Gamma Catcher and chimneys were glued by the manufacturer. Air conditions in the laboratory were carefully controlled. During the 24h of polymerization of the glue, the temperature had to be kept above 20 °C and the relative humidity at 60 %.

10.2.2 My role during integration

During the acrylic vessels integration, my role in Chooz was first to ensure the cleanliness goals were met, and if not to stop the integration. This was not necessary, since the whole team

respected the cleanliness rules and cleaned thoroughly throughout the whole integration. I checked the cleanliness level every day thanks to the particle counter. Also, I monitored the laboratory conditions to verify whether gluing could happen. The different interfaces with the different sub-systems to be integrated in the vessels were also one of my duties. For this task, I worked with the German filling team to define what filling tubes were needed, to buy and install them. Concerning the other sub-systems, I was the link between Néotec and the collaboration to define what fixtures were needed and where to glue them. I was then present with Néotec during the various fixtures gluing, but also during the sub-systems installation to make sure the integrity of the vessels were not endangered. Finally, since the whole vessels integration was Saclay's responsibility, I participated to all the mechanical work during my being on site, which was throughout the entire integration.

10.2.3   Humidity in the laboratory

Water in the Target liquid scintillator degrades Gd encapsulation; it is a mandatory that this liquid is not in contact with water. Acrylic is hygroscopic, but, since liquid scintillator is more hydrophilic than the vessel material (more free protons in alcanes and therefore a strong urge of water to make H liaisons), if no care is taken to dry the acrylic vessel, water in the acrylic would migrate in the liquid scintillator and degrade it. So, this vessel had to be dried intensely before the filling phase (water content has to be below 100 ppm).

Nominal conditions in the laboratory are 14 °C (which can go up to 16 °C in summer) and 100 % relative humidity. As already said, during Target and Gamma Catcher integration we reached 21 °C and 60 % relative humidity, necessary conditions for gluing (see section 8.2.2.1). Moreover, the water amount had also to be reduced since acrylic is hydrophilic, but less than the Target liquid scintillator.

10.2.3.1   Heaters and dehumidifiers

On the Mollier diagram (figure 10.4), one can see that water amount in the air, relative humidity and temperature are linked. Our goal was to get the humidity and water content down in the laboratory. First, the use of heaters reduced the relative humidity. We raised the temperature to 21 °C, which according to the Mollier diagram corresponds to roughly 65 % relative humidity. As already said, the gluings could then be performed. Moreover, the dehumidifiers lowered the water content in the air and therefore the relative humidity. We reached a humidity of 60 %, therefore the water content in the laboratory went from ten grams of water per kilogram of air to roughly 8.5, according to the Mollier diagram.

10.2.3.2   Dehydrating bags

During the exposition of the Target vessel to the laboratory air, highly humid, after its integration, a dehydrating bag was to be deployed in the Target vessel, along with a temperature and humidity counter. The dehydrating bags were made with inert drying clay in a
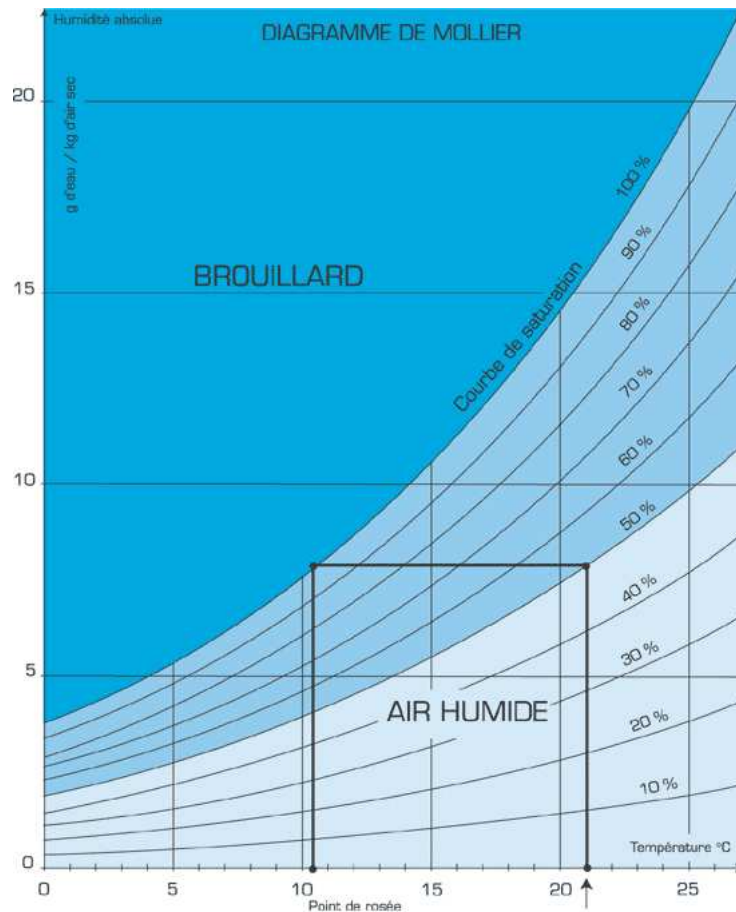
Figure 10.4: The Mollier diagram represents the link between temperature (X axis), the relative humidity (percentage curves) and the amount of water in air (Y axis). As an example, an environment at 10.5 °C and 100 % relative humidity (dew point) would keep the same water amount in air if we raise the temperature. At 21 °C, the relative humidity is lowered to 50 %. Therefore, to decrease the relative humidity in the laboratory, we decided to combine the use of heaters (to raise the temperature and therefore decrease the relative humidity) and dehumidifiers (to decrease the water amount in the air, and thus the relative humidity).

Tyvek bag, untearable and tested to meet clean room requirements.The bags dimensions were 90×180×25 mm, with a weight of roughly 150 g, to enter in the Target chimney of 150 mm inner diameter. The idea was to attach them to a special flange designed to this purpose, on top of the Target chimney, by a Nylon fishing thread, with Resistance to tension of 4.5 kg. One of this bag represented ¼ dehydrating unit (DU). For our volume, we needed 120 of these bags; we decided to change the bag in the Target every four days. To determine the amount of water extracted from the vessel, bags were to be weighed before insertion and after retrieval. The humidity and particle counter was to be deployed the same way.

Due to technical difficulties and planning delays, the bags were never deployed in the Target. Since the latter was flushed with Nitrogen before filling, it was decided this would be sufficient for drying the acrylic material. The humidity counter was deployed to monitor humidity in the Target.

10.2.4   Systems in the vessels

10.2.4.1   Filling tubes

All filling tubes are in PFA. In the Target one ½ inch tube runs along the wall to reach the center of the bottom of the vessel. This tube is for filling, the same tube would be use in case we have to empty the detector. It was installed at the Néotec factory, before the lid gluing. In the Gamma Catcher, two ¾ inch (filling and level measurement) and one ¼ inch (liquid sampling) tubes run along the wall to reach the center of the vessel, like in the Target. They were installed before the Gamma Catcher was transported to the laboratory. All tubes are fixed on the walls by glued GS0Z18 pieces. The tubes are transparent and therefore should not be a problem for the optics of the detector. At the manufacture, they were made and bagged in an ISO 4 environment. Therefore, we did not unpack the tubes before getting in the ISO 6 laboratory.

10.2.4.2   Level measurement systems

At the bottom of the Gamma Catcher was installed a pressure sensor of roughly 200 g, to monitor the liquid level. It was installed at the same time as the filling tubes, since its cable was fixed on the Gamma Catcher wall with the same fixtures. Laser systems were installed in the Target chimney.

10.2.4.3   Guide Tube

The Guide Tube is a calibration system allowing deployment of radioactive sources inside the Gamma Catcher. The major part of the Guide Tube system is made of stainless steel, providing rigid impenetrable source guide while occupying minimum amount of space in a sensitive region of the detector. Néotec glued fixtures on the Target and Gamma Catcher, making sure those

were well aligned; otherwise the tube could not be integrated. The steel part of the tube was integrated on November 2nd, before the Gamma Catcher lid was installed.

This thin tube is running close to the lid and wall of the Target to probe spill in. It also runs on the Gamma Catcher/ Buffer boundary region. An ultra miniature Americium-Beryllium neutron source was designed and built at University of Alabama to study effects of neutron detection systematics. To the best of our knowledge, the source has the smallest outer diameter for a composite neutron source (2 mm). All regions of near and far detector can be cross calibrated with the same sources.

Before and after integration, a survey was conducted to know the dimensions and position of the Guide Tube relative to inner detector. End of May 2010, the flexible tubes, which were stored on the Target chimney, were routed through the Gamma Catcher flange. To make sure no damage was done to the inner sleeve during storage, routing, and feedthrough tightening, a test was successfully conducted with the wire driver pushing the source capsule through the detector. Finally, black tubing was put on top of the flexible tubes to ensure light isolation.

10.2.4.4   Buffer Tube

The Buffer Tube is a simple system to deploy calibration sources around the boundary region between Gamma Catcher and Buffer. It is a vertical double Teflon tube in the Buffer. The outer Teflon tube is installed on the outside of the Gamma Catcher wall. It starts from the level of the bottom of the Gamma Catcher, vertically crosses the Buffer top lid, the veto top lid and the shielding. The tube is tightly closed at the bottom. Inside is an inner Teflon sleeve, guiding the source (calibration source capsule + thin wire gamma ray sources) down the outer tube. Neutron sources are not so important around the boundary region between the Gamma Catcher and the Buffer. The design is such that internal materials can be removed when fatal trouble happens.

The Buffer Tube was successfully installed on the outside wall of the Gamma Catcher vessel on September 2009. Fixations were glued by Néotec and their leveling was checked. The installation team then attached the outer sleeve to the fixtures and installed the inner sleeve afterwards. The tube was safely kept below the bridge during the acrylic vessels installation). During Buffer and Inner Veto closing, the tube was passed through the lids successfully.

10.3   Conclusion

Fabrication and integration of the acrylic vessels and their sub-systems was successful, despite a few anomalies. Once their integration was completed, the rest of the detector integration could go on. To close the Buffer and Inner Veto, special care had to be taken not to damage the chimneys; the lids had to be lifted high enough to be above the chimneys, for these to pas in the lids chimney holes. Also, the Buffer Tube was to be taken care of, since it had to go though both vessels. Indeed, one kink on the Teflon tube would block the calibration source and highly endanger the experiment.

Conclusion

What one can call the golden age of neutrino physics started with the discovery of oscillations of solar and atmospheric neutrinos. Until today, two mixing angles and two squared mass differences are given by data from various experiments. The determination of the remaining mixing angle, θ_{13}, is a priority nowadays; indeed, leptonic CP violation can only be studied if the last angle is not equal to zero.

Double Chooz is one of the new generation experiment designed to measure the last unknown leptonic mixing angle, θ_{13}. Its goal is to measure the oscillation of electronic antineutrinos produced by the Chooz power plant, located in the French Ardennes. This is the very same site where the CHOOZ experiment constrained this parameter, more than ten years ago: $\sin^2 2\theta_{13} < 0.14$ at 90 % C.L. To improve the first Chooz experiment, one has to reduce both statistical errors, by increasing both the detector size and run time, and systematic errors coming from the production and detection of the antineutrinos, and the knowledge of the detector. For this, the key idea is to use a near and a far detector, canceling or reducing this way most of the systematic errors. Moreover, the experiment benefited from twenty years of research and development to reach a state of art technology, for example in the liquid scintillator field, allowing reduction of systematics and therefore a high precision measurement. Thus, any background or interfering signal was carefully studied to be identified during data taking and not mistaken for an antineutrino signal.

The work presented here mostly focus on the Target and Gamma Catcher acrylic vessels, located in the core of the detector. More specifically, a new material designed for the experiment was developed in cooperation between Degussa and CEA, since no pre-existing material met the required conditions for the detector. This material was characterized optically, to maximize light transmission and reduce the dead zone induced by the acrylic to the maximum. With this in mind, a physics study of the Target vessel design was performed, to identify any spectral distortion or count rate modification it could induce. Also, the material resistance to liquid was certified. Indeed, since the Target vessel defines the fiducial volume, no leak from this volume into another is admissible. It appeared the new material is more resistant to liquid scintillator than the pre-existing ones. As far as backgrounds are concerned, the material is radiopure enough so that the singles rate coming from acrylic is negligible compared to the one from the photomultiplier tubes. Throughout the work of the collaboration, the total singles rate expected has been computed. This is the first check when we turn the detector on; if the counting rate is in agreement with what was computed, then we will know we understood the detector well and that it is functioning properly. An unsure single source is coming from the external contamination in the detector, such as dust. Indeed, considering our low background

experiment, a small amount of "radioactive" dust will create a non negligible singles rate. This is why we defined cleanliness goals for the detector fabrication and integration. These goals were met, thanks to well-defined protocols and careful team work. All vessels for the near detector are soon to be produced, except for the Target which is already done. Indeed, we decided to build three Targets during the first phase of the experiment, in order to chose the most similar ones and thus have similar Target volumes. All experience acquired during the first integration will be of use for the near detector, reducing the integration time from almost two years to thirty weeks.

The far detector construction finished in June 2010, for the detector filling to begin. The detector is switched on during filling, to start commissioning. After one and a half year of data taking, the sensitivity to $\sin^2 2\theta_{13}$ will reach 0.06, improving already the CHOOZ limit. The near hall excavation will start in January 2011, for a detector integration in 2011. The near hall will be designed to increase its cleanliness, thanks to the work done in the far hall. The Double Chooz expertise was used to start a project at CEA on non proliferation, called Nucifer. This project is developed in cooperation with the International Atomic Energy Agency. Its goal is to follow up the nuclear combustion of reactors in order to detect any abnormality in the fuel evolution, possible theft for making nuclear weapons.

Double Chooz could ensure a non-zero value for θ_{13} at 3σ for $\sin^2 2\theta_{13} > 0.05$ - 0.06. In case that no oscillation signal is observed, the experiment could give an upper limit on $\sin^2 2\theta_{13}$ of 0.02 - 0.03 at 90 % C.L. The measurement of θ_{13} is necessary to determine completely the parameters of the neutrino mixing matrix. The long term goal of these new generation experiments is to measure the CP violation phase δ, potential key to understanding why the Universe essentially contains matter and mostly no antimatter.

Bibliography

[1] A. Grinbaum, *On the eve of the LHC: conceptual questions in high-energy physics*, 2008, hep-ph/0806.4268

[2] B.R. Martin & G. Shaw, *Particle Physics*, J. Wiley and Sons, 1997

[3] F. Mandl, *Quantum Mechanics*, J. Wiley and Sons, 1972

[4] W. Pauli, Offener Brief an die Gruppe der Radioaktiven bei der Gauvereins-Tagung zu Tübingen, 1930

[5] E. Fermi, Z. Phys. **88**, 161 (1934)

[6] C.L. Cowan, F. Reines et al., *Detection of the free neutrino: a confirmation*, Science **124**, 103, 1956

[7] G. Danby et al., *Observation of high-energy neutrino reactions and the existence of two kinds of neutrinos*, Phys. Rev. Lett **9**, 36-44, 1962

[8] K. Kodama et al. (DONuT Collaboration), *Observation of tau neutrino interactions*, Phys. Lett. **B504**, 218, 2001

[9] C. Rubbia, *Experimental observation of the intermediate vector bosons W^+, W^- and Z^0*, Rev. Mod. Phys. **57**, 699-722, 1985

[10] C. Amsler et al. (Particle data Group), Phys. Lett. **B667,** 1, 2008

[11] G. Mention, *Etude des sensibilités et bruits de fond de l'expérience Double Chooz pour la recherche du paramètre de mélange leptonique θ_{13}*, Thèse de Doctorat, Université Claude Bernard - Lyon I, 2005

[12] C. S. Wu et al., *Experimental test of parity conservation in beta decay*, Phys. Rev. **105**, 1413, 1957

[13] M. Goldhaber, L. Grodzin & A. W. Sunyar, Phys. Rev. **109**, 1015, 1958

[14] D.H. Perkins, *Introduction to High Energy Physics*, Addison-Wesley Publishing company, 1987

[15] B.T. Cleveland et al., *Measurement of the solar neutrino flux with the Homestake chlorine detector*, Astrophys. J. **496**, 505-526, 1998

[16] SNO collaboration, *The Sudbury Neutrino Observatory*, NIM **A449**, 172-207, 2000, nucl-ex/9910016

[17] SNO collaboration, *Measurement of Charged Current Interactions Produced by ^8B Solar Neutrinos at the Sudbury Neutrino Observatory*, Phys. Rev. Lett. **87**, 071301, 2001

[18] SNO collaboration, *Direct Evidence for Neutrino Flavor Transformation from Neutral-Current Interactions in the Sudbury Neutrino Observatory*, Phys. Rev. Lett **89**, 011301, 2002

[19] B. Pontecorvo, Sov. Phys., JETP,6, 429, 1957.

[20] C. Giunti & C. W. Kim, *Fundamentals of Neutrino Physics and Astrophysics*, Oxford, 2007

[21] Z. Maki, M. Nakagawa, S. Sakata, Prog. Theor. Phys.,28, 870, 1962.

[22] C. Amsler et al. (Particle data Group), B. Kayser, *Neutrino mass, mixing and flavor change*, Phys. Lett. **B667,** 1, 2008

[23] L. Wolfenstein, *Neutrino oscillations in matter*, Phys. Rev. **D17**, 2369-2374, 1978

[24] C. Weinheimer, *The neutrino mass direct measurements*, Proceedings of 10th International Workshop on Neutrino Telescopes, 2003, hep-ex/0306057

[25] L. Bornschein, *KATRIN - Direct Measurement of Neutrino Masses in the Sub-Ev Region*, ECONF, C030626: FRAP14, 2003, hep-ex/0309007

[26] M. Altmann et al., *Complete results for five years of GNO solar neutrino observations*, Phys. Lett. **B616,** 174-190, 2005, hep-ex/0504037

[27] SAGE Collaboration, *Measurement of the solar neutrino capture rate with gallium metal*, Phys. Rev. **C60**, 055801, 1999, astro-ph/9907113

[28] M. Koshiba, *Observational neutrino astrophysics*, Phys. Rep. **220**, 229-381, 1992

[29] SNO Collaboration, *Low Energy Threshold Analysis of the Phase I and Phase II Data Sets of the Sudbury Neutrino Observatory*, submitted to Phys. Rev. C., 2009, 0910.2984v1

[30] Y. Fukuda et al., *Evidence for oscillation of atmospheric neutrinos*, Phys. Rev. Lett. **81**, 1562-1567, 1998, hep-ex/9807003

[31] KamLAND Collaboration, *First Results from KamLAND: Evidence for Reactor Anti-Neutrino Disappearance*, Phys. Rev. Lett. **90**, 021802, 2003, hep-ex/0212021

[32] M. Apollonio et al., *Search for neutrino oscillations on a long base-line at the CHOOZ nuclear power station*, Eur. Phys. J. **C27**, 331, 2003, hep-ex/0301017

[33] F. Boehm et al., *Final results from the Palo Verde Neutrino Oscillation Experiment,* Phys. Rev. **D64**, 112001, 2001, hep-ex/0107009

[34] Y.Fukuda et al., *Atmospheric ν_μ/ν_e ratio in the multiGeV energy range*, Phys. Lett., **B335**, 237-245, 1994

[35] M. Apollonio et al., *Limits on neutrino oscillations from the Chooz experiment*, Phys. Lett., **B466**, 415-430, 1999, hep-ex/9907037

[36] F. Boehm et al., *Results from the Palo Verde Neutrino Oscillation Experiment*, Phys. Rev. , **D64**, 112001, 2001, hep-ex/0003022

[37] K2K collaboration, *Evidence for muon neutrino oscillation in an accelerator-based experiment*, Phys. Rev. Lett., **94**, 081802, 2005, hep-ex/0411038

[38] K2K collaboration, *Search for Electron Neutrino Appearance in a 250 km Long-baseline Experiment*, Phys. Rev. Lett., **93**, 051801, 2004, hep-ex/0402017

[39] K2K collaboration, *Measurement of Neutrino Oscillation by the K2K Experiment*, Phys. Rev., **D74**, 072003, 2006, hep-ex/0606032v3

[40] D. G. Michael et al., *Observation of muon neutrino disappearance with the MINOS detectors and the NuMI neutrino beam*, Phys. Rev. Lett. **97**, 191801, 2006

[41] M. Mauzetto & T. Schwetz, θ_{13}: *phenomenology, present status and prospect*, 2010, 1003.5800v1

[42] K. Anderson et al., *A New Nuclear Reactor Neutrino Experiment to Measure θ_{13}*, 2004, hep-ex/0402041

[43] G. Mention, T. Lasserre & D. Motta, *A unified analysis ot the reactor neutrino program towards the measurement of the θ_{13} mixing angle*, 2007, 0704.0498v2

[44] Double Chooz collaboration, *Double Chooz: a search for the neutrino mixing angle θ_{13}*, 2006, hep-ex/0606025

[45] F. X. Hartmann, *Low Level Scintillators and Gadolinium*, Presentation at the Workshop on Future Low Energy Neutrino Experiments, Munich, 2003 October 9th-11th

[46] Daya Bay collaboration, *A precision measurement of the neutrino mixing angle θ_{13} using reactor antineutrinos at Daya Bay*, 2007, hep-ex/0701029

[47] J. Link, *The Daya Bay Reactor Neutrino Experiment*, Presentation at the Workshop on Low Energy Neutrino Physics (Neutrino Champagne), Reims, 2009 October 19th-21st

[48] M. Chu, *Precise Measurement of θ_{13} at Daya Bay*, Presentation at the 34th International Conference on High Energy Physics, Philadelphia, 2008 July 29th-August 5th

[49] RENO collaboration, *RENO: an Experiment for Neutrino Oscillation Parameter θ_{13} Using Reactor Neutrinos at Yonggwang*, 2010, 1003.1391

[50] K. K. Joo, Status of the RENO rector experiment, Presentation at the Neutrino 2010 conference, Athens, 2010 June 14th-19th

[51] NOνA collaboration, *NOνA proposal to build a 30 Kiloton Off-Axis Detector to Study Oscillations in the Fermilab NuMI Beamline*, 2005, hep-ex/0503053

[52] Y. Itow et al., *The JHF-Kamioka neutrino project*, Nucl. Phys. Proc. Suppl. **111**, 146, 2001, hep-ex/0106019

[53] N. S. Bowden, *Reactor monitoring and safeguards using antineutrino detectors*, J. Phys. Conf. Ser., **136**, 022008, 2008, nucl-ex/0809.2128

[54] C. Bemporad et al., *Reactor-based Neutrino Oscillation Experiments*, Rev. Mod. Phys., **74**, 297, 2002, hep-ph/0107277.

[55] T. Mueller, *Expérience Double Chooz: simulation des spectres antineutrinos issus de réacteur*, Thèse de Doctorat, Université Paris XI, 2010

[56] http://bama.ua.edu/~busenitz/rnu2003_talks/lasserre1.doc

[57] H. de Kerret, Double Chooz: systematic errors and background, Presentation at the Future Low Energy Neutrino Experiments conference, Niigata, 2004 March 20th-22nd

[58] Communication interne Double Chooz

[59] Cours de l'Ecole Centrale Nantes

[60] I.B. Berlman, *Handbook of fluorescence spectra of aromatic molecules*, Academic Press, 1971, 2nd edition.

[61] B. Littlejohn et al., *UV degradation of the optical properties of acrylic for neutrino and dark matter experiments*, JINST, 2009, 0907.3706

[62] G. Heusser, M. Laubenstein & H. Neder, *Low-level germanium gamma-ray spectrometry at the $\mu Bq.kg^{-1}$ level and future developments towards higher sensitivity*, Radioactivity in the Environment, **8**, 495-510, 2006

[63] Internal Double Chooz documentation: Cleanliness plan

[64] www.algade.com

[65] J.H. Seinfeld & S.N. Pandis, *Atmospheric chemistry and physics: From air pollution to climate change*, Wiley-Intersciences, 1998.

[66] L. Katz & A.S. Penfold, Revs. Modern Phys. **24**, 28, 1952.

Abstract:

Double Chooz is one of the new generation experiments designed to measure the last unknown leptonic mixing angle, θ_{13}. It studies the oscillations of electronic antineutrinos produced by the Chooz nuclear power plant, on the very same site where the CHOOZ experiment constrained this parameter. Our knowledge on θ_{13} can be improved by reducing both statistical errors (increasing both the detector size and run time) and systematic errors. For this, the key idea is to use identical near and far detectors, canceling or reducing most of the systematic errors coming from the production and detection of antineutrinos. Also, special care is dedicated to analyze backgrounds generated by natural radioactivity and cosmic ray interactions. The work presented here mostly focuses on the Target and Gamma Catcher acrylic vessels, located in the core of the detector. A new material designed for the experiment was developed since no pre-existing material met the required conditions for the detector. This material was characterized optically, to maximize light transmission and reduce the dead zone induced by the acrylic to the maximum. With this in mind, a physics study of the Target vessel design was performed to identify any spectral distortion or count rate modification it could induce. Also, the material resistance to liquid was certified. As far as backgrounds are concerned, the material is radiopure enough so that the singles rate coming from acrylic is negligible compared to the one from the photomultiplier tubes. An unknown single source is coming from the external contamination in the detector, such as dust. This is why we defined cleanliness goals for the detector fabrication and integration. These goals were met, thanks to well-defined protocols and careful team work. After three years of data taking, Double Chooz could disentangle an oscillation signal at 3σ for $\sin^2 2\theta_{13} > 0.05$ -0.06. If no oscillations were observed, the experiment could give an upper limit on $\sin^2 2\theta_{13}$ of 0.02 -0.03 at 90 % C.L.

Résumé:

Double Chooz est une des expériences nouvelle génération dédiée à la mesure de l'angle de mélange θ_{13}. Elle étudie les oscillations des antineutrinos électroniques produits par la centrale nucléaire de Chooz, site où s'est déroulée l'expérience CHOOZ qui a contraint ce paramètre. Notre connaissance sur θ_{13} peut être améliorée en réduisant à la fois les erreurs statistiques (grâce à l'augmentation de la taille du détecteur et de la durée de l'expérience) et systématiques. Pour cela, l'idée est d'utiliser un détecteur proche et un lointain identiques, annulant ou réduisant la plupart des erreurs systématiques liée à la production et la détection des antineutrinos. Egalement, une attention particulière est apportée aux bruits de fond engendrés par la radioactivité naturelle et les interactions des rayons cosmiques. Le travail présenté ici s'intéresse principalement aux enceintes acryliques Cible et Gamma Catcher, situées au cœur du détecteur. Un nouvel acrylique a été développé pour l'expérience puisque les matériaux pré-existant ne satisfaisaient nos exigences pour le détecteur. Ce matériau a été caractérisé optiquement, afin de maximiser la transmission de lumière et de réduire au maximum la zone morte créée par l'acrylique. De plus, une étude physique du dessin de la cible a été réalisée, pour identifier une possible distorsion spectrale ou modification du taux de comptage possiblement induites. La résistance du matériau au liquide a été certifiée. Egalement, l'acrylique est suffisamment radiopur pour que le taux de bruit induit soir négligeable comparé à celui venant des tubes photomultiplicateurs. Cependant, une source incertaine de bruits de fond est représentée par la possible contamination du détecteur, par entre autres de la poussière. C'est pourquoi nous avons défini des contraintes de propreté lors de la fabrication et l'intégration du détecteur, qui ont été respectées durant toutes les phases. Après trois ans de prise de données, Double Chooz pourra observer un signal d'oscillation à 3σ pour $\sin^2 2\theta_{13} > 0.05$ -0.06. Si aucune oscillation n'est observée, l'expérience mettra une limite sur $\sin^2 2\theta_{13}$ à 0.02 -0.03 à 90 % de confiance.